



HAL
open science

Laser ultrasonics in a diamond anvil cell for investigation of simple molecular compounds at ultrahigh pressures

Sergey Nikitin

► **To cite this version:**

Sergey Nikitin. Laser ultrasonics in a diamond anvil cell for investigation of simple molecular compounds at ultrahigh pressures. Acoustics [physics.class-ph]. Université du Maine, 2015. English. NNT : 2015LEMA1005 . tel-01259629

HAL Id: tel-01259629

<https://theses.hal.science/tel-01259629>

Submitted on 20 Jan 2016

HAL is a multi-disciplinary open access archive for the deposit and dissemination of scientific research documents, whether they are published or not. The documents may come from teaching and research institutions in France or abroad, or from public or private research centers.

L'archive ouverte pluridisciplinaire **HAL**, est destinée au dépôt et à la diffusion de documents scientifiques de niveau recherche, publiés ou non, émanant des établissements d'enseignement et de recherche français ou étrangers, des laboratoires publics ou privés.

THESE DE DOCTORAT

spécialité : Acoustique

Présentée par

Sergey NIKITIN

Laser ultrasonics in a diamond anvil cell for investigation of simple molecular compounds at ultrahigh pressures

Soutenue le 19 janvier 2015 devant le jury composé de:

B. Perrin	Directeur de Recherche, INSP, Paris	Rapporteur
A. Devos	Directeur de Recherche, IEMN, Lille	Rapporteur
T. Dekorsy	Professeur, Universitaet Konstanz, Konstanz	Examineur
E. Bossy	Maître de conférences, ESPCI, Paris	Examineur
B. Castagnede	Professeur, LAUM, Le Mans	Examineur
N. Chigarev	Ingénieur de recherche, LAUM, Le Mans	Co-directeur de thèse
A. Zerr	Chargé de recherche, LSPM, Villetaneuse	Co-directeur de thèse
V. Gusev	Professeur, LAUM, Le Mans	Directeur de thèse
A. Bulou	Professeur, IMMM, Le Mans	Invité

Le Mans, France

THESE DE DOCTORAT

spécialité : Acoustique

Présentée par

Sergey NIKITIN

Ultrasons laser dans les cellules à enclume de diamant pour l'étude des composés moléculaires simples à ultra- hautes pressions

Soutenue le 19 janvier 2015 devant le jury composé de:

B. Perrin	Directeur de Recherche, INSP, Paris	Rapporteur
A. Devos	Directeur de Recherche, IEMN, Lille	Rapporteur
T. Dekorsy	Professeur, Universitaet Konstanz, Konstanz	Examineur
E. Bossy	Maître de conférences, ESPCI, Paris	Examineur
B. Castagnede	Professeur, LAUM, Le Mans	Examineur
N. Chigarev	Ingénieur de recherche, LAUM, Le Mans	Co-directeur de thèse
A. Zerr	Chargé de recherche, LSPM, Villetaneuse	Co-directeur de thèse
V. Gusev	Professeur, LAUM, Le Mans	Directeur de thèse
A. Bulou	Professeur, IMMM, Le Mans	Invité

Acknowledgements

I am grateful to Agence National de la Recherche of France for the fellowship which provided opportunity to participate in and to contribute to a challenging laser ultrasonics application.

I would like to thank **Dr. Andreas Zerr** with whom I started my PhD at Université Paris 13. I really liked how I was supervised at that time. We had many interesting discussions, ideas and experimental works. I improved my experimental skills in optics and I opened myself to high pressure techniques. Andreas Zerr was always opened for explanation and discussion. He helped me a lot in science and in life questions. Also he always created positive work atmosphere. Despite the fact that during the first year of PhD I had a lot of work I enjoyed spending time at the laboratory from morning until night.

After Université Paris 13 I moved to Université du Maine and I started to tightly cooperate with **Dr. Nikolay Chigarev**. I was extremely impressed by all the optics devices which were presented to me. It was very interesting to investigate principle of work pump-probe system and picosecond laser ultrasonic technique. Nikolay Chigarev supervised and guided me very well in experimental work and also helped a lot with administrative matters. I want to say many thanks for the patient and understandable explanations during the work. I was very glad to do experimental investigations at Le Mans. I got strong experimental basis for working with ultrafast optics and picosecond acoustics.

During working in Université Paris 13 and Université du Maine my PhD researches were controlled by the director of thesis, **Prof Vitalyi Gusev**. I am very grateful for his help with my thesis. Also the installation process in France was very easy thanks to him. It was very interesting to listen to the explanation of physical phenomena at the elementary level. We had very interesting meetings and discussions. Vitalyi Gusev gave me a lot of useful advices. He helped me to organize a lot of administrative papers during my work, and helped in managing my time. He helped me a lot in the 'writing processes'. He was always cheerful and confident and was willing to work both day and night which inspires optimism towards the work.

I also want to say many thanks to **Alain Bulou** and **Vincent Tournat** who helped me a lot with the experiment and data processing. They gave me a lot of useful advices. Our cooperative discussions were very helpful and interesting.

I want to extend my gratitude to the entire staff, colleagues and friends of Université Paris 13 and Université du Maine. In particular, I want to thank **James Blondeau, Damien Gasteau, Samuel Raetz, Lei Xiong, Alberto Munoz, Mariusz Lejman, Frédéric Faese, Thibaut Devaux, Judith Bourguille and Hélène Pichard.**

Finally I would like to say special thanks to **Eloïse Maget** who helped in writing and presenting my thesis, and, especially, **Olga Nikitina**, who prepared and organized the day of my defense.

General introduction

History of optoacoustics (OA) had started in the end of the 19th century from the works of Alexander Graham Bell. This domain of physics is studying the conversion by a medium of light energy (UV, visible and IR ranges) to mechanical energy (acoustic waves). The modern optoacoustics is applied in many different areas (for measuring the properties of materials, for non-destructive testing, for imaging in biology and medicine, etc).

There are plenty different impacts on the material (mechanical, electrical, thermal, etc.) which can create acoustic waves in it if the exposure time is sufficiently small (much less than the characteristic travel time of an acoustic wave in the medium). When the source of acoustic generation is light, we are talking about optoacoustics. The mechanisms of optical excitation of sound (thermo-elastic mechanism, electrostriction mechanism, deformation potential mechanism, inverse piezoelectric effect, etc.) and parameters of acoustic field (amplitude, pulse width, pulse shape, directivity pattern, etc.) can be different. They depend on the material chosen for excitation of sound and the parameters of light source. Now the light source is usually a laser because it enables to work in a certain optical spectral range, to reach high electromagnetic energy density and to choose different optical pulse durations. The laser can also be used to detect the acoustic field since acoustic waves can change the optical properties of a material.

There are four main features of optoacoustics compared to other acoustic techniques:

1. small size of acoustic sources and detectors (several micrometers);
2. contactless operation achievable from a significant distance if necessary (generation and detection of sound in the sample can be carried out remotely);
3. opportunity, by using fs lasers, to generate and detect acoustic pulses with the duration shorter than 10 ps, corresponding frequencies higher than 10 GHz and acoustic wave lengths shorter than hundreds of nanometers;
4. access to imaging of the samples with high sensitivity and high spatial resolution.

The first feature is very important when dealing with small samples (e.g. with a size of a few cubic mm or less). The second feature may be useful when it is very difficult or impossible to reach or to contact the investigated object (extreme temperature of the object, radioactive object, object compressed to high pressures, etc.). The third feature allows investigating the sub- μm -scale properties of the samples (small cracks and defects, spatial inhomogeneity, thin films and small particles, nanostructures, etc.). Finally, the last feature is currently widely used in biology and medicine when it

is necessary to get deep images of objects with high spatial resolution (significantly better than 1 mm). The depth-profiling solid with a spatial resolution better than few tens of nanometers can be achieved.

In this work all the advantages of optoacoustics are used. Objects under study have dimensions smaller than 10^{-3} cubic millimeters, so it is necessary to have a small size of an acoustic generator and detector. The thickness of sample may be about 10 micrometers. Therefore the acoustic pulses for its testing should be very short. Objects, which are studied in this research work, are inside a special mechanical construction (diamond anvil cell) for creating extreme environmental conditions (high pressures and high temperatures); hence acoustic generation and detection must be remote. Finally in this study the opportunity to receive optoacoustic images of transparent substances under pressure with high sensitivity and high spatial resolution will be demonstrated.

This work is devoted to the study of the acoustic properties of materials at high pressure using optoacoustics. Material is divided into four chapters.

The first chapter is the overview of optoacoustics. Initially the general idea of optoacoustics is described. After this, the reader can find a brief history of optoacoustics development. Then several modern laser optoacoustic experiments are reviewed with an accent on possible applications of laser ultrasonics in imaging. At the end of this chapter the goals of the PhD research are formulated.

In the second chapter analytical theory of laser ultrasound in diamond anvil cell is described. The general solution for laser ultrasound generation via thermo-elastic effect at solid/solid interface is obtained. This theory assumes the use of the scheme “line-source - point-receiver”, sub-nanosecond laser pulses and two materials in contact - a transparent substance and an opaque substance (for illustration cases iron/diamond and aluminum/diamond are investigated). Under these conditions the profiles of the longitudinal and shear acoustic waves and the directivity patterns of ultrasound are obtained. The acoustic reflections at the interfaces of transparent substance and of opaque substance are also taken into account. The analysis demonstrates that the ultrasound, generated in the transparent medium due to its heating caused by the thermal conduction process across the interface, can provide important contribution to the total directivity patterns in both media. Using the general theoretical solutions, the directivity patterns for the ultrasound emitted into H_2O ice in contact with light absorbing iron film are predicted. They are evaluated at different pressures which can be obtained in diamond anvil cell and are favorably compared with available experimental data.

The third chapter is devoted to measurements of the refractive index of transparent media in diamond anvil cell. In general, the determination of the refractive index is direct way to probe the electronic structure of substance because the refractive index expresses the response of the distribution of charges to a perturbing electric field. So the measurements of refractive index are highly important and valuable by themselves. However, to have information about the optical properties of the medium

is also of particular importance for the evaluation of acoustic properties of the transparent medium using optoacoustics. In fact, the parameters accessible to optoacoustic measurements could be the combinations of acoustical and optical parameters and, because of this, the knowledge of optical parameters could be required to extract the acoustic parameters. In this work, for example, for the picosecond laser ultrasonics measurements in diamond anvil cell described later in Chapter IV, it is important to know the refractive index and the thickness of a sample. The product of these two parameters is known as the optical thickness of the sample. In Chapter III an interference method for measuring separately the thickness and the refractive index of the transparent sample in diamond anvil cell is used. This interference technique is applied for studying H₂O ice. The refractive index, the thickness and the volume of H₂O are measured as a function of pressure. Bending under pressure of the surfaces of the diamond anvil cell, which are in contact with transparent substance, is revealed.

Finally, in the fourth chapter the measurements of the acoustic velocity of H₂O in diamond anvil cell at high pressure are presented. For this purpose we use pump probe technique (picosecond ultrasonic interferometry or time-domain Brillouin scattering technique). The diamond anvil cell filled with water and metallic optoacoustic generator are prepared for these experiments. The acoustic signal laser-generated in Fe optoacoustic transducer and propagating in H₂O ice is detected optically. The sound velocity is obtained by analyzing the transient optical reflectivity signal. The acoustic properties of H₂O are evaluated up to 84GPa. Additionally the technique allowed imaging of elastic inhomogeneities and texturing of polycrystalline ice in the direction normal to the diamond anvil surfaces with sub-micrometer spatial resolution via time-resolved measurements of variations in the propagation velocity of the acoustic pulse traveling in the compressed sample. The achieved two-dimensional imaging of the polycrystalline ice aggregate in-depth and in one of the lateral directions indicates the feasibility of three-dimensional imaging and quantitative characterization of acoustical, optical and acousto-optical properties of transparent polycrystalline aggregates in diamond anvil cell with tens of nanometers in-depth resolution and lateral spatial resolution controlled by pump laser pulses focusing.

Contents

Chapter I.

Introduction	1
§I.1. Basic idea of optoacoustics.....	1
§I.2. History of optoacoustics.....	6
I.2.1. Early photoacoustics (1881-1961).....	6
I.2.2. Laser optoacoustics (1962-now).....	6
§I.3. Modern applications of optoacoustics.....	7
I.3.1. Nondestructive testing	7
I.3.2. Biology and Medicine.....	16
I.3.3. Material parameters in extreme conditions.....	21
§I.4. Goals of the PhD research.....	27
References (I).....	29

Chapter II.

Analytical theory of laser ultrasound in diamond anvil cell	33
§II.1. Generation of acoustic waves by laser.....	34
II.1.1. Optoacoustics equations in an isotropic solid.....	34
II.1.2. Acoustic potentials.....	35
§II.2. Solution for optoacoustics equations for solid/solid interface.....	36
II.2.1. Solution in the Fourier space.....	37
II.2.2. Reflection and transmission coefficients. Determinant Stoneley.....	39
II.2.3. Solution in the real space.....	40
§II.3. Description of the laser-induced thermo-elastic source.....	41
§II.4. Directivity patterns of laser ultrasound in diamond anvil cell.....	43
II.4.1. General case and delta-localized sources.....	43
II.4.2. Directivity patterns for Fe in diamond anvil cell.....	46
§II.5. Pulse profiles of the laser ultrasound.....	53
§II.6. Discussion and conclusions.....	59
References (II).....	64

Chapter III.

Measurement of the refractive index and thickness of a transparent H₂O sample compressed in a diamond anvil cell

66

§III.1.	Interference technique.....	67
III.1.1.	Optical measurement by using interference technique.....	67
III.1.2.	Interference of broadband light in diamond anvil cell.....	69
§III.2.	Experimental setup.....	70
III.2.1.	Scheme, functioning and elements of experimental setup.....	70
III.2.2.	Software for controlling the experimental setup.....	72
§III.3.	Samples (H ₂ O in diamond anvil cell).....	73
§III.4.	Refractive index of H ₂ O as a function of pressure.....	75
III.4.1.	Using iron and diamond wedge to get refractive index.....	75
III.4.2.	Using the equation of state of the diamond to get refractive index.....	79
§III.5.	Volume of H ₂ O as a function of pressure.....	81
III.5.1.	Thickness of H ₂ O in DAC as a function of pressure.....	81
III.5.2.	Transverse size of H ₂ O in DAC as a function of pressure.....	82
III.5.3.	Volume of H ₂ O and bulk modulus as a function of pressure.....	83
§III.6.	Curvature of the working surfaces of diamond anvil cell under pressure.....	84
§III.7.	Discussion and conclusions.....	85
References (III).....		90

Chapter IV.

Investigation of polycrystalline aggregates of H₂O ice in diamond anvil cell

91

§IV.1.	Picosecond acoustic interferometry technique.....	92
§IV.2.	Experimental setup.....	96
IV.2.1.	Pump and probe optical setup.....	96
IV.2.2.	Diamond anvil cell and the samples.....	98
§IV.3.	Experimental signals and their processing.....	98
§IV.4.	On the role of the induced optical anisotropy.....	106
§IV.5.	On the role of the acoustic refraction and diffraction.....	107
§IV.6.	On the amplitude of the TDBS signal.....	108

§IV.7	Measurements of sound velocities.....	109
§IV.8.	Discussion and conclusions.....	111
	References (IV).....	114
Conclusions and perspectives		117
<u>Appendices</u>		119
Appendix A.		
	Directivity patterns of laser ultrasound emitted from the interface of two solids in the 3D case....	119
Appendix B.		
	Directivity patterns of laser ultrasound emitted from mechanically free and rigid surfaces.....	120
Appendix C.		
	On the duration of the photo-generated acoustic pulse and ultimate in-depth spatial resolution of time-domain Brillouin scattering.....	122
Appendix D.		
	On the role of the induced optical anisotropy.....	122
Appendix E.		
	On the role of the acoustic rays refraction.....	124
Appendix F.		
	On the amplitude of the time-domain Brillouin scattering signal.....	124
	References(A).....	126

Chapter I

Introduction

In this Chapter, the basic modern applications of laser optoacoustics will be discussed with the emphasis on its imaging applications. The narrative begins with qualitative explanations of the optoacoustic effect. For simplicity the thermo-elastic mechanism for laser-induced generation of the acoustic wave in media with low thermal conductivity is considered. A more rigorous and complete approach for the description of the optoacoustic effect will be presented in Chapter III. Then the main events in the history of the optoacoustics are briefly presented. After this, several modern examples of using optoacoustics are given. In the end of this chapter a list of the goals of the PhD research is given.

§I.1. Basic idea of optoacoustics

As it was mentioned earlier (in General introduction) optoacoustic effect is based on the transformation of light energy into mechanical energy of the medium [1,2,3,4]. A part of this mechanical energy can propagate in form of the acoustic waves. Mechanisms for converting light into sound can be different and depend on the material and such parameters of laser action as laser pulse wavelength, duration and fluence. For illustration of the optoacoustic effect, let's consider the thermo-elasticity mechanism of generation acoustic wave in media with low thermal conductivity.

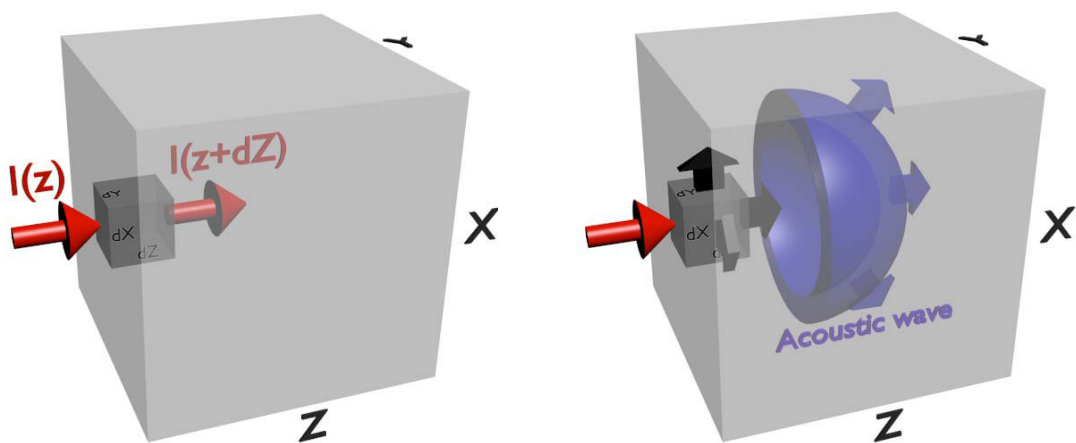


Figure I. 1. (left) Absorption of light energy by an infinitely small volume of the substance, $dV = dXdYdZ$. (right) Expansion of an infinitesimal volume caused by its heating and the generation of an acoustic wave in the substance.

Suppose that we irradiate the test substance by a short rectangular laser pulse of intensity $I(t) = I_0$ and duration τ_L (for example $\sim 100\text{fs}$). In this case, the surface density of laser pulse energy,

i.e., laser fluence, is $F_o = I_o \tau_L$. Let's take an infinitesimal volume in this substance, $dV = dXdYdZ$ (Fig.I.1). On the left boundary of the volume the intensity of laser radiation is equal to $I(z)$. After passing through the volume (towards the right boundary) intensity becomes $I(z + dZ)$. From this we can conclude that the energy absorbed by a given volume is

$$dQ = (I(z) - I(z + dZ)) \tau_L dS = (F(z) - F(z + dZ)) dXdY \quad (I.1)$$

where $dS = dXdY$ is the lateral surface area of the volume, i.e., normal to the light penetration direction. If we take into account that $F(z + dZ) = F(z) + \frac{dF(z)}{dz} dZ + \dots$, then the energy absorbed by a given volume is

$$dQ \cong -\frac{dF(z)}{dz} dZ dXdY \quad (I.2)$$

Very often the intensity of the laser radiation in matter obeys the Beer–Lambert law. This means that $F(z) = F_o e^{-\alpha z}$, where α is the attenuation coefficient of the substance, F_o is the laser fluence on the surface $Z=0$ of the substance. Then $\frac{dF(z)}{dz} = -\alpha F_o e^{-\alpha z}$ and the energy absorbed by a given volume is

$$dQ \cong \alpha F_o e^{-\alpha z} dZ dXdY \quad (I.3)$$

According to thermodynamics, if this absorbed laser energy is entirely transformed into heat then the temperature of the volume increases according to the law:

$$c_p m_v dT = c_p (\rho_o dV) dT = c_p (\rho_o dZ dXdY) dT = dQ \quad (I.4)$$

where c_p - the specific heat of the medium at constant pressure, m_v - the mass of a given volume, dT is the temperature increase of the volume, ρ_o - the density of the medium. If we take into account the equation of state of the medium $p = p(\rho, T)$ [5] and that $\rho \cong \text{const}$ ($d\rho \cong 0$) during rapid heating,

then it is possible to write the following relationship between the increase of temperature dT and the additional pressure $p' \equiv dp$ induced in the medium:

$$p_{ac} \equiv p' = p(\rho, T) - p_0 \cong dp(\rho, T) = (c_0^2)d\rho + (c_0^2\rho_0\beta)dT \cong (c_0^2\rho_0\beta)dT \quad (I.5)$$

Where $p_{ac} \equiv p'$ - the additional pressure in medium (acoustic pressure), p_0 - the equilibrium pressure in medium, c_0 - the adiabatic speed of sound (longitudinal), β - the volumetric coefficient of thermal expansion. Thus Eq. (I.4) can be rewritten as

$$\frac{c_p(\rho_0 dZdXdY)}{c_0^2\rho_0\beta} p' = \frac{c_p(dZdXdY)}{c_0^2\beta} p' = dQ \quad (I.6)$$

From Eqs. (I.3) and (I.6) we can find that as a result of short laser heating of volume dV this volume becomes a point source of the acoustic waves with the characteristic amplitude of pressure:

$$p_{ac}(z, t = 0) = p' = \frac{c_0^2\beta\alpha F_0 e^{-\alpha z}}{c_p} \quad (I.7)$$

It is extremely important to note that even if we are able to excite in the infinitesimal volume dV the acoustic waves propagating in all the directions, i.e., spherical source in the case of isotropic media, the amplitude of the emitted acoustic wave outside the region of laser-induced heating will be different in different directions of wave propagation depending on the spatial distribution of heat release and the mechanical boundary conditions on the surface of the light absorbing medium. The latter is due to the following feature of optoacoustics: the acoustic waves are not generated on the surface of the sample; the acoustic waves appear beneath the surface. Thus there are two parts/contributions in the photo-generated waves launched in the sample by pulsed laser action. One part of the initially generated waves propagating after the generation directly towards the bulk of the sample, while another part propagates first towards the surface. The latter part reaches the sample surface from inside and is reflected. The reflection coefficient at the boundary of a substance depends on the angle of incidence of the sound wave. Since there are all possible angles of incidence of the sound in a spherical wave incident on the (including even complex pure imaginary angles corresponding to evanescent waves [6]), then the acoustic wave reflected from the surface will be not spherical any more in a sense that the amplitude and the phase in the reflected wave depend on the

direction of its propagation. Thus the total acoustic field emitted by the volume dV in the bulk of the medium will have two contributions: direct spherical wave whose amplitude does not depend on the direction of propagation and the wave reflected from the boundary, for which amplitude and phase depend on the direction of propagation.

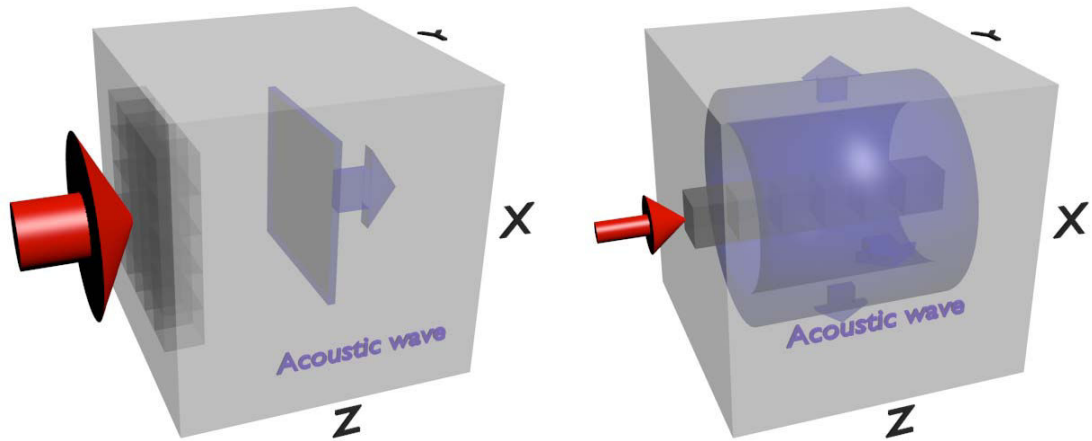


Figure I. 2. (left) Generation of a plane acoustic wave by a wide laser beam in strongly light absorbing medium. (right) Generation of a cylindrical acoustic wave using a narrow laser beam and weakly light absorbing medium.

From symmetry considerations it is possible to imagine different situations in optoacoustic generation depending on the spatial form/localisation of the laser-induced heating. For example, if the elementary sound generation volumes dV are located in the vicinity of the sample surface (wide laser beam and strong light absorption in the substance), then a nearly plane wave will be generated (Fig. I.2. (left)). In the opposite case, when the laser beam is extremely narrow while the sample is nearly transparent (weakly absorbing medium), then a cylindrical acoustic wave is created (Fig.I.2 (right)).

It is also possible to qualitatively understand the form of an acoustic pulse which could be generated in the sample. Let us first consider the situation where the laser pulse duration is much shorter than the time of acoustic wave propagation across the light penetration depth. After the absorption of laser radiation by matter, each element dV creates an acoustic wave. According to equation (I.7) the elements which are deeper from the border create acoustic waves of smaller amplitude. In the case when the generation of sound by infinitely large laser beam occurs near an acoustically rigid boundary the shape of the acoustic pulse will look like one presented in Fig. I. 3 (left). Full profile consists of direct and reflected from the rigid boundaries waves. Note that the reflection coefficient for pressures waves normally incident on the rigid boundary is equal to 1. The leading front profile of the acoustic pulse replicates in the considered case the spatial distribution of the light fluence and of the temperature rise in the medium. The shape of the trailing front is completely symmetrical to that of the leading front. In a general case of the non-instantaneous laser

action, the time profile of the pressure wave will be a convolution of the pressure profile presented in Fig. I. 3 (left) and with the temporal envelope of the laser pulse intensity. Imagine an asymptotic situation which is an opposite to instantaneous laser action: the laser pulse is so long that during the laser action the acoustic waves have enough time to penetrate in the material up to the depths significantly exceeding the light absorption depth. In this case, the optical pulse can be divided into multiple short parts. Each pulse generates an acoustic wave which immediately begins to penetrate in the medium. When the next part of the laser pulse reaches the sample it creates the next acoustic wave, but the first wave had already some time to shift from the generation region. Thus, the acoustic pulse generated by long rectangular laser pulse could be imagined as a long continuous sequence of the individual pulses of the shape presented in Fig. I.3. (left). It is clear that the profile of the total acoustic pulse will be approximately rectangular and the duration of the acoustic pulse will be approximately equal to the duration of the laser pulse (see Fig. I.3. (right)). The slight deviations between the shapes of the acoustic and laser pulses take place at the leading and trailing fronts at the time scale of sound propagation across the heated region, which is assumed to be much shorter than the laser pulse duration, and, thus, are practically negligible and are not presented in Fig. I.3. (right). In the general case of long laser pulses with smooth profiles of laser intensity envelope $I(t)$ the profile of the acoustic pressure pulse generated near mechanically rigid boundary replicates the profile $I(t)$ [7].

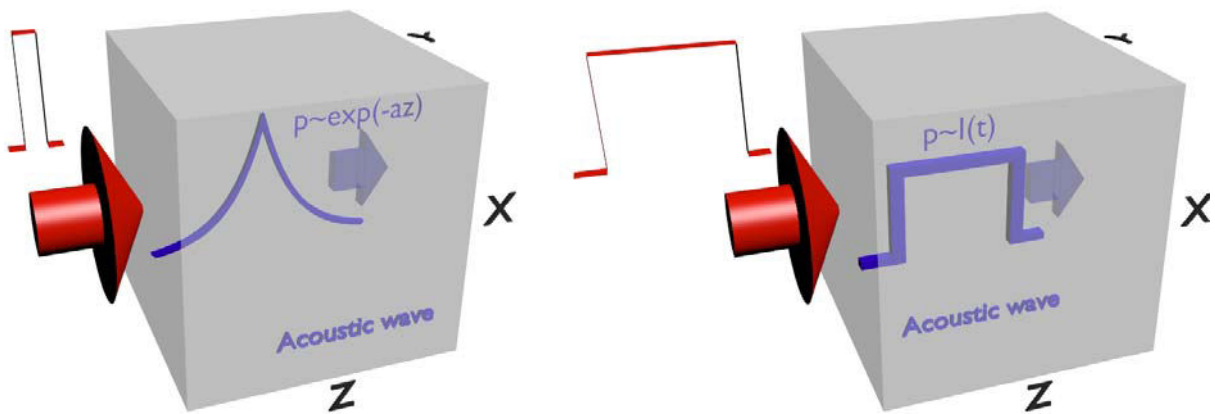


Figure I. 3. (left) The shape of the acoustic pulse which is excited by an “short” laser pulse in media with low thermal conductivity (under rigid boundary conditions). (right) The shape of the acoustic pulse which is excited by a “long” laser pulse (under rigid boundary conditions and negligible light penetration depth).

The above qualitative discussion provides opportunity to list the steps which are commonly followed in solving the problem of the sound generation by lasers:

1. To find the distribution of light energy deposited in the material after laser irradiation. In most cases, this distribution obeys the Beer–Lambert law. But in some cases (for example highly scattering medium) this distribution is more complicated [10].

2. To describe how light energy is transformed into pressure (stress) by each element dV of sample which absorbed light. Mechanisms for energy transformation can be different, i.e., not only thermo-elasticity mechanism [8,9]. In the general case both the spatial distribution of the photo-induced stresses and their temporal dynamics should be predicted.

3. To find the solution of the acoustic wave equation with a known spatio-temporal dynamics of laser-induced stresses in the sample.

§I.2. History of optoacoustics

I.2.1. Early photoacoustics (1881-1961)

For the first time optoacoustic effect was observed by Alexander Graham Bell in 1880 [11]. He noticed the pressure pulsations in a closed gas volume which absorbed modulated light beam. This discovery was shortly confirmed by Tyndall [12] and Röntgen [13]. Bell proposed to use this effect to study the spectral dependence of light absorption by gases and vapours. However, at the time the studies and applications of optoacoustic effect did not spread widely due to the lack of sufficiently powerful light sources and reliable tools of measuring the acoustic signals.

I.2.2. Laser optoacoustics (1962-now)

Invention of the laser in the early 60's of the last century, once again aroused significant interest in the optoacoustic effect. The first optoacoustic experiments in liquid medium using a laser as a light source were conducted in the Soviet Union in 1963 by Askar'yan, Prokhorov, Chanturiya, and Shipulo [14]. Generation of acoustic waves in solids using a laser were performed in the USA by White at the same time [15,16]. Optoacoustics reached a new level of quality with the use of the lasers. Description of the advances in this area of that time can be found in reviews [17,18,19].

One of the first books devoted to laser techniques for the generation and detection of ultrasonic waves in materials is *Laser Ultrasonics: Techniques and Applications*, which was published in 1990 [1]. This book provides a full description of the state of the art in several research fields involving both lasers and ultrasonics. This practical book focuses mainly on the possible applications of the

optoacoustic techniques, leaving the studies of the physical mechanisms of optoacoustic transformation aside.

Another well-known book which is devoted to the optoacoustic effect is *Laser Optoacoustics* [7]. This book was published in 1991 (in Russian). The English version of this book was published in 1993. In this book, the basic mechanisms and features of the optoacoustic excitation of sound are considered. Also in the book the basic theoretical/mathematical approaches for the analysis of optoacoustic phenomena are presented, the general approach for the analysis of pulse-mode optical excitation of sound is described.

Now there exist books and reviews which describe various particular applications of optoacoustics. For example non-destructive testing of physical and mechanical properties of materials via optoacoustic techniques is described in the book *Ultrasonic Nondestructive Evaluation: Engineering and Biological Material Characterization* [20]. Applications of the optoacoustics for biology and medicine are described in the book *Photoacoustic Imaging and Spectroscopy* published in 2009 [21].

§I.3. Modern applications of optoacoustics

In this paragraph several modern optoacoustic experiments are reviewed with an emphasis on possible applications of laser ultrasonics in imaging and in the study of various properties of materials.

I.3.1. Nondestructive testing

Nondestructive testing is a wide group of the practical techniques used in science and industry to evaluate the properties of a material, component or system without causing damage.

The problem of nondestructive testing of composite materials is rather urgent, since defects in structures arising during manufacture and operation of articles can reduce considerably the strength of materials. Therefore, the elaboration of methods for nondestructive evaluation and defectoscopy of composite materials which would make it possible to carry out investigations either at a stage of manufacturing or during operation of the articles is of great importance. The typical damages and defects of the structure of composites are microcracks and pores in the sample, rupture of the fibers and their separation from the binder, and defects such as folds and discontinuities. It is worth mentioning here that the most important task is the confirmation and imaging of the damage, i.e., revealing the existence of the defects and determining their sizes and localization/distribution, while the task of quantitative characterization of the defect physical parameters could be a secondary one.

One of the most widespread methods for nondestructive evaluation is the ultrasonic method. The ultrasonic diagnostics in most cases is based on investigation of the frequency dependence of the attenuation, scattering or velocity of ultrasonic waves upon their propagation through a specimen [22]. The frequency dependence of the attenuation coefficient of the ultrasound in a sufficiently wide spectral range can be used for estimating the characteristic sizes of inhomogeneities of the composite structure [23]. The detection of scattered ultrasound is the most developed method of ultrasonic imaging.

For solving the problems of non-destructive evaluation, the use of laser thermo-elastic generation of sound is rather promising [1]. Upon thermo-elastic generation of sound in a medium with known thermo-physical and acoustic parameters and at given parameters of the absorbed laser radiation (energy and pulse length), it is possible to obtain high-power wide-band acoustic pulses with known characteristics—the amplitude and duration (or frequency spectrum)—and to use them for the acoustic spectroscopy and imaging of composite materials. Laser pulses of different durations can be used in laser optoacoustic setups for non-destructive testing depending on particular required applications.

In Ref. [24], the possibility of applying an optoacoustic technique for the solution of the problems of non-destructive ultrasonic imaging of composite materials is considered. In that case, short acoustic sounding signals (~ 10 ns) had to be used, since effective reflection from a defect occurs only when the pulse length is comparable with the dimensions of the defect. The length of the shortest of the acoustic pulse fronts determines the resolving power of this method of defectoscopy/imaging. Laser ultrasonics based on the use of the nanosecond laser is perfect for the noncontact generation of the required type of the acoustic pulses [7,24].

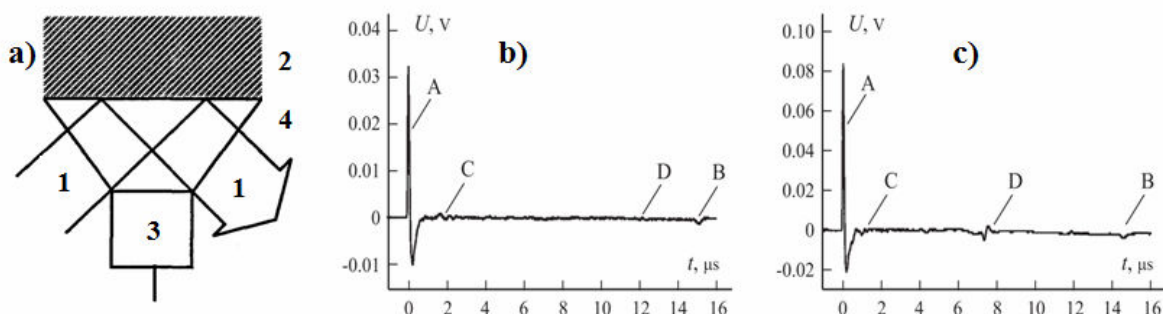


Figure 1.4. Experimental scheme (a) and temporal profiles of OA pulses obtained by a laser optoacoustic technique in graphite-epoxy composite specimens containing a compaction-type defect (b) and an air cavity (c). (a): 1-laser pulse, 2 - sample under investigation, 3 - wide-band piezoelectric sensor, 4 - a prism transparent to laser radiation, A—the reference pulse generated upon absorption of a laser pulse in the near-surface layer, B is the pulse passing through the specimen and reflected from its back surface, C is the part of the reference pulse backscattered by the structural inhomogeneities and defects of the composite (or the “structural noise”). The latter occupies the space between the pulses A and B on the time scale and forms a long disordered track/image. Symbol D designates the part of a reference acoustic pulse reflected from the defect of the composite structure and registered by the receiver with a time delay corresponding to the travel time of the ultrasound toward the defect and back [24].

However, the technique developed in Ref. [24], which used the laser pulses of 10-12 ns duration for the generation of the acoustic pulses, was not all-optical (Fig.I.4a). The acoustic pulses backscattered by structural inhomogeneities and defects were registered by a wide-band piezoelectric transducer, which makes it possible to detect acoustic pulses with very high sensitivity in the frequency range from 0.1 to 30MHz. Since the generation and detection of acoustic pulses takes place on the front surface of the specimen, this method allows carrying out nondestructive evaluation with one-sided access to the object under study. The developed method makes it possible to determine the type of defects and the depth of their location by measuring the arrival times of acoustic echoes (Fig.I.4). Thus the detected signal provides an image of the defects distribution in the sample.

In [25] a new type of a balanced fiber-optic Sagnac interferometer is presented as a part of an all-optical laser ultrasonic pump-probe system for non-destructive testing and evaluation of aircraft composites.

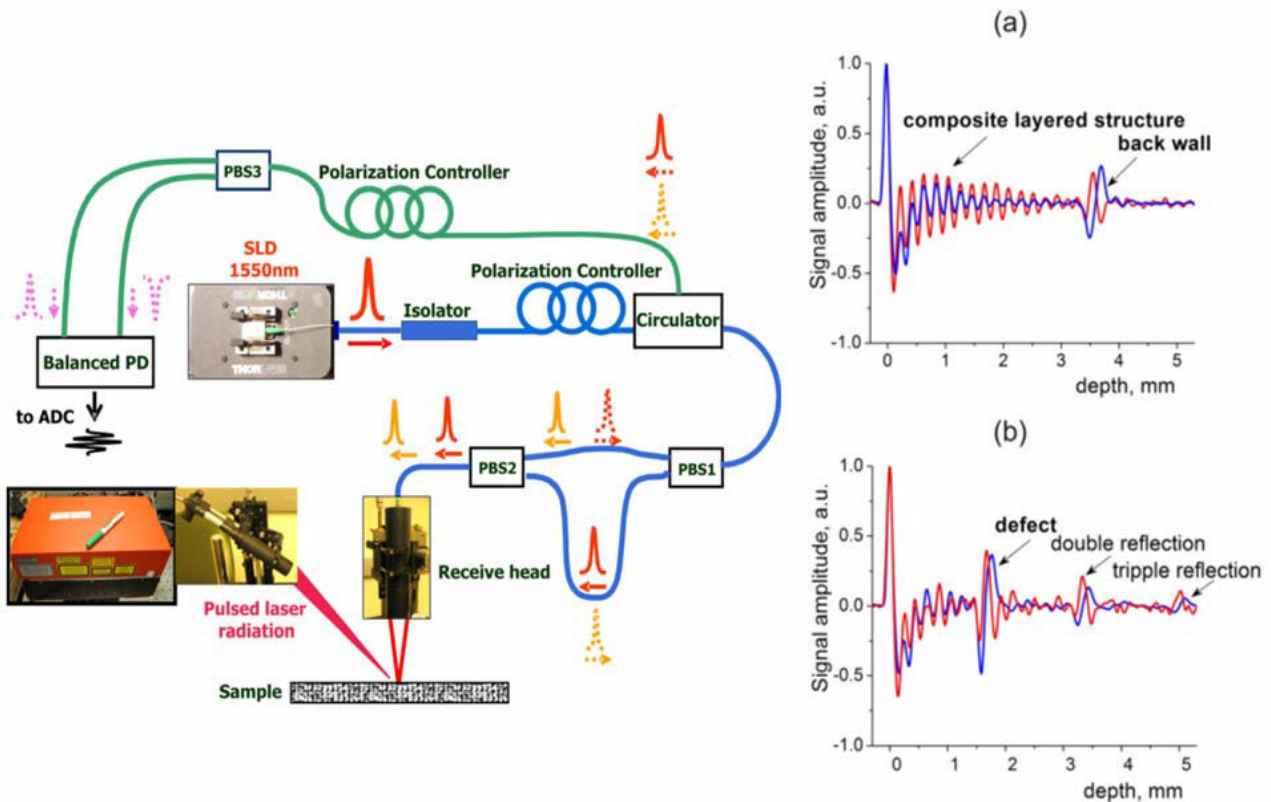


Figure 1. 5. (left) Main components and operating principle of the all-optical pump probe system for NDT&E of composite materials. A compact, very high repetition-rate (up to 76kHz) fiber laser with transmit head connected to the fiber laser using a 3m fiber bundle (in the left corner) irradiates the sample surface with nanosecond laser pulses, inducing optoacoustic generation; the receive head connected to the fiber-optic balanced Sagnac interferometer with a polarization-maintaining optical fiber is used for non-contact ultrasound signal detection. (right) Single shot (without signal averaging) A-scan (line) images recorded with Sagnac interferometer (red line) and with contact PVDF detector (blue line) in the region without (a) and with (b) inclusion (brass foil) [25].

The performance of the LU imaging system is demonstrated on a composite sample with known defects. Wide-band ultrasound probe signals are generated directly at the sample surface with a

pulsed fiber laser delivering nanosecond laser pulses of 60 ns duration at a repetition rate up to 76kHz rate with a pulse energy of 0.6 mJ. A balanced fiber-optic Sagnac interferometer is employed to detect pressure signals at the same point on the composite surface. A- and B- scans obtained with the Sagnac interferometer are compared to those made with a contact wide-band polyvinylidene fluoride transducer (Fig. I.5). It is worth mentioning here that laser ultrasonics, being a non-contact technique, has obvious advantages for imaging applications in comparison with contact techniques. The lateral scans (B- scans) can be produced by relative lateral displacement of the sample and the pump/probe focus positions normally to the directions of the pump and probe laser beams.

The examples presented above demonstrated the typical applications for imaging of laser ultrasonics based on the use of the nanosecond lasers. At the same time optoacoustic technique allows the characterization of thin films with thicknesses from a few tens of Angstroms to greater than 10μ [26,27,28,29,30]. For these purposes, laser sources with the duration of the light pulse fs and ps are commonly used (picosecond ultrasonics technique [32,33]). A thin-film optical testing methods are described in [26,27] for both thickness and sound velocity measurements of transparent films on opaque substrates with laser picosecond acoustics using the optical pump-probe technique. The experimental results in [28] are presented for sputtered thin films of silica of thickness from 200 nm up to 2 μ m thickness on amorphous germanium substrates. The experimental results in [27] are presented in Fig. I.6. In [27] it was demonstrated that the propagation time and attenuation of the acoustic pulses in transparent film on a transparent substrate can be monitored through the analysis of the onset and of the amplitude of the Brillouin oscillation induced by the transmission of the picosecond acoustic pulse into the substrate.

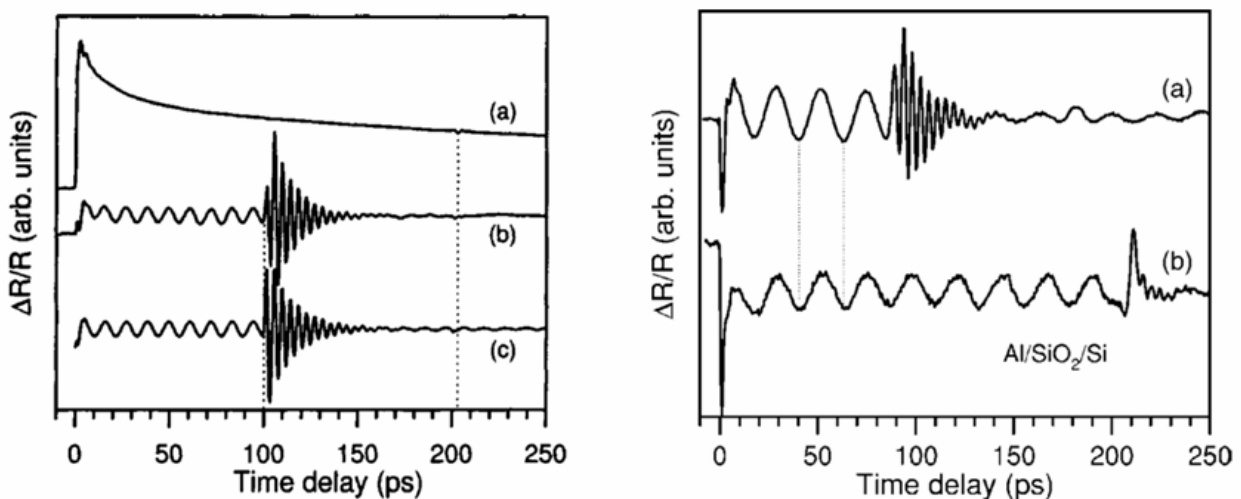


Figure I. 6. (left) (a) Experimental result obtained in a Al/Si₃N₄/Si sample in picosecond ultrasonics with pump and probe both centered at 804 nm; (b) idem with a probe centered at 402 nm; (c) theoretical simulation of (b). (right) Experimental results obtained in Al/SiO₂/Si samples which differ by the SiO₂ thickness [(a) 500 nm, (b) 1200 nm]. One should note that both low frequency oscillations have the same period and the different starts of the high frequency oscillations [27].

Now several picosecond laser ultrasonic technologies are used in industry. For example, the company Rudolph Technologies, Inc. proposes picosecond ultrasonics technologies for thickness measurements of opaque films [31] and for controlling the bumps [30].

In [28], using an ultrafast optical pump/probe technique ultrafast, mechanical displacements of the surface of thin opaque films in the 0.1-THz range have been directly observed in the time domain. An exceptional sensitivity to atomic-scale inhomogeneities by observing an anomalous reflection from a buried film of monolayer order in thickness was demonstrated. In [29] a picosecond ultrasonics technique was used to detect interfacial fluorocarbon C_Fx layers as thin as 0.5 nm between aluminum and silicon. This provides means for non-invasive identification of organic/polymeric contaminants at the buried interface and potentially for characterizing interfacial mechanical properties. The experiments reported in [28] and [29] are the first picosecond laser ultrasonics experiments where the imaging of the highly in-depth localized buried inhomogeneities/defects was achieved by optoacoustic techniques at nanoscale.

In [34, 35] nanoscale noncontact depth profiling of mechanical and optical properties of transparent sub-micrometric low-k material film exhibiting inhomogeneities which are distributed in the depth of the film was achieved by picosecond acoustics interferometry (Fig. I.6).

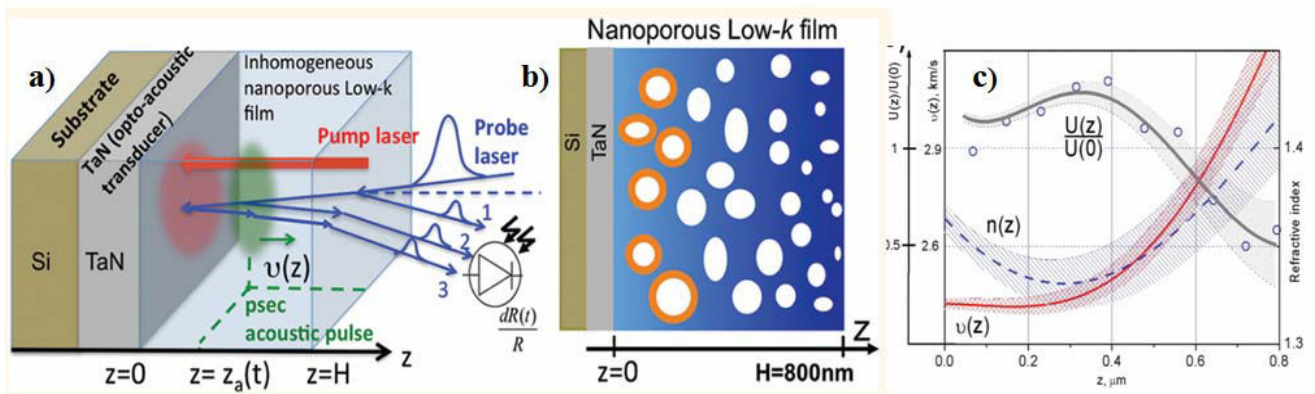


Figure I. 7. (a) Pump laser (in red) excites acoustic pulse (in green) of about 10 nm spatial length. This acoustic pulse scatters probe laser pulses, which are measuring the transient optical reflectivity of the sample. (b) Representation of the sub-micrometric inhomogeneities that exist within nanoporous transparent film. The white disks are nanopores. Their dimension varies from the free surface toward the TaN low-k interface. The blue matrix is organo-siloxane medium. The color gradient reads that the deeper (lighter) blue is in the region of higher (smaller) elastic modulus. Some nanopores still contain polymeric porogen (orange edge of pores) that was not completely removed during nanomanufacturing. (c) Depth profiles of the refractive index, $n(z)$, the sound velocity, $v(z)$, and the normalized photoelastic coefficient, $P(z)/P(0) \approx U(z)/U(0)$, obtained by opto-acoustic nanometrology [35].

In this experimental opto-acousto-optic technique the transient reflectivity signal, measured at a particular delay time of the probe laser pulse relative to the pump laser pulse, contains extractable

information on the acoustical, optical and acousto-optical parameters of the inhomogeneous media in the region of the picosecond acoustic pulse localisation at this particular time instance (see Chapter IV for the details). In the experimental data accumulated in inhomogeneous transparent media [34, 35] both the amplitude and the frequency of the so-called Brillouin oscillation, which in the case of homogeneous film in Fig. I. 8 are constant, vary with the increasing time delay. Thus, from the record of the transient reflectivity signal the in-depth profiles of the material parameters can be extracted. The in-depth resolution of this imaging technique is potentially limited neither by the optical wave length in the media, nor by the acoustic wave length at the Brillouin frequency.

As it was mentioned above all-optical laser ultrasonics techniques, being non-contact, provide rather simple opportunities for producing lateral images. In particular, imaging of the sample surface could be achieved by applying acoustic waves propagating along the surface.

All-optical monitoring of the nonlinear motion of a surface-breaking crack is reported in [36]. The experiments were conducted both in the reflection geometry [Fig. I. 8a] and in the transmission geometry [Fig. I. 8b]. A solid-state laser with pulse duration of 0,75 ns, pulse repetition rate of 1 kHz at wavelength of 1064 nm is used for the generation of the ultrasound. The incident laser beam is focused into a line with the length of 200 μm and width of 10 μm . A continuous laser at wavelength of 532 nm is used for the detection of the surface acoustic disturbances. The diameter of the probe beam on the surface of the sample is approximately 10 μm , and the distance between the pump and the probe beams is fixed at $d \approx 422 \mu\text{m}$. The radiation of a 800 nm wavelength diode laser modulated at frequency of $f \approx 0.05 \text{ Hz}$ (square modulation) was focused on the crack in a spot with a radius of approximately $a \approx 80 \mu\text{m}$ to achieve periodic heating. The optical power of the heating laser varies in the range of 0 to 0.28 W. The distance between the crack and the pump is approximately $s \approx 85 \mu\text{m}$.

Crack closing is induced by quasi-continuous laser heating, while Rayleigh surface acoustic pulses and bulk longitudinal surface skimming acoustic pulses are also generated and detected by lasers. By exploiting the strong dependence of the acoustic pulses reflection and transmission efficiency on the state—open or closed—of the contacts between the crack faces, the parametric modulation of ultrasonic pulses is achieved. It is observed that bulk acoustic waves skimming along the surface can be more sensitive to crack motion than Rayleigh surface waves (Fig.I.8). Directly arriving surface skimming longitudinal wave, is marked by “L”. The surface skimming longitudinal wave reflected by the crack is marked by “rL”. The directly arriving surface Rayleigh wave is “R” and the Rayleigh wave mode-converted by the crack from the skimming longitudinal wave is “rR-L”. The latest clearly detectable signal is the surface Rayleigh pulse reflected by the crack (“rR”).

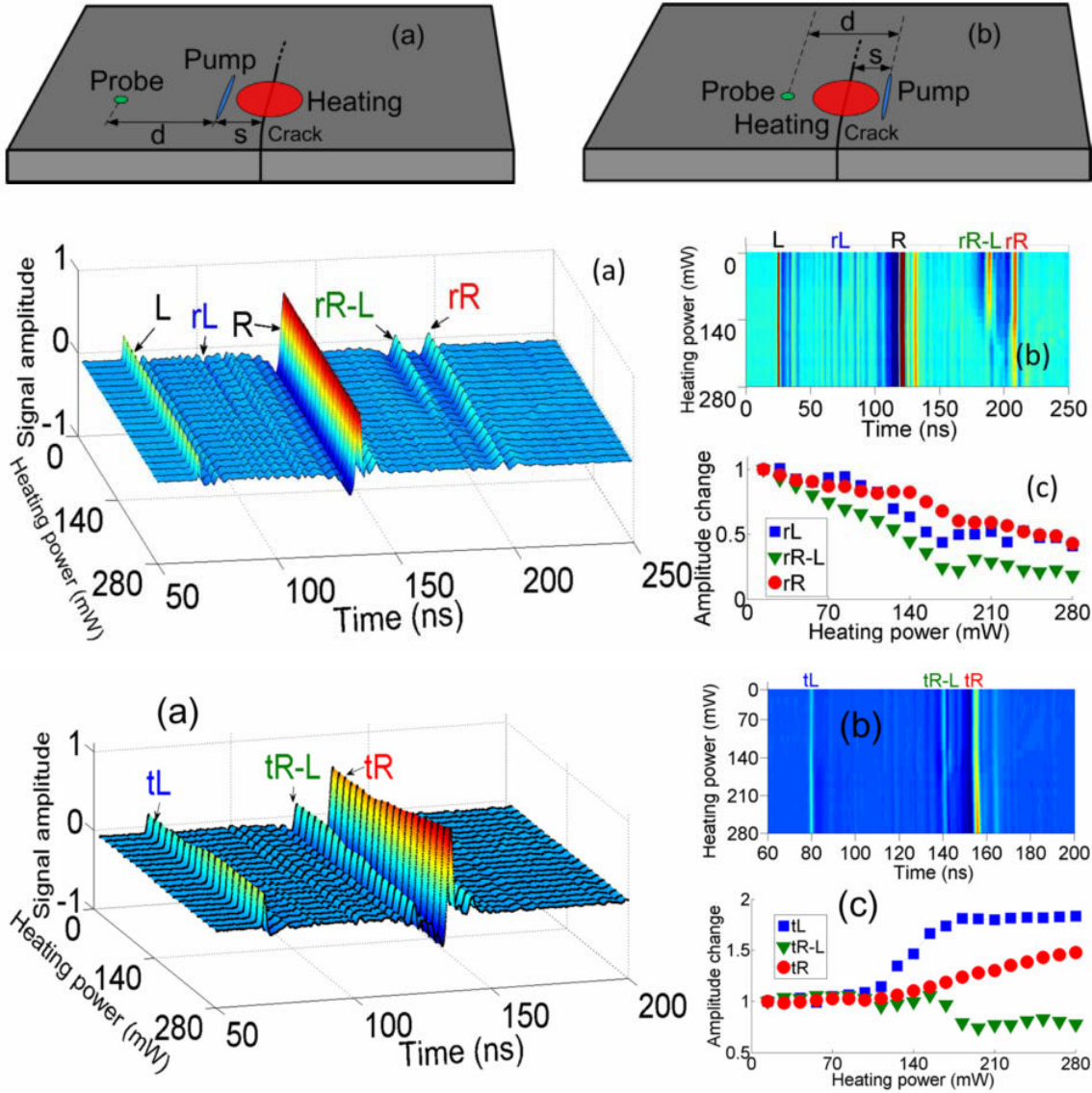


Figure I. 8. (top) Schematic diagram of the experiment. (a) Reflection configuration; (b) transmission configuration. (middle). Experimental results in reflection configuration. (a) Variation of the acoustic pulse profiles with increasing heating power; (b) top view of (a); (c) peak-to-peak amplitudes of signals rL, rR-L, and rR as a function of the heating laser power. (down) Experimental results in transmission configuration. (a) Variation of the acoustic pulse profiles with increasing heating power; (b) top view of (a); (c) peak-to-peak amplitudes of signals tL, tR-L, and tR as a function of the heating laser power [36].

Two-dimensional imaging of a crack by nonlinear frequency-mixing photo-acoustic method is reported in [37]. The excitation of the thermo-elastic pump wave is realized by a 532 nm wavelength 2W power continuous wave laser (Coherent, Inc., Verdi) intensity modulated at f_L . The 100% intensity modulation is achieved by an acousto-optic modulator (AA Opto-Electronics, Inc., Model MQ180) at frequency $f_L \approx 1$ Hz. The acoustic probe wave is generated by a 800 nm wavelength, 1W power diode laser, 100% intensity modulated at frequency f_H . The frequency f_H , is chosen of 25 kHz, so that it coincides with a resonance frequency of the sample. Both pump and probe laser beams are focused on the same location on the sample surface. The $1/e$ diameters are 100 and 300 μm for the pump and

probe beam, respectively. The signal, detected by an accelerometer of 50 kHz bandwidth, is sent to a spectrum analyzer.

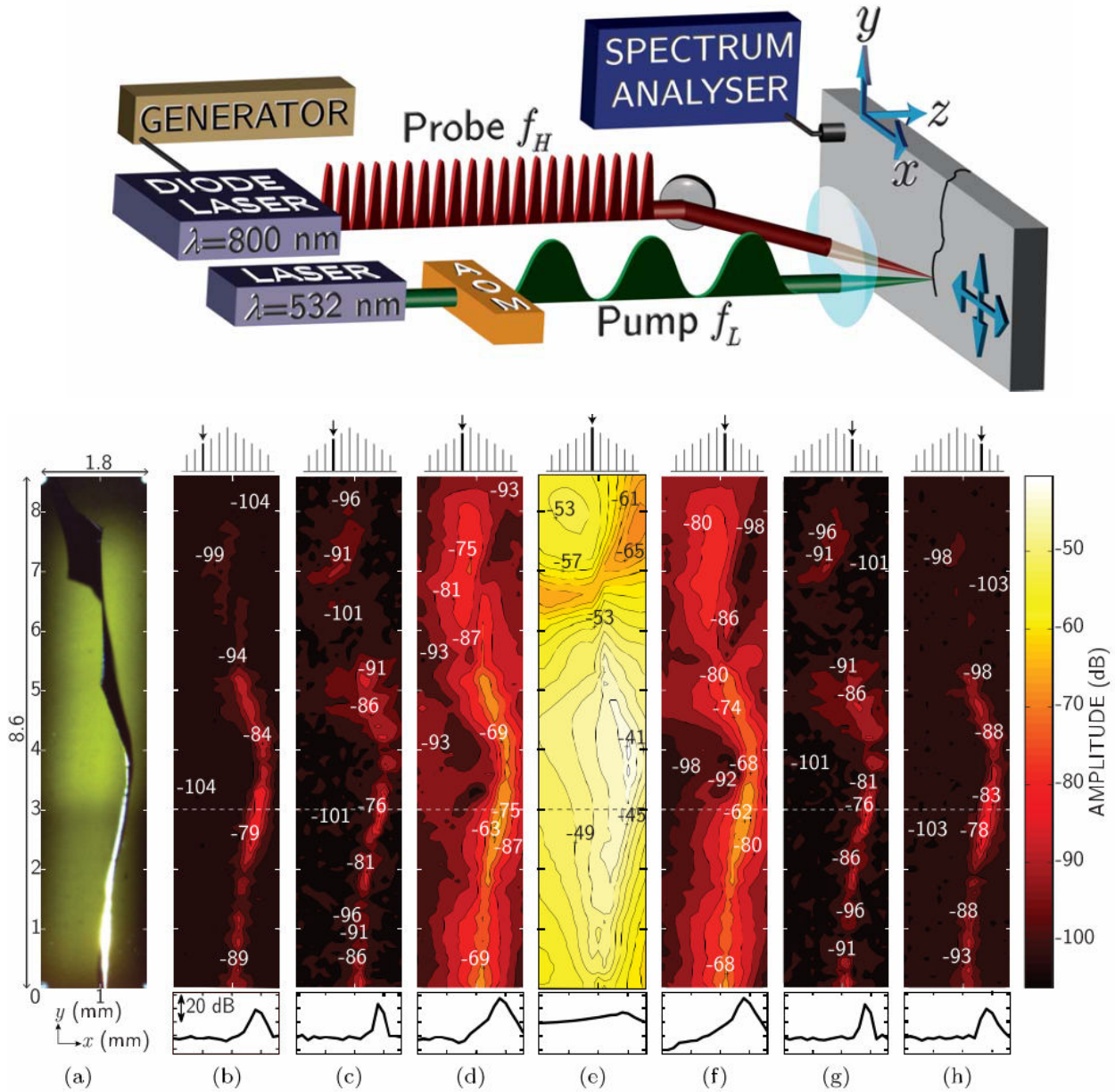


Figure 1. 9. (top) Schematic representation of the experimental set-up. (a) Optical image of the scanned area with the crack. (b)–(h) Top: Schematic representation of the analyzed spectrum component. Middle: Two dimensional optoacoustic images of the crack achieved by detection of different side-lobes at $f_H \pm n f_L$. From left to right, the first three nonlinear left side-lobes: $n=-3$ (b), $n=-2$ (c), $n=-1$ (d), the main peak, at f_H (e), and the first three nonlinear right side-lobes for $n=1, 2, 3$ (f)–(h). All scans are represented with the same amplitude scale. Amplitude difference between two isolines is of 2dB for $n=0$, 6dB for $n=\pm 1$, and 5dB for $n=\pm 2, \pm 3$. Bottom: Scan section along x for $y=3\text{mm}$ (dotted line in middle figures). All scans are represented with the same amplitude scale [37].

The imaging contrast is due to nonlinear photo-thermo-acoustic processes taking place in case of simultaneous excitation by lasers of thermo-elastic and acoustic waves in the vicinity of the cracks. The images are obtained by scanning of two co-focused laser beams in region of crack location. The first cw laser beam, modulated in intensity at low frequency f_L , generates a thermoelastic wave, which

is able to strongly periodically modulate the local crack rigidity up to complete closing/opening of the crack. The second cw laser beam, intensity modulated at much higher frequency f_H , generates an acoustic wave incident on the breathing crack. The crack rigidity is also influenced by the stationary non-modulated inhomogeneous thermal stresses caused by the stationary heating of the sample by both lasers. The main contribution to imaging contrast comes from the strong dependence of the reflectivity of acoustic waves on the crack rigidity. The modulation of crack rigidity by thermo-elastic wave leads to the parametric modulation of the reflected acoustic waves and the generation in the spectrum of the acoustic field of the side lobes, which are separated from f_H by the integer number of f_L . Optoacoustic images of a crack with an amplitude dynamics up to 40dB and a spatial resolution better than 100 μm , are obtained through the mapping of nonlinear side lobe amplitudes (Fig.I.9).

Picosecond laser ultrasonics has been also recently applied for lateral surface/subsurface imaging [38].

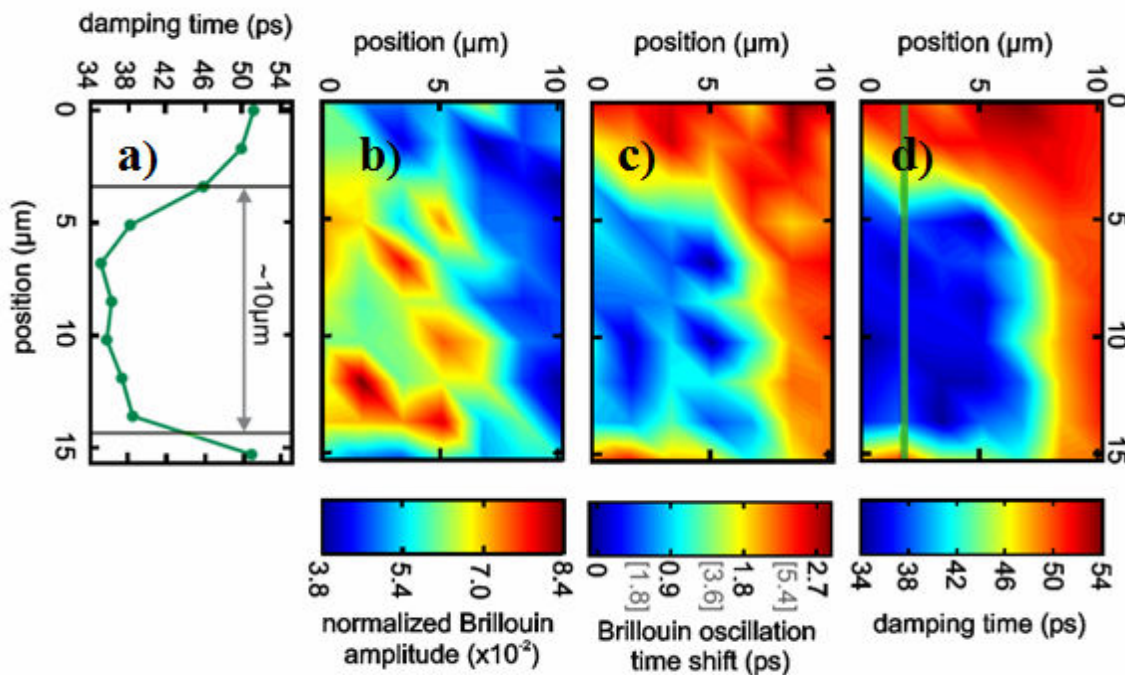


Figure I. 10. Color-coded area scans of the square with a base-dose multiplier of 300. (d) Damping time with blue regions corresponding to areas where the molecules are removed. (c) Time offset shift of the Brillouin oscillation. Numbers in square brackets denote corresponding APTES layer thicknesses for a sound velocity of 2000m/s in nanometers. (b) Brillouin amplitude normalized to the gold film amplitude. (a) Line profile of the solid green line in (d) [38].

In this research a molecular layer of aminopropyltriethoxysilane is patterned with a focused ion beam and subsequently covered by a gold film. The gold-polymer-substrate structures are afterwards imaged by ultrafast coherent acoustic phonon spectroscopy in reflection geometry. The lateral structure of the covered polymer layer can be imaged either by determining damping time of the

vibrational mode of the gold film (Fig. I. 10 (d)) or detecting the onset of the Brillouin oscillations in the substrate in different lateral positions on the surface. Note that both the delay time in the onset of the Brillouin oscillations Fig. I. 10 (c)) and their amplitude Fig. I. 10 (b)) can be applied in this imaging technique providing information on the molecular layers connecting gold and the substrate. The lateral spatial resolution of this imaging is controlled by focusing of the laser radiation.

I.3.2. Biology and Medicine

Another fast-growing applications of laser optoacoustics are in biology and medicine. Similarly to the case of the nondestructive testing in biological and medical applications both laser ultrasonics and picosecond laser ultrasonics can be used.

The main physical mechanism responsible for the optoacoustic transformation when using nanosecond optoacoustics is usually the thermoelastic effect [7]. A general idea of the photoacoustic imaging can be explained in this case as follows. Laser pulse is absorbed by the sample. This light energy absorption leads to the spatially distributed material heating. After this the ultrasonic wave is generated in the sample due to the thermal expansion. Profile of registered ultrasonic signal in this case (low thermal conductivity) corresponds to the distribution of acoustic sources in the sample [7,39,40]. For the case of spatially homogeneous samples this distribution replicates the distribution of laser fluence, as it has been explained above in Section I.1. However if the medium is inhomogeneous then the spatial distribution of the laser-induced acoustic sources will also depend on the spatial distribution of such parameters as light absorption coefficient, thermal expansion coefficient and others. For example, if there is a region inside the sample which absorbs the laser light differently than surroundings then the position of this region and the information on the spatial distribution of light absorption in this region can be obtained by analysing the arrival time and the profile of the detected optoacoustic signals. Thus photoacoustic imaging in this case is the imaging of the laser-induced sources of the acoustic waves.

Optoacoustics as well as other optical methods (optical coherence tomography [41] and diffuse optical imaging [42]) can be applied to any problem, which requires visualization of an object with different absorption coefficient of light relative to its surroundings. These problems include, for example, the visualization of blood vessels [43,44]. Optical diagnostic techniques provide usually higher contrast images compared with X-rays, ultrasound or Magnetic resonance imaging [45,46]. Furthermore, optical methods are non-invasive below a certain threshold and do not have the ionizing effects on the human body. However, optical coherence tomography has a limit in the depth scanning (2-3 mm) for biological samples [41], while diffuse optical imaging has a rather low spatial resolution

at a depth of several centimeters in the biotissue [42]. Optoacoustics combines the advantages of optical diagnostic techniques and diagnostic ultrasound methods. It means that this technique has high contrast of the obtained images and high spatial resolution.

One of the important areas of application of optoacoustics is monitoring of high intensity focused ultrasound (HIFU) therapy of tumors [47,48,49]. In HIFU therapy, powerful ultrasonic waves are focused inside the human body. This causes heating and consequent destruction of tissues in the focal region due to the absorption of ultrasound energy [50]. Typically, a single region damaged by HIFU has the size about 0.5-1 cm in length and 2-3 mm in cross section. For the destruction of a large mass of tissue the focus of transducer is scanned over the desired area. For monitoring of HIFU therapy measurements of the temperature distribution should be carried out with a time resolution less than 1 sec, also it is necessary to have a spatial resolution of about 1 mm and temperature sensitivity about 1°C [51]. To solve the problem of measuring the temperature distribution inside a biological tissue or an organ, an optoacoustic method [7] can be potentially used. Usually, the nanosecond range of laser pulses is employed to excite optoacoustic signals in biological tissues. It allows one to operate in the megahertz range of acoustic frequencies, providing a sub-mm spatial resolution. The amplitude and shape of the excited acoustic signal depends on the optical (light absorption and scattering coefficients) and thermophysical properties of the medium under examination and on the laser fluence within it. These characteristics are temperature dependent. Therefore, the amplitude and shape of the excited optoacoustic signal will also depend on the temperature. Because in biological media (media with low thermal conductivity) the speed of ultrasound is usually several orders of magnitude higher than the characteristic speed of heat diffusion, the temperature distribution inside biological tissues can be determined by solving the optoacoustic imaging problem [52,53,54].

The potential applicability of the optoacoustic method in diagnostics of thermal impact induced by HIFU on biological tissues was apparently first demonstrated in [47]. A lesion of sufficiently large size (25×30 mm), located at a relatively small depth (~1 cm) inside the tissue (porcine liver), was examined. Due to changes in the optical and thermo-physical parameters of the lesion relative to those in the surrounding tissue region, the temporal profile of the optoacoustic signal had a specific feature (local maximum). This feature made it possible to determine the location of the lesion that was exposed to focused ultrasound (Fig.I.11). However, the authors of [47] did not consider the dynamics of the temperature impact (only the contrast between the lesion and the surrounding tissue was observed), i.e., features of optoacoustic conversion as functions of tissue transient heating were not studied.

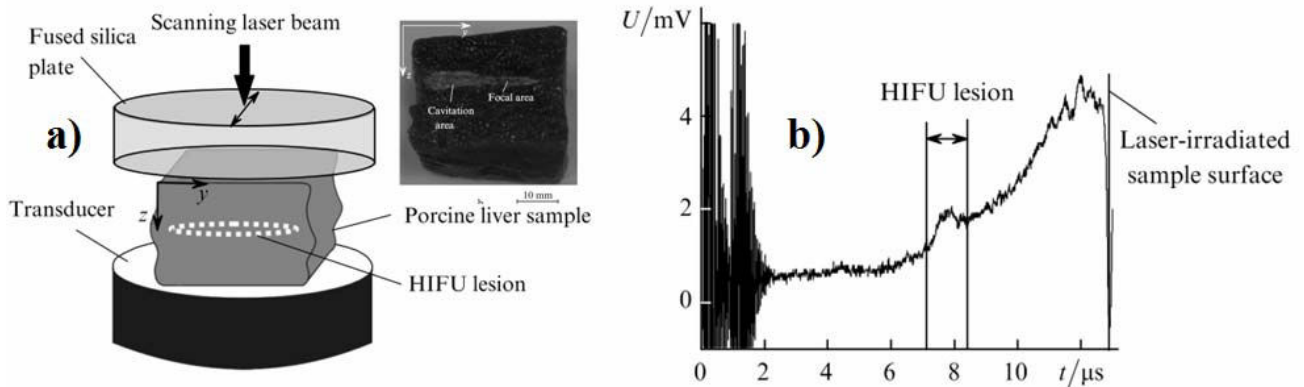


Figure 1.11. (a) Diagram of the OA diagnostics of porcine liver sample containing a thermal lesion. (Insert) the sample cross section. (b) Opto-acoustic image of a porcine liver sample containing a thermal lesion obtained when the laser spot was located over the assumed lesion location [47].

In [55,56] the applicability of the optoacoustic method for monitoring temperature during thermal impact on biological tissues was studied experimentally. Tissues under study were chicken breast (as a model of muscle), porcine lard (as a model of fatty tissue) and porcine liver (as a model of richly perfused tissue). The temperature dependences of the amplitude of the OA signals excited in biological tissues were measured in-vitro in the temperature range of 20 – 80 °C under the narrow laser beam conditions. Measurements were performed in two regimes: during heating and cooling. Similarities and differences in the behaviour of the dependences in different temperature ranges associated with different structural composition of the samples were obtained. The accuracy of temperature reconstruction from experimental data for the investigated tissue types was evaluated. It is shown that during tissue coagulation its temperature can be determined with an accuracy of about 1 °C. Numerical calculation of optoacoustic signal profiles during HIFU impact was performed with the use of the temperature dependencies measured experimentally for the different detector locations [57] for the comparison with experimentally accumulated data. 2D optoacoustic images of the heat release distribution within the model medium for the focal zone of the HIFU source were obtained. It was shown that the temperature dependence of the optoacoustic image amplitude coincides within a constant factor with the measured calibrating dependence. Thus, the possibility of quantitative monitoring of tissue heating during HIFU impact was demonstrated.

A method of focusing high intensity ultrasound by time-reversing the photoacoustic response of an optically selective target in a nonselective background was presented in [48]. In [49] the creation of a HIFU lesion at the location of an optical absorber, by the use of photoacoustic signals emitted by the absorber and detected on a dual mode transducer array was experimentally demonstrated.

The optoacoustics was also applied to the problem of cancer. The spread of cancer cells between organs is the cause of most cancer deaths [58]. Detecting circulating tumour cells-a common

marker for the development of metastasis is difficult because *ex vivo* methods are not sensitive enough owing to limited blood sample volume and *in vivo* diagnosis is time-consuming as large volumes of blood must be analysed. A way to magnetically capture circulating tumour cells in the bloodstream of mice followed by their rapid photoacoustic detection was demonstrated [58]. Magnetic nanoparticles, which were functionalized to target a receptor commonly found in breast cancer cells, bound and captured the circulating tumour cells under a magnet. To improve detection sensitivity and specificity, gold-plated carbon nanotubes conjugated with folic acid were used as a second contrast agent for photoacoustic imaging. This technique could have potential for the early diagnosis of cancer and the prevention of metastasis in humans. Another important area is the diagnosis of human breast cancer at an early stage of development disease. In this problem it is necessary to visualize/image the object with size about 10 mm, located at depths of several centimetres. Optoacoustic method were already used for *in vivo* imaging of tumors with size 1-2 cm [59]. It was demonstrated that this method is a promising, but images for smaller tumors have not been obtained because of an insufficient development of the detection systems.

The optoacoustics is also applied in the studies of the brain. The increasing use of mouse models for human brain disease studies presents an emerging need for a new functional imaging modality. The image of living mouse brain vasculature was made by optoacoustic tomography using hollow gold nanospheres as contrast agents in [60]. The hemodynamics within the entire cerebral cortex of a mouse were studied by using photoacoustic tomography in real time (Fig. I.12) [61]. The system received photoacoustic signals primarily from a slice of 2-mm thickness. This system can provide high-resolution brain vasculature images. In the paper [62] the feasibility of imaging mouse brain metabolism using photoacoustic computed tomography has been demonstrated. It is a fast, non-invasive and functional imaging modality with optical contrast and acoustic resolution. Brain responses to stimulation of the limb were imaged. Bilateral correlations were observed in eight functional regions, including the olfactory bulb, limbic, parietal, somatosensory, retrosplenial, visual, motor, and temporal regions, as well as in several subregions [63]. The borders and locations of these regions agreed well with the Paxinos mouse brain atlas.

The most recent achievements in the extremely fast developing domain of tomographic imaging can be found in [64, 65, 66]. For example the article [64] describes how photoacoustic tomography (PAT) can create multiscale multicontrast images of living biological structures ranging from organelles to organs. A small-animal whole-body imaging system called ring-shaped confocal photoacoustic computed tomography was reported in [66].

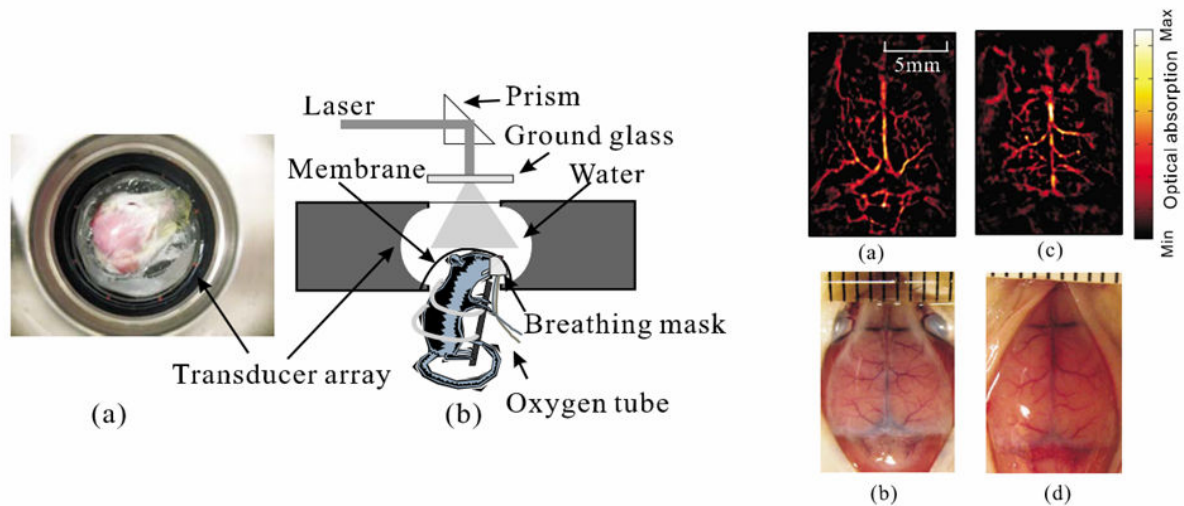


Figure I.12. (left) Full-ring array photoacoustic tomography system. (a) Top view of the full-ring array and the animal head. (b) Side view of the array system and the position of the animal. (right) Non-invasive cortical vascular structural imaging of two mice. (a) and (c): The photoacoustic images obtained at 532-nm wavelength. (b) and (d): Photographs of the cortices corresponding to (a) and (c). The photographs were taken with the scalps removed after the mouse was euthanized [61].

Currently photoacoustics keeps finding more and more new applications in biology and medicine. Section-illumination photoacoustic microscopy for dynamic 3D imaging of microcirculation in vivo was demonstrated in [67]. Functional photoacoustic imaging of the ocular microvasculature in living animals was presented in [68]. A 2.5-mm outer diameter integrated photoacoustic and ultrasonic mini-probe which can be inserted into a standard video endoscope's instrument channel was described in [69].

The picosecond ultrasonics technique was also applied in biology but, obviously, at completely different spatial scales. For example this technique was used in [70] to investigate the viscoelastic properties of nucleus of fixed single osteoblast progenitor cells adhering on a titanium alloy substrate. A two-color probing picosecond ultrasonics and a fluorescence visualization setups were developed and combined to allow to distinguish subcomponents inside the cell under investigation. It opens the way for quantitative measurements of the viscoelastic properties of single cells and of their sub-micrometer thickness. Transverse mechanical properties of cell walls of a single living plant cell were studied in [71] by using laser-generated acoustic waves. Probing the mechanical properties of plant cell wall is crucial to understand tissue dynamics. Remote opto-acoustic probing of single-cell adhesion on metallic surfaces was demonstrated in [72]. The measurements in all the above described experiments could be conducted in parallel with lateral displacement of the samples, thus providing 3D or 2D images optoacoustic images. In particular, the images/maps of the distribution of the adhesion strength of the cells along the surface were obtained [72,73].

I.3.3. Material parameters in extreme conditions

Optoacoustics is also widely used to study the acoustic properties of materials. A recent example of application of laser-based surface acoustic waves is the determination in [74] of elastic moduli of dense polycrystalline oxygen bearing η -Ta₂N₃, a novel hard and tough high-pressure material. Several recently emerged additional applications of picosecond laser ultrasonics at ambient conditions can be cited. The relaxation of coherent acoustic phonon modes with frequencies up to 500GHz in ultrathin free-standing silicon membranes was studied by optoacoustics in [75]. In the paper [76] complete mechanical measurements of submicron films were performed using the picosecond ultrasonic technique. Young's modulus and Poisson's ratio of any isotropic thin film can be obtained from these type of measurements. Three-dimensional acoustic wave front imaging in anisotropic systems by picosecond acoustics was presented in [77]. Such experiment allows the determination of the whole set of elastic constants for various experimental conditions. The picosecond photo-acoustics was applied to study amorphous solids in [78]. At the same time optoacoustics can be used for investigation the acoustic properties of substance in extreme conditions, in particular under extreme pressure, the latter being the major topic/goal of the present PhD thesis.

Knowledge of the pressure-dependences of the sound velocities and elastic moduli of liquids and solids is of extreme importance for a few branches of natural sciences such as condensed matter physics, physics of the Earth, seismology, and planetology, as well as for monitoring of earthquakes, tsunamis or nuclear weapons tests. Laser ultrasonics technique provides opportunity for remote non-contact generation and detection of acoustic waves at high pressures. One of the main tools for creating of high pressure is a diamond anvil cell (DAC) (Fig.I.13) [79].

DAC allows compressing a small (of a sub-millimeter size) piece of material to extreme pressures, which can exceed of 500 GPa [80]. The technique had been used to generate pressures existing in the deep planets interior, to synthesize materials and phases not observed under ambient conditions.

A DAC consists of two opposing diamond anvils with a sample compressed between the anvil culets (Fig.I.13 (a)). To contain the sample (for example fluids) between the diamond anvils a gasket is used (foil of ~0.2 mm thickness, Fig.I.13 (b)). Standard gasket materials are stiff metals and their alloys, such as stainless steel (e.g. Inconel) rhenium, or tungsten carbide. Pressure may be monitored using a reference material whose behaviour under pressure is known. Common pressure standards include ruby fluorescence [81], and various structurally simple metals, such as copper or platinum [82]. The sample can be viewed through the diamond anvils and illuminated by X-rays and visible light. In Fig. I.13 (c), the diamond anvil cell "Boehler-Almax Plate DAC" is shown. In this type of the diamond

anvil cell, two kinematically-mounted steel plates are elastically deflected with the use of a driving gearbox. Based on the lever principle, the symmetrical deflection of the plates, although very small, is enough to bring into near-contact the diamond anvils (which are mounted in steel plates) and hence to generate the required pressures in the sample space [83].

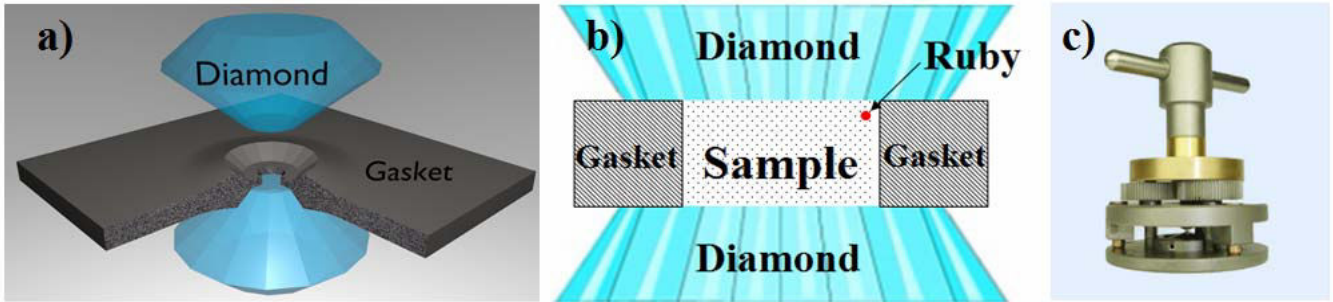


Figure I.13. (a) The working part of diamond anvil cell: two diamonds and the gasket with a hole for the sample between them. (b) The sample in the diamond anvil cell. The sample is sandwiched between two diamonds and is constrained by the gasket. There is a ruby inside the sample for measurement of pressure by fluorescence. (c) The image of diamond anvil cell “Boehler-Almax Plate DAC” [83].

Ruby fluorescence is very commonly used for pressure measurement. Ruby is chemically inert, has strong fluorescence when hit with a laser light (for example with a green laser light) and it can be purchased in the form of small spheres created precisely for this purpose. Typical spectra of ruby fluorescence at different pressures are presented in the fig.I.14.

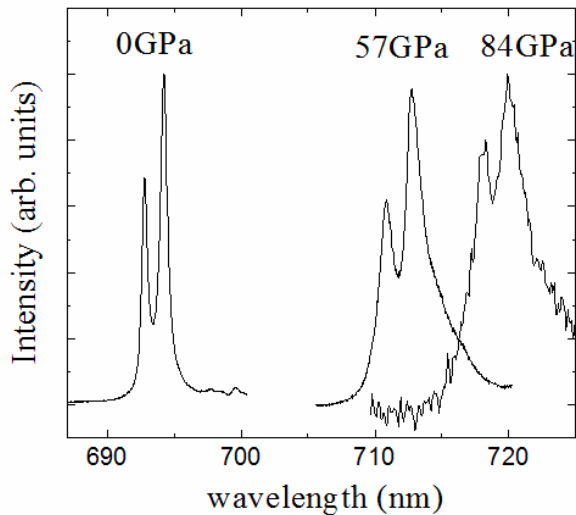


Figure I.14. Ruby fluorescence for pressure measurement. Typical spectra of ruby fluorescence at different pressures. Measurements were made with a ruby in the DAC under pressures 0 GPa, 57 GPa, 84 GPa. Intensity of signals was normalized.

Small spheres of ruby can be put in DAC with a test substance. After that, the spectra of ruby fluorescence can be measured at different pressures. If we know the position of the maximum in the spectrum λ_R then we can find pressure P of a substance in DAC with using equation (I.8) [81]:

$$P[\text{GPa}] = \frac{1904}{7.665} \left(\left(\frac{\lambda_R[\text{nm}]}{694.2} \right)^{7.665} - 1 \right) \quad (\text{I.8})$$

Transparency of diamond in visible and infrared light allows application of laser radiation for investigation of samples confined in DACs. The techniques based on utilisation of lasers and relevant for the present thesis work are Brillouin spectroscopy and laser ultrasonics. The laser ultrasonics had been first used in high pressure experiments to increase the Brillouin scattering signals through generation of monochromatic coherent acoustic waves by laser-induced gratings, i.e. by interference patterns of two pump laser beams propagating at an angle. The laser ultrasonics technique of impulsive stimulated Brillouin scattering (ISBS) had been applied at high pressures to measure the velocities of both bulk [84,85] and interface [86,87] acoustic waves.

The laser ultrasonics technique in point-source – point-receiver configuration [88,89], with the use of subnanosecond lasers producing the pulses of about 500 ps duration at 20 KHz repetition frequency for the generation of strongly diffracting acoustic waves, had been demonstrated at high pressures in [90,91]. This technique had been called laser ultrasonics in diamond anvil cell (LU DAC) technique. The technique provides opportunity to determine from the acoustic measurements both the sound velocities and the thickness of the sample, which is about 10-50 micron thick. The measurements of the velocities of shear acoustic waves with this technique are not more complicated than the measurements of the longitudinal wave velocities. Both can be obtained simultaneously with the same experimental geometry (Fig. I.15). The detection of the acoustic waves can be achieved by using a continuous probe laser radiation, fast photodetectors and an oscilloscope.

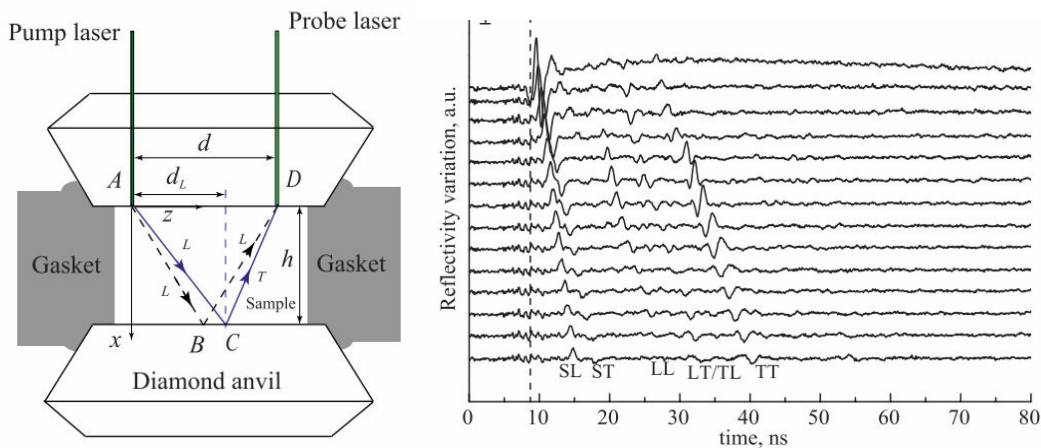


Figure I.15. (left) Sketch of the LU experiment in point-source–point receiver configuration and the diagram of the sound rays propagation in the DAC. The following notations are introduced in the sketch: h is the thickness of the layer, d is the distance between the pump and a probe laser beams, x and z are Cartesian coordinates. (right) Raw data for the transient reflectivity change at different separation distances d at pressure of 16.2 GPa. The scales are common for all the curves, which are shifted vertically for clarity. The step of the scan is $7.3 \mu\text{m}$. The top signal was measured when $d=16 \mu\text{m}$. The lowest signal was measured when $d=95.6 \mu\text{m}$. Vertical dashed line marks an instance of maximum intensity in the pump laser shot [90].

For example in [91] a comprehensive description of the propagation and detection of the acoustic head waves in an iron layer inside a DAC under high pressures was presented. Three types of acoustical waves have been detected in LU-DAC experiments: bulk shear and longitudinal waves in iron, skimming waves in diamond and in iron and “mixed” waves. Detection of the head waves provides an opportunity to find the velocities of the bulk acoustic waves skimming along the iron/diamond interface. It is important to distinguish the echoes caused by head waves from the echoes related to bulk acoustic wave propagation in order to accurately determine the longitudinal and shear wave velocities in iron under high pressures. The experimental data demonstrate that the overlap of the head wave echoes with bulk wave echoes can make the analysis of the echoes rather complex and determination of the velocities less precise.

The acoustic frequency band of the point-source – point-receiver LU DAC technique proposed in [90,91] is inevitably limited by the pulse duration of subnanosecond laser at the level of about 1 GHz. That is why in order to access the frequencies up to 10 GHz in wide-band acoustic spectroscopy and to improve the preciseness of sound velocity measurements with the point-source – point-receiver technique, a picosecond laser having pulse duration of about 5-10 ps can be used for the generation and for the detection of both longitudinal and shear hypersound at high pressures.

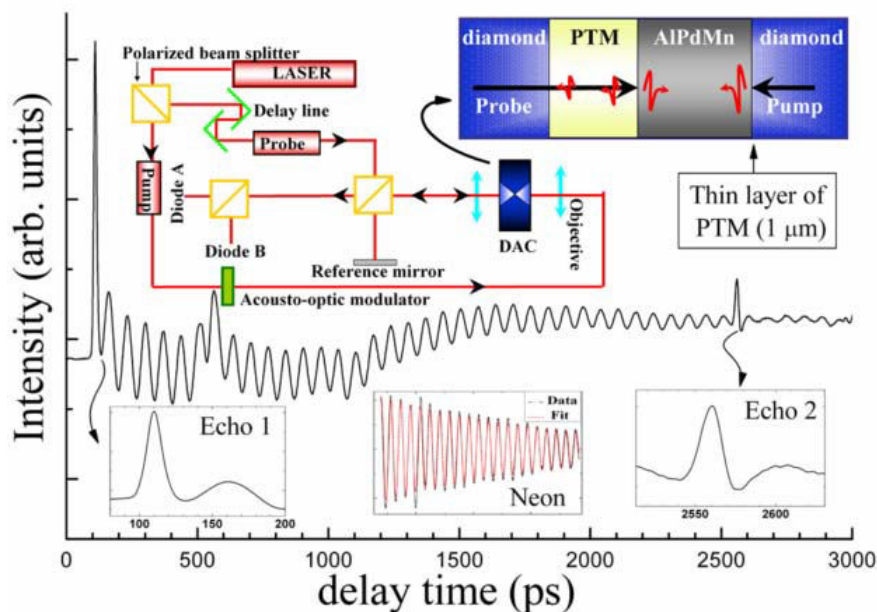


Figure 1.16. Change in the reflectivity imaginary part of AIPdMn at 9.7 GPa as a function of the optical probe-pulse time delay. Upper part: experimental schema used to perform picosecond laser acoustics studies at high pressure. The arrow indicates the schematic illustration of generation and detection process for AIPdMn in diamond anvil cell. Insets: left: enlarged part of the first acoustic echo. Center: Brillouin oscillation detected in the pressure transmitting medium where the thermal background has been subtracted. The red line corresponds to the data fit carried out to determine the attenuation. Right: enlarged part of the second acoustic echo[92].

The technique of picosecond laser ultrasonics [33,32] that uses femtosecond laser pulses of about 100 fs typical duration emitted at about 80 MHz repetition rate, can generate and detect acoustic

pulses with the duration as short as a few picoseconds and is known to be a powerful tool for the evaluation at ambient conditions of the elastic properties of films with submicron thickness. This technique will become, perhaps, a unique tool to evaluate the moduli of the materials at extremely high pressures exceeding 100 GPa, when the thickness of the tested samples become of the order of a few micrometers or smaller. In [92] a high pressure laser ultrasonics technique combining the diamond anvil cell device with the technique of picosecond laser ultrasonics was pioneered. Such an approach allows to measure sound velocity and attenuation of solids and liquids under pressure of tens to hundreds of GPa. The opportunities of this experimental technique is demonstrated in studies of lattice dynamics and relaxation processes in a metallic single grain of AlPdMn quasicrystal, and in rare gas solids neon and argon (Fig. I.16). Also ultrafast picosecond ultrasonic interferometry [33,32] with sub-picosecond laser pulses was used in [93] to measure acoustic wave at high static pressure in a diamond anvil cell.

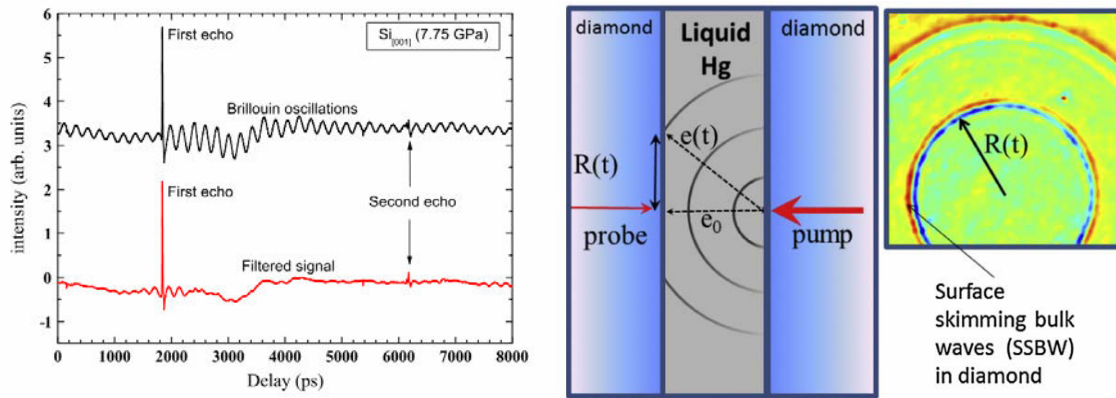


Figure I.17. (left) The method for the detection of the acoustic echoes. Upper trace: raw reflectivity change as a function of the optical probe-pulse time delay in a single crystal of silicon along the [1 0 0] propagation direction at 7.75 GPa. First and second echoes of the longitudinal acoustic wave can be detected. The time Δt necessary for traveling from one surface of the sample to the opposite one corresponds to the time difference between the occurrence of these two echoes. Lower trace: same signal but processed through a band block filtering at the frequency of the Brillouin oscillations in the pressure transmitting medium. (right) The imaging method. Produced by the tightly focused laser beam, spherical wave fronts occur in acoustic propagation. Consequently, the radius $R(t)$ of the circles appearing on the surface depends on the sample thickness e_0 and on the length of the acoustic wave front straight propagation $e(t)$ [94].

In [94] picosecond acoustics method was presented for measuring the thermo-dynamical properties of solids and liquids at high pressure and high temperature. This work describes recent improvements in accurate measurements of hypersonic sound velocities of liquids and solids under extreme conditions. To illustrate the capability of this technique, results are given on the pressure and temperature dependence of acoustic properties for three prototypical cases: polycrystal (iron), single-crystal (silicon) and liquid (mercury) samples. It is shown that such technique also enables the determination of the density as a function of pressure for liquids, of the complete set of elastic constants for single crystals, and of the melting curve for any kind of material. To measure the

acoustic properties the method of detection acoustic echoes and “imagery method” were used in this work (Fig. I.13). This work demonstrated that picosecond laser ultrasonics can be used in high pressure physics to study the sound velocity as a function of the pressure and temperature in the range one order of magnitude higher than what was previously attainable, the equation of state with a better accuracy than what is usually reached with other techniques (such as X-ray diffraction).

High pressure ultrafast acoustic technique clearly opens opportunities to measure thermodynamical and acoustical properties under extreme conditions. Combined with laser heating, this technique would also open a way of determining the sound velocity under the thermodynamical conditions of the Earth’s core (around 3 millions of atmospheres and 6000 K), but also to determine the nature and way of heat and mass transfer within the interiors of the Earth and terrestrial planets.

An important part of this PhD research will be connected with H_2O . H_2O is the most abundant fluid on the Earth’s surface. It is also present as solid ice subjected to compression and large compression in glaciers. Ice is the major constituent of such giant planets of the solar system as Neptune and Uranus [95]. Thus, the elastic and thermodynamic properties of water-ices at ultrahigh pressures are the subject of interest not only for physicists and chemists but also for geoscientists and planetologists. At high pressures, water ice is known to form at least thirteen phases, most of which exist at temperatures below 300 K and pressures below 1 GPa (Fig.I.18 [96]). H_2O is a type of molecular solid with triatomic molecules which first solidify on compression. This is the object allowing simple modelling of intramolecular and intermolecular interactions by the theory. Also, in contrast to compounds which are solid at ambient conditions, much less is known about the acoustic, elastic and thermal properties of this solid object, especially at high pressures. There are doubtful conclusions on the existence/nonexistence of some phase transitions in this material such as the transition to ice X.

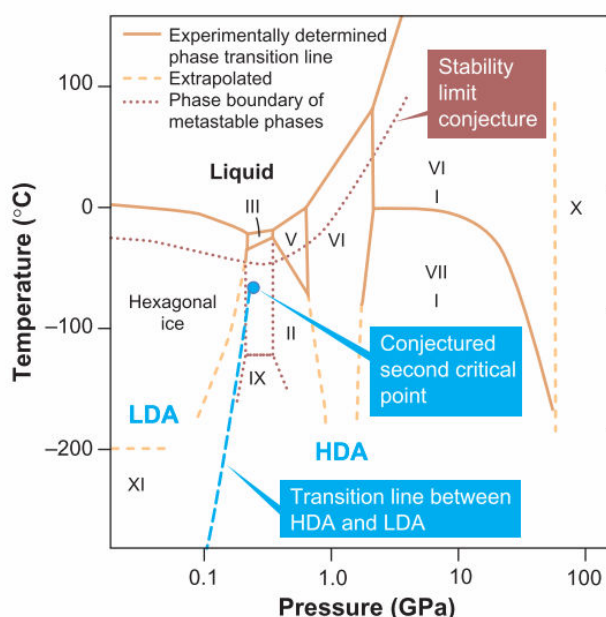


Figure I.18. A simplified phase diagram of water and ice [96]

§1.4. Goals of the PhD research

This PhD research work was devoted to the use of laser ultrasound in high-pressure physics for investigation of elastic behaviour of condensed matter at ultrahigh pressures. The research was conducted using the recently established technique of laser ultrasonic measurements in a diamond anvil cell which allows investigation of the sound propagation and determination of the acoustic wave velocities at ultrahigh pressures.

The goals of the PhD research can be summarized as follows:

- 1) Development of analytical theory of laser ultrasound in the diamond anvil cell which is able to interpret the previously accumulated experimental observations [90,91]. In these studies it was observed that the amplitude of the laser ultrasonic signal depends on the direction of propagation of the sound in the material compacted by diamond anvil cell. This means that the source of sound (which was created by a short laser pulse) has a structured directivity pattern. Description of the laser generation of the acoustic pulses at the interface of light absorbing and optically transparent media can contribute to a better understanding of laser ultrasonic measurements in a diamond anvil cell. Also, this theory could help to optimize the laser ultrasonic experiments in DAC. The developed analytical theory is presented in Chapter II.
- 2) Development and building up of an experimental setup for measurement of the refractive indexes and thickness of transparent materials compressed to ultrahigh pressures in a diamond anvil cell, in particular of H₂O. The refractive index of a material is a fundamentally important property that represents the response of the electronic charge distribution to the disturbance caused by the electric field component of incident electromagnetic radiation [97,98]. The thickness of the sample as a function of pressure can be used to calculate the equation of state and bulk modulus. Also knowledge of the refractive index and the thickness of materials as a function of pressure is extremely useful for ultrasonic experiments because their values can be used to calculate the acoustic velocity [35,90,91,92,94]. Realization of this goal is presented in Chapter III.
- 3) Development and building up of an experimental setup for measurement of acoustic signal in materials compressed to ultrahigh pressures in a diamond anvil cell. The measurements are based on the application of the picosecond ultrasonic interferometry, also called time-domain

Brillouin scattering [32,34]. Measurements of the acoustic properties using this technique are carried out in H₂O up to 84 GPa. In addition laser ultrasound technique in diamond anvil cell can give new information about the acoustic properties of transparent materials: detection of spatial variations of the acoustic properties inside the material compressed in DAC can be achieved. This technique opens the possibility to obtain three-dimensional images of acoustic inhomogeneities of the samples in diamond anvil cell. It can be used to study the formation and evolution of texture in transparent microcrystalline aggregates following the changes in the applied pressure. Detailed description of these experiments and the obtained results is provided in Chapter IV.

References (I)

1. C.B Scruby, L.E Drain. *Laser Ultrasonics: Techniques and Applications*. **CRC Press (1990)**
2. Allan Rosencwaig *Photoacoustics and photoacoustic spectroscopy* **Wiley (1980)**.
3. Hutchins D, Tam AC. *Pulsed photoacoustic materials characterization*. **IEEE Trans Ultrason Ferroelectr Freq Control. 33(5):429 (1986)**
4. Daniel Royer, Eugene Dieulesaint *Elastic Waves in Solids II: Generation, Acousto-optic Interaction, Applications* **Springer Science & Business Media (2000)**
5. L.D. Landau, E.M. Lifshitz. *Fluid Mechanics. Vol. 6 (2nd ed.)*. **Butterworth–Heinemann (1987)**
6. Sergey M. Nikitin, Vincent Tournat, Nikolay Chigarev, Alain Bulou, Bernard Castagnede, Andreas Zerr and Vitalyi Gusev. *Directivity patterns and pulse profiles of ultrasound emitted by laser action on interface between transparent and opaque solids: Analytical theory*. **J. Appl. Phys. 115, 044902 (2014)**
7. V. E. Gusev; A. A. Karabutov. *Laser optoacoustics*. **New York : AIP Press (1993)**; Gusev V.E., Karabutov A.A. *Lazernaya optoakustika (Laser Optoacoustics)*. **Moscow: Nauka, 1991**
8. Pascal Ruello, Vitalyi E. Gusev. *Physical mechanisms of coherent acoustic phonons generation by ultrafast laser action*. **Ultrasonics, In Press, (2014)**
9. S A Akhmanov, V E Gusev. *Laser excitation of ultrashort acoustic pulses: New possibilities in solid-state spectroscopy, diagnostics of fast processes, and nonlinear acoustics*. **SOV PHYS USPEKHI 35 (3), 153 (1992)**
10. P. S. Grashin, A. A. Karabutov, A. A. Oraevsky, I. M. Pelivanov, N. B. Podymova, E. V. Savateeva, V. S. Solomatn *Distribution of the laser radiation intensity in turbid media: Monte Carlo simulations, theoretical analysis, and results of optoacoustic measurements*. **Quantum Electronics, 32(10), 868 (2002)**
11. Alexander Graham Bell. *On the production and reproduction of sound by light*. **Am. J. Sci. 3 (20), 305 (1880)**.
12. Tyndall, J. *Action of an intermittent beam of radiant heat upon gaseous matter*. **Proc. R. Soc. London 31, 307 (1881)**.
13. W.C. Röntgen *On tones produced by the intermittent irradiation of a gas* **Philos. Mag., 11(68), 308 (1881)**
14. G. A. Askar'yan, A. M. Prokhorov, G. F., chanturiya, and G. P. Shipulo. *The effects of a laser beam in a liquid* **J.Exptl. Theoret. Phys. (U.S.S.R.) 44, 2180 (1963)**
15. R. M. White. *Elastic Wave Generation by Electron Bombardment or Electromagnetic Wave Absorption*. **J. Appl. Phys. 34, 2123 (1963)**
16. R. M. White. *Generation of Elastic Waves by Transient Surface Heating*. **J. Appl. Phys. 34, 3559 (1963)**
17. Bunkin F.V., Komissarov V.M. *Optical excitation of sound waves*. **Akusticheskij Zhurnal, 19, 3, 305 (1973)**
18. Lyamshev L.M., Naugol'nikh K.A. *Optical generation of sound. Nonlinear effects (Review)*. **Akusticheskij Zhurnal, 27, 5, 641 (1981)**
19. Zharov, V.P., Letokhov, V.S. *Laser Optoacoustic Spectroscopy*. **Springer-Verlag (1986)**
20. T. Kundu. *Ultrasonic Nondestructive Evaluation: Engineering And Biological Material Characterization*. **CRC (2004)**
21. Lihong V. Wang. *Photoacoustic Imaging and Spectroscopy*. **CRC (2009)**
22. D. W. Fitting and L. Adler. *Ultrasonic Spectral Analysis for Nondestructive Evaluation*. **Plenum Press, New York (1981)**
23. W. R. Scott and P. F. Gordon. *Ultrasonic spectrum analysis for nondestructive testing of layered composite materials*, **J. Acoust. Soc. Am., 62 , 108 (1977)**
24. A. A. Karabutov, I. M. Pelivanov, N. B. Podymova *Nondestructive Evaluation of Graphite-Epoxy Composites by the Laser Ultrasonic Method*. **Mechanics of Composite Materials, 36 (6), 497 (2000)**
25. Ivan Pelivanov, Takashi Buma, Jinjun Xia, Chen-Wei Wei and Matthew O'Donnell *A new fiber-optic non-contact compact laser-ultrasound scanner for fast non-destructive testing and evaluation of aircraft composites*. **J. Appl. Phys. 115, 113105 (2014)**
26. O. B. Wright. *Thickness and sound velocity measurement in thin transparent films with laser picosecond acoustics*. **J. Appl. Phys. 71, 1617 (1992)**
27. Devos, A., Cote, R., Caruyer, G. & Lefèvre, A. *A different way of performing picosecond ultrasonic measurements in thin transparent films based on laser-wavelength effects*. **Appl. Phys. Rev. 86, 211903 (2003)**.
28. O. B. Wright and K. Kawashima *Coherent phonon detection from ultrafast surface vibrations* **Phys. Rev. Lett. 69, 1668 (1992)**

29. G. Tas, R. J. Stoner, H. J. Maris, G. W. Rubloff, G. S. Oehrlein and J. M. Halbout. *Noninvasive picosecond ultrasonic detection of ultrathin interfacial layers: CF x at the Al/Si interface.* **Appl. Phys. Lett.** **61**, 1787 (1992)
30. Johnny Dai, Priya Mukundhan, Tim Kryman *Controlling Bumping Processes with Picosecond Ultrasonic Metrology.* **Chip Scale Review**, **17(5)** 26 (2013)
31. <http://www.rudolphtech.com/products/library/optical-and-acoustic-metrology-techniques-for-25-and-3d-advanced-packaging/>
32. Grahn H.T., Maris H.J., Tauc J. *Picoseconds ultrasonics.* **IEEE Journal of Quantum Electronics** **25(12)** 2562 (1989)
33. C. Thomsen, H. T. Grahn, H. J. Maris, and J. Tauc *Surface generation and detection of phonons by picosecond light pulses.* **Phys. Rev. B** **34**, 4129 (1986)
34. C Mechri, P Ruello, JM Breteau, MR Baklanov, P Verdonck, V Gusev *Depth-profiling of elastic inhomogeneities in transparent nanoporous low-k materials by picosecond ultrasonic interferometry.* **Applied Physics Letters** **95 (9)**, 091907 (2009)
35. Alexey M Lomonosov, Adil Ayouch, Pascal Ruello, Gwenaëlle Vaudel, Mikhail R Baklanov, Patrick Verdonck, Larry Zhao, Vitalyi E Gusev *Nanoscale Noncontact Subsurface Investigations of Mechanical and Optical Properties of Nanoporous Low-k Material Thin Film* **ACS Nano** **6 (2)**, 1410 (2012)
36. Chen-Yin Ni, Nikolay Chigarev, Vincent Tournat, Nicolas Delorme, Zhong-Hua Shen and Vitalyi E. Gusev. *Probing of laser-induced crack modulation by laser-monitored surface waves and surface skimming bulk waves* **J. Acoust. Soc. Am.** **131**, EL250 (2012)
37. Sylvain Mezil, Nikolay Chigarev, Vincent Tournat and Vitalyi Gusev. *Two dimensional nonlinear frequency-mixing photo-acoustic imaging of a crack and observation of crack phantoms* **J. Appl. Phys.** **114**, 174901 (2013)
38. M. Hettich, K. Jacob, O. Ristow, C. He, J. Mayer, M. Shubert, V. Gusev, A. Bruchhausen, T. Dekorsy. *Imaging of a patterned and buried molecular layer by coherent acoustic phonon spectroscopy,* **Appl. Phys. Lett.** **101**, 191106 (2012).
39. I M Pelivanov, S A Belov, V S Solomatin, T D Khokhlova, A A Karabutov. *Direct opto-acoustic in vitro measurement of the spatial distribution of laser radiation in biological media.* **QUANTUM ELECTRON**, **36 (12)**, 1089 (2006)
40. Tatiana D. Khokhlova, Ivan M. Pelivanov, Victor V. Kozhushko, Alexei N. Zharinov, Vladimir S. Solomatin, and Alexander A. Karabutov *Optoacoustic imaging of absorbing objects in a turbid medium: ultimate sensitivity and application to breast cancer diagnostics* **Applied Optics**, **46(2)** 262 (2007)
41. Valerij Viktorovich Tuchin *Handbook of Optical Biomedical Diagnostics* **SPIE Press**, (2002)
42. A. P. Gibson, J. C. Hebden and S. R. Arridge *Recent advances in diffuse optical imaging* **Med. Biol.** **50** R1–R43 (2005)
43. Francis A. Duck. *Physical properties of tissue: a comprehensive reference book* **Academic Press**, (1990)
44. Roggan A, Friebel M, Do Rschel K, Hahn A, Mu Ller G. *Optical Properties of Circulating Human Blood in the Wavelength Range 400-2500 nm.* **J. Biomed. Opt.** **4(1)**, 36 (1999)
45. R. L. P. van Veen ; H. J. C. M. Sterenborg ; A. W. K. S. Marinelli ; M. Menke-Pluymers. *Intraoperatively assessed optical properties of malignant and healthy breast tissue used to determine the optimum wavelength of contrast for optical mammography* **J. Biomed. Opt.** **9(6)**, 1129 (2004)
46. Frederick W. Kremkau. *Diagnostic Ultrasound: Principles and Instruments.* **W.B. Saunders** (2002)
47. T D Khokhlova, I M Pelivanov, O A Sapozhnikov, V S Solomatin, A A Karabutov. *Opto-acoustic diagnostics of the thermal action of high-intensity focused ultrasound on biological tissues: the possibility of its applications and model experiments,* **QUANTUM ELECTRON**, **36 (12)**, 1097 (2006)
48. Arik R. Funke, Jean-François Aubry, Mathias Fink, Albert-Claude Boccara and Emmanuel Bossy *Photoacoustic guidance of high intensity focused ultrasound with selective optical contrasts and time-reversal* **Appl. Phys. Lett.** **94**, 054102 (2009)
49. Amaury Prost , Arik Funke , Mickaël Tanter , Jean-François Aubry , Emmanuel Bossy *Photoacoustic-guided ultrasound therapy with a dual-mode ultrasound array* **J. Biomed. Opt.** **17(6)**, 061205 (2012)
50. Bailey M.R., Khokhlova V.A., Sapozhnikov O.A., Kargl S.G., Crum L.A. *Physical Mechanisms of the Therapeutic Effect of Ultrasound* **Akusticheskij Zhurnal**, **49, 4**, p. 437-464 (2003)
51. Irina V Larina, Kirill V Larin and Rinat O Esenaliev. *Real-time optoacoustic monitoring of temperature in tissues* **J. Phys. D: Appl. Phys.** **38** 2633 (2005)
52. Changhui Li and Lihong V Wang *Photoacoustic tomography and sensing in biomedicine* **Phys. Med. Biol.** **54** R59 (2009)

53. Robert A. Kruger, William L. Kiser Jr., Daniel R. Reinecke and Gabe A. Kruger *Thermoacoustic computed tomography using a conventional linear transducer array* **Med. Phys.** **30**, 856 (2003)
54. T. D. Khokhlova, I. M. Pelivanov, A. A. Karabutov. *Methods of optoacoustic diagnostics of biological tissues.* **Akusticheskiĭ Zhurnal**, **55**, 4-5, 672 (2009)
55. S M Nikitin, T D Khokhlova and I M Pelivanov *In-vitro study of the temperature dependence of the optoacoustic conversion efficiency in biological tissues* **Quantum Electron.** **42** 269 (2012)
56. Sergey M. Nikitin , Tatiana D. Khokhlova , Ivan M. Pelivanov. *Temperature dependence of the optoacoustic transformation efficiency in ex vivo tissues for application in monitoring thermal therapies* **J. Biomed. Opt.** **17**(6), 061214 (2012)
57. Nikitin S.M., Khokhlova T.D., Pelivanov I.M. *Application of the optoacoustic method in monitoring of the thermal impact on biological tissues: numerical simulations and in-vitro study.* **16th International Conference on Photoacoustic and Photothermal Phenomena, Book of Abstracts**, 111(2011)
58. Ekaterina I. Galanzha, Evgeny V. Shashkov, Thomas Kelly, Jin-Woo Kim, Lily Yang & Vladimir P. Zharov. *In vivo magnetic enrichment and multiplex photoacoustic detection of circulating tumour cells.* **Nature Nanotechnology** **4**, 855 (2009)
59. Khokhlova T. D., Zharinov A.M., Kozhushko V. V., Pelivanov I.M., Karabutov A.A., *Opto-acoustic imaging system for, early breast cancer diagnostics: experimental and numerical studies.* **Proc. SPIE**, **6257**, pp. 62570R: 1-7 (2006)
60. Wei Lu, Qian Huang, Geng Ku, Xiaoxia Wen, Min Zhou, Dmitry Guzatov, Peter Brecht, Richard Su, Alexander Oraevsky, Lihong V. Wang, and Chun Li. *Photoacoustic imaging of living mouse brain vasculature using hollow gold nanospheres* **Biomaterials** **31** (9) 2617 (2010)
61. Changhui Li ; Andres Aguirre ; John Gamelin ; Anastasios Maurudis ; Quing Zhu ; Lihong V. Wang. *Real-time photoacoustic tomography of cortical hemodynamics in small animals.* **J. Biomed. Opt.** **15**(1), 010509 (2010)
62. Junjie Yao, Jun Xia, Konstantin I. Maslov, Mohammadreza Nasiriavanaki, Vassiliy Tsytarev, Alexei V. Demchenko, and Lihong V. Wang. *Noninvasive photoacoustic computed tomography of mouse brain metabolism in vivo.* **Neuroimage** **64** 257 (2013)
63. Nasiriavanaki M, Xia J, Wan H, Bauer AQ, Culver JP, Wang LV. *High-resolution photoacoustic tomography of resting-state functional connectivity in the mouse brain.* **Proc Natl Acad Sci (USA)** **111**(1) 21-6 (2014)
64. L. V. Wang and S. Hu. *Photoacoustic tomography: in vivo imaging from organelles to organs.* **Science** **335**, 1458 (2012).
65. John Gamelin, Anastasios Maurudis, Andres Aguirre, Fei Huang, Puyun Guo, Lihong V. Wang, and Quing Zhu. *A real-time photoacoustic tomography system for small animals.* **Opt Express.** **17**(13) 10489 (2009)
66. J Xia, MR Chatni, K Maslov, Z Guo, K Wang, M Anastasio, LV Wang. *Whole-body ring-shaped confocal photoacoustic computed tomography of small animals in vivo* **Journal of Biomedical Optics** **17** (5), 050506 (2012)
67. Liang Song, Konstantin Maslov, and Lihong V. Wang. *Section-illumination photoacoustic microscopy for dynamic 3D imaging of microcirculation in vivo.* **Optics Letters**, **35**, 9, 1482 (2010)
68. Song Hu, Bin Rao, Konstantin Maslov, and Lihong V. Wang. *Label-free photoacoustic ophthalmic angiography.* **Optics Letters**, **35**, 1, 1-3 (2010)
69. Joon-Mo Yang, Ruimin Chen, Christopher Favazza, Junjie Yao, Chiye Li, Zhilin Hu, Qifa Zhou, K. Kirk Shung, and Lihong V. Wang. *A 2.5-mm diameter probe for photoacoustic and ultrasonic endoscopy* **Optics Express**, **20**, **21**, 23944 (2012)
70. Mathieu Ducouso, Omar El-Farouk Zouani, Christel Chanseau, Céline Chollet, Clément Rossignol, Bertrand Audoin and Marie-Christine Durrieu *Evaluation of mechanical properties of fixed bone cells with sub-micrometer thickness by picosecond ultrasonics* **Eur. Phys. J. Appl. Phys.**, **61** 1 11201 (2013)
71. Gadalla A, Dehoux T, Audoin B. *Transverse mechanical properties of cell walls of single living plant cells probed by laser-generated acoustic waves.* **Planta.** **239**(5) 1129 (2014)
72. Abi Ghanem M, Dehoux T, Zouani OF, Gadalla A, Durrieu MC, Audoin B. *Remote opto-acoustic probing of single-cell adhesion on metallic surfaces.* **J Biophotonics.** **7**(6) 453-9 (2014)
73. Thomas Dehoux, Maroun Abi Ghanem, Omar F. Zouani, Mathieu Ducouso, Nikolay Chigarev, Clément Rossignol, Nicolas Tsapis, Marie-Christine Durrieu, Bertrand Audoin *Probing single-cell mechanics with picosecond ultrasonics* **Ultrasonics**, **56** 160 (2015)
74. Andreas Zerr, Nikolay Chigarev, Ovidiu Brinza, Sergey M. Nikitin, Alexey M. Lomonosov and Vitalyi Gusev. *Elastic moduli of η -Ta₂N₃, a tough self-healing material, via laser ultrasonics* **physica status solidi (RRL)** **6**(12) 484 (2012)

75. J. Cuffe, O. Ristow, E. Chávez, A. Shchepetov, P-O. Chapuis, F. Alzina, M. Hettich, M. Prunnila, J. Ahopelto, T. Dekorsy, and C. M. Sotomayor Torres. *Lifetimes of Confined Acoustic Phonons in Ultrathin Silicon Membranes* **Phys. Rev. Lett.** **110**, 095503 (2013)
76. P. A. Mante, J. F. Robillard and A. Devos. *Complete thin film mechanical characterization using picosecond ultrasonics and nanostructured transducers: experimental demonstration on SiO₂* **Appl. Phys. Lett.** **93**, 071909 (2008)
77. Shuo Zhang, Emmanuel Péronne, Laurent Belliard, Serge Vincent and Bernard Perrin. *Three-dimensional acoustic wavefront imaging in anisotropic systems by picosecond acoustics* **J. Appl. Phys.** **109**, 033507 (2011)
78. C. Ferrante, E. Pontecorvo, G. Cerullo, A. Chiasera, G. Ruocco, T. & W. Schirmacher Scopigno. *Acoustic dynamics of network-forming glasses at mesoscopic wavelengths* **Nature Communications** **4**, 1793 (2013)
79. Bassett, W.A. *Diamond Anvil Cell, 50th Birthday.* **High Pressure Research** **29**, 163 (2009)
80. Ruoff, A. L., H. Xia & Q. Xia. *The effect of a trapped aperture on x-ray diffraction from sample with a pressure gradient: Studies on three samples with a maximum pressure of 560 GPa,* **Rev. Sci. Instrum.** **63**, 4342 (1992).
81. H. K. Mao, J. Xu, P. M. Bell. *Calibration of the ruby pressure gauge to 800 kbar under quasi-hydrostatic conditions.* **Journal of Geophysical Research: Solid Earth** **91**, B5, 4673 (1986)
82. Ray Kinslow, A. J. Cable. *High-velocity impact phenomena.* **Academic Press**, 1970
83. Reinhard Boehler & Koen De Hantsetters. *New anvil designs in diamond-cells.* **High Pressure Research** **24** (3) 391 (2004)
84. B. J. Baer, J. M. Brown, J. M. Zaug, D. Schiferl and E. L. Chronister. *Impulsive Stimulated Scattering in Ice VI and Ice VII.* **J. Chem. Phys.** **108**, 4540 (1998)
85. Abramson, E.H., L. J. Slutsky, and J. M. Brown. *Elastic constants, interatomic forces and equation of state of β -oxygen at high pressure.* **J. Chem. Phys.**, **100**, 4518-4526, 1994.
86. J. C. Crowhurst, E. H. Abramson, L. J. Slutsky, J. M. Brown, J. M. Zaug, and M. D. Harrell. *Surface acoustic waves in the diamond anvil cell: An application of impulsive stimulated light scattering* **Phys. Rev. B** **64**, 100103(R) (2001)
87. Jonathan C Crowhurst, Alexander F Goncharov and Joseph M Zaug. *Impulsive stimulated light scattering from opaque materials at high pressure* **J. Phys.: Condens. Matter** **16** S1137 (2004)
88. B. Audoin, C. Bescond and M. Deschamps. *Measurement of stiffness coefficients of anisotropic materials from pointlike generation and detection of acoustic waves.* **J. Appl. Phys.** **80**, 3760 (1996)
89. B. Castagnede, Kwang Yul Kim, Wolfgang Sachse and Michael O. Thompson *Determination of the elastic constants of anisotropic materials using laser-generated ultrasonic signals.* **J. Appl. Phys.** **70**, 150 (1991)
90. N. Chigarev, P. Zinin, L.-C. Ming, G. Amulele, A. Bulou, and V. Gusev. *Laser generation and detection of longitudinal and shear acoustic waves in a diamond anvil cell.* **Appl. Phys. Lett.** **93**, 181905 (2008).
91. N. Chigarev, P. Zinin, D. Mounier, A. Bulou, L. C. Ming, T. Acosta, and V. Gusev. *Analysis of ultrasonic echoes induced by pulsed laser action on an iron film in a diamond anvil cell.* **High Pressure Res.** **30**, 78 (2010).
92. F. Decremps, L. Belliard, B. Perrin, and M. Gauthier. *Sound Velocity and Absorption Measurements under High Pressure Using Picosecond Ultrasonics in a Diamond Anvil Cell: Application to the Stability Study of AlPdMn.* **Phys. Rev. Lett.** **100**, 035502 (2008)
93. Michael R. Armstrong, Jonathan C. Crowhurst, Evan J. Reed and Joseph M. Zaug. *Ultrafast high strain rate acoustic wave measurements at high static pressure in a diamond anvil cell* **Appl. Phys. Lett.** **92**, 101930 (2008)
94. F. Decremps, M. Gauthier, S. Ayrinhac, L. Bove, L. Belliard, B. Perrin, M. Morand, G. Le Marchand, F. Bergame, J. Philippe. *Picosecond acoustics method for measuring the thermodynamical properties of solids and liquids at high pressure and high temperature.* **Ultrasonics** (in press 2014)
95. W. B. Hubbard, *Planetary Interiors* (Van Nostrand Reinhold Company, 1984)
96. A. K Soper *WATER AND ICE.* **Science**, **297** (5585), 1288-9 (2002)
97. Chang-Sheng Zha, Russell J. Hemley, Stephen A. Gramsch, Ho-kwang Mao and William A. Bassett. *Optical study of H₂O ice to 120GPa: Dielectric function, molecular polarizability, and equation of state.* **J. Chem. Phys.** **126**, 074506 (2007)
98. A. Dewaele, J. H. Eggert, P. Loubeyre, and R. Le Toullec. *Measurement of refractive index and equation of state in dense He, H₂, H₂O, and Ne under high pressure in a diamond anvil cell.* **Phys. Rev. B** **67**, 094112 (2003)

Chapter II

Analytical theory of laser ultrasound in diamond anvil cell

In the previous Chapter I, the optoacoustic effect was briefly illustrated. In this chapter the analytical theory for the directivity patterns of ultrasounds emitted from laser-irradiated interface between two isotropic solids (typical situation for the substance in diamond anvil cell) is developed. This theory can be applied in the future for the dimensional scaling of the laser ultrasonic measurements in a diamond anvil cell, the optimization of these experiments and the interpretation of the experimental results.

In the recent years the application of all-optical non-contact laser ultrasonics (LU) techniques for the evaluation of compressed material properties through high pressure experiments in a diamond anvil cell attracted an increasing number of researchers (see [1-5] and Chapter I, section I.3.3)).

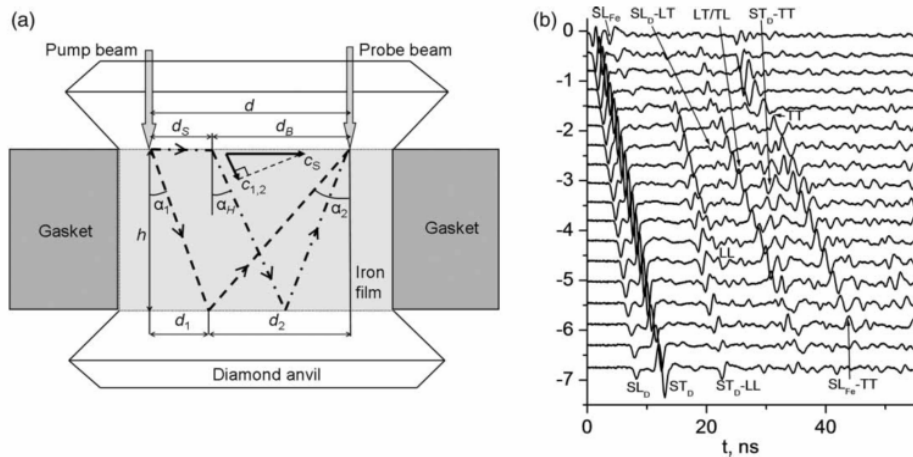


Figure II. 1. (a) line-source – point-detector schema of experiment in [4]. Ray trajectories of acoustic waves in DAC are indicated. (b) Photoacoustic signals at 2.8 GPa measured at different distances. The step of the scan is $7.4\mu\text{m}$. The top signal was measured at $d=25\mu\text{m}$ [4].

In [2, 4] the longitudinal and shear acoustic waves were detected in the iron inside diamond anvil cell at different angles of propagating in the so-called line-source – point-detector schema (Fig. II. 1), where the pump maser radiation is focused into a line while probe laser radiation is focused into a spot. In these studies it was observed that the amplitude of the laser ultrasonic signal depends on the direction of propagation of the sound in the material compacted in diamond anvil cell. This means that the source of sound (which was created by a short laser pulse) has a structured directivity pattern. Thus the knowledge of the directivity patterns of acoustical waves, emitted from laser-irradiated interface between transparent materials (e.g. diamond) and light-absorbing materials (e.g. metals), could be

useful for scaling and interpretation of the experiments on sound waves propagation in metals and transparent media compressed in a diamond anvil cell.

Earlier, both theoretical and experimental studies of the directivity patterns of laser ultrasound in solids mostly concentrated on the case when laser irradiates a mechanically free surface of a solid half-space [6-18]. Directivity patterns were evaluated both for the compression/dilatation and for the shear acoustic waves. The profiles of the emitted acoustic pulses were the subject of the analysis both in the case of longitudinal and of shear acoustic waves [10, 11, 15-16].

The investigations of the directivity patterns of laser ultrasound emitted from an interface between an optically transparent and an optically opaque solids have been fueled by the applications of laser ultrasound in high pressure research, which started just a few years ago [1-5]. Recently the directivity patterns of longitudinal and shear acoustic waves emitted by focusing laser radiation at the interface of diamond with aluminum have been simulated for the first time numerically [19].

In the present Chapter the analytical descriptions for the directivity patterns of laser ultrasound, which are valid for arbitrary combinations of transparent and opaque materials are presented. The directivity patterns are derived as particular cases of the known general solution for the acoustic fields generated by laser radiation in layered media [20, 21] by accounting for the specific features of the sound generation by thermo-elastic stresses distributed in the volume, which are essential for laser ultrasonics. Also the analytical solutions for the profiles of the longitudinal and shear acoustic pulses emitted in different directions are presented. The derived mathematical formulas provide straight opportunity to predict the acoustic field, which is formed in the diamond anvil cell after photo-generation and several reflections of bulk acoustic waves at the interfaces, relevant for the experiments in diamond anvil cell. Additionally, in this PhD research work, comparison of experimental results [2,4] with the analytical theory is given.

§II.1. Generation of acoustic waves by laser

II.1.1. Optoacoustics equations in an isotropic solid

For the analytical theory of laser ultrasound in diamond anvil cell in this Chapter, the thermo elasticity mechanism of generation acoustic wave is assumed. To describe the thermo-elastic generation of the acoustic wave in a solid the well-known equation can be used [22]:

$$\rho \frac{\partial^2 u_k}{\partial t^2} = \frac{\partial \sigma_{kl}}{\partial x_l}, \quad (\text{II.1})$$

where ρ - the density of the medium, u_k - the components of the displacement vector of the particles of the medium, index k, l can be 1($\equiv x$), 2($\equiv y$), 3($\equiv z$). σ_{kl} is the stress tensor:

$$\sigma_{kl} = 2\mu\eta_{kl} + \lambda\eta_{jj}\delta_{kl} + \sigma^i\delta_{kl} \quad (\text{II.2})$$

where η_{kl} is denotes the linearized strain tensor $\eta_{kl} = 1/2(\partial u_k / \partial x_l + \partial u_l / \partial x_k)$ (η_{jj} is the trace of this tensor), μ, λ are the Lamé constants ($\mu = \rho v_t^2$ and $\lambda = \rho(v_l^2 - 2v_t^2)$, $v_{l,t}$ are the velocities of bulk homogeneous compression/dilatation and shear acoustic waves), σ^i is the laser-induced stress magnitude.

II.1.2. Acoustic potentials

The equations for scalar ϕ and vector $\vec{\psi}$ potentials of acoustic displacement ($\vec{u} = \vec{u}_l + \vec{u}_t$, $\vec{u}_l = \text{grad}\phi$, $\vec{u}_t = \text{rot}\vec{\psi}$) in 2D rectangular co-ordinates, which can be obtained from (II.1), are

$$\frac{1}{v_l^2} \frac{\partial^2 \phi}{\partial t^2} - \Delta \phi = \sigma_n^i, \quad (\text{II.3})$$

$$\frac{1}{v_t^2} \frac{\partial^2 \psi}{\partial t^2} - \Delta \psi = 0, \quad (\text{II.4})$$

where $\sigma_n^i = \sigma^i / (\rho v_l^2)$ is the normalized laser-induced stress and ψ is the single nonzero component of the vector potential. In the case, where the laser-excitation is homogeneous along the y axis, ψ is the y-component of the vector potential and the Laplace operator in Eq. (II.3) and Eq. (II.4) is $\Delta = \partial^2 / \partial x^2 + \partial^2 / \partial z^2$. The displacement field has only two non-zero components

$$\vec{u} = \left(\frac{\partial \phi}{\partial x} - \frac{\partial \psi}{\partial z} \right) \vec{e}_x + \left(\frac{\partial \phi}{\partial z} + \frac{\partial \psi}{\partial x} \right) \vec{e}_z = \left(\frac{\partial \phi}{\partial x} - \frac{\partial \psi}{\partial z}, 0, \frac{\partial \phi}{\partial z} + \frac{\partial \psi}{\partial x} \right), \quad (\text{II.5})$$

where $\vec{e}_{x,z}$ are the unit vector directed along x and z coordinate axes, respectively. The non-zero components of the stress tensor, acting on a surface, which is normal to the z -axis, that can be found using, Eq. (II.2) and Eq. (II.5), are

$$\begin{aligned}\sigma_{zz} &= 2\mu\left(\frac{\partial^2\phi}{\partial z^2} + \frac{\partial^2\psi}{\partial x\partial z}\right) + \lambda\left(\frac{\partial^2\phi}{\partial x^2} + \frac{\partial^2\psi}{\partial z^2}\right) + \sigma^i, \\ \sigma_{zx} &= \mu\left(2\frac{\partial^2\phi}{\partial x\partial z} + \frac{\partial^2\psi}{\partial x^2} - \frac{\partial^2\psi}{\partial z^2}\right).\end{aligned}\tag{II.6}$$

Using for the Lamé constants the relations $\mu = \rho v_t^2$ and $\lambda = \rho(v_l^2 - 2v_t^2)$ and the wave equations Eq. (II.3) and Eq. (II.4) for the potentials, the stress components in Eq. (II.6) are presented in the form convenient for the application of the method of integral transforms

$$\begin{aligned}\sigma_{zz} &= \rho v_t^2 \left[\frac{1}{v_l^2} \frac{\partial^2\phi}{\partial t^2} + 2\left(\frac{\partial^2\psi}{\partial x\partial z} - \frac{\partial^2\phi}{\partial x^2}\right) \right], \\ \sigma_{zx} &= \rho v_t^2 \left[-\frac{1}{v_l^2} \frac{\partial^2\psi}{\partial t^2} + 2\left(\frac{\partial^2\phi}{\partial x\partial z} + \frac{\partial^2\psi}{\partial x^2}\right) \right].\end{aligned}\tag{II.7}$$

In order to solve the 2D problem of acoustic waves photo-generation, it is possible to use Fourier transforms.

§II.2. Solution for optoacoustics equations for solid/solid interface

In order to derive an analytical presentation of the directivity patterns of the acoustic waves when the laser radiation is incident from the transparent media “(2)” onto its plane interface with the light-absorbing media “(1)” (Fig. II.2), we use the general solution obtained for the optoacoustic transformation at these type of the interfaces in [21]. We present mathematical formalism for the case of two-dimensional (2D) geometry, which is experimentally realized by focusing laser radiation into a stripe with the length significantly exceeding its width (Fig. II. 2). The generalization of mathematical approach for the case of three-dimensional (3D) geometry, which is experimentally realized by focusing laser radiation into a circular spot, is presented in Appendix A. For definiteness we analyze the directivity patterns of acoustic waves in medium “(1)”, because the solutions for the medium “(2)” can be obtained by symmetry principles.

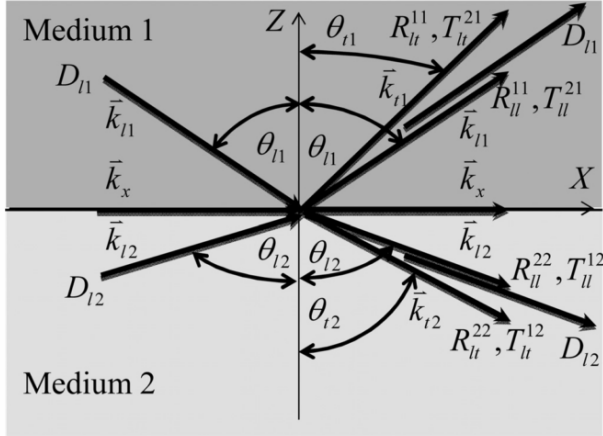


Figure II. 2. Reflection and refraction, with and without mode conversion, of plane compression/dilatation waves at a plane boundary between isotropic media.

II.2.1. Solution in the Fourier space

If the origin of the coordinate system is chosen at the interface of media “(1)” and “(2)” and z-axis is perpendicular to the interface and directed toward media “(1)”, the solutions for the Fourier spectra of scalar ϕ and vector ψ acoustic potentials [21], which satisfy the conditions of continuity of the mechanical displacements and stresses at the interface and the conditions of radiation in the far field [22, 23, 24], are

$$\begin{aligned} \tilde{\phi}_1(\omega, k_x, z) &= \frac{-i}{2\alpha_1} \left[\tilde{\sigma}_{n1}^i(\omega, k_x, \alpha_1) + R_{ll}^{11} \tilde{\sigma}_{n1}^i(\omega, k_x, -\alpha_1) + \frac{\alpha_1}{\alpha_2} T_{ll}^{21} \tilde{\sigma}_{n2}^i(\omega, k_x, \alpha_2) \right] e^{-i\alpha_1 z} \equiv \\ &\equiv \tilde{\phi}_1(\omega, k_x) e^{-i\alpha_1 z}, \end{aligned} \quad (\text{II.8})$$

$$\begin{aligned} \tilde{\psi}_1(\omega, k_x, z) &= \frac{-i}{2\alpha_1} \left[R_{lt}^{11} \tilde{\sigma}_{n1}^i(\omega, k_x, -\alpha_1) + \frac{\alpha_1}{\alpha_2} T_{lt}^{21} \tilde{\sigma}_{n2}^i(\omega, k_x, \alpha_2) \right] e^{-i\beta_1 z} \equiv \\ &\equiv \tilde{\psi}_1(\omega, k_x) e^{-i\beta_1 z}. \end{aligned} \quad (\text{II.9})$$

The Fourier transforms for the derivation and manipulation of the solutions in Eqs. (II.8) and (II.9) are defined by

$$\begin{aligned}\tilde{\tilde{F}}(\omega, k_x, k_z) &= \int_{-\infty}^{\infty} \int_{-\infty}^{\infty} \int_{-\infty}^{\infty} F(t, x, z) e^{-i(\omega t - k_x x - k_z z)} dt dx dz, \\ F(t, x, z) &= \frac{1}{(2\pi)^3} \int_{-\infty}^{\infty} \int_{-\infty}^{\infty} \int_{-\infty}^{\infty} \tilde{\tilde{F}}(\omega, k_x, k_z) e^{i(\omega t - k_x x - k_z z)} d\omega dk_x dk_z.\end{aligned}\tag{II.10}$$

In Eqs. (II.8) and (II.9), ω is the cyclic frequency of the laser-induced normalized stress fields $\sigma_{n1,2}^i$ and of the acoustic fields, k_x is the projection of the acoustic wave vectors on the x -axis, which is in the plane of the interface. We remind here that photo-induced thermo-elastic stress tensor σ_{kl}^i is isotropic in isotropic and cubic solids, i.e., $\sigma_{kl}^i \equiv \sigma^i \delta_{kl}$. Note that x -components of the wave vectors are equal for longitudinal and shear waves and also in both media [23, 24] (see Fig.II.2), while the z -components are different, i.e., $k_{z1,2} \equiv \alpha_{1,2} = \sqrt{k_{l1,2}^2 - k_x^2}$ and $k_{z1,2} \equiv \beta_{1,2} = \sqrt{k_{t1,2}^2 - k_x^2}$, where $\text{sgn}(\text{Re}\alpha_{1,2}) = \text{sgn}(\text{Re}\beta_{1,2}) = \text{sgn}(\omega)$ for real $\alpha_{1,2}$ and $\beta_{1,2}$ and $\text{sgn}(\text{Im}\alpha_{1,2}) = \text{sgn}(\text{Im}\beta_{1,2}) = -1$ for imaginary $\alpha_{1,2}$ and $\beta_{1,2}$. Here $\omega/v_{l1,2} \equiv k_{l1,2}$ and $\omega/v_{t1,2} \equiv k_{t1,2}$ are the wave numbers of the compression/dilation and shear acoustic waves in medium “1” and “2”, with $v_{l1,2}$ and $v_{t1,2}$ denoting the velocities of the longitudinal and shear waves, respectively. Although the physical nature of laser-induced stresses in Eqs. (II.8) and (II.9) is not specified yet, below we analyze the case of thermo-elastic stresses caused by laser heating of the media. They are normalized on the longitudinal moduli of the corresponding media, $\sigma_{n1,2}^i = \sigma_{1,2}^i / (\rho_{1,2} v_{l1,2}^2)$, where $\rho_{1,2}$ are the densities. Although solutions (II.8) and (II.9), borrowed from [21], are written for the two-dimensional problem and are well-suited only for the line-source-point-receiver LU-DAC technique [4,5], the extension of the general solution to the three-dimensional case is straightforward (Appendix A).

The solutions in Eqs. (II.8) and (II.9) have a transparent physical sense. They account for the fact that the stresses are induced by laser radiation, in general, in both contacting media. They also account for the fact that thermo-elastic stress in isotropic media can generate only compression/dilatation acoustic waves [22, 25]. In the qualitative illustration of the phenomena under consideration in Fig. II.1, the wave vectors of the compression/dilatation waves excited by thermo-elastic sources are marked by $D_{11,12}$. Those of these waves, which propagate from the interface, contribute to the directivity patterns of laser ultrasound without any additional transformations. Those of these waves, which are directed towards the interface are transformed in reflection/transmission into four waves, both compression/dilatation and shear, which could contribute to directivity patterns of laser ultrasound. In the solution (II.8) for the compression/dilatation waves, i.e., for the scalar

potential in the first medium, the first term describes the wave generated in the first medium and propagating in the bulk of the first medium without any interaction with the interface. This wave is denoted in the right-hand-side of Fig. II.2 by D_{l1} . The second term describes the waves also generated in the first medium, but redirected in the bulk of this medium only after the reflection on the interface (R_{ll}^{11} is the reflectivity coefficient). This wave is denoted in Fig. II.2 by R_{ll}^{11} . The third term describes the waves that are generated in the second medium and transmitted into the first medium across the interface (T_{ll}^{21} is the transmission coefficient). This wave is denoted in Fig. II.2 by T_{ll}^{21} . In the solution (II.9) for the shear waves, *i.e.*, for the vector potential in the first medium, the first term describes the wave which is generated at the interface due to mode conversion of the compression/dilatation waves, denoted in the left-hand-side of Fig. II.2 by D_{l1} , in reflection from the interface (R_{ll}^{11} is the reflection coefficient with mode conversion). The corresponding shear wave, contributing to the directivity pattern of laser ultrasound is denoted in Fig. II.2 by R_{ll}^{11} . The second term describes the generation of the shear waves at the interface due to mode conversion of the compression/dilatation waves, denoted in the left-hand-side of Fig. II.2 by D_{l2} , in transmission across the interface (T_{ll}^{21} is the transmission coefficient with mode conversion). The corresponding shear wave, contributing to the directivity pattern of laser ultrasound in the first medium is denoted in Fig. II.2 by T_{ll}^{21} . The physical nature of the waves contributing to the directivity patterns of laser ultrasound in the second medium (see Fig. II.2) can be understood similarly.

II.2.2. Reflection and transmission coefficients. Determinant Stoneley.

The reflection and transmission coefficients, which are necessary for using the solution in Eq. (II.8), can be found in the textbooks [23, 24, 26]. In [21] the classical approach of deriving the system of algebraic equations for R_{ll}^{11} , R_{ll}^{12} and T_{ll}^{21} of acoustic potentials was reminded. The resultant system is

$$\begin{pmatrix} \beta_1 & \beta_2 & -k_x & k_x \\ k_x & -k_x & \alpha_1 & \alpha_2 \\ \beta_1 & \mu_{21}\beta_2 & -\gamma_1 & \mu_{21}\gamma_2 \\ \gamma_1 & -\mu_{21}\gamma_2 & \alpha_1 & \mu_{21}\alpha_2 \end{pmatrix} \begin{pmatrix} R_{ll}^{11} \\ T_{ll}^{12} \\ R_{ll}^{11} \\ T_{ll}^{12} \end{pmatrix} = \begin{pmatrix} k_x \\ \alpha_1 \\ \gamma_1 \\ \alpha_1 \end{pmatrix}, \quad (\text{II.11})$$

where the compact notations $\mu_{21} \equiv \mu_2 / \mu_1$ and $\gamma_{1,2} \equiv k_x - k_{t1,2}^2 / (2k_x)$ are introduced, $\mu_{1,2}$ are the second Lamé constants (shear moduli). The principal determinant of this system is the so-called Stoneley determinant [26].

The transmission coefficients T_{ll}^{21} and T_{ll}^{12} necessary for the evaluation of Eq. (II.9) can be obtained either from T_{ll}^{12} and T_{ll}^{21} in Eq. (II.11), using symmetry considerations [23], or by solving the following system, which in turn can be derived from Eq. (II.11) using symmetry principles

$$\begin{pmatrix} \beta_2 & \beta_1 & k_x & -k_x \\ -k_x & k_x & \alpha_2 & \alpha_1 \\ \beta_2 & \mu_{12}\beta_1 & \gamma_2 & -\mu_{12}\gamma_1 \\ -\gamma_2 & \mu_{12}\gamma_1 & \alpha_2 & \mu_{12}\alpha_1 \end{pmatrix} \begin{pmatrix} R_{ll}^{22} \\ T_{ll}^{21} \\ R_{ll}^{22} \\ T_{ll}^{21} \end{pmatrix} = \begin{pmatrix} -k_x \\ \alpha_2 \\ -\gamma_2 \\ \alpha_2 \end{pmatrix}, \quad (\text{II.12})$$

Thus the general solution for the laser-generated acoustic field in medium “1” in the (ω, k_x, z) space is complete.

II.2.3. Solution in the real space

To get the description of the emitted acoustic field in (ω, x, z) space it is sufficient to apply to Eqs. (II.8) and (II.9) the following inverse Fourier transformation (Eq. (II.10)) over k_x :

$$\begin{pmatrix} \tilde{\phi}_1(\omega, x, z) \\ \tilde{\psi}_1(\omega, x, z) \end{pmatrix} = \frac{1}{2\pi} \int_{-\infty}^{+\infty} \begin{pmatrix} \tilde{\phi}_1(\omega, k_x) e^{-i\alpha_1 z} \\ \tilde{\psi}_1(\omega, k_x) e^{-i\beta_1 z} \end{pmatrix} e^{-ik_x x} dk_x. \quad (\text{II.13})$$

To find the directivity pattern of the laser-induced acoustic source it is necessary to evaluate the integral only at large distances from the source, where the phase of the integrand is strongly changing even with small variations of k_x . This provides opportunity to approximate the integrals in Eq. (II.13) in the general case by using the method of steepest descent (method of the stationary phase) [26]. The derived dependences of the complex amplitudes of the compression/dilatation and shear cylindrical waves at large distances $r = \sqrt{x^2 + z^2}$ from their excitation region on the angle of emission θ , *i.e.*, the angle between the direction of observation and the z -axis (see Fig. II.2), are

$$\begin{pmatrix} \tilde{\phi}_1(\omega, r, \theta) \\ \tilde{\psi}_1(\omega, r, \theta) \end{pmatrix} = \cos \theta \begin{pmatrix} \sqrt{k_{11}} \tilde{\phi}_1(\omega, k_{11} \sin \theta) \\ \sqrt{k_{11}} \tilde{\psi}_1(\omega, k_{11} \sin \theta) \end{pmatrix} \sqrt{\frac{i}{2\pi r}} \begin{pmatrix} e^{-ik_{11}r} \\ e^{-ik_{11}r} \end{pmatrix}. \quad (\text{II.14})$$

The solution in Eq. (II.14) has been derived by assuming that $\omega > 0$. The solution for negative frequencies $\omega < 0$, can be derived using $\tilde{\phi}_1(\omega, r, \theta) = \tilde{\phi}_1^*(-\omega, r, \theta)$ and $\tilde{\psi}_1(\omega, r, \theta) = \tilde{\psi}_1^*(-\omega, r, \theta)$, *i.e.*, with the application of complex conjugation. It should be also noted, that neither the interface waves (Stoneley waves, if they exist) nor the contribution to far fields from the head waves are included in the solution in Eq. (II.13). They could be evaluated through the analysis of the pole (if it exists) and the branch points of the integrand in Eq. (II.13). However it is worth noting that the head waves, *i.e.*, contributions from branch cut integrals, are asymptotically negligible at large distances, because they diminish in amplitude faster than the bulk waves [26, 27]. To proceed to the analysis of the particular possible experimental situations the distribution of the laser-induced stresses in the contacting media should be specified.

§II.3. Description of the laser-induced thermo-elastic source

The spectrum of the normalized thermo-elastic stress is controlled by the spectrum of the laser-induced temperature rise [21, 22]

$$\tilde{\tilde{\sigma}}_{n1,2}^i(\omega, k_x, k_z) = -\bar{\alpha}_{1,2} [(1 + \nu_{1,2}) / (1 - \nu_{1,2})] \tilde{\tilde{T}}'_{1,2}(\omega, k_x, k_z), \quad (\text{II.15})$$

where $\bar{\alpha}$, ν and T' are the linear thermal expansion coefficient, Poisson ratio and the temperature rise. The laser-induced heating is described in 2D rectangular geometry, dictated by the line-type spatial structure of the focused laser radiation [4,5] (Fig.II.1), using the equations of heat conduction in the contacting materials [20, 21, 22]. The equation of heat conduction in the light absorbing material is inhomogeneous. The laser-induced heat release $Q_1(t, x, z)$ in the light-absorbing material, *i.e.*, the increase of the material thermal energy density per unit time in a unit volume, can be presented in the form $Q_1 = f(t)\Phi(x)W(z)$ [22, 24], where the function $f(t)$ describes the laser pulse intensity envelope in time, the function $\Phi(x)$ describes the lateral distribution of the absorbed laser energy release controlled by laser intensity distribution at the irradiated surface, *i.e.*, by focusing, and

the function $W(z)$ describes the distribution of the absorbed laser energy release in depth controlled by the optical penetration depth and some other physical parameters of the light absorbing medium [22, 25]. The solution of the thermal conductivity equations, satisfying the conditions of continuity of the temperature and of the heat flux at the interface between the opaque and the transparent media, can be derived by the same method of integral transforms, which has been applied in [21] to derive the solutions in Eqs. (II.8) and (II.9) of the inhomogeneous wave equations. It is sufficient to find the solution in the reciprocal Fourier spaces, where it can be factorized in the following form

$$\tilde{\tilde{T}}'_{1,2}(\omega, k_x, k_z) \equiv \Theta_{1,2}(\omega, k_x, k_z) \tilde{f}(\omega) \tilde{\Phi}(k_x). \quad (\text{II.16})$$

The general expressions of the functions $\Theta(\omega, k_x, k_z)$ are

$$\begin{aligned} \Theta_1(\omega, k_x, k_z) &= \frac{1}{\chi_1(k_z^2 - \delta_1^2)} \left[\tilde{W}(k_z) + \frac{\chi_1 k_z - \chi_2 \delta_2}{\chi_1 \delta_1 + \chi_2 \delta_2} \tilde{W}(-\delta_1) \right], \\ \Theta_2(\omega, k_x, k_z) &= \frac{(-1)}{(\chi_1 \delta_1 + \chi_2 \delta_2)(k_z + \delta_2)} \tilde{W}(-\delta_1). \end{aligned} \quad (\text{II.17})$$

Here $\delta_{1,2} \equiv \sqrt{-i\omega/D_{1,2} - k_x^2}$ can be associated to the projection of the thermal wave vector $\sqrt{-i\omega/D_{1,2}}$ on the z -axis, $D_{1,2}$ are the thermal diffusivities and $\chi_{1,2}$ are the thermal conductivities of the media in contact. It is worth mentioning here that, if future experiments in DAC indicate the importance of thermal boundary resistance at the interface between the diamond and the sample, then the solution of the heat conduction problem with modified interface conditions for temperature field and heat flux, could be still obtained by the same mathematical formalism of integral transforms.

The description of the laser-induced stresses presented in Eqs. (II.15) – (II.17) finalizes the general solution for the ultrasound emission by thermoelastic sources. The specific problems of interest for the practical analysis differ only by the characteristics of the laser induced heat release $Q_1 = f(t)\Phi(x)W(z)$. The common models for the laser pulse intensity envelope, distribution of laser intensity across the focus and distribution of laser intensity in depth of light absorbing medium are $f(t) = \exp[-(2t/\tau_L)^2]$, $\Phi(x) = \exp[-(2x/d)^2]$, $W(z) = (I/l)\exp(-z/l)$, respectively where τ_L is the laser pulse duration at 1/e level, d is the diameter of the focus at 1/e level, I is the absorbed part of the laser intensity incident on the interface and l is the characteristic heating depth, which in metals

can depend not only on the penetration depth of laser radiation but also on the penetration depth of the non-equilibrium overheated electrons [28, 29, 30]. In the Fourier domain the description of the heat release is

$$\begin{aligned}\tilde{f}(\omega) &= (\sqrt{\pi}\tau_L/2)\exp[-(\tau_L\omega/4)^2], \\ \tilde{\Phi}(k_x) &= (\sqrt{\pi}d/2)\exp[-(dk_x/4)^2], \\ \tilde{W}(k_z) &= (I/l)(l^{-1} - ik_z)^{-1}.\end{aligned}\tag{II.18}$$

In some particular experimental situations, depending on laser focusing, duration of the laser pulses, penetration depth of the laser radiation and physical properties of the contacting solids, the general theoretical formulas for the temperature rise and thermo-elastic stresses can be significantly simplified.

§II.4. Directivity patterns of laser ultrasound in diamond anvil cell

II.4.1. General case and delta-localized sources

The boundary between laser ultrasonics and laser hypersonics (picosecond laser ultrasonics) is commonly and qualitatively considered to pass near 1 GHz frequency. For example, in accordance with Eq. (II.18) the spectrum of acoustic waves emitted in the LU-DAC type experiments with sub-nanosecond laser, with $\tau_L \geq 0.5$ ns, are limited in frequencies by $f \leq 1.3$ GHz. So these experiments can be considered as laser ultrasonics experiments. At ultrasonic frequencies in metals and other good thermal conductors (in diamond, for example) the depth of the zone heated either by penetrating laser radiation or by the transport of the overheated electrons, is thin both thermally and acoustically. In other words, the initially heated depth is much shorter than both thermal and acoustic wavelengths, and the heating can be well approximated by interface-localized heating. From the mathematics point of view for laser ultrasound the relation $\tilde{W}(k_z) \cong \tilde{W}(-\delta_1) \cong I$, holds, and consequently the description in Eq. (II.17) simplifies to

$$\Theta_{1,2}(\omega, k_x, k_z) = \frac{(\pm 1)I}{(\chi_1\delta_1 + \chi_2\delta_2)(k_z \mp \delta_{1,2})}.\tag{II.19}$$

Additionally at ultrasonic frequencies the acoustic wavelengths are longer than the thermal wavelengths. In this case, neglecting the acoustic wave numbers in comparison with the thermal wave numbers $\left| \sqrt{-i\omega/D_{1,2}} \right|$, the solution in Eq. (II.19) is reduced to

$$\Theta_{1,2}(\omega, k_x, k_z) = -\frac{\sqrt{D_{1,2}}I}{(-i\omega)(\sqrt{e_1} + \sqrt{e_2})} \quad (\text{II.20})$$

Here $e_{1,2}$ denote the thermal effusivities of the contacting media. The description of the laser-induced stresses at ultrasonic frequencies, which is derived above in Eqs. (II.15), (II.16) and (II.20), provides opportunity to present the directivity patterns of the laser ultrasound, i.e., Eq. (II.14), in the following form

$$\begin{aligned} \tilde{\phi}_1(\omega, r, \theta) = P_1 I \left\{ 1 + R_{ll}^{11}(\theta) + P_{2/1} \frac{\cos\theta}{\sqrt{(\nu_{l1}/\nu_{l2})^2 - \sin^2\theta}} T_{ll}^{21}(\theta) \right\} \\ \times \frac{\tilde{\Phi}(k_{l1} \sin\theta) \tilde{f}(\omega)}{\omega} \sqrt{\frac{i}{2\pi k_{l1} r}} e^{-ik_{l1} r} \end{aligned} \quad (\text{II.21})$$

$$\begin{aligned} \tilde{\psi}_1(\omega, r, \theta) = P_1 I \left\{ \frac{\cos\theta}{\sqrt{(\nu_{l1}/\nu_{l1})^2 - \sin^2\theta}} R_{ll}^{11}(\theta) + P_{2/1} \frac{\cos\theta}{\sqrt{(\nu_{l1}/\nu_{l2})^2 - \sin^2\theta}} T_{ll}^{21}(\theta) \right\} \\ \times \frac{\tilde{\Phi}(k_{l1} \sin\theta) \tilde{f}(\omega)}{\omega} \sqrt{\frac{i}{2\pi k_{l1} r}} e^{-ik_{l1} r} \end{aligned} \quad (\text{II.22})$$

Here the compact notation P_l is introduced for the following combination of physical parameters $P_1 \equiv \frac{\bar{\alpha}_1(1+\nu_1)\sqrt{D_1}}{2(1-\nu_1)(\sqrt{e_1} + \sqrt{e_2})}$. The parameter $P_{2/1} \equiv \frac{\bar{\alpha}_2(1+\nu_2)(1-\nu_1)\sqrt{D_2}}{\bar{\alpha}_1(1+\nu_1)(1-\nu_2)\sqrt{D_1}}$ characterises the relative efficiency of laser light transformation into ultrasound in the contacting media in the case of interface absorption of laser radiation.

From the physics point of view the mathematical combinations in the figure brackets in Eqs. (II.21) and (II.22) describe the directivity of the emission of compression/dilatation and shear acoustic waves, respectively, by laser radiation delta-localized in 2D geometry, i.e., when laser radiation is

focused on y -axis. Formally this limiting situation is realized due to $\tilde{\Phi}(k_x) = \text{const} \propto d$, when the dependence on angles rests only in the terms inside the figure brackets. These terms are the most important parts of the directivity patterns, which are expected to be sensitive to the relative parameters of the materials in contact. So we need to evaluate

$$\Xi_\phi(\theta) \equiv 1 + R_{li}^{11}(\theta) + P_{2/1} \frac{\cos \theta}{\sqrt{(\nu_{l1}/\nu_{l2})^2 - \sin^2 \theta}} T_{li}^{21}(\theta), \quad (\text{II.23})$$

$$\Xi_\psi(\theta) \equiv \frac{\cos \theta}{\sqrt{(\nu_{l1}/\nu_{l1})^2 - \sin^2 \theta}} R_{li}^{11}(\theta) + P_{2/1} \frac{\cos \theta}{\sqrt{(\nu_{l1}/\nu_{l2})^2 - \sin^2 \theta}} T_{li}^{21}(\theta) \quad (\text{II.24})$$

The role of the other factors in Eqs. (II.21) and (II.22), which are angle-dependent, *i.e.*, of $\tilde{\Phi}(k_{l,t1} \sin \theta) \propto (\sqrt{\pi}d/2) \exp[-(d\omega \sin \theta / 4\nu_{l,t1})^2] \equiv (\sqrt{\pi}d/2) \exp[-(\pi d \sin \theta / 2\lambda_{l,t1})^2]$ is physically clear. These factors, which depend on laser focusing, indicate that the higher is the ratio between the laser beam diameter d and the acoustic wavelength $\lambda_{l,t1}$ – the smaller is the emission angle. Or, saying differently, these factors control the transition from a structured directivity pattern in the case of tight focusing of laser radiation ($d \ll \lambda_{l,t1}$) to the plane compression/dilatation wave emission in the case of defocused laser irradiation ($d \gg \lambda_{l,t1}$). At the same time these factors, being frequency dependent, also influence the profiles of the emitted ultrasound pulses.

As demonstrated in the Appendix A, the solutions (II.23) and (II.24) describe not only the directivity of a delta-localized at the interface line source in the 2D geometry by also the directivity of a delta-localized at the interface point source in the 3D geometry. The similar situation of the absence of difference in the directivity patterns of delta-localized sources in 2D and 3D geometries was earlier noticed for the case of laser action on the mechanically free surface of a solid [15]. That is why we start the analysis of the directivity patterns in the next Section from the evaluation of the structure of the directivity patterns of delta-localized sources in Eqs. (II.23) and (II.23). The analysis of the role of the frequency-dependent factors in Eqs. (II.21) and (II.22) will be presented later in Section II.5. In the case of the laser action on mechanically free surface of a solid it was noticed [15] that the profiles of the emitted ultrasound pulses could be different in 2D and in 3D geometries, although we are not aware of any, even theoretical, confirmation of this expectation. In Section II.5 we confirm this difference analytically and we also demonstrate that frequency-dependent factors in Eqs. (II.21) and (II.22) provide in 2D and 3D geometries different modulations of the point-source directivity patterns.

It is worth noting here that our general theory, presented above, describes as limiting cases the mechanically free and the infinitely rigid (immobile) interfaces (see Appendix B).

II.4.2. Directivity patterns for Fe in diamond anvil cell

In this Section, in view of the perspectives to apply the developed theory to the laser ultrasonics experiments in diamond anvil cell (LUDAC technique [2-5]) we present the theoretical results for laser ultrasound emitted by a thermo-elastic source delta-localized on the interface of diamond, i.e., carbon in the cubic diamond phase denoted as C_d , and iron (Fe). Important feature of this interface is that both bulk acoustic velocities in the first of the contacting media (in Fe) are slower than both acoustic velocities in the second of the contacting media (in C_d), $v_{t1} < v_{l1} < v_{t2} < v_{l2}$. This situation, expected to be typical for practically all the materials in the diamond anvil cell, is qualitatively illustrated in Fig. II.2. As it has been mentioned above, the translation invariance of the system along the x - axis requires the conservation in interaction of the acoustic waves the x - components of their wave vectors (see Fig. II.2). Because of this, particular ordering of the acoustic velocities, i.e., $v_{t1} < v_{l1} < v_{t2} < v_{l2}$, results in particular ordering of the propagation angles of the interacting waves $\theta_{t1} < \theta_{l1} < \theta_{t2} < \theta_{l2}$ and, most significantly, in particular ordering and the number of critical angles, which could play role in the reflection/transmission of the compression/dilatation acoustic waves by the interface. We define here as critical angles those angles of observation, at which one of the acoustic waves interacting at the interface, propagates along the interface [24]. For the angles defined as in Fig. II.2, this definition means, that at angles larger than the critical one the x -component of the wave vector for these waves becomes larger than the total wave vector, while the z -component becomes imaginary valued. Thus, this wave becomes evanescent and stops to transfer acoustic energy away from the surface. The analysis which follows, demonstrates that critical angles are the characteristic angles in structuring of the directivity patterns of laser ultrasound, although they are not the only angles that could be of importance.

In Fig. II. 3 we present the results for longitudinal waves emitted in iron (medium (1)) from its laser-irradiated interface with diamond. The materials parameters, used in the evaluation are listed in Table II. 1. The estimated critical angles are listed in Table II. 2. We present in Fig. II.3 and in some of the following Figures the dependencies on the angle of observation both of the amplitudes and of the phases of the emitted potentials. The knowledge of phase directivity patterns is important for the understanding of some features of the amplitude directivity patterns and is necessary for the evaluation of the emitted acoustic pulse profiles (Section II.5).

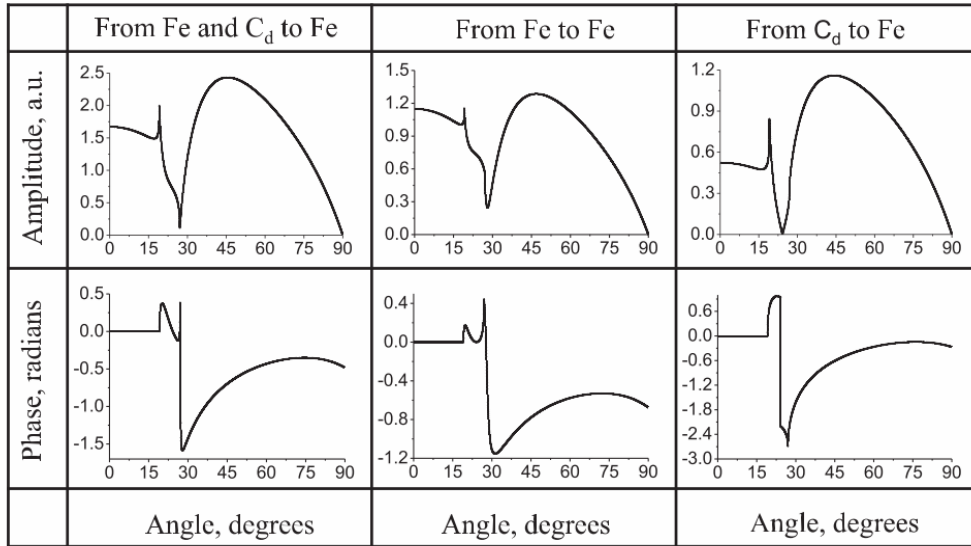


Figure II. 3. Amplitude and phase directivity patterns of longitudinal ultrasound emitted in iron by delta-localized sources, created by laser-irradiation of plane interface between iron and diamond.

Physical properties	diamond	iron	aluminum
Longitudinal velocity of sound (m s^{-1})	18000	5900	6420
Transverse velocity of sound (m s^{-1})	13000	3200	3040
Density (kg m^{-3})	3500	7900	2700
Linear thermal expansion coefficient (K^{-1})	1.1×10^{-6}	11.3×10^{-6}	23.1×10^{-6}
Poisson's ratio	0.20	0.30	0.34
Thermal diffusivities ($\text{m}^2 \text{s}^{-1}$)	7.80×10^{-4}	0.23×10^{-4}	0.84×10^{-4}
$P_{2/1}$	\otimes	0.46	0.07

Table II. 1. Values of physical parameters of diamond, iron and aluminum, applied in the manuscript for the estimates and the evaluation of the directivity patterns.

The results presented in the middle column in Fig. II.3 demonstrate the contribution to the total longitudinal laser ultrasound signal in Fe (Eq. (II.23)) which is due to the compression/dilatation waves initially generated in Fe. At angles smaller than all the critical ones, all five acoustic waves coupled by the interface, *i.e.*, the incident on the interface longitudinal wave and four acoustic waves created by the interface, are all propagating, and the latter four transport the acoustic energy from the interface to the bulk of contacting media. The first characteristic feature in the directivity patterns of both amplitudes and phases appears at critical angle $\theta_{1/12} = \arcsin(v_{11}/v_{12}) \approx 19.1^\circ$. At angles larger than $\theta_{1/12}$ the longitudinal acoustic waves in diamond are evanescent and they stop to transport acoustic energy away from the interface.

critical angles	v_{11}/v_{12} $\arcsin(v_{11}/v_{12})$	v_{11}/v_{12} $\arcsin(v_{11}/v_{12})$	v_{11}/v_{12} $\arcsin(v_{11}/v_{12})$	v_{11}/v_{12} $\arcsin(v_{11}/v_{12})$	v_{11}/v_{11} $\arcsin(v_{11}/v_{11})$	v_{12}/v_{12} $\arcsin(v_{12}/v_{12})$
(1)iron	0.328	0.454	0.178	0.246	0.542	0.722
(2)diamond	19.1°	27.0°	10.2°	14.2°	32.8°	46.2°
(1)aluminum	0.357	0.494	0.169	0.234	0.473	0.722
(2)diamond	20.9°	29.6°	9.7°	13.5°	28.3°	46.2°

Table II. 2. The values of acoustic velocities ratios and of the related critical angles, which manifest themselves in the phenomena of reflection and refraction of compression/dilatation waves at the interfaces between iron and diamond and between the aluminum and diamond.

The second characteristic feature in the directivity patterns of both amplitudes and phases appears at critical angle $\theta_{11/12} = \arcsin(v_{11}/v_{12}) \approx 27.0^\circ$. At angles larger than $\theta_{11/12}$ the shear acoustic waves in diamond are evanescent and they stop to transport acoustic energy away from the interface. Thus, at angles larger than $\theta_{11/12}$, the incident from Fe on the interface acoustic energy does not induce the emission of the acoustic energy flux into diamond (medium (2)). From the physics point of view it would be reasonable to expect that, under these conditions, the emission of acoustic waves in Fe would increase with angle increasing above $\theta_{11/12}$. At the same time the emission of the longitudinal waves in Fe should stop at angles above $\theta_{11/11} = \arcsin(v_{11}/v_{11}) = 90.0^\circ$, when they become evanescent. So the position of the second maximum in the amplitude directivity pattern, which in the middle column of Fig. II.3 is between $\theta_{11/12}$ and 90.0° , looks reasonable. It is worth noting that the directivities presented in the middle column of Fig. II.3 are very different from the expected directivities of the reflection coefficient R_{ll}^{11} , which are presented for comparison in Fig. II.4, and are in accordance with known theoretical predictions [24, 26, 31].

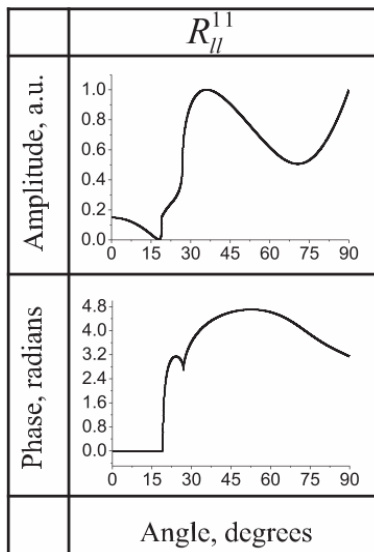


Figure II. 4. Amplitude and phase of the reflection coefficient for the plane longitudinal acoustic wave incident from iron on its interface with diamond.

The reason of this strong difference is in the particularity of laser ultrasound, where the total field of longitudinal waves in Eq. (II.23) emitted from Fe into Fe is due to both direct and reflected waves (see the sum $1 + R_{ii}^{11}$ in Eq. (II.23)) and due to crucial role played by the phases of the acoustic waves in this summation.

The results presented in the right column in Fig. II.3 demonstrate the contribution to the total longitudinal laser ultrasound signal in Fe of the compression/dilatation waves initially generated in C_d . The compression/dilatation waves generated in diamond are incident on the interface as propagating waves and carry energy in the bulk of the diamond after reflection only at the angles smaller than the first critical angle $\theta_{11/12} = \arcsin(\nu_{11} / \nu_{12}) \approx 19.1^\circ$. At angles larger than $\theta_{11/12}$ these are the evanescent compression/dilatation waves thermo-elastically generated in diamond that are transformed into propagating acoustic waves carrying energy from the interface. At angles larger than the second critical angle $\theta_{11/12} = \arcsin(\nu_{11} / \nu_{12}) \approx 27.0^\circ$ the shear waves in diamond also become evanescent and the acoustic energy incident on the interface from the diamond side could be transported only into Fe. Both critical angles are clearly manifested in the right column in Fig. II.3 in the directivity pattern of the phase. However, in the directivity pattern of the phases an additional feature in the form of a phase jump of 180° is clearly seen at an angle of 24.2° between the two critical angles. This phase shift is a definite fingerprint of the zero in the amplitude directivity pattern. Thus our analysis indicates the existence of an angle at which the evanescent longitudinal waves incident on the interface from the C_d side cannot be transformed into propagating longitudinal waves in Fe. It can be seen that this zero in the transmission coefficient T_{ii}^{21} suppresses the possible feature related to the second critical angle in the amplitude directivity pattern. The position of the local maximum in the amplitude directivity pattern between the second critical angle and 90° can be explained similar to the case of the middle column in Fig. II.3.

The results presented in the left column of Fig. II.3 demonstrate the total longitudinal laser ultrasound signal in Fe which is due to the compression/dilatation waves initially generated both in Fe and in C_d . The directivities in the left column are obtained by summation of those in the middle and right columns and accounting for the relative phase of different acoustic contributions. Because the efficiencies of the opto-acoustic conversion in Fe and C_d are comparable (see the estimate of the characteristic parameter $P_{2/1}$ in Table II.1) both contacting materials importantly contribute to the resultant directivity pattern. The characteristic features related to the above discussed two critical angles and the local maximum in amplitude directivity between the second critical angle and 90° is predicted. However, it is worth noting that if, for different pairs of contacting materials, the zero in the

transmission of the longitudinal waves across the interface without mode conversion takes place at an angle larger than the second critical angle, then the local maximum in the directivity pattern could be between this angle and 90° .

In Fig. II.5 we present the results of our evaluation of the transversal waves emitted in iron (medium (1)) from its laser-irradiated interface with diamond. The results presented in the middle column in Fig. II.5 demonstrate the contribution to the total shear laser ultrasound signal in Fe (Eq. (II.24)), which is due to the compression/dilatation waves initially generated in Fe. At angles smaller than all the critical ones all five acoustic waves coupled by the interface, *i.e.*, the incident on the interface longitudinal wave and four acoustic waves created by the interface, are all propagating, and the latter four waves are transporting the acoustic energy from the interface to the bulk of contacting media. The emission of the shear acoustic waves in the direction normal to the laser-irradiated surface is forbidden by symmetry principles [25, 32, 33]. This explains the growth in amplitude of the emitted shear waves at small angles. The first characteristic feature in the directivity patterns of both amplitudes and phases appears at critical angle $\theta_{t1/t2} = \arcsin(\nu_{t1} / \nu_{t2}) \approx 10.2^\circ$. At angles larger than $\theta_{t1/t2}$ the longitudinal acoustic waves in diamond are evanescent and they stop to transport acoustic energy from the interface. The second characteristic feature in the directivity patterns of both amplitudes and phases appears at critical angle $\theta_{t1/l2} = \arcsin(\nu_{t1} / \nu_{l2}) \approx 14.2^\circ$. At angles larger than $\theta_{t1/l2}$ the shear acoustic waves in diamond are evanescent and they stop to transport acoustic energy from the interface. Thus, at angles larger than $\theta_{t1/l2}$, the incident from Fe on the interface acoustic energy does not induce the emission of acoustic waves into diamond (medium (2)). The third critical angle $\theta_{t1/l1} = \arcsin(\nu_{t1} / \nu_{l1}) \approx 32.8^\circ$ most clearly manifests itself in the directivity pattern of the phase. Above this critical angle the shear acoustic waves are emitted in Fe due to the mode conversion in reflection from the interface of the evanescent compression/dilatation waves generated by laser radiation in Fe. Shear waves become the only wave transporting the acoustic energy from the interface. The reasoning, similar to the one devoted above to longitudinal waves directivity patterns, leads to the conclusion that a local maximum in the amplitude directivity pattern, observed in the middle column in Fig. II.5 at angles between the largest critical angle and 90° , could be expected theoretically. Additional structuring of the directivity patterns presented in the middle column in Fig. II.5 is due to the existence of an angle of 18.8° , at which there is no reflection of the compression/dilatation waves with mode conversion into the shear waves (in Eq. (II.24) $R_{tt}^{11} = 0$) [24, 26, 31]. In the directivity pattern of the phases, this angle manifests itself as -180° phase jump. It is worth noting here, that the absence of mode conversion of the compression/dilatation waves in

reflection from a mechanically free surface is known to take place at the angle of 45° (Appendix B) [23, 25].

The results presented in the right column in Fig. II.5 show the contribution to the total shear laser ultrasound signal in Fe (Eq. (II.24)), which is due to the compression/dilatation waves initially generated in diamond. They could be interpreted similarly to those in the middle column. Three critical angles clearly manifest themselves in the directivity patterns both of the amplitudes and of the phases. However the directivity patterns for the emission of shear waves in Fe due to the compression/dilatation waves laser-generated in C_d (right column in Fig. II.5) are less structured in comparison with those in the middle column, because there is no angle between 0° and 90° where the transmission of the compression/dilatation waves with mode conversion is impossible (in Eq. (II.24) $T_{li}^{21} \neq 0$).

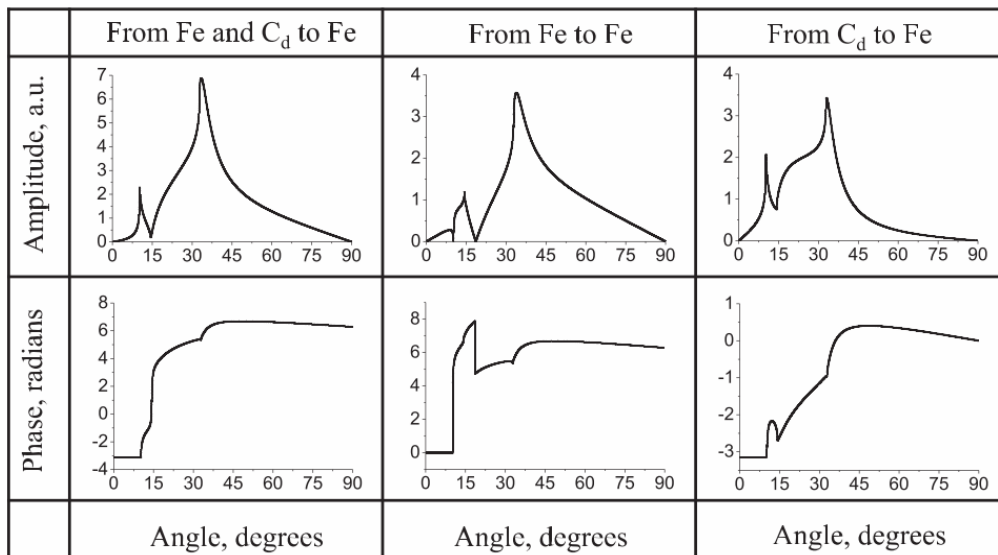


Figure II. 5. Amplitude and phase directivity patterns of shear ultrasound emitted in iron by delta-localized sources, created by laser-irradiation of plane interface between iron and diamond.

The results presented in the left column in Fig. II.5 show the total shear laser ultrasound signal in Fe which is due to the compression/dilatation waves initially generated both in Fe and in C_d . The directivities in the left column are obtained by summation of those in the middle and right columns and accounting for the relative phases of different acoustic contributions. Both contacting materials significantly contribute to the resultant directivity pattern because the efficiencies of the opto-acoustic conversion in Fe and C_d are comparable (see the estimate of the characteristic parameter $P_{2/1}$ in Table II. 1). The characteristic features related to the above discussed three critical angles and the local maximum in amplitude directivity between the third critical angle and 90° are predicted. However, if for different pairs of the contacting materials, the zero in the transmission of the longitudinal waves

across the interface with mode conversion takes place at an angle larger than the third critical angle, then the local maximum in the directivity pattern could be between this angle and 90° .

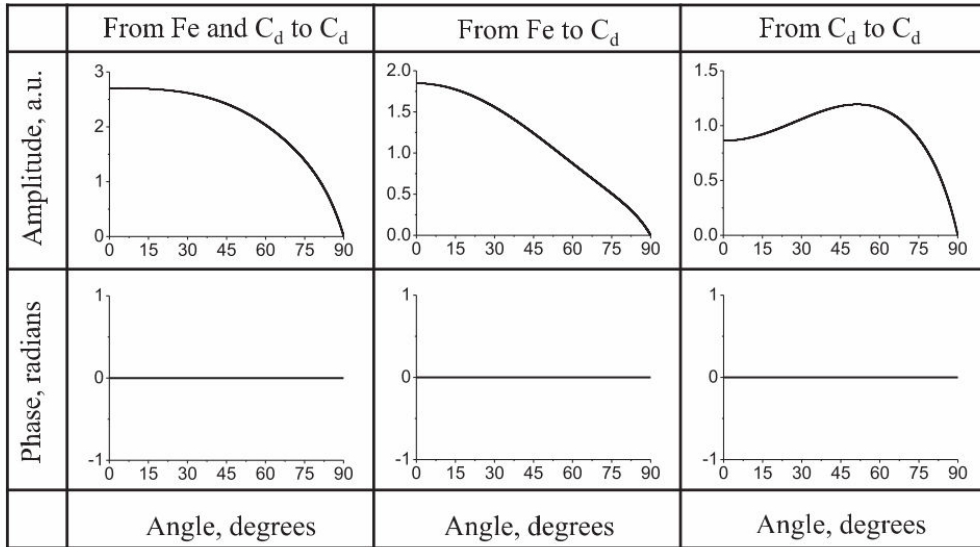


Figure II. 6. Amplitude and phase directivity patterns of longitudinal ultrasound emitted in diamond by delta-localized sources, created by laser-irradiation of plane interface between iron and diamond.

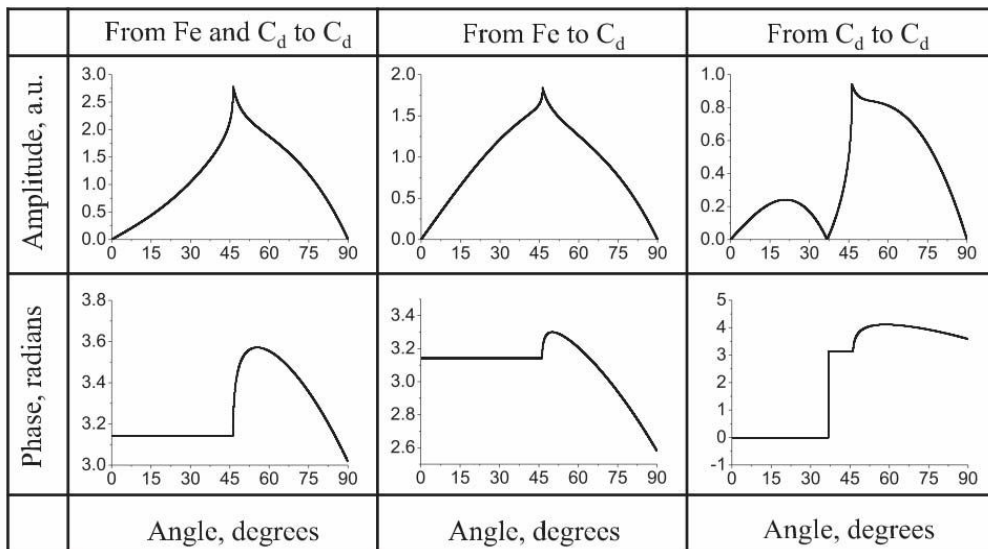


Figure II. 7. Amplitude and phase directivity patterns of shear ultrasound emitted in diamond by delta-localized sources, created by laser-irradiation of plane interface between iron and diamond.

In Figs. (II.6) and (II.7) the directivity patterns of the acoustic waves emitted in diamond are presented for a qualitative comparison with the directivity patterns of the acoustic waves emitted in iron (Figs. II.3 and II.5). The longitudinal wave in diamond is the fastest of all acoustic waves in the considered system. As a consequence, there are no critical angles for the emission of this wave in

diamond and its directivity patterns are poorly structured (Fig. II. 6). To the structuring of the directivity patterns of the shear waves emitted in diamond contribute a single critical angle $\theta_{l_2/l_2} = \arcsin(v_{l_2}/v_{l_2}) \approx 46.2^\circ$ and the angle of 36.7° , at which the reflection of the compression/dilatation waves with mode conversion into shear waves is absent ($R_{ll}^{22} = 0$).

The results presented in Figs. II. 3, 5-7 provide the complete description of the directivity patterns of laser ultrasound emitted by laser-induced sources delta-localized on Fe/C interface. The influence on the directivity patterns of the laser pulse duration and focusing is analyzed in the next Section.

§II.5. Pulse profiles of the laser ultrasound

In this section we first evaluate the profiles of the emitted ultrasound pulses, which could be of interest in the applications of laser ultrasound to high-pressure research. Then we analyze the deviations in the directivity patterns of the laser ultrasound, which are caused by the deviation of the acoustic sources from the delta-localization.

In the common experimental investigations of the directivity patterns of laser ultrasound the acoustic waves are usually detected either at the free curved surface of a half-cylinder, when the radiation is focused along the axis of the cylinder plane cut [8, 10, 12, 15, 18], or on the rear surface of the plate, when the radiation is focused on the front surface [16, 17]. So the detection is on a mechanically free surface where the strain has a minimum, while the displacement has a maximum. So the detection is done by the optical interferometry or by beam deflection technique, while in the analytical theories it is common to analyze the mechanical displacement component u_L in the compression/dilatation wave, which in the far field is purely longitudinal, and so this component is just parallel to the wave propagation direction. The wave, propagating with shear velocity, is purely transversal in the far field, and it is common to analyze the displacement component u_T , which is perpendicular to the wave propagation direction. As the relations of the mechanical displacement vector to the acoustic potentials are known Eq. (II.5), then it is straightforward to evaluate that

$$\begin{aligned}\tilde{u}_L(\omega, r, \theta) &= -(2/v_l)(i\omega)\tilde{\phi}_1(\omega, r, \theta), \\ \tilde{u}_T(\omega, r, \theta) &= (2/v_l)(i\omega)\tilde{\psi}_1(\omega, r, \theta).\end{aligned}\tag{II.25}$$

In the high pressure laser ultrasonics experiments, the detection is on the surface strongly loaded by diamond, and the detection by the reflectometry can be much more efficient than by the interferometry [2-5]. So it would be more useful to analyze not the displacements, but strains, which are producing the changes in the optical refractive index of the media. In the wave propagating at longitudinal sound velocity the strain, which can be probed by laser radiation, is equal to one half of the relative change of the material volume

$$\tilde{\eta}(\omega, r, \theta) \equiv \frac{1}{2} \operatorname{div} \tilde{u} = \frac{1}{2} (\tilde{\eta}_{xx} + \tilde{\eta}_{zz}) = \frac{1}{2} \left(\frac{\partial \tilde{u}_x}{\partial x} + \frac{\partial \tilde{u}_z}{\partial z} \right) = (1/2v_l^2)(i\omega)^2 \tilde{\phi}_1(\omega, r, \theta). \quad (\text{II.26})$$

In the wave propagating at shear acoustic velocity, the strain component which can be probed by laser radiation, is

$$\tilde{\eta}_{xz}(\omega, r, \theta) = \frac{1}{2} \left(\frac{\partial \tilde{u}_x}{\partial z} + \frac{\partial \tilde{u}_z}{\partial x} \right) = (1/2v_t^2) \cos(2\theta)(i\omega)^2 \tilde{\psi}_1(\omega, r, \theta). \quad (\text{II.27})$$

The solutions in Eqs. (II.25) – (II.27) demonstrate that the directivity patterns of laser ultrasound could differ depending on the measured physical parameter. From the solutions in Eqs. (II.26), (II.27) and in Eqs. (II.21), (II.22) it follows that, for the applications in high pressure experiments, it would be interesting to evaluate theoretically

$$\tilde{\eta}(\omega, r, \theta) = -\frac{P_1 I}{2v_l^{3/2}} \sqrt{\frac{1}{2\pi r}} |\Xi_\phi(\theta)| \sqrt{\omega} \tilde{\Phi}(\omega \sin \theta / v_{l1}) \tilde{f}(\omega) e^{-ik_{l1}r + i\pi/4 + i\varphi_\Xi} \quad (\text{II.28})$$

and

$$\tilde{\eta}_{xz}(\omega, r, \theta) = -\frac{P_1 I}{2v_t^{3/2}} \sqrt{\frac{1}{2\pi r}} |\Xi_\psi(\theta)| \cos(2\theta) \sqrt{\omega} \tilde{\Phi}(\omega \sin \theta / v_{t1}) \tilde{f}(\omega) e^{-ik_{t1}r + i\pi/4 + i\varphi_\Xi} \quad (\text{II.29})$$

Note, that, to derive Eqs. (II.28) and (II.29), we have just substituted Eqs. (II.21) and (II.22) into Eqs. (II.26) and (II.27), separated explicitly the amplitudes $|\Xi_{\phi,\psi}(\theta)|$ and the phases φ_Ξ of the functions

$\Xi_{\phi,\psi}(\theta)$ and factorized the diminishing of the signal amplitude characteristic to 2D geometry, $\propto 1/\sqrt{r}$.

From the forms of Eqs. (II.28) and (II.29) it is clear that, when transforming the solutions into the time domain, i.e., by performing the inverse Fourier transform, the dependence of both strain profiles on time can be factorized by the same integral:

$$\eta(\tau = t - r/\nu) = \frac{1}{2\pi} \int_{-\infty}^{+\infty} \sqrt{\omega} \tilde{\Phi}(\omega \sin \theta / \nu) \tilde{f}(\omega) e^{i\omega\tau + i\pi/4 + i\varphi_{\Xi}} d\omega, \quad (\text{II.30})$$

where $\tau = t - r/\nu$ is the retarded time, while $\nu = \nu_{l1,l1}$ and $\Xi = \Xi_{\phi,\psi}$, when evaluating normal and shear strains, respectively. The integral in Eq. (II.30) for the description of laser radiation given in Eq. (II.18) can be calculated analytically. It should not be however forgotten that, when integrating over negative frequencies, the integrand should be modified to provide finally real valued profile. The result of the integration is

$$\begin{aligned} \eta(\tau) &= \frac{\pi d \tau_L}{2\tau_a^{3/2}} \frac{\partial}{\partial \bar{\tau}} \left\{ \sqrt{|\bar{\tau}|} e^{-\bar{\tau}^2/2} \left[\cos\left(\frac{\pi}{4} + \varphi_{\Xi}\right) \text{sgn}(\tau) I_{\frac{1}{4}}(\bar{\tau}^2/2) + \sin\left(\frac{\pi}{4} + \varphi_{\Xi}\right) I_{-\frac{1}{4}}(\bar{\tau}^2/2) \right] \right\} \equiv \\ &\equiv \frac{\pi d \tau_L}{2\tau_a^{3/2}} \frac{\partial}{\partial \bar{\tau}} \Psi(\bar{\tau}) = \frac{\pi d \tau_L}{2\tau_a^{3/2}} \frac{e^{-\bar{\tau}^2/2}}{\sqrt{|\bar{\tau}|}} \left\{ \text{sgn}(\tau) \left[\bar{\tau}^2 I_{-\frac{5}{4}}(\bar{\tau}^2/2) - (\bar{\tau}^2 - 1) I_{-\frac{1}{4}}(\bar{\tau}^2/2) \right] \sin\left(\frac{\pi}{4} + \varphi_{\Xi}\right) \right. \\ &\quad \left. + \bar{\tau}^2 \left(I_{-\frac{3}{4}}(\bar{\tau}^2/2) - I_{\frac{1}{4}}(\bar{\tau}^2/2) \right) \cos\left(\frac{\pi}{4} + \varphi_{\Xi}\right) \right\} \equiv \frac{\pi d \tau_L}{2\tau_a^{3/2}} \Theta(\bar{\tau}) \end{aligned} \quad (\text{II.31})$$

where $\bar{\tau} \equiv 2\tau/\tau_a$, $\tau_a(\theta, \tau_L, d/\nu) = \sqrt{\tau_L^2 + (d \sin \theta / \nu)^2} \equiv (d/\nu) \sqrt{(\nu \tau_L / d)^2 + \sin^2 \theta}$ is the angle-dependent characteristic duration of the strain pulse and $I_{\pm\frac{1}{4}, \frac{3}{4}, \frac{5}{4}}$ are the modified Bessel functions.

The characteristic duration of the strain pulse depends on the time of sound propagation across the laser focus (d/ν), on the laser pulse duration τ_L , through the non-dimensional parameter $\bar{\tau}_L \equiv \tau_L \nu / d$, and on the propagation direction (on the angle of observation θ). The pulses propagating at larger angles to the surface normal are longer in duration. In Fig. II.8 the profiles of the

compression/dilatation strain pulses in 2D geometry are presented for different phases φ_{\pm} possible in Eq. (II.31).

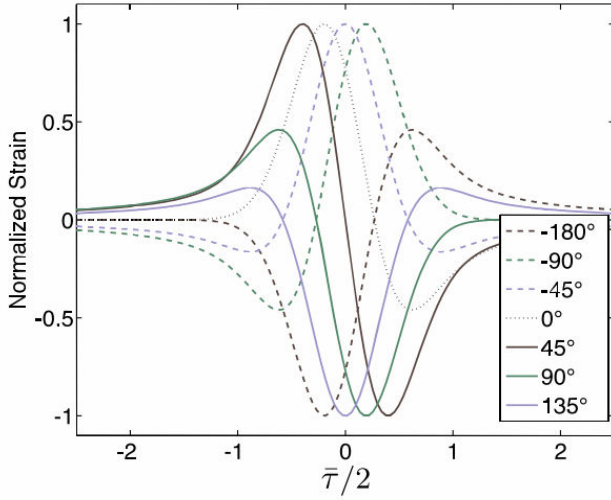


Figure II.8. Normalized strain profiles for acoustical pulses emitted by focusing 2D Gaussian beam of Gaussian laser pulses on the interface between opaque and transparent media. Profiles are presented for various possible phases of the directivity pattern of delta-localized sources.

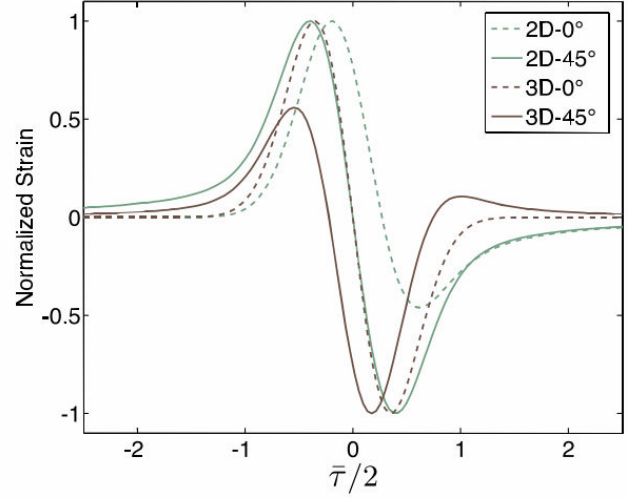


Figure II.9. Comparison of acoustic strain profiles emitted by Gaussian laser beams and Gaussian laser pulses in 2D and 3D experimental geometries at two particular phases of the directivity pattern of delta-localized sources.

The profiles of the compression/dilatation strain pulses in 3D geometry, relevant to the earlier reported experiments in point-source - point-receiver configuration [2, 3], are presented in Fig. A. 1 in Appendix A. Our analytical results in Eq. (II.31) and Eq. (A5) demonstrate that the strain pulse profiles photo-generated in 2D and in 3D configurations, although being relatively similar, are in general different. This is illustrated for two particular values of the phase in Fig. II.9. Note, that earlier this possible difference in the strain pulse profiles generated by line and point sources had been mentioned for the case of thermoelastic sound generation at the mechanically free surface of the medium [15].

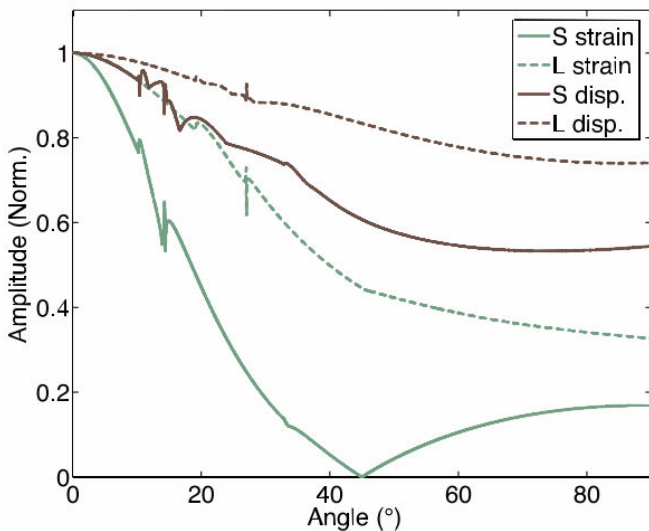


Figure II.10. Additional modulations of delta-localized sources directivities, which are caused by finite duration of the laser pulse and finite width of the laser focus, for emission of acoustic strain and acoustic displacements in 2D geometry. The modulation functions for compression/dilatation waves are evaluated for non-dimensional parameter $\bar{\tau}_{L,i} \equiv \tau_L v_i / d = 0.59$. The modulation functions for shear waves are evaluated for non-dimensional parameter $\bar{\tau}_{L,i} \equiv \tau_L v_i / d = 0.32$.

The analytical result for the acoustic strain and displacement profiles in Eq. (II.31) in combination with the phases φ_{Ξ} of the delta-localized sources, which have been evaluated in Section II.4 (see Figs. II. 3 and II. 5) for different angles of observation, are used to calculate the peak-to-peak amplitudes, i.e., maximum minus minimum values in the pulse profiles, as a function of the emission direction. This “peak-to-peak directivities” provide additional angle-dependent modulation of the directivities patterns evaluated for the delta-localized sources in Section II.4 (see Figs. II. 3 and II. 5). It should be also taken into account that in comparison with the solutions for the particle displacements in Eq. (II.25) and the solution for the compression/dilatation strain in Eqs. (II.26) and (II.28), the solution for the shear strain in Eqs. (II.27) and (II.29) contains the additional angle-dependent factor $\cos(2\theta)$. The evaluated angle-dependent functions, providing modulation of the directivity patterns of laser ultrasound, emitted by delta-localized sources and described by the amplitudes of the solutions in Eqs. (II.23) and (II.24), are presented for the 2D case in Fig. II.10. They are evaluated for the following values of the parameters, $\tau_L = 0.5$ ns, $d = 5$ μ m and $v_l = 5900$ m/s, $v_t = 3200$ m/s, $\bar{\tau}_{L,l} \equiv \tau_L v_l / d = 0.59$, $\bar{\tau}_{L,t} \equiv \tau_L v_t / d = 0.32$, which are characteristic to the earlier reported LU-DAC experiments in line-source-point-receiver configuration with Fe [4, 5]. The modulation functions for the 3D case are presented in Fig. A. 2 of the Appendix A. It can be concluded that apart of the zero in modulation function of the shear strain, which is a formal effect related to the definition of the shear strain in Eq. (II.27), the modulation functions in Fig. II.10 are smooth and do not provide additional qualitative structuring of the directivity patterns. However this conclusion, based on the analysis of Fig. II.10, is valid only because the characteristic non-dimensional parameter, i.e., $\bar{\tau}_{L,l} = 0.59$, is rather close to 1. The dependence of the modulation functions on angle could be much more important if the characteristic non-dimensional parameter $\bar{\tau}_L \equiv \nu \tau_L / d$ is significantly smaller than 1, while, when $\bar{\tau}_L \gg 1$, the dependence of the strain pulse duration on the angle is negligible.

To illustrate this we present in Fig. II.11 the modulation functions for longitudinal strain and displacement directivities evaluated at different values of the non-dimensional parameter $\bar{\tau}_{L,l}$. It can be seen that for $\bar{\tau}_{L,l} = 5.9$ the modulation of the compression/dilatation strain/displacement directivity due to pulse shape effects is practically negligible and thus, the directivity of laser ultrasound practically equals the directivity of delta-localized source. For $\bar{\tau}_{L,l} = 0.059$, the modulation functions of compression/dilatation strain/displacement in Fig. I.11 significantly support the emission at angles smaller than 10° - 20° and suppress the emission at larger angles. This results in the expectation of drastic differences between the experimental directivity patterns of laser ultrasound and the

directivities of delta-localized sources. The side lobe in longitudinal wave emission, which is predicted around the angle of $\approx 45^\circ$ in Fig. II.3, will be suppressed.

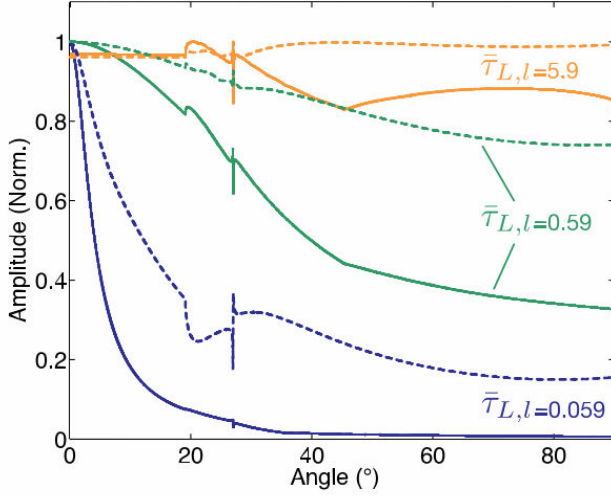


Figure II. 11. Additional modulations of delta-localized sources directivities, which are caused by finite duration of the laser pulse and finite width of the laser focus, for acoustic strain (continuous curves) and acoustic displacement (dashed curves) in compression/dilatation wave. The modulation functions are evaluated for few characteristic values non-dimensional parameter $\bar{\tau}_{L,l} \equiv \tau_L \nu_l / d$.

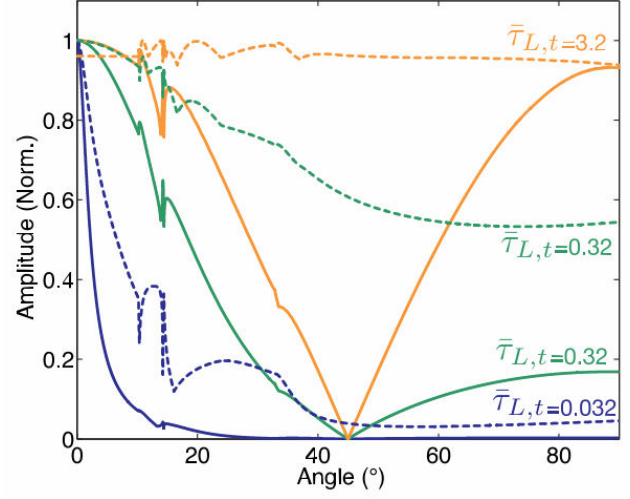


Figure II. 12. Additional modulations of delta-localized sources directivities, which are caused by finite duration of the laser pulse and finite width of the laser focus, for acoustic strain (continuous curves) and acoustic displacement (dashed curves) in shear wave. The modulation functions are evaluated for few characteristic values non-dimensional parameter $\bar{\tau}_{L,t} \equiv \tau_L \nu_t / d$.

In Fig. II.12 we presented the modulation functions for shear strain/displacement directivities evaluated at different values of the non-dimensional parameter $\bar{\tau}_{L,t}$. It can be seen that for $\bar{\tau}_{L,t} = 0.032$ the modulations of the compression/dilatation strain/displacement directivity due to pulse shape effects suppress the second lobe in the shear wave emission, which is predicted around $\approx 35^\circ$ in Fig. II.5 for delta-localized sources. As the first lobe in the directivity of shear waves emission by delta-localized sources is also expected at non-zero angle from symmetry considerations (see Section 2.4) and is around $\approx 10^\circ$ angle in Fig.II.5, then the pulse shape related modulation function significantly suppresses this first shear lobe as well.

From the physics point of view these theoretical predictions correspond to the transition, with diminishing parameter $\bar{\tau}_L$, from delta-localized sources to plane sources, accompanied by preferential photo-generation of plane compression/dilatation waves propagating normally to the laser-irradiated surface, and to suppression of shear waves photo-generation. The above developed theory provides opportunity to evaluate the directivity patterns of LU for any intermediate situations between the

emission of strongly divergent acoustic fields and the emission of the acoustic beams, which are quasi-collinear with the normal to the interface.

§II.6. Discussion and conclusions

The interpretations of the multiple lobes in the amplitude directivity patterns had been proposed in Section II.4 on the basis of the evaluation of the critical angles and the possible angles for the absence in reflection/transmission of the acoustic waves across the interface. These interpretations indicate that the theoretically predicted in Figs. II. 3 and II.5 directivities of the delta-localized thermo-elastic stresses can be understood qualitatively from the physics point of view. In addition we demonstrate in the Appendix B, that the developed theory perfectly reproduces the well-known results [12, 14, 15] for the directivity patterns of the laser ultrasound emitted from the laser-irradiated mechanically free surface of the media.

The predictions of the analytical theory have been compared with the recently published results of the numerical evaluation of the directivities patterns in diamond anvil cell by the finite element method [19]. Because in [19] the interface between the aluminum (Al) and the diamond is considered, the theory has been applied to this combination of the materials. The directivity patterns for the delta-localized sources, presented in Fig. II.13, are evaluated for the similar material parameters as in [19]. They should be compared with the directivity patterns presented in Fig. 6 (c), (d) in [19].

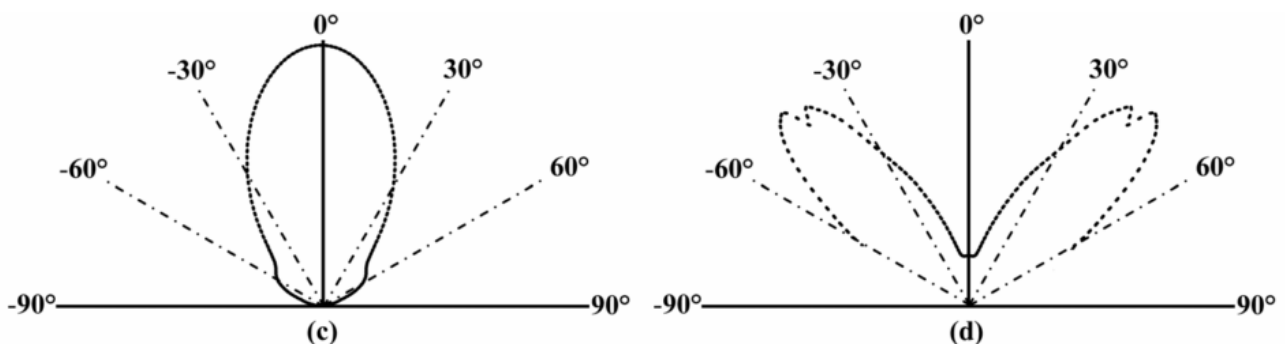


Figure II. 13. (c) Longitudinal-wave directivity patterns generated in a DAC from [19]. (d) Shear-wave directivity patterns generated in DAC from [19].

By comparing the results in Fig. II.13 with those in Figs. II.3 and II.5, it can be concluded that the main theoretical predictions for the interface Al/C_d and the interface Fe/C_d are qualitatively similar, as it could have been expected from the absence of important difference between Al and Fe in values of acoustic velocities, Poisson ratios and critical angles on the interface with diamond (See Tables II. 1

and II. 2), and consist in the description of structuring of the directivity patterns. The analytical theory predicts several lobes in the directivity patterns both for the longitudinal and shear waves. These analytical predictions are not supported by the results of the numerical evaluations presented in Fig. 6 (c),(d) of [19], where both directivity patterns are poorly structured (Fig. II.13).

In particular, numerical investigation in [19] (Fig. II.13) does not predict the dominant lobe in the directivity pattern of the longitudinal waves around $\approx 45^\circ$, which is analytically predicted in Fig. II.14. It should be mentioned here, that we have evaluated the pulse-shape effects, predicted in Section II.5, using the same parameters of the laser radiation as in [19], i.e., $\tau_L = 0.5$ ns, $d = 5$ μ m. We have found (section II.5) that the additional angle-dependent modulation, i.e., due to pulse-shape effects, cannot cut the side lobe predicted in Fig. II.14 for longitudinal waves around $\approx 45^\circ$. Thus, our analytical results are in contradiction with the numerical evaluations in [19]. However, we are not considering the predictions obtained in [19] as a strong argument against our analytical theory, because some of the other numerical evaluations in [19] (for example Fig. 5a,b in [19]) are also in contradiction and not only with the results of the analytical theory, but also with the available experimental results. In fact, the numerically evaluated directivity patterns for the emission of the shear acoustic waves from the laser-irradiated mechanically free surface, presented in Fig. 6 (b) of in [19], does not contain the second side lobe at large angles exceeding 60° (see Fig. B.1 of the Appendix B), which is not only well-established by analytical theories results [12, 14, 15] but has been recently observed experimentally [18].

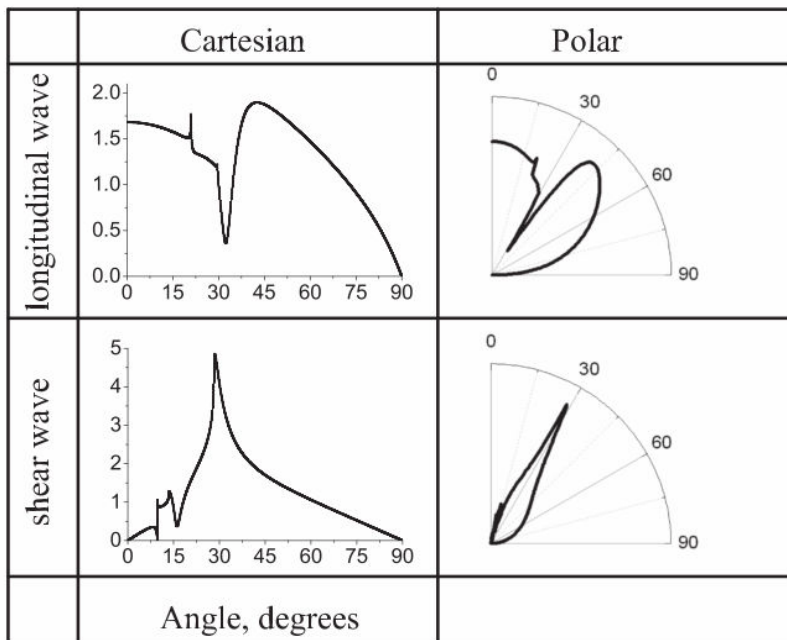


Figure II. 14. Amplitude directivity patterns of longitudinal and shear ultrasound emitted in aluminum by delta-localized sources, created by laser-irradiation of plane interface between aluminum and diamond.

Then we compared the results of experimental work [4] with this analytical theory. In [4] the results of laser ultrasonic experiments with iron film inside the diamond anvil cell are described. In experimental setup, the Nd:YAG laser with a pulse width of 0.75 ns and with diameter of a spot on the sample surface 5 μ m was used for generating acoustic waves in iron film inside the diamond anvil cell. In this experiment it was possible to change the distance between the source and the detector of the acoustic wave along the iron/diamond interface (Fig.II.1). These experimental conditions correspond to those under which the analytical theory was developed. In this experiment, the generation and detection of acoustic waves were on the same side of the iron film (Fig.II.1). A photoacoustic signals in iron film were detected for different propagation angles of acoustic waves from the source. The ability to measure the acoustic signals propagating at different angles from the source was due to their effective emission in a large band of angles in the case of strong laser focusing (the characteristic acoustic wavelength in the emitted acoustic pulse was of the order the heated region dimensions). Photoacoustic signals in iron film inside the diamond anvil cell at 2.8 GPa measured at different distances between the source and the detector of the acoustic wave (and, respectively, at different emission angles) [4] are presented in Fig. II. 15 (b). Using these data, we determined the amplitude of the longitudinal acoustic wave (area outlined by the red dotted line) as a function of the angle Fig. II. 15 (d). To compare the theoretical results of the directivity pattern for the longitudinal acoustic wave in the iron in Fig. II. 15 (a) with experiment Fig. II. 15 (d) it is necessary to take into account the angle-dependent reflections of the acoustic wave on the rear and front interfaces of iron film with diamond. This is required because after the generation acoustic wave starts propagating inside the iron. After this the wave reaches the rear iron-diamond boundary and is reflected back into iron. When this once reflected wave reaches the front iron-diamond boundary at which the detection is realized and it is again reflected back into iron. This means that the analytical solution for the directivity pattern for the longitudinal acoustic wave in the iron must be multiplied by $R_{ii}^{11}(1 + R_{ii}^{11})$ Fig. II. 15(c).

From comparison of the curves presented in Fig. II. 15 (c) and Fig. II. 15 (d), it can be concluded that there is agreement between the directivity patterns of the longitudinal laser ultrasound into the iron obtained from the experiment and predicted by the analytic theory.

Finally, although indirect, argument in favour of validity of the theory, presented in this Chapter, is the known theoretical prediction [34] for the modification of the directivity pattern of the laser ultrasound emitted in liquid in case, when the surface of the liquid is loaded by a solid plate. Additional structuring of the directivity pattern, relative to the pattern of laser ultrasound emitted from a mechanically free surface of laser-irradiated liquid, had been predicted [34]. Several lobes in the directivity pattern are theoretically expected [34].

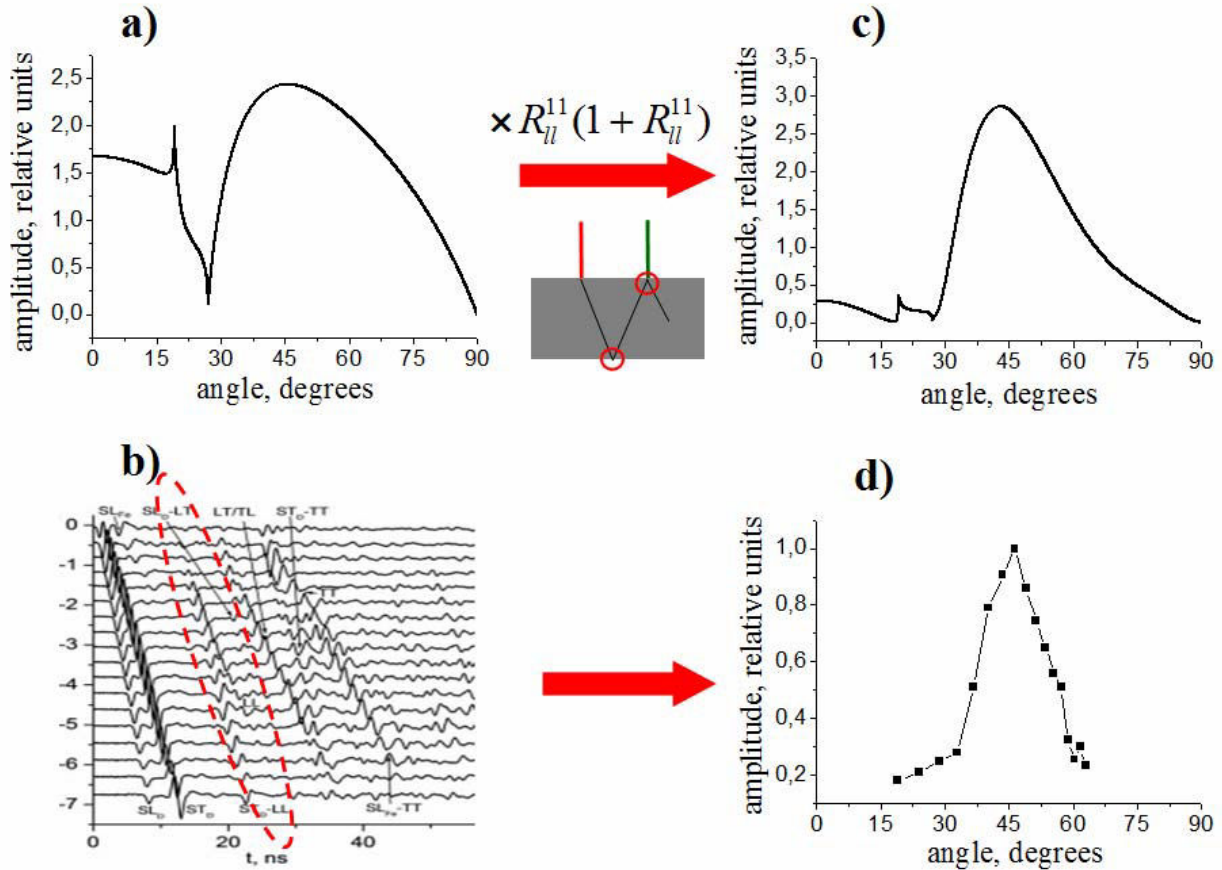


Figure II. 15. (a) The theoretical directivity pattern of the laser ultrasound emitted in the iron inside the diamond anvil cell for the longitudinal acoustic wave. (b) Photoacoustic signals in iron film inside the diamond anvil cell at 2.8 GPa measured at different distances between the source and the detector of the acoustic wave [4]. (c) The directivity pattern (a) accounting for the reflection of sound at the rear and front interfaces of iron film with diamond. (d) The amplitude of the longitudinal acoustic wave from (b) as a function of the angle [4].

Conclusions

In conclusion, in this Chapter the analytical descriptions for the directivity patterns of ultrasound (LU), emitted from the laser-irradiated interface between two isotropic solids was presented. The solutions are valid for arbitrary combinations of transparent and opaque materials. The directivity patterns are derived by accounting for the specific features of the sound generation by the thermo-elastic stresses distributed in the volume, which are essential for laser ultrasonics. The analytical solutions for the profiles of longitudinal and shear acoustic pulses emitted in different directions are also evaluated. The derived mathematical formulas provide straight opportunity to predict the acoustic field, which is formed in the diamond anvil cell (DAC) after photo-generation and several reflections of bulk acoustic waves at the interfaces. The developed theory can be applied in the

future for the dimensional scaling the LU-DAC experiments, optimization of these experiments (in terms of a choice of the optimal directions/positions for acoustic waves detection) and the interpretation of the experimental results. It has been already successful in interpretation of some earlier existing experimental observations.

References (II)

1. F. Decremps, L. Belliard, B. Perrin, M. Gauthier, *Sound Velocity and Absorption Measurements under High Pressure Using Picosecond Ultrasonics in a Diamond Anvil Cell: Application to the Stability Study of AlPdMn* **Phys. Rev. Lett.** **100**, 035502 (2008).
2. N. Chigarev, P. Zinin, L-C. Ming, G. Amulele, A. Bulou, V. Gusev, *Laser generation and detection of longitudinal and shear acoustic waves in a diamond anvil cell* **Appl. Phys. Lett.** **93**, 181905 (2008).
3. P. V. Zinin, N. Chigarev, D. Mounier, A. Bulou, L. C. Ming, T. Acosta, V. Gusev, *Evaluation of elastic properties of iron in diamond anvil cell by laser ultrasonics technique* **J. Phys.: Conf. Series** **215**, 012053 (2010).
4. N. Chigarev, P. Zinin, D. Mounier, A. Bulou, L. C. Ming, T. Acosta, V. Gusev, *Analysis of ultrasonic echoes induced by pulsed laser action on an iron film in a diamond anvil cell* **High Pressure Research** **30**, 78 (2010).
5. N. Chigarev, P. Zinin, D. Mounier, A. Bulou, A. Zerr, L. C. Ming, V. Gusev, *Laser ultrasonic measurements in a diamond anvil cell on Fe and the KBr pressure medium* **J. Phys.: Conf. Series** **278**, 012017 (2011).
6. C. B. Scruby, R. J. Dewhurst, D. A. Hutchins, S. B. Palmer, *Quantitative studies of thermally generated elastic waves in laser irradiated metals* **J. Appl. Phys.** **51**, 6210 (1980)
7. C. B. Scruby and L. E. Drain, *Laser Ultrasonics Techniques and Applications* **Hilger, Bristol**, (1990).
8. D. A. Hutchins, R. J. Dewhurst, S. B. Palmer, *Laser generated ultrasound at modified metal surfaces* **Ultrasonics**, **19**, 103 (1981); **J. Acoust. Soc. Am.** **70**, 1362 (1981)
9. L. F. Rose, *Point source representation for laser generated ultrasound* **J. Acoust. Soc. Am.** **75**, 723 (1984).
10. J. D. Aussel, A. Le Brun, J. C. Baboux, *Generating acoustic waves by laser: theoretical and experimental study of the emission source* **Ultrasonics** **26**, 245 (1988).
11. S. Y. Zhang, M. Paul, S. Fassbender, U. Schleichert, W. Arnold, *Experimental Study of Laser-Generated Shear Waves Using Interferometry* **Res. Nondestr. Eval.** **2**, 143 (1990).
12. P. Zhang, C. F. Ying, J. Shen, *Directivity patterns of laser thermoelastically generated ultrasound in metal with consideration of thermal conductivity* **Ultrasonics** **35**, 238 (1997).
13. B. Yuhai, P. Liwei, F. Qiping, Y. Yuping, Y. Chongfu, *Experimental studies of directivity patterns of laser generated ultrasound in neutral glasses* **Ultrasonics** **33**, 429 (1995).
14. W. Japing, S. Dufang, H. Yulong, *Study of the directivity of laser generated ultrasound in solids* **J. Appl. Phys.** **83**, 1207 (1998).
15. J. R. Bernstein, J. B. Spicer, *Line source representation for laser-generated ultrasound in aluminum* **J. Acoust. Soc. Am.** **107**, 1352 (2000).
16. S. Raetz, T. Dehoux, B. Audoin, *Effect of laser beam incidence angle on the thermoelastic generation in semi-transparent materials* **J. Acoust. Soc. Am.** **130**, 3691 (2011).
17. J. M. S. Sakamoto, B. R. Tittman, A. Baba, G. M. Pacheco, *Directivity measurements in aluminum using a laser ultrasonics system* **J. Phys.: Conf. Series** **278**, 0122032 (2011).
18. C. Pei, K. Demachi, H. Zhu, T. Fukuchi, K. Koyama, M. Uesaka, *Inspection of cracks using laser-induced ultrasound with shadow method: Modeling and validation* **Optics & Laser Technology** **44**, 860 (2012).
19. W. Feng, D. Yang, X. Zhu, Y. Guo, W. Liao, *Simulation of laser-generated longitudinal and shear ultrasonic waves in a diamond anvil cell by the finite element method* **J. Appl. Phys.** **11**, 013107 (2012).
20. V. Gusev, C. Desmet, W. Lauriks, C. Glorieux, and J. Thoen, *Theory of Scholte, leaky Rayleigh, and lateral wave excitation via the laser induced thermoelastic effect* **J. Acoust. Soc. Am.** **100**, 1514 (1996).
21. M. Kouyate, T. Pezeril, D. Mounier, V. Gusev, *Generation of inhomogeneous plane shear acoustic modes by laser-induced thermoelastic gratings at the interface of transparent and opaque solids* **J. Appl. Phys.** **110**, 123526 (2011).
22. V. E. Gusev and A. Karabutov, *Laser Optoacoustics* **New York, AIP** (1993).
23. L. M. Brekhovskikh and O. A. Godin, *Acoustics of Layered Media I: Plane and Quasi-Plane Waves* **Berlin, Springer-Verlag**, (1990).
24. B. A. Auld, *Acoustic Fields and Waves in Solids, Second Edition, Volume 2* **Krieger, Malabar**, (1990).
25. V. E. Gusev, *On generation of picosecond inhomogeneous shear strain fronts by laser-induced gratings* **Appl. Phys. Lett.** **107**, 114906 (2010).
26. W. M. Ewing, W. S. Jardetzky, F. Press, *Elastic Waves in Layered Media* **McGRAW-HILL, New York**, (1957).
27. G. F. Miller, H. Purcey, *The Field and Radiation Impedance of Mechanical Radiators on the Free Surface of a Semi-Infinite Isotropic Solid* **Proc. R. Soc. London Ser. A** **223**, 521 (1954).

28. V. E. Gusev, *On the duration of acoustic pulses excited by subpicosecond laser action on metals* **Opt. Commun.** **94**, 76-8 (1992).
29. G. Tas and H. Maris, *Electron diffusion in metals studied by picosecond ultrasonics* **Phys. Rev. B** **49**, 15046-54 (1994).
30. V. E. Gusev and O. B. Wright, *Ultrafast nonequilibrium dynamics of electrons in metals* **Phys. Rev. B** **57**, 2878-88 (1998).
31. <http://www.crewes.org/ResearchLinks/ExplorerPrograms/ZE/ZEcrewes.html>
32. T. Pezeril, N. Chigarev, P. Ruello, S. Gougeon, D. Mounier, J.-M. Breteau, P. Picart, V. Gusev, *Laser acoustics with picosecond collimated shear strain beams in single crystals and polycrystalline materials* **Phys. Rev. B** **73**, 132301 (2006).
33. T. Pezeril, P. Ruello, S. Gougeon, N. Chigarev, D. Mounier, J.-M. Breteau, P. Picart, V. Gusev, *Generation and detection of plane coherent shear picosecond acoustic pulses by lasers: Experiment and theory* **Phys. Rev. B** **75**, 174307 (2007).
34. L. M. Lyamshev, *Optical sound generation in liquid semi-space in contact with elastic layer* **Sov. Phys. Acoustics** **25**, 322 (1979) [translated into English from: *Akust. Zh.* **25**, 566 (1979)].

Chapter III

Measurement of the refractive index and thickness of a transparent H₂O sample compressed in a diamond anvil cell

In this Chapter III an interference method for measuring the thickness and refractive index of a transparent sample compressed in a diamond anvil cell is used. This interference technique is applied here for studying of H₂O water and ice. The refractive index, thickness and volume of H₂O samples are measured as a function of pressure. Bending under pressure of the surfaces of the diamond anvil culets which are in contact with the transparent sample, is revealed.

Measurement of refractive indexes of transparent materials at high pressures is a quite important area of research [1,2]. In general, determination of refractive index is a direct way to probe electronic structure of the substance of interest because the refractive index expresses the response of the distribution of charges to the perturbing electric field. So measurement of refractive index as a function of pressure is highly important and valuable by itself. However, information about the optical properties of sample materials is also of particular importance for the evaluation of their acoustic properties using optoacoustic techniques. In fact, parameters accessible from optoacoustic measurements could be combinations of acoustical and optical parameters and, because of this, the knowledge of the optical parameters could be required to extract the acoustic parameters. For example, the refractive index under pressure has a clear metrological importance for Brillouin spectroscopy [3] and picosecond laser ultrasonics [4]. In this work the refractive index of water ice and the ice sample thickness were needed in the picosecond laser ultrasonics measurements on this material compressed in a diamond anvil cell (see Chapter IV).

Change of the thickness of a transparent sample in a diamond anvil cell with pressure is also required in laser ultrasonic measurements [5,6,7]. Usually in a laser ultrasonic experiment the propagation time of sound through a sample is measured [7] but the sample thickness remains unknown. Also, measurement of the sample thickness in a diamond anvil cell on pressure increase allows to control the distance between the anvils and thus to preclude a direct contact of the anvils leading to their failure. Such measurement of the thickness should be performed regularly upon pressure increase. Finally, the thickness of a transparent material in a diamond anvil cell can be used to determine volume of the transparent sample as a function of pressure, denoted as the equation of state, which contains information about the bulk modulus and its first pressure derivative [2].

In an earlier study [8] refractive index of the transparent mixture of methanol and ethanol in the ratio 4:1 was measured using an optical method where a reference object of known size was used. This means for the determination of the refractive index of the sample material as function of pressure, the known properties of the reference object were used [8] which have been measured by other methods. For example, the equation of state can be determined from X-ray diffraction measurements of the specific sample volume performed on compression.

The refractive index of H₂O as a function of pressure was investigated in [1]. For these purposes, the optical method involving use of a reference object was employed. In [2] measurement of the refractive indexes of transparent materials (H₂O, He, N₂) under pressure in a diamond anvil cell was conducted without using a reference object. Unfortunately, the latter optical method of measurement has been employed only at pressures below 40 GPa. In [2], it is assumed that the transparent sample compressed in diamond anvil cell is plane parallel. However, this assumption is, in general, incorrect (see section III.6) and could cause significant systematic errors due to curvature of the diamond anvil culets.

In this part of the thesis, an interference method for measuring thickness and refractive index of the H₂O ice sample in a diamond anvil cell is used. The refractive index, the thickness and the volume of the sample are measured on pressure increase. Bending under pressure of the diamond anvil culets, which are in contact with the sample, is revealed.

§III.1. Interference technique

III.1.1 Optical measurement by using interference technique

Let's imagine that a plane-parallel transparent plate (n - the refractive index of the material, H - the plate thickness) is irradiated by a broadband light. A part of the light will be reflected from the top surface of the plate, another part of the light from the bottom surface of the plate (Fig. III. 1). The optical path difference between the two reflected beams is $2nH$ (nH is the product of these two parameters, denoted as the optical thickness of the sample). These two reflected beams are interfering with each other at the entrance of the spectrometer used to measure the interference intensities.

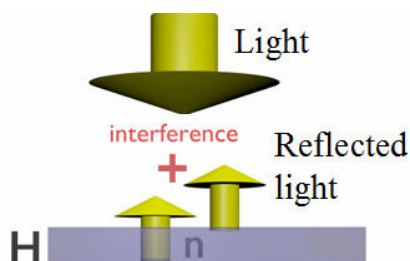


Figure III. 1.1 Illustration of the interference of the reflected light from a plane-parallel transparent plate. The arrow directing downwards represents the incident light. Two arrows directing upwards represent reflected light from the lower and upper plate surfaces. The interference intensity of these reflected beams is defined by the optical path difference $2nH$.

The intensity of the reflected light depends on the wavelength of light according to the equation [9]:

$$I(\lambda) \propto \cos^2\left(\pi \frac{2nH}{\lambda} + \varphi\right) \tag{III.1}$$

where φ is a constant, which can arise due to changes in the phase of the reflected light waves at the interface of two media. For example, in the illustration shown in Fig.III.1 φ is equal to $\pi/2$. Now, we suppose that the incident light radiation is continuous in a broad range of wavelengths from $\tilde{\lambda}$ to $\tilde{\tilde{\lambda}}$: $|\tilde{\tilde{\lambda}} - \tilde{\lambda}| \ll \tilde{\lambda}, \tilde{\tilde{\lambda}} < nH$ (Fig III. 2a). If this wavelength range contains the wavelengths at which the maximum and the minimum in the reflected signal take place then the intensity of the reflected light will have the form shown in Fig. III. 2b.

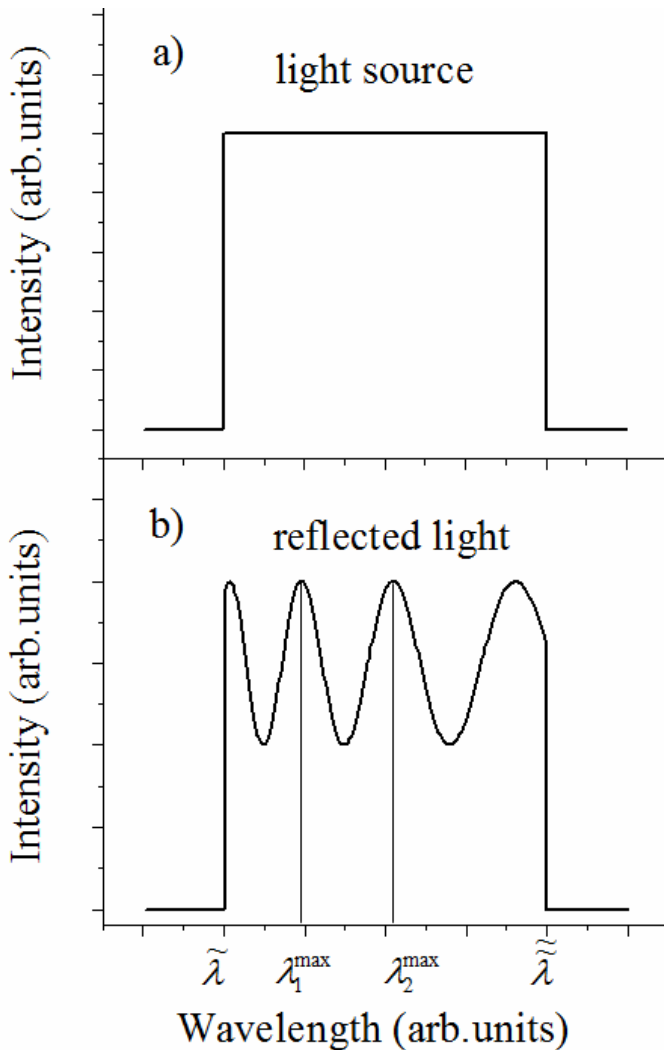


Figure III. 2. The idea of measuring nH from the interference of the reflected broadband light. (a) An idealized spectrum of the incident light having a constant intensity in the wavelength range from $\tilde{\lambda}$ to $\tilde{\tilde{\lambda}}$ $I(\lambda) = \text{const} \neq 0$. (b) Spectrum of the light reflected from the two surfaces of a plane-parallel plate. Because of the interference effect the initial spectrum (a) is modulated in the intensity. The λ_1^{\max} and λ_2^{\max} are two adjacent wavelengths at which the intensity of the interfering reflected light has maxima.

To illustrate the method for measuring the optical thickness, let's consider two neighbouring maxima in the intensity of the interfering reflected light. The first maximum λ_1^{\max} obeys the law (III.1) $2nH/\lambda_1^{\max} + \varphi/\pi = m$. For the second maximum λ_2^{\max} , we can write $2nH/\lambda_2^{\max} + \varphi/\pi = m - 1$. From these relations, the product nH can be written as:

$$nH = \frac{\lambda_1^{\max} \lambda_2^{\max}}{2\Delta\lambda} \quad (\text{III.2})$$

where $\Delta\lambda = |\lambda_1^{\max} - \lambda_2^{\max}|$. So the product of the refractive index of the material of plate and plate thickness can be obtained from the interference pattern of the reflected broadband light. The refractive index of the material can be obtained if the thickness of the plate can be measured independently. Conversely, if the refractive index is known, then the thickness can be obtained.

This is just one opportunity to estimate nH from the interference of a broadband light. More accurate determination of nH can be made by fitting of experimental curve (see section III.2.2) by using equation (III.1).

III.1.2 Interference of broadband light in a diamond anvil cell

To study substances under high pressure a diamond anvil cell technique can be used (see Chapter I). In this technique, a transparent substance is sandwiched between two diamond anvils and is confined on sides by a metal gasket (Fig. III. 3a).

In this work, interference of a broadband light (as described above) was used to measure the refractive index and sample thickness at high pressures. The interference is occurring due to the fact that the light reflected from the two interfaces of the sample: upper interface diamond/sample, and lower interface sample/diamond. From the analysis of the resulting interference signal the value nH at different pressures can be obtained. Interferometric measurements in a diamond anvil cell provide only the product of the refractive index of the material with its thickness. Independent measurements of the thickness are difficult due to inaccessibility of the material inside the diamond anvil cell. Also, the refractive index at high pressures is known only for a very limited number of substances.

Some ideas how to separate the measurement of the refractive index and of the thickness of the sample compressed in a diamond anvil cell are considered below.

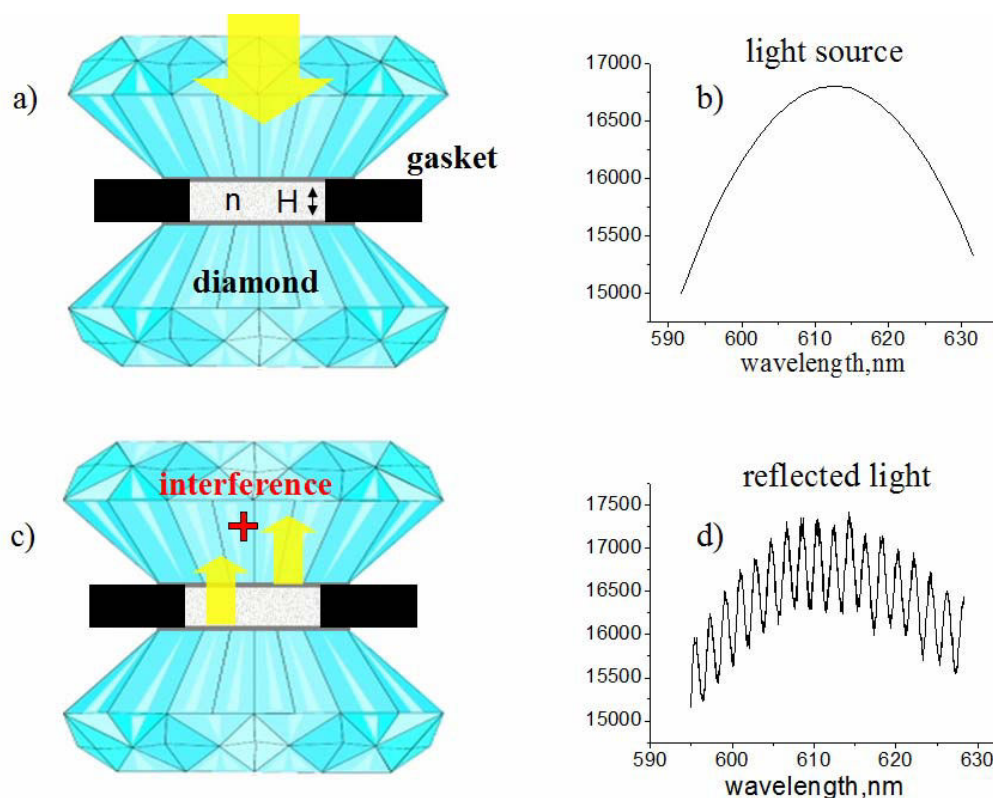


Figure III. 3. Illustration for the interference of the reflected light for a transparent sample in a diamond anvil cell. (a) The substance is sandwiched between two diamond anvils and confined by a gasket. The sample is irradiated with a broadband light (arrow downwards). (b) Spectrum of the broadband light source $I(\lambda)$. (c) Light reflected from the sample surfaces in a diamond anvil cell. (d) Spectrum of the interfering reflected light.

§III.2. Experimental setup

III.2.1. Scheme, functioning and elements of experimental setup

The principal scheme of the experimental setup for measurement of refractive indexes and thicknesses of materials compressed to ultrahigh pressures in a diamond anvil cell is presented in Fig. III. 4. The photo of the experimental setup is shown in Fig. III. 5.

The main elements of the experimental setup are:

- **Source of a continuous broadband light.** Maximum of the radiation corresponds to the wavelength of about 611 nm.
- **Beamsplitting cube.** This cube transmits half of the radiation. The other half of the radiation is reflected by 90 degrees.
- **Aspheric achromatic lens.** This lens is focusing the broadband light on a sample compressed in the diamond anvil cell with. the same lens is used to collect the interference signal. The lens diameter is 14 mm. The focal length is 12,5mm.

- **Diamond anvil cell** with the studied transparent substance. We used a mechanical ALMAX diamond anvil cell of the type “Boehler-Almax Plate DAC” [10] (see Chapter I and section III.3).
- **Compact motorized actuator (TRA Series)**. It allows to move the diamond anvil cell perpendicular to the optical radiation in the plane of the optical table with the resolution 0,03 μm .
- **Monochromator with a CCD camera** (shamrock sr-303i). This system allows recording the spectrum of the reflected from the diamond anvil cell broadband light with the resolution of 0,03nm.
- **Visualization system**. This system consists of an ocular and a flip mirror to redirect light before the monochromator for visual examination of the sample in the diamond anvil cell.

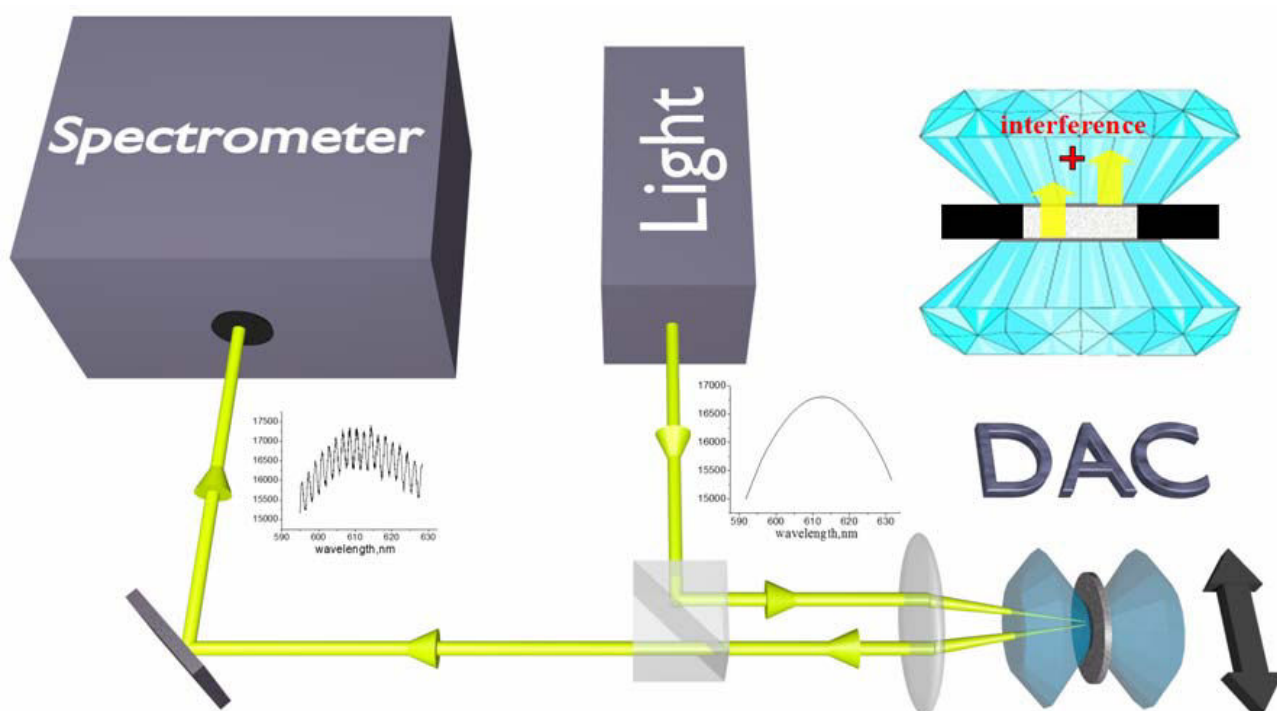


Figure III. 4. The basic scheme of experimental setup for measurement of refractive indexes and thickness of materials compressed to ultrahigh pressures in a diamond anvil cell.

The measurements are based on the appearance of light interference between two nearly parallel surfaces such as a surface of the examined sample and culets of the diamond anvils. The beam of light travels from the source to the beam-splitting cube. After the cube a part of the light beam is redirected towards the diamond anvil cell through the lens. The white light is focused into the diamond anvil cell with a compressed sample by this lens which also is used to collect the interference signal. The interference signal was projected, through a beam-splitting cube, on the pin hole in the front of the monochromator. The lateral resolution of the system was chosen to be 1 μm (on the sample in the diamond anvil cell). The sample in the diamond anvil cell can be observed through an ocular using a

flip mirror. The measurements are performed in the spectral range from 595 nm to 628 nm. From the interference measurements we determined the product of the sample refraction index and the distance between the corresponding plane surfaces nH . Compact motorized actuator allows moving of the sample with a high precision along the horizontal axis.

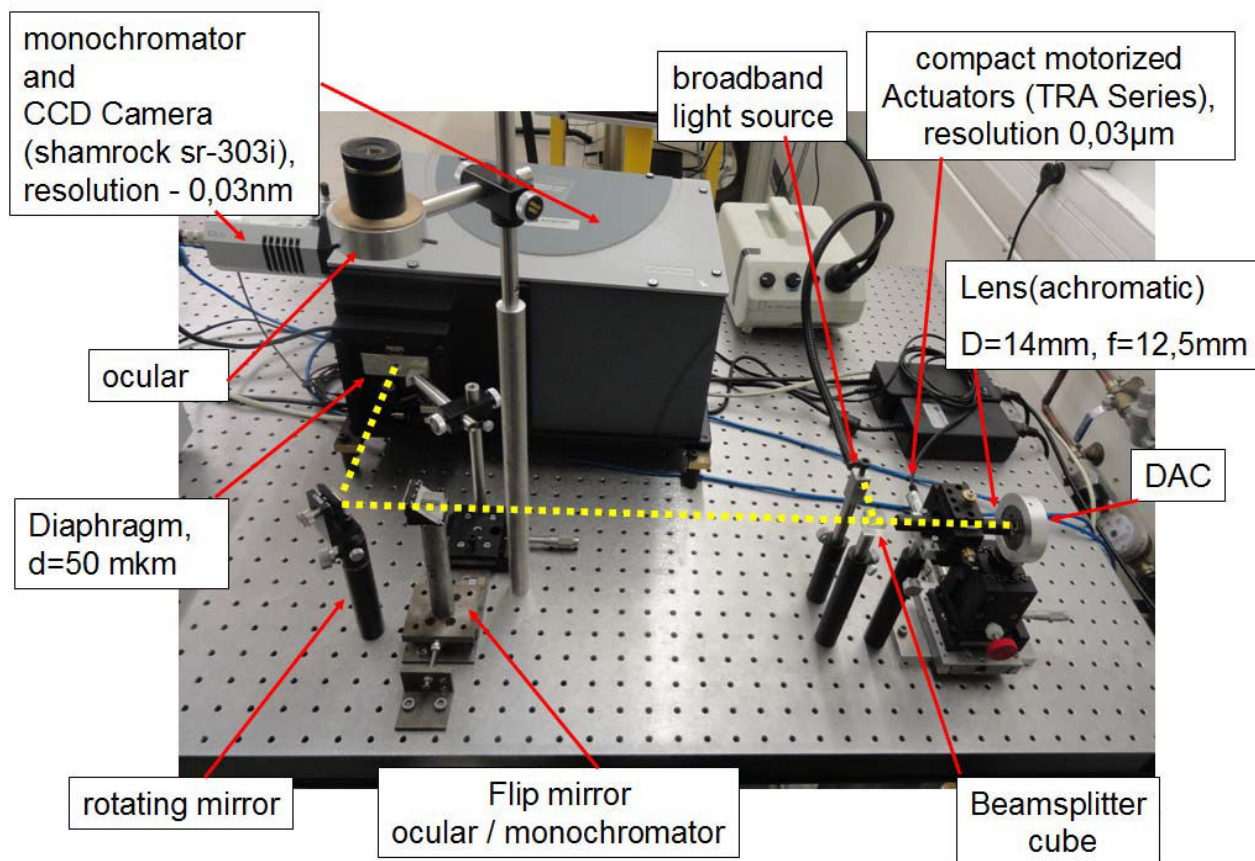


Figure III. 5. The photo of the experimental setup

III.2.2. Software developed for controlling the experimental setup

In order to facilitate the experiment and accelerate the measurements, a program controlling the experimental setup was developed. The program was written using the LabView software.

The program allows to control and read data from the CCD camera of the monochromator. The controlled parameters are the exposure time and the detector temperature. The exposure time defines intensity of the optical signal. The detector temperature defines the noise level of the detector. Typical temperature was -25°C . The program also reads data (the light spectrum) from the CCD camera with a delay time between reading defined by the exposure time. The collected spectra were averaged in order to obtain a better statistics. A spectrum of light without the diamond anvil cell was used to determine the background which was then removed from the interference signal (background

subtraction). Averaged signal without background was processed using the Fast Fourier transform (FFT), the signal frequency determined and recalculated to nH . This was a rough estimate for the nH used subsequently for a more accurate determination of the nH by fitting the equation (I.1) to the interference signal. The position of the fitting on the intensity axis and the amplitude were fixed (chosen from the experimental data) and the nH value varied until the best agreements with the experimental signal was achieved.

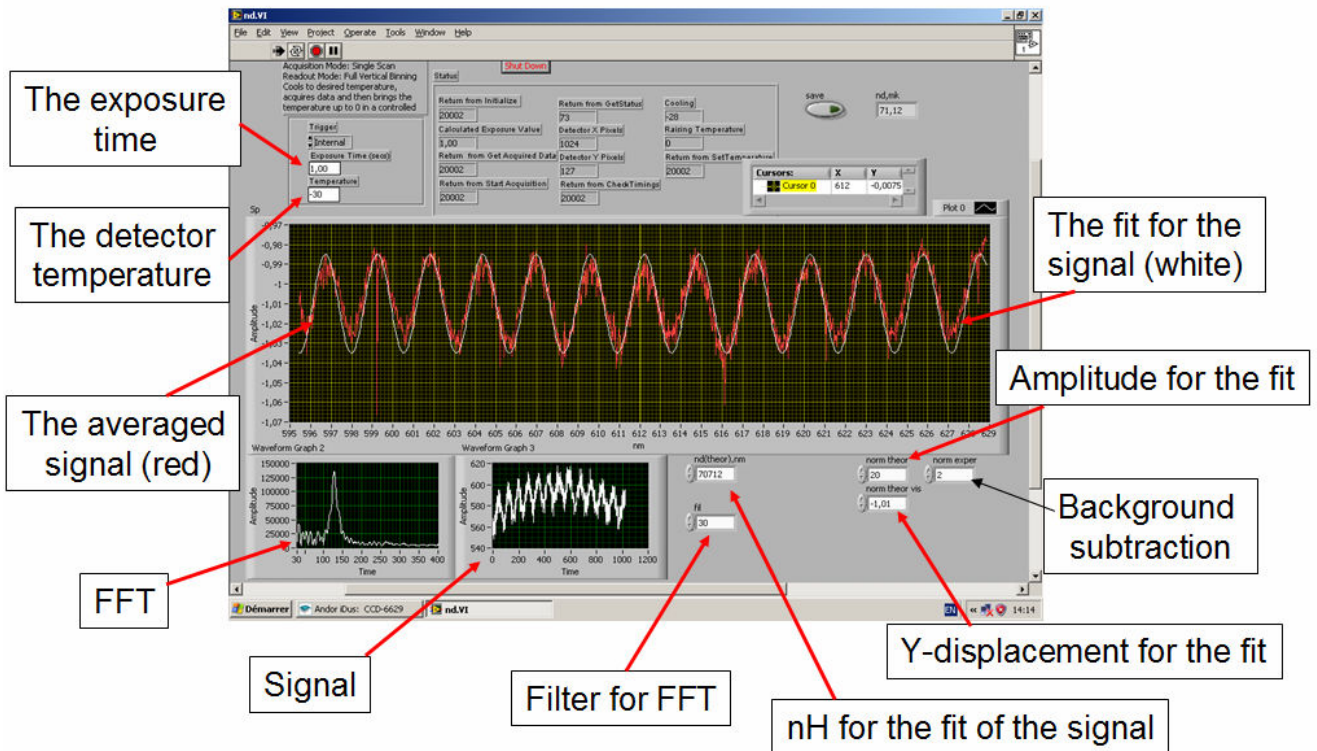


Figure III. 6. View of the control panel of the LabView program for the collection of experimental data.

Thus, the program (Fig.III.6) allows you to quickly determine the optical thickness of the transparent material in a diamond anvil cell using the interference technique.

§III.3. Samples (H₂O in diamond anvil cell)

In our experiments we used the “Boehler-Almax Plate DAC” (Fig. III. 7a, Chapter I). Single beveled diamond anvils with culet size of 300 micrometers (C=0,3mm, Cb=0,35mm) having 16 lateral sides were used (Fig. III. 7b). The diamonds were of the type Ia, (ultra)low Raman fluorescence. The optical aperture of the anvils was chosen to be 78° and the aperture of the carbide seat of the Boehler-Almax design was 70°. For the chosen parameters of the diamond anvils and the carbide sits the

maximal pressure is limited by the manufacturer to 80 GPa. To confine the sample laterally in the cell a steel gasket was used.

The procedure for the sample (H₂O ice) preparation was as follows:

1. preparation of a gasket with a hole for the loading of water, which center should coincide with the center of the diamond culets;
2. preparation of deionized water
3. preparation of the reference object (iron or diamond wedge)
4. placing of the reference object in the center of one of the culets of diamond anvils
5. filling with water of the hole in the gasket
6. fixing of the gasket with water on diamond with the reference object
7. adding of ruby particles in the gasket hole filled with water and the reference object
8. closing and pressurizing of the sample volume

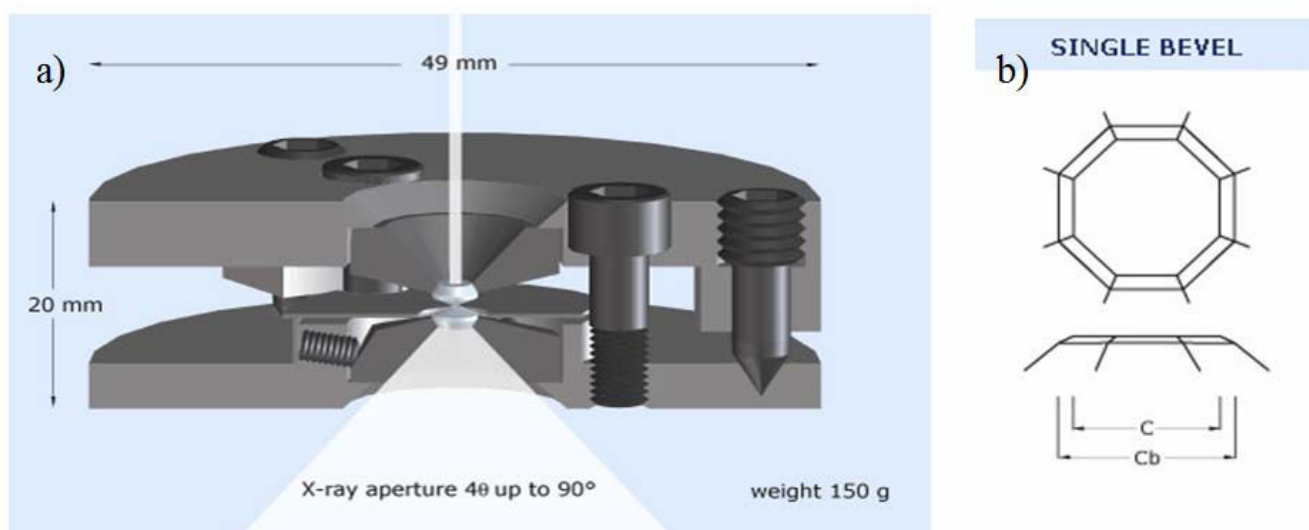


Figure III. 7. (a) ALMAX diamond anvil cell. (b) Diamonds with a Single Bevel [10].

The refractive indexes of water and of two solid phases of solid ice (phase VI and VII) were measured as functions of pressure using the above described interference method. The measurements were performed at room temperature. We do not take into account the heating of the sample by light source because we used a low-power broadband light source and also diamond anvils provide a powerful heat sink (the thermal conductivity of diamond is about 1000W/mK). The maximum pressure of these experiments was 31 GPa. Two different methods, described below, have been used to obtain the refractive index of H₂O as a function of pressure.

§III.4. Refractive index of H₂O as a function of pressure

III.4.1. Using of iron or diamond wedges to get the refractive index of H₂O

In the first method we used iron- and diamond wedges imbedded in H₂O to derive refractive index of the H₂O phases as a function of pressure. This idea is based on the assumption that the reference object in the diamond anvil cell with H₂O is under hydrostatic pressure or, more precisely, that the shape of the reference object does not change on pressure increase. For example, if the reference object is a linear wedge with sides *A* and *B* (Fig. III. 8), then under pressure the sizes of the wedge will be *A'* and *B'*. Because of the hydrostatic pressure in the H₂O sample the wedge shape remains the same. This means that $(A/A') = (B/B')$ or the angle α (Fig. III. 8) is same at any pressure.

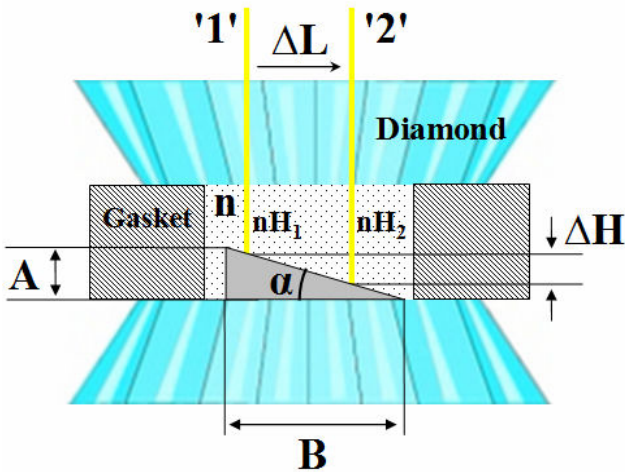


*Figure III. 8. Illustration of the first method for measuring the refractive index *n* of the transparent material in the diamond anvil cell employed in this work. The wedge with known parameters is in the diamond anvil cell with H₂O under pressure (*n* is unknown, α is known). To obtain the refractive index *n* of H₂O the optical thickness measurement is performed at two positions at a certain distance ΔL .*

If the wedge is imbedded in H₂O as shown in Fig. III.8, then the optical thickness measurement can be carried out for the sample material between the wedge and the diamond anvil surface in positions '1' and '2' with the respective values nH_1 and nH_2 measured using the interference method.

At first step, the slope of the wedge should be determined. To do this, the optical thickness measurement can be performed in air when $n=1$ and hence in position '1' the optical thickness is $nH_1=H_1$ and in position '2' $nH_2=H_2$. If the distance between the positions '1' and '2' is ΔL then the variation of the wedge height $\Delta H=H_2-H_1$ can be obtained directly. Thereafter, the wedge angle can be determined from $(\Delta H/\Delta L)=tg(\alpha)$.

Then we can load the water into the sample volume. For measuring the refractive index of the transparent material under pressure it is necessary to know only angle α of the wedge. Measuring the variation in optical thickness $n\Delta H$ as a function of ΔL we get $n(\Delta H/\Delta L)=ntg(\alpha)$. Since $tg(\alpha)$ is already known we obtain *n* immediately.

To increase the precision of the measurements it would be better to make them at several different distances between '1' and '2'. Typical scan included 10 -15 points between the positions '1' and '2'. Also the advantage of scanning is a high accuracy in determining the change in optical thickness (if we have a gradual shift of the optical beam ΔL). For example, we can choose one of the maxima of the interference signal (see Fig. III. 6). Suppose that for this maximum we have $\lambda^{\max} : 2nH = m\lambda^{\max}$. If the optical beam is slightly displaced ΔL along the wedge then variation in optical thickness is $n\Delta H$. This means that the position of λ^{\max} will be shifted: $2n\Delta H = m\Delta\lambda^{\max}$. So if the displacement $\Delta\lambda^{\max}$ is measured (it is possible if the displacement $\Delta\lambda^{\max}$ is less than the distance between neighbouring maxima in the interference signal) then we can obtain the relative change of the optical thickness $n\Delta H$. Here the value m can be find from comparison of λ^{\max} for the neighboring maxima at the same position on the sample . In this case, the relative change in optical thickness can be measured with a high precision. In our experiments the accuracy was estimated to be about 30 nm.

The first experiment to measure the refractive index in the H₂O sample compressed in the diamond anvil cell was performed using an iron wedge prepared from iron particles by using a misaligned cell: In this cell the diamond anvils were inclined by about 1 degree and then the iron particle was pressed between the anvils. This wedge has an elongated shape (see Fig. III.9) with the average diameter of about 50 μm . The scanning area between position '1' and '2' is marked by yellow arrow in Fig. III. 9. For this wedge having $\text{tg}(\alpha)=0,01438$ the refractive index of the H₂O was measured up to 6.7GPa. Above 6.7GPa we observed changes in the wedge shape.

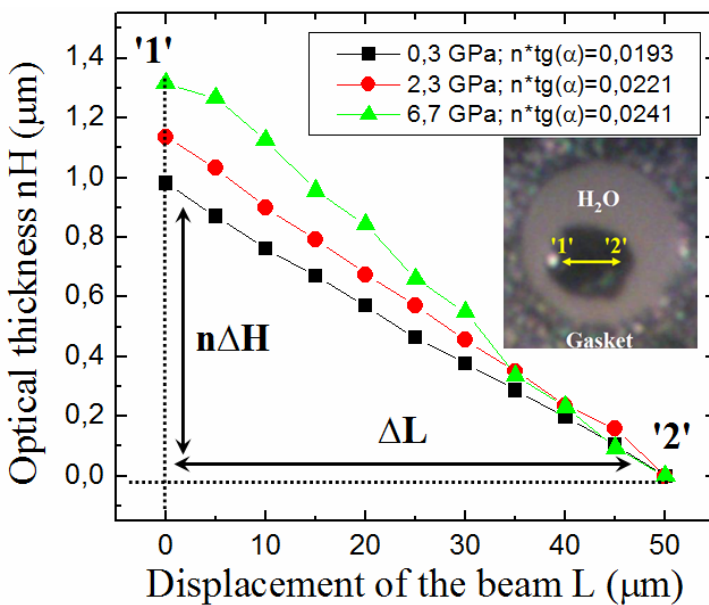


Figure III. 9. Dependence of the optical depth nH of H₂O above the wedge as a functions of displacement L (from position 1 to position 2) at different pressures. (Insert) Photograph of the wedge in H₂O ice filling the gasket hole (top view). Position of the measurements between positions '1' and '2' is indicated by a yellow arrow.

Fig. III. 9 shows the measured dependence of nH on L at different pressures. Here the distance between the positions '1' and '2' was $L=50\ \mu\text{m}$. This graph shows that the optical thickness of H₂O varies linearly with the displacement of the sample. The angle of inclination of each curve yields the value $n(\Delta H/\Delta L)=ntg(\alpha)$. It can be seen that the angle of inclination of the curves increases with increasing pressure which indicates an increase of the refractive index n of H₂O and thus of the optical thickness $n\Delta H$. It is also seen that at a pressure of 6.7 GPa the wedge shape began to change. This is due to the fact that the pressure in the sample volume is not truly hydrostatic and shear stresses start to act on the iron wedge. Since iron is not sufficiently stiff the shape of the wedge started to change under relatively low shear stresses and determination of the slope of the curve in Fig. III. 9 becomes difficult.

Nevertheless, the refractive indexes of water and of the two solid phases of ice (phase VI and VII) [11,12] were measured as functions of pressure using the interference method. The pressure dependence of the refractive index of H₂O, obtained in this experiment to 6.7 GPa, is shown in Fig. III. 10. These data are in a reasonable agreement with the earlier results [1,2].

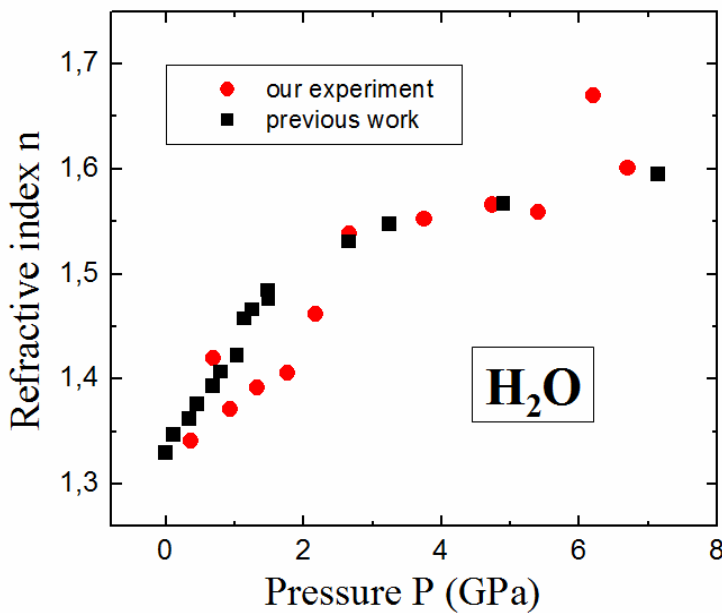


Figure III. 10. Dependence of the refractive index n of H₂O on pressure P . These data were obtained from the analysis of the slope of the curves shown in Fig. III. 9. Iron wedge was used as a reference object. The maximum pressure which is achieved in this experiment is 6.7 GPa.

After this test experiment we decided to use a stiffer material than iron for the wedge namely diamond. In particular we used specially fabricated wedges with a square base. The side size of the base is about $50\ \mu\text{m}$. The average height of the wedge was about $20\ \mu\text{m}$ (Fig. III. 11). In order to increase the reflection of the light from the boundary H₂O/wedge a thin platinum (Pt.) film with thickness of about 35 nm was deposited on the top surface of the diamond wedge (Fig. III. 11a).

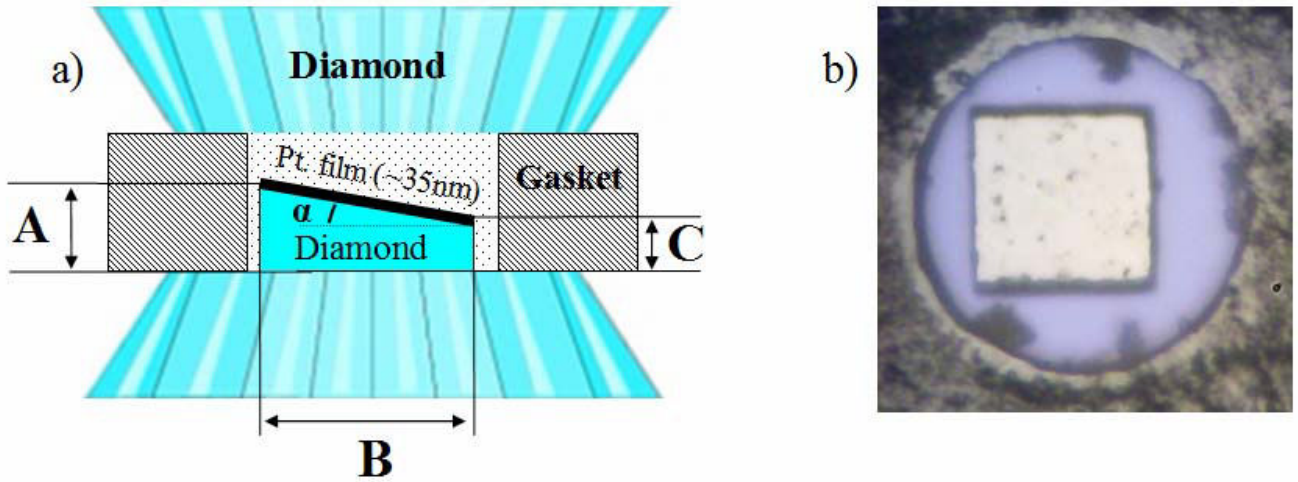


Figure III. 11. (a) Schematic image of the diamond wedge inside the diamond anvil cell compressed together with H₂O. The side size of the base are $B \approx 50 \mu\text{m}$, the height of the wedge $C \approx 20 \mu\text{m}$, the height difference of the wedge $A - C \approx 2 \mu\text{m}$. For the reflection of light from the wedge, a platinum film of about 35nm in thickness is deposited on the upper wedge surface. (b) Photograph of the diamond wedge in the diamond anvil cell with water H₂O (top view). The pressure is 0,4GPa. Diameter of the hole is about 114 μm . At the sample periphery a few rubies used to measure pressure can be recognised.

This diamond wedge was placed in the diamond anvil cell together with water and the pressure was only slightly increased in order to insure that the diamond anvil cell is closed. The initial pressure of 0,44 GPa falls in the range of 0,05 GPa to 1,2 GPa where the pressure dependence of the refractive index of fluid H₂O is measured precisely to be [2]:

$$n(P) = 0,900 + 0,4323(1 + 1,769P)^{0,164} \quad (\text{III.3})$$

where P is pressure in GPa. Thus, we could calculate the refractive index of H₂O to be $n(0,44\text{GPa}) = 1,375$ and derived the slope of the wedge to be $\text{tg}(\alpha) = 0,0423$.

The measurement procedure with the diamond wedge was the same as with the iron wedge as described above. First, we measured dependence of the optical thickness along the wedge as a function of the displacement of the sample at different pressures. Then we determined the values of $ntg(\alpha)$ and derived refractive index of H₂O as a function of pressure. The maximum pressure which was reached in this experiment was 31 GPa.

We also carried out a second set of measurements with another diamond wedge for pressures between 0,4 GPa and 23,4 GPa. The results of the two experiments are shown in Fig. III. 12. These results show that starting from 5 GPa pressure, the refractive index of water as function of pressure obtained by our method is very different from the results of the previous works [2]. Possible reasons for this behaviour are discussed in section III. 7.

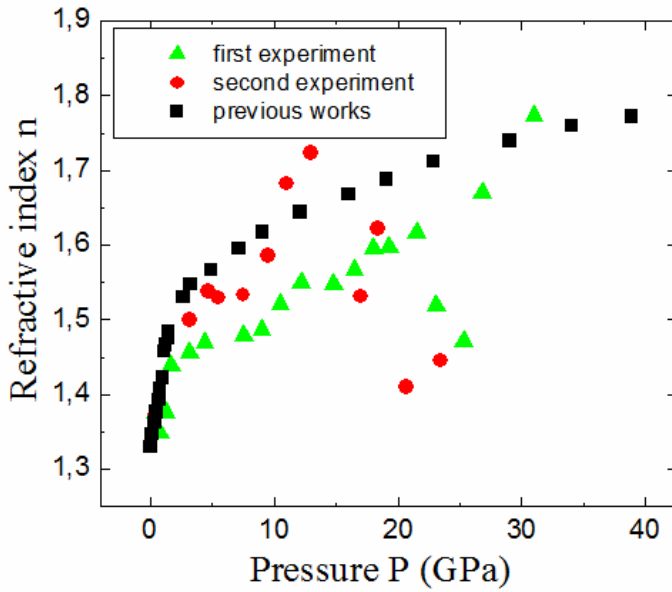


Figure III. 12. Dependence of the refractive index n of H₂O as a function of pressure P using diamond wedge as a reference object. Green triangles are results of the first set of measurements up to 31 GPa. Red circles are results of the second set of measurements to 23.4 GPa. Black squares represent results of a previous work [2].

We also carried out a second set of measurements with another diamond wedge for pressures between 0,4 GPa and 23,4 GPa. The results of the two experiments are shown in Fig. III. 12. These results show that starting from 5 GPa pressure, the refractive index of water as function of pressure obtained by our method is very different from the results of the previous works [2]. Possible reasons for this behaviour are discussed in section III. 7.

III.4.2. Using the equation of state of the diamond to get refractive index

Another method of measuring the refractive index of the transparent material under pressure in a diamond anvil cell was used in [8] where a plane-parallel object was placed in the cell together with a transparent sample substance Fig. III. 13.

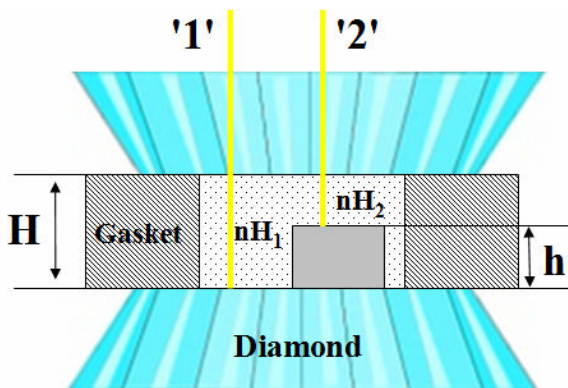


Figure III. 13. Illustration of a method of measuring the refractive index of a transparent material in a diamond anvil cell by using a plane-parallel plate. Thickness measurement was carried out in two positions '1' and '2' using the interference method'. The plate thickness h and its change with pressure is known from preliminary measurements.

If the object thickness is almost independent of pressure in the investigated pressure range or if we know the equation of state of the substance (from experiment or theory), then we can find the thickness of the object h at any pressure using the equation given below (eq. III.5). In this case it is

sufficient to make two measurements of thickness (by using the interference method) at the position '1' (the space between the two diamond anvils is filled only with a transparent sample substance) and at the position '2' (a part of the space is occupied by the reference object). Thickness measurement in the position '1' will give the value nH_1 . And the thickness measurement in the position '2' will give the value $nH_2=n(H_1-h)= nH_1-nh$. Then, from these two measurements applying the known thickness of the object h the refractive index of the transparent medium n can be found as

$$n = \frac{nH_1 - nH_2}{h} \quad (\text{III.4})$$

This kind of experiments to measure the refractive index of transparent material in the diamond anvil cell was carried out up to 31 GPa. We used the same samples as described in Section III.4.1 where a diamond wedge was loaded together with the sample. The thickness measurements were carried out at all pressures at two points: outside the wedge and close to the wedge edge where its thickness is A (see Fig. III. 11).

When the pressure in the diamond anvil cell is changed the thickness of the wedge A changes too. To determine the thickness of the wedge A' under pressure, we have assumed that the pressure in the diamond anvil cell is hydrostatic (the diamond is so stiff that a small degree of nonhydrostaticity can be neglected) so $(A'/A)=(V'/V_0)^{1/3}$ where V_0 is the volume of the diamond wedge at zero pressure and V' is volume of wedge the under pressure. We determined V'/V_0 using the Murnaghan's equation of state [13]:

$$\frac{V_0}{V'} = \left(1 + \frac{K'_0}{K_0} P \right)^{1/K'_0} \quad (\text{III.5})$$

where K_0 is the zero pressure bulk modulus of diamond, K'_0 is the first pressure derivative of the bulk modulus at zero pressure, and P is the pressure in diamond. We used the measured bulk modulus, $K_0 = 442$ GPa [14,15] and estimated the value for its first pressure derivative to be $K'_0=4$ [16].

Using these values we have calculated change in the diamond wedge thickness with pressure. In the first set of measurements the initial thickness of the wedge A was $\sim 19,3\mu\text{m}$ and pressure was increased to 31GPa. Thus, using eq. (III.4) we calculated the thickness of the wedge at a pressure of 31GPa A' to be $18,9\mu\text{m}$. In the first approximation, we have neglected the variation in the thickness

of the diamond wedge (see section III.7) and assumed it to be 19,3 μ m at all pressures ($A \cong A' \cong 19,3\mu\text{m}$). The same assumption was made in the second set of measurements.

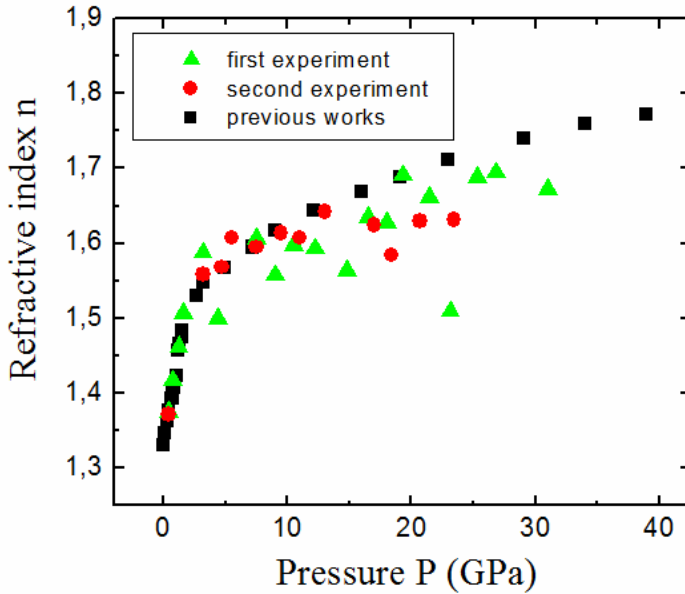


Figure III. 14. Dependence of the refractive index n of H₂O on pressure P . Green triangles represent the first experiments set up to 31 GPa. Red circles are the second set of measurements up to 23.4 GPa. Black squares represent previous results [2]. Our data were obtained using the equations (III.4) and (III.5).

The results of our measurements of the refractive index of H₂O on pressure increase using equation (III.4) is shown in Fig. III. 14. Here the results of our two measurements (red and green symbols) are compared with those obtained in an earlier work (black squares) [2]. These results are discussed in section III. 7.

§III.5. Volume of H₂O as a function of pressure

III.5.1. Thickness of H₂O in DAC as a function of pressure

Interference method applied to a transparent sample compressed in a diamond anvil cell allows measuring of the nH value on pressure increase. The value nH can be the optical thickness between the diamonds or the optical thickness between the reference object and the upper diamond anvil. If the refractive index of a transparent medium n is known as a function of pressure (from the experiments described above in sections III.4.1 and III.4.2, from a previous work or from theory), then the thickness H can be immediately calculated.

In this work we used again the two samples with a diamond wedge which are described above. Measurement of the optical thickness of the H₂O is carried out outside the wedge (Fig. III. 13, position '1') at each pressure. Refractive index of H₂O as a function of pressure was taken from our measurements (Fig. III. 14). Dependences of the thickness of our H₂O samples compressed in the diamond anvil cell on pressure are shown in Fig. III. 15.

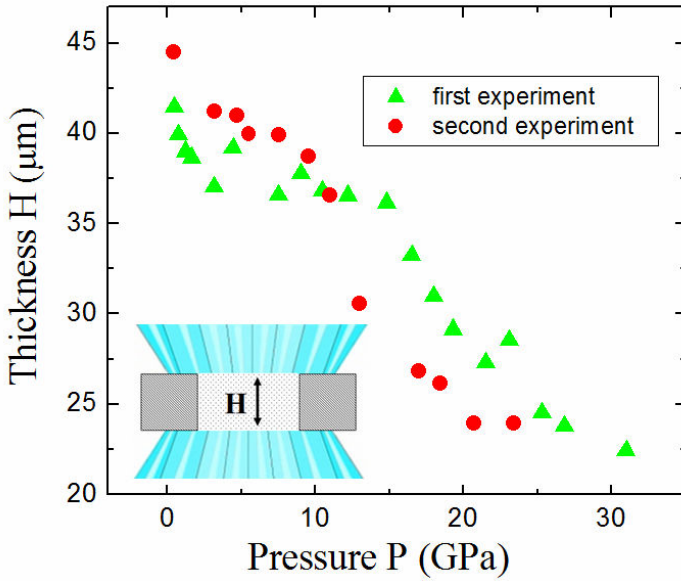


Figure III. 15. Thickness of the H₂O layer in the diamond anvil cell as a function of pressure. Optical thickness is obtained from the interference measurements between two diamonds. The refractive index of H₂O was taken from the experimental results presented in Fig. III.14. Two experiments were carried out. The same samples as in the section III.4.2 were used.

III.5.2. Transverse size of H₂O in DAC as a function of pressure

The transverse size of a transparent material compressed in a diamond anvil cell can be used to calculate the volume of the sample at high pressures (Fig. III. 16a). This sample diameter *D* can be determined simply from the sample image analysis (Fig. III. 16b).

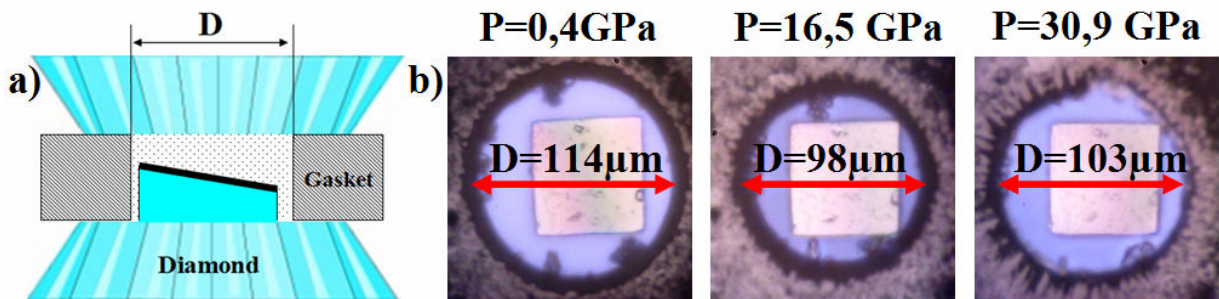


Figure III. 16. (a) Illustration of the sample size change with pressure: H₂O with the diamond wedge in the diamond anvil cell. (a) - side view. *D* is the sample diameter. (b) Photographs of the H₂O sample in the diamond anvil cell at different pressures (top view).

In our case we used the possibility to move the diamond anvil cell in the horizontal plane with a high precision using the visualization system and a compact motorized actuator (TRA Series). We recorded the initial and final position of the diamond anvil cell when the sample edge is approached and thus determined the sample diameter. We measured the diameter of our H₂O samples at all pressures. The area was calculated as $S = (\pi/4)D^2$. The same samples as in the previous sections were used (H₂O with the diamond wedge). The area of the H₂O samples as a function of pressure for two experiments is shown in Fig. III. 17.

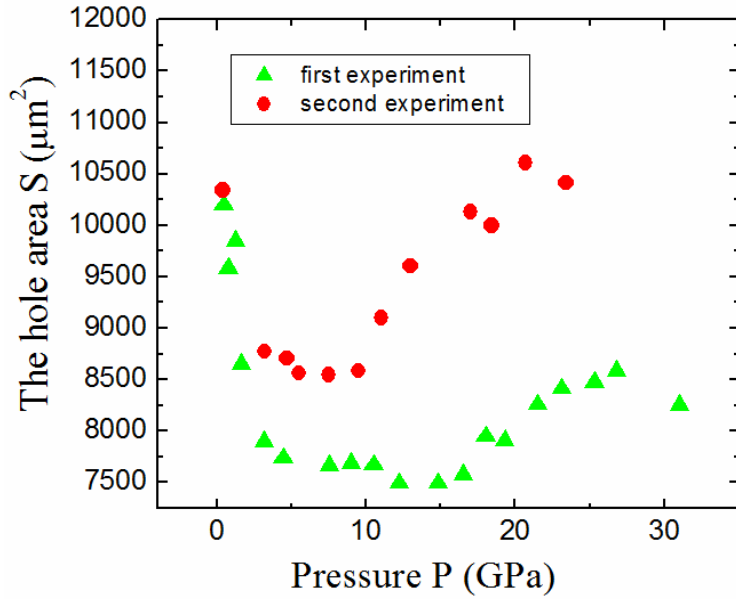


Figure III. 17. Transverse area S of our H₂O samples in the diamond anvil cell at different pressures. Two experiments were carried out. The same samples as in the section III.4.2 were used. To determine the transverse size the visualization system and the ability to precisely move the diamond anvil cell in one direction were applied.

Thus measurement of the transverse size of the transparent sample compressed in a diamond anvil cell is performed using the imaging systems. This value is necessary for calculation of the sample volume under pressure. Also a visual examination of the sample allows to draw conclusions about the state of the sample and about stability of the confining gasket.

III.5.3. Volume of H₂O and bulk modulus as a function of pressure

The volume of a transparent sample compressed in a diamond anvil cell is given by the expression $V=H*S$ where H is the sample thickness obtained in section III.5.1 and S the transverse sample area obtained in section III.5.2. Measurement of both H and S were conducted simultaneously for each sample and pressure. The volume as a function of pressure for two experiments is shown in Fig. III. 18. The initial volume V_0 for first experiment $V_0= 422750 \mu\text{m}^3$, for the second experiment $V_0= 460405 \mu\text{m}^3$.

It is important to note that the volume of study consists of two contributions, the contribution from the water (or water ice) and the contribution from the diamond wedge $V= V_{H2O} + V_{wedge}$. The approximate volume of diamond wedge $V_{wedge} \cong 50000\mu\text{m}^3$. However, as shown in section III.4.2, the wedge volume is almost constant when the pressure changes (changes in the volume of wedge are not more than 6% and the initial volume of the wedge is approximately 10 times smaller than the total initial volume). Thus we can say that the volume change occurs mainly because of the contributions of H₂O: $V(P)=V_{H2O}(P)+V_{wedge}=V_{H2O}(P)+ const$. If it is necessary the contribution of the wedge can be taken into consideration by using equation (III.5).

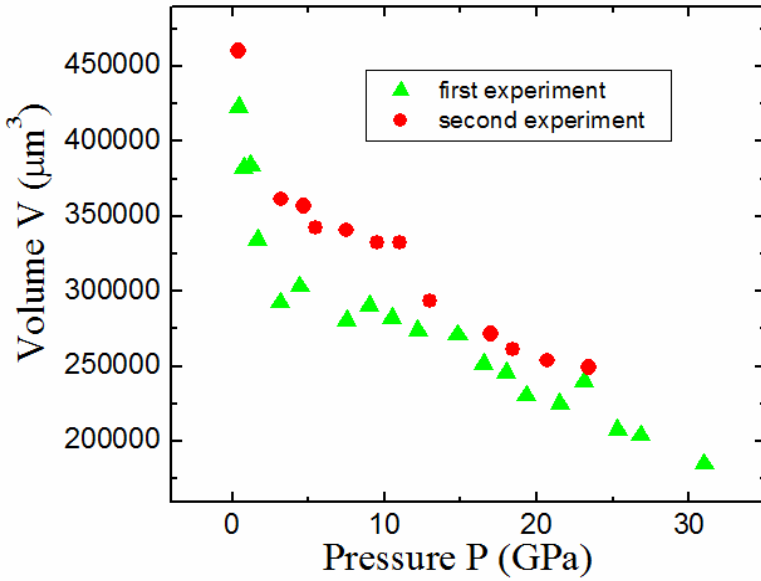


Figure III. 18. The volume of H₂O with diamond wedge in the diamond anvil cell at different pressures. Two experiments were carried out. The same samples as in the section III.4.2 were used. To determine the volume data obtained for H and S (Fig. III. 15 and Fig. III. 17) were used.

§III.6. Curvature of the diamond culets on sample compression

Finally we used our experimental system to assess the curvature of diamond anvil culets on compression. In many of optoacoustic experiments in a diamond anvil cell it is assumed that the sample has a plane-parallel top and bottom surfaces [5,6,7]. In general, at high pressures, this statement is not true. At high pressures, there is a large pressure gradient in diamond anvils [17,18]. Under the influence of the pressure gradients, the diamond anvil culets become curved. The thickness of the sample between the diamond anvils is usually thicker in the anvils centre and thinner on the edges. The sample shape resembles that one of a lens (Fig. III. 19a) instead of a plane-parallel plate (Fig. III. 3a). Since the sample curvature increases with pressure it can introduce errors in the optoacoustic data.

To study the curvature of diamond culets under pressure, we used the same interference method. We performed thickness measurement from position '1' to position '2' as described in section III.4.1. But in this case, we moved perpendicular to the wedge slope. This means that the wedge thickness did not change between positions '1' and '2'. Since the thickness of the wedge is constant, we could assume that in this direction the wedge has a plane-parallel surface (Fig. III. 19a) and any changes in optical thickness should be due to curvature of the upper anvil culet.

We have performed a few measurements along the wedge surface at different pressures in the H₂O sample. We found the maximum thickness H_0 in the range from '1' to '2', and then we found the thickness deviation from the maximum thickness $H-H_0$ as a function of the position on the sample. The

position of the maximal thickness is identified as zero (center of the curvature). Changes in the thickness of the H₂O ice layer, $H-H_0$, for the 'first' sample caused by the curvature of the surface of the diamond anvil culets as a function of the displacement are shown in Fig. III. 19b for two pressures 23 GPa and 31 GPa.

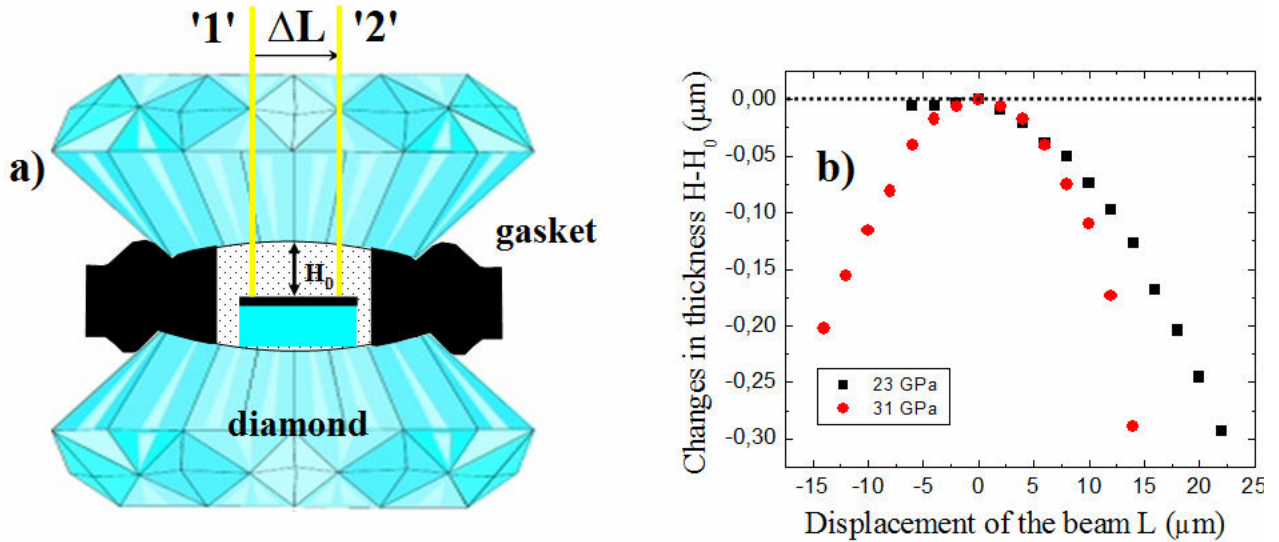


Figure III. 19. (a) . Illustration of the measuring the curvature of the diamond anvil culets under pressure. The H₂O sample with diamond wedge compressed in the diamond anvil cell (side view from the direction parallel to the slope of the wedge). The diamond anvil culets are curved due to the pressure gradient. The measurements of the thickness were accomplished along the direction perpendicular to the slope of the wedge (in the direction where the wedge has a constant thickness). (b) The change in thickness of the H₂O layer at different positions from the centre of curvature measured for the 'first' sample at 23 and 31 GPa.

Fig. III. 19b shows the presence of curvature of surfaces of diamond anvil even at a relatively low pressures of 23 and 31 GPa. Here we do not take into account changes in the refractive index of H₂O since the pressure gradient is low and does not exceed 2 GPa. As we can see from Fig.III.19 even at a moderate pressure of 23 GPa a lateral shift by 15 μm from the curvature center results in the sample thickness change of ~0,13μm. When pressure is 31 GPa, this value approaches 0,3 μm for the same lateral displacement.

§III.7. Discussion and conclusions

We used interference of a broadband light reflected from different surfaces of a sample compressed in a diamond anvil cell to measure the refractive index and the thickness at different pressures. In this work we studied the refractive index of H₂O. The result shown in Fig. III. 12 indicates that starting from 5 GPa the refractive index of water as the function of pressure obtained by

method described in section III.4.1 importantly deviated from the results of the previous work [2]. These differences may be due to several factors.

Firstly, these differences may be due to the fact that the contact between the diamond wedge and the culet of the bottom diamond is not tight. During the sample preparation the water could penetrate between the surfaces of the diamond wedge and the diamond anvil. In this case the wedge can change its position and orientation with increasing pressure. This will lead to a situation that the angle is not constant and changes in an unpredictable manner. So the value $tg(\alpha)$ fluctuates with pressure. However, this appears to be less possible when the water is frozen to ice and compressed to significant pressures since the layer of water between the diamond wedge and the anvil should be thin due to the surface tension of water. Changes in the thickness of this ice layer would be smooth and thus can not explain jumps in the n values at pressures between 10 and 31 GPa.

Another reason for these differences is the process of relaxation of the diamond anvil cell after pressure rises. For example, after increasing load the constant pressure distribution is reached after some relaxation time. Also position of the sample can shift slightly during such relaxation. And the thickness of the H₂O layer between the diamond anvils perhaps can change during relaxation. If the relaxation time is significantly long then the value nH can change during the scan. This means that the slope of the curves (for example in Fig. III. 9) depends not only on the slope of the wedge but also on the relaxation process in the diamond anvil cell. And again the value $tg(\alpha)$ is not exactly constant.

Also, variations of n above 5 GPa could be due to minor variations in experimental conditions. To increase pressure, the diamond anvil cell had to be removed from the experimental setup. It is possible that the angle between the normal of the diamond anvil cell and direction of the incident light is not exactly the same when the cell was returned for the next set of measurements. Perhaps these differences in initial conditions have affected the slope of the curves.

Finally, the differences may be explained by curvature of the two diamond anvil culets on pressure increase (see section III.6) resulting in the deviation of the shape from that used for the data analysis. This means that the slope of the curves (for example, Fig. III. 9) contains curvature of the anvil culet. In this case the value $tg(\alpha)$ can vary significantly to be recognized in the measured values. For example, for the measured slope of the wedge $tg(\alpha)=0,0423$, if the sample is shifted along the inclination of the wedge by 15 μm , the change in height of the wedge will be approximately 0,6 μm . At the same time we found that at 23 GPa a change in the sample thickness due to the culets curvature can be about 0,13 μm (Fig. III. 19). This means that the error in determining the sample thickness (and consequently of the refraction index) will be about 22 %. In our measurements the displacements of the sample along the wedge slope was about 50 μm for iron wedges and about 30 μm for diamond wedges. This means that the errors can exceed 22 %. This could well explain a smooth and increasing

deviation of our n values from previous results as can be recognized in Figure III.12 for the first set of measurements. However, the sudden jumps in the n -values (jumps down and jumps up) can not be explained by the smooth change of curvature of the two diamond anvil culets on pressure increase.

All these assumptions can cause an error in the measuring the refractive index using the interference method. Each of these assumptions can be studied separately. It is also possible that there are other causes of errors. For example, inaccurate determination of the initial optical thickness nH and the interference order m , or inhomogeneous change of optical and mechanical properties of the Pt film deposited on the wedge surface.

Dependence of the refractive index of H₂O on pressure obtained by the method described in section III.4.2 (Fig. III. 14.) is in a good agreement with previous results [2]. A slight deviation in the refractive index at high pressure can be explained by omitting the thickness change of the wedge Λ . The maximum variation of the thickness of the wedge in our experiment is about 2% and the error is systematic. At the same time experiments show that the error of measurement of the refractive index by this method can be around 7 %. This can be explained by the low accuracy in determining the absolute value of nH . In our case, the accuracy of determining the optical thickness is about 0,3 - 0,6 μm . This means that the error in determining the refractive index of the given method can be more than 10 % if the thickness of the reference object is only a few microns.

Also, during the sample preparation, the water could penetrate between the surfaces of the diamond wedge and the diamond anvil. In this case the value h in eq. III.4 will include the thickness of the reference object and the thickness of the water (or ice) layer between the wedge and the bottom diamond anvil. The thickness of this layer can change with increasing pressure, especially when the surface of diamond culets starts to curve. Thus the error in the determination of the refractive index by this method may be due to an uncertainty in h .

However, the described method of measuring the refractive index overcomes some of the problems of the approach described in Section III.4.1. In this method it is not necessary to perform a scan along a large sample section, it is sufficient to make the optical thickness measurements at only two points which can be very close to each other. Also, the experiment duration decreases and the measurement error is not accumulated due to scanning.

Thus, this second method allows measuring of the refractive index of a transparent medium compressed in a diamond anvil cell to high pressures. This method is quite simple and rapid. If high accuracy in determining the refractive index of the transparent material at high pressure is not required, then this method can be applied.

Both methods have a common limitation: thickness of the transparent sample should be greater than 3 μm . Otherwise, it is almost impossible to detect oscillations in the intensity of reflected light

due to interference as shown in Fig. III. 3d. The distance between two neighboring maximum $\Delta\lambda = |\lambda_1^{\max} - \lambda_2^{\max}|$ becomes comparable with the size of the studied spectral region (for example, the studied spectral region from $\tilde{\lambda}$ to $\tilde{\lambda}$ in Fig. III. 2).

In the two types of measurements, we do not take into account the polarization of the incident light. It means we assume that a transparent substance is optically isotropic. Otherwise, a light polarizer can be installed in the experimental set-up. In our measurements we did not take into account the dispersion of the refractive index in the studied spectral region (from 595nm to 630 nm) which suggests that the pressure dependence of the refractive index of H₂O was measured at the wavelength of 611 nm.

Dependence of the thicknesses of the two compressed H₂O samples on pressure were obtained using the interference method (Fig. III. 15, section III.5.1). From this dependences follows that on compression the sample thicknesses changed by more than 20 μm . At pressures from 0 to 5 GPa an abrupt fall in the thickness is observed for both cases. This may be explained by phase transitions in the H₂O sample: Due to crystallization of water in ice VI at 1,1 GPa and a phase transition from ice VI to ice VII at 2,1 GPa [12]. The density of ice VI is 8% higher than the density of water and that of ice VII is 14% higher than the density of ice VI. Thus, the interference method allows an easy and quick method of thickness measurement for a transparent material compressed in a diamond anvil cell. This method was used in the next chapter to determine the average speed of sound in H₂O at different pressures applying acoustic data.

In section III.5.2 diameter of the H₂O samples compressed in a DAC was obtained using the visualization system. The curves corresponding to two different samples are different (Fig. III. 17) because the initial conditions for the two samples were not identical. For example, the initial sample thickness was different and position of the sample center with respect to the diamond anvils was not exactly the same. Despite of this the pressure dependences of the sample surface areas show similarities. In the pressure range from 0 to 5 GPa both measurements show a strong reduction of the sample area on increase of pressure. This could be explained by phase transitions from water to ice VI and from VI to ice VII [12]. Behavior of the curves at around 15 GPa again may be associated with a phase transition in the gasket. For the first measurements set the gasket become to be unstable (asymmetrically deformed) above 27 GPa. In Fig. III. 16b the imaged made at 30.9 GPa shows that the gasket has lost a round shape. In such case further increase of pressure was not possible.

Data from the section III.5.1 and III.5.3 were used to calculate the volume of H₂O as a function of pressure. From Fig. III. 18 it can be seen that the two experimental results are in a good agreement. At pressures between 0 GPa to 5 GPa a sharp volume decrease is detected due to phase transitions

from water to ice VI and from VI to ice VII [12]. Above 5 GPa the changes in volume of the H₂O sample are smaller. At about 15 GPa no discontinuous changes similar to those in Fig. III. 15 and Fig. III. 17 could be observed since the equation of state should not depend on phase transitions in the gasket.

Thus we have demonstrated that by means of optical measurements in the diamond anvil cell the volume of a transparent substance can be obtained as a function of pressure. This dependence allows us to calculate the isothermal bulk modulus [13] at high pressure, which is an important elastic parameter. However, it is important to bear in mind that the presented results are only estimates. Accuracy of the determining the volume is about 10 %. In this volume various sample parts are under different pressure conditions due to pressure gradients. For more exact and local study of the equation of state the X-ray diffraction method seems to be more appropriate [20].

Conclusions

We presented here measurement of the refractive index and thickness of H₂O samples at different pressures using interference of a broadband light reflected from surfaces of a sample compressed in a diamond anvil cell. Two different ways of the refractive index measurement are considered. The first method involves the use of a wedge with a known angle. The second method involves the use of a low compressibility of diamond. Refractive index of H₂O was measured by both methods up to 31 GPa. Reasons for differences of the obtained experimental dependences are discussed. The thickness, area, and volume of H₂O samples are obtained as functions of pressure. Curvature of the diamond anvil culets under pressure is measured.

References (III)

1. C.S. Zha, R. J. Hemley, S.A. Gramsch, H. Mao and W.A. Bassett. *Optical study of H₂O ice to 120GPa: Dielectric function, molecular polarizability, and equation of state.* **J. Chem. Phys.** **126**, 074506 (2007)
2. A. Dewaele, J. H. Eggert, P. Loubeyre, and R. Le Toullec. *Measurement of refractive index and equation of state in dense He, H₂, H₂O, and Ne under high pressure in a diamond anvil cell.* **Phys. Rev. B** **67**, 094112 (2003)
3. M. Ahart, M. Somayazulu, S. A. Gramsch, R. Boehler, H. Mao and R. J. Hemley. *Brillouin scattering of H₂O ice to megabar pressures.* **J. Chem. Phys.** **134**, 124517 (2011)
4. A. M. Lomonosov, A. Ayouch, P. Ruello, G. Vaudel, M. R. Baklanov, P. Verdonck, L. Zhao, and V. E. Gusev. *Nanoscale Noncontact Subsurface Investigations of Mechanical and Optical Properties of Nanoporous Low-k Material Thin Film.* **ACS Nano** **6** (2), 1410 (2012)
5. N. Chigarev, P. Zinin, L.-C. Ming, G. Amulele, A. Bulou, and V. Gusev. *Laser generation and detection of longitudinal and shear acoustic waves in a diamond anvil cell.* **Appl. Phys. Lett.** **93**, 181905 (2008).
6. N. Chigarev, P. Zinin, D. Mounier, A. Bulou, L. C. Ming, T. Acosta, and V. Gusev. *Analysis of ultrasonic echoes induced by pulsed laser action on an iron film in a diamond anvil cell* **High Pressure Res.** **30**, 78 (2010).
7. F. Decremps, M. Gauthier, S. Ayrinhac, L. Bove, L. Belliard, B. Perrin, M. Morand, G. Le Marchand, F. Bergame, J. Philippe. *Picosecond acoustics method for measuring the thermodynamical properties of solids and liquids at high pressure and high temperature.* **Ultrasonics**, In Press, (2014)
8. J. H. Eggert, L. Xu, R. Che, L. Chen and J. Wang. *High pressure refractive index measurements of 4:1 methanol:ethanol.* **J. Appl. Phys.** **72**, 2453 (1992)
9. Max Born & Emil Wolf. *Principles of Optics (4th.ed.)* Pergamon Press (1970)
10. <http://www.almax-easylab.com/ProductDetails.aspx?PID=52>
11. A. K Soper *WATER AND ICE.* **Science**, **297** (5585), 1288-9 (2002)
12. A. Polian and M. Grimsditch. *Brillouin scattering from H₂O: Liquid, ice VI, and ice VII.* **Phys. Rev. B** **27**, 6409 (1983)
13. Jean-Paul Poirier. *Introduction to the Physics of the Earth's Interior,* Cambridge University Press, 2000
14. H. J. McSkimin and P. Andreatch Jr. *Elastic Moduli of Diamond as a Function of Pressure and Temperature.* **J. Appl. Phys.** **43**, 2944 (1972)
15. M. H. Grimsditch and A. K. Ramdas. *Brillouin scattering in diamond.* **Phys. Rev. B** **11**, 3139 (1975)
16. Karl A. Gschneidner Jr. *Physical Properties and Interrelationships of Metallic and Semimetallic Elements* **Solid State Physics**, **16**, 275 (1964)
17. C.M. Sung, C. Goetze and H.K. Mao. *Pressure distribution in the diamond anvil press and the shear strength of fayalite.* **Rev. Sci. Instrum.** **48**, 1386 (1977)
18. W. A. Bassett. *Diamond anvil cell, 50th birthday.* **High Pressure Research** **29**(2), 163 (2009)
19. A. F. Guillermet, P. Gustafson. *An assessment of the thermodynamic properties and P,T phase diagram of iron.* **Stockholm** (1984)
20. P. Loubeyre, R. L.Toullec, E. Wolanin, M. Hanfland and D. Hausermann. *Modulated phases and proton centring in ice observed by X-ray diffraction up to 170 GPa.* **Nature** **397**, 503 (1999)

Chapter IV

Investigation of polycrystalline aggregates of H₂O ice in diamond anvil cell

This chapter is devoted to the use of laser ultrasonic measurements (picosecond laser ultrasonics) in a diamond anvil cell which allow investigation of the sound propagation and determination of the acoustic wave velocities at ultrahigh pressures. Time domain Brillouin scattering was applied to depth-profiling of polycrystalline aggregate of ice compressed in a diamond anvil cell to Megabar pressures. The technique allowed examination of characteristic dimensions of elastic inhomogeneities and texturing of polycrystalline ice in the direction, normal to the diamond anvil surfaces with sub-micrometer spatial resolution via time-resolved measurements of variations in the propagation velocity of the acoustic pulse travelling in the compressed sample. It was applied to measure the acoustic velocities in H₂O ice up to 84 GPa. The developed imaging technique provides for each crystallite (or a group of crystallites) in chemically homogeneous transparent aggregate usable information on its orientation as well as on the value of the elastic modulus along the direction of the sound propagation.

As noted in Chapter I, the sound velocities and elastic moduli of liquids and solids (amorphous or crystalline) at Megabar pressures are of great interest for natural sciences, but quantitatively they are known for a limited number of substances and for a limited range of pressures [1,2]. The high-pressure parameters of materials, which can be measured at pressures above 25 GPa in laboratory conditions only using a diamond anvil cell (DAC), can be importantly influenced by the polycrystallinity of the material and the existence of spatial inhomogeneities and texture in polycrystalline aggregates even in the samples of several μm characteristic size [3]. It is well known that the aggregate sound velocity depends on the characteristic dimensions of the individual crystallites, which are elastically anisotropic [4], and that, even a partial alignment of the crystallites in a material, i.e., orientational texture, causes the modification of the measured aggregate sound velocities [5]. Both these factors are preventing precise evaluation of the elastic moduli on the basis of sound velocity measurements and make necessary the development of the experimental methods for the three-dimensional imaging of the microscopic samples in-situ when compressed in a high-pressure apparatus with the goal of characterization both their morphological and orientational/directional texture.

In the past decade significant progress has been achieved in X-ray imaging of isolated objects and multigrain bodies with the spatial resolution better than 100 nm in cases where inhomogeneities

have a chemical contrast [6]. In the cases where grain orientations in polycrystalline bodies are derived from X-ray diffraction, the spatial resolution approaches today submicron level [7,8]. These methods based on the use of synchrotron X-ray radiation have also been applied for examination of samples recovered from high-pressure experiments [9,10]. However, a limited access to the sample compressed in a diamond anvil cell reduces significantly the lateral resolution for in-situ characterisation of polycrystalline samples [11,12]. The resolution degradation in the axial sample direction, i.e., along in-depth direction parallel to the load axis of the DAC, is even more dramatic and was expected to be 2 μm or even worse [13]. The nanoscale resolution can be maintained for samples compressed in a DAC only when a small number of grains or an isolated grain are illuminated, or when the sample is chemically and texturally uniform (e.g. single crystal or glass) [14-16]. Finally, none of the considered methods provides any independent information on elastic properties of the sample material or individual grains.

In this PhD research work an experimental method which overcomes the above listed limitations and allows in-situ texture examination of transparent samples compressed in DAC to pressures approaching 1 Mbar and provides spatially resolved information (both in lateral and axial directions) about sample elastic behaviour is introduced.

§IV.1. Picosecond acoustic interferometry technique

Important role for the evaluation of the elastic parameters of the condensed media at high pressures is played by methods which are based on the interaction of laser radiation with acoustical phonons. Application of optical radiation is particularly suited for the DAC technique where both extreme stiffness-hardness, needed to achieve high pressures, and transparency of diamond, needed for optical access to compressed sample, are essential. In classic, i.e., frequency domain, Brillouin scattering (BS) technique the frequency shift of light scattered by thermal (incoherent) acoustic phonons in the sample provides information on the velocities of the longitudinal and shear sound [17-19]. In laser ultrasonic techniques light is employed not only for the detection of acoustic phonons, like in classic BS, but also for their generation [20,21]. Moreover, the acoustic phonons, monitored inside the sample, are coherent. Laser ultrasonics had been first used in high pressure experiments to increase the photo-elastic scattering of probe light through the generation of monochromatic coherent acoustic waves by laser-induced gratings, i.e., by interference patterns of two pump pulsed laser beams propagating at an angle. The probe light is predominantly scattered not by the thermal but by the laser-generated phonons. This laser ultrasonic technique of impulsive stimulated Brillouin scattering (ISBS) [22] had been applied at high pressures to measure velocities of both bulk [23,24] and interface [25,26]

acoustic waves. Recently other laser ultrasonic techniques were tested in studies of materials at high pressures in DACs. Picosecond laser ultrasonic technique [27], based on both the generation and the detection of wide-frequency-band coherent acoustic pulses by femtosecond laser pulses was first applied in [28] (see Fig. I. 12 in Chapter I). Laser ultrasonic technique based on the generation of acoustic pulses by sub-nanosecond laser pulses and their detection by the continuous laser radiation was introduced in [29] (see Fig. I. 12 in Chapter I). In both experimental configurations the spectrum of the detected acoustic pulses extended up to GHz frequencies range. In [28] the transient optical reflectivity signals obtained by the technique of picosecond acoustic interferometry [30], also called time-domain Brillouin scattering (TDBS), were reported for the first time at high pressures. Later this technique has been also realized with picosecond laser pulses instead of femtosecond laser pulses [31].

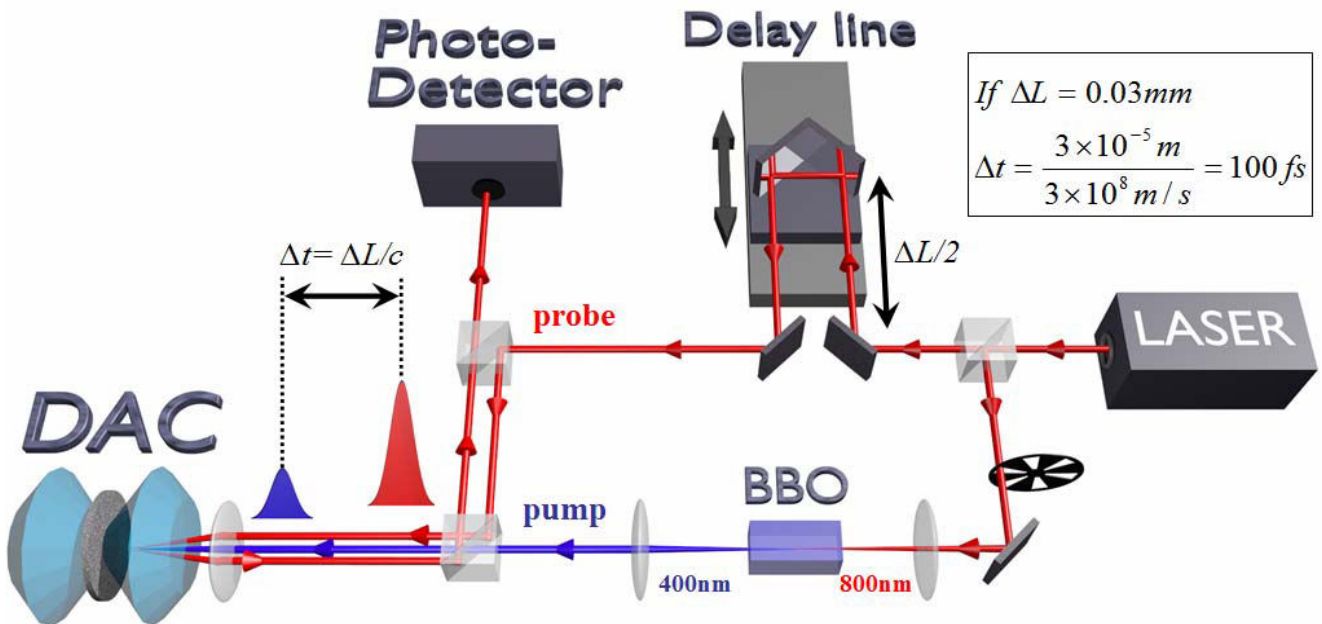


Figure IV. 1. The illustration of a typical scheme for picosecond acoustic interferometry technique.

In the picosecond acoustic interferometry, which is a particular optical pump – probe technique (Fig. IV. 1), the pump laser pulse generates in a light absorbing opto-acoustic transducer picosecond acoustic pulse which propagates through a sample. Since a typical length of picosecond acoustic pulse is in the nanometers to sub-micrometers spatial scale, the technique is perfectly suitable for examination of materials confined in DACs where sample sizes are typically from several tens of micrometers down to a few micrometers and grains in polycrystalline samples are typically below 1 μm in size. In case of an optically transparent material the probe laser pulse, delayed in time relative to the pump laser pulse, preferentially interacts with those coherent GHz phonons of the acoustic pulse spectrum which satisfy the momentum conservation law in photon-phonon photo-elastic interaction,

i.e., satisfy the BS condition. Weak light pulses scattered by acoustic pulse interfere at the photo-detector with the probe light pulses of significantly higher amplitude scattered/reflected at various surfaces and interfaces of the tested structure, for example at the interfaces of the sample with the diamond and of the opto-acoustic transducer with the sample (Fig. IV 2a). The detected modification of the transient optical reflectivity is proportional, in leading order, to the product of these two scattered light fields. Thus, a heterodyning of a weak field against a strong one is achieved in picosecond ultrasonic interferometry. The measured transient reflectivity signal varies with time because the relative phase of the light scattered by the propagating acoustic pulse and scattered by immobile surfaces/interfaces continuously changes with time due to the variation in the spatial position of the propagating acoustic pulse.

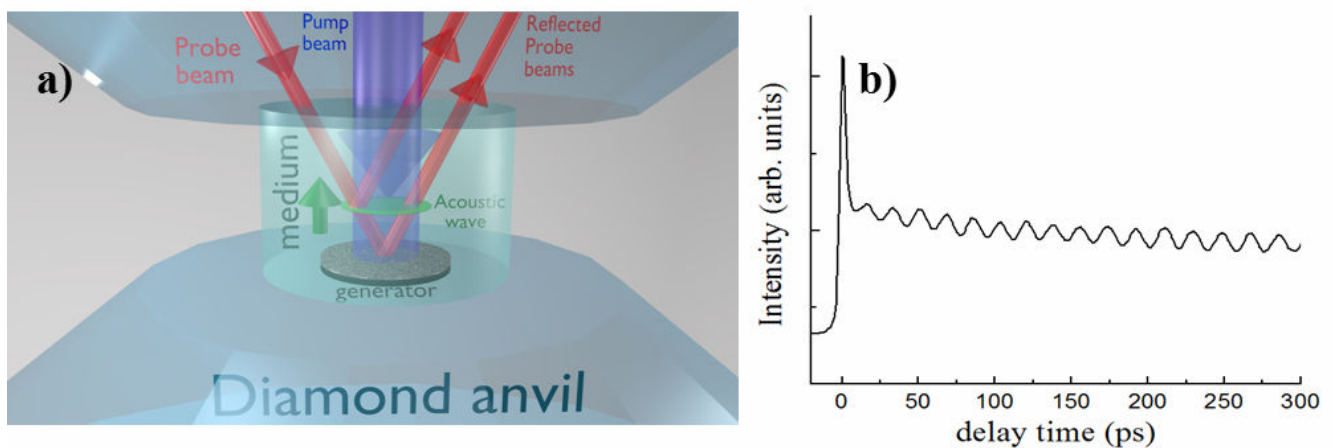


Figure IV. 2. (a) Transparent spatially homogeneous medium in the diamond anvil cell which is studied using picosecond acoustic interferometry technique. (b) The amplitude of the reflected probe beam is modulated in time in sinusoidal manner for spatially homogeneous medium.

If acoustic pulse propagates at a constant velocity, i.e., in a spatially homogeneous medium (Fig. IV. 2a), the phase difference between the interfering light fields linearly changes in time and, as a consequence, the amplitude of the signal changes in time in sinusoidal manner (Fig. IV. 2b) at a GHz frequency precisely equal to the Brillouin frequency [30]. Thus, measuring the period/frequency of this time-domain Brillouin oscillation provides information on the velocity of the acoustic wave in the sample. In the collinear scattering geometry of the TDBS experiments [28,31] the Brillouin frequency is proportional to the product of sound velocity and of the optical refractive index of the medium at the probe wave length (see Eq. (IV. 1)).

In an inhomogeneous medium the TDBS signal at each time instance contains information on the local parameters of the medium in the spatial position of the laser generated light-scattering acoustic pulse at this time instance. It has been demonstrated earlier, although under ambient conditions, that this effect can be used for the depth-profiling of inhomogeneous transparent media

with nanometers scale resolution limited by the spatial length of the laser-generated coherent acoustic pulse [32,33] (see Fig. I. 7 in Chapter I). The in-depth profiles of the sound velocity, of the optical refractive index and of the photo-elasticity with the spatial resolution of 50 nm, which is not limited by the wavelength of acoustic phonon at Brillouin frequency, were determined in the sub-micrometer thick film of low-k nanoporous material by conducting TDBS measurements at several different angles of probe light incidence [32].

Below in this Chapter there is a description of the application of the TDBS technique to the diagnostics of water ice in a DAC at pressures of 57 and 84 GPa revealing the characteristic features of its micro-crystallinity. While the classic, i.e., frequency domain, BS experiments with single crystal H₂O ice are extremely rare [34,35] and were reported only at relatively low pressures below 10 GPa, the experiments at higher pressures are conducted on polycrystalline ice [34,36-38]. The problems in application of the classic BS of light by thermal phonons in polycrystalline materials and, in particular, in H₂O ice are well known [19,36-38]. The Brillouin spectral lines are not just importantly broadened [19,36] but are split [19,36,38] because of the simultaneous contributions to the scattered light from multiple differently oriented crystallites, i.e., elastically anisotropic grains, inside the scattering volume. Detection of the broad Brillouin lines provides opportunity to extract only the orientation-averaged, i.e., so-called aggregate, sound velocities [36], while the detection of the split Brillouin peaks requires data collection through a large number of different scattering volumes covering many randomly oriented grains with the goal to establish the maximum and the minimum boundaries of compressional and shear sound velocities [38]. Additional complexity/inconvenience in the experiments with cubic polycrystalline ices arrives from their optical isotropy [39], which makes impossible visualization/characterization of the grain distribution, i.e., of the polycrystalline aggregate texture, by birefringence, which could be very useful in the case of grains without inversion symmetry [34,40]. In-depth spatial resolution in classic BS microscopy [41] applied for three-dimensional imaging [42] exceeds nowadays tens of micrometers.

In this Chapter experimental “visualization” of the texture in the polycrystalline aggregate of H₂O ice by TDBS technique is described. The demonstrated two-dimensional, in-depth and lateral, imaging of texture in cubic, i.e., optically isotropic, ice is mostly due to the contrast provided by the difference in sound wave velocities inside the crystallites, differently oriented relative to the propagation direction of the acoustic and probe laser pulses. When coherent acoustic pulse of the nanometers to sub-micrometers spatial length propagates inside the sample, the Brillouin frequencies corresponding to the particular orientations of the spatial domains, in which the coherent acoustic pulse is currently localized, are resolved in time/space. The lateral dimension of the photo-generated acoustic pulse is controlled by pump laser pulse focusing.

§IV.2. Experimental setup

TDBS is an optical pump – probe technique, where the pump laser pulse generates in a light absorbing opto-acoustic transducer picosecond acoustic pulse which propagates through an optically transparent sample contacting the transducer, while the probe laser pulse monitors the propagation of the acoustic pulse. The probe laser pulse, delayed in time relative to the pump laser pulse, preferentially interacts with those coherent GHz phonons of the acoustic pulse spectrum which satisfy the momentum conservation law in photon-phonon photo-elastic interaction [31,43].

The TDBS experiments on samples compressed in a DAC were conducted using a pump/probe configuration for transient reflectivity optical measurements presented in Fig. IV. 3.

IV.2.1 Pump and probe optical setup

The experiments on ice compressed in the DAC were performed using a typical pump/probe configuration for transient reflectivity optical measurements (Fig. IV. 3a) involving a pulsed Ti:Sapphire laser with the following characteristics: 2 W average power, 808 nm wavelength, 2.7 ps FWHM duration of the laser pulses at the repetition rate of 80 MHz. This radiation was divided by a polarizing cube in the pump- and probe beams. The pump laser beam was modulated acousto-optically at frequency 161.1 kHz for the subsequent realization of the synchronous detection of the probe laser radiation scattered by the sample. Then, it was frequency-doubled by 1 cm-long BBO non-linear crystal to obtain 25 mW of 404 nm wavelength light pulses of 1.9 ps duration at FWHM for the generation of coherent acoustic pulses in the Fe-foil near its interface with H₂O ice. Computer-controlled optical delay line of two-passage configuration allowed introducing the delays of the probe laser pulses relative to the pump laser pulses in the interval 0-8 ns. The time-delayed probe laser pulses, for time-resolved detection of the BS induced by the coherent acoustic pulse, were at the fundamental wave length 808 nm of the laser. The photo-acoustic signals have been obtained with the steps in time of 1.5 ps. Both pump and probe radiation were focused by a 50X-objective lens (numerical aperture 0.5, working distance 10.5mm on the DAC from the same side and the scattered probe radiation was also gathered from the same side. The system of optical imaging including a web-camera and the source of white light has been installed for the visualization of the laser spots and the surface of the sample in DAC. The pump laser beam was focused on the Fe/ice interface into the elliptical spot, which dimensions, 9 μm in the horizontal and 5 μm in the vertical directions, are determined at FWHM of the intensity of the image obtained by the camera.

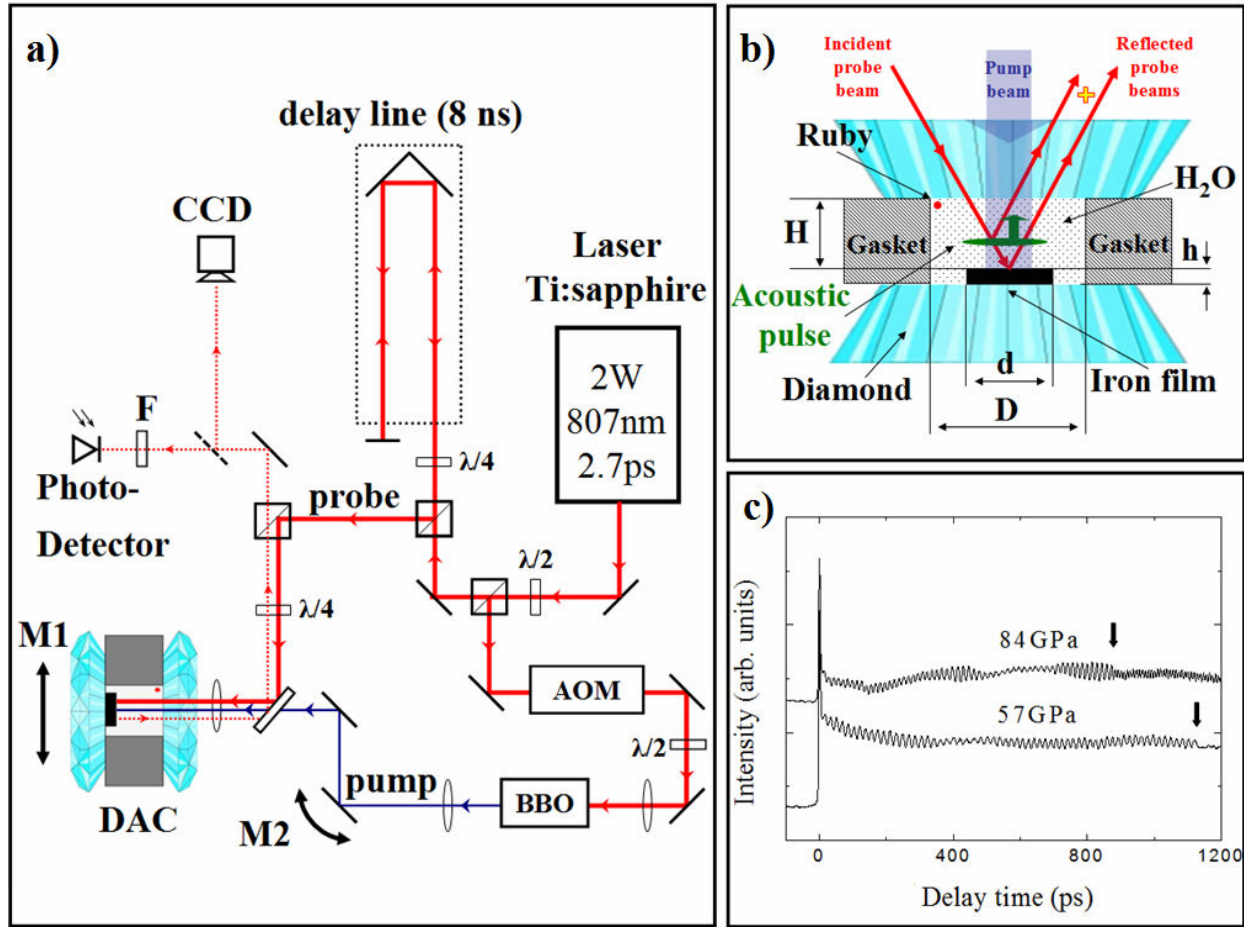


Figure IV. 3. Time – domain Brillouin scattering in a diamond anvil cell. (a): Schematic presentation of the experimental setup. (b): Sample in a DAC with qualitative presentation of some of the probe optical rays contributing to the TDBS detection. (c): Transient reflectivity signals detected in the ice samples compressed in a DAC to 57 and 84 GPa as a function of the delay time between the probe- and the pump laser pulses. Arrows indicate the times for the first arrival of the photo-generated acoustic pulse at the interface of ice and diamond anvil.

The probe laser pulse was focused into a circular spot. The pump spot was scanned relative to the probe in vertical lateral direction along the Fe/ice interface perpendicular to the long axis of the ellipse. The scan was achieved using a variation of an angle $\Delta\theta$ of incidence of pump beam, provided by the rotation of a dielectric mirror installed on the computer controlled support (M2 in Fig. IV. 3a). The displacement Δx of the pump beam on the surface of Fe is the following: $\Delta x = [f - h(1 - 1/n)]\Delta\theta$, where $f=4$ mm is the focusing distance of the objective, $h=2.5$ mm and $n=2.4$ are the thickness and the refractive index of diamond, respectively. The position of the delay line was fixed at the maximum of amplitude of the transient thermo-reflectance signal, which corresponds to the coincidence in time of pulses of pump and probe beams. Then, the pump beam was scanned in vertical direction to obtain the amplitude of the transient thermo-reflectance signal as a function of the position. This function, showing the correlation of the pump and probe beams in the vertical direction, has provided the width of 3 μm at FWHM. This indicates a 4 μm radius of the probe

laser focus and 4.5 μm FWHM of the correlation function of the two beams in the direction of the long (horizontal) axis of the pump laser elliptical focus. In addition, DAC was mounted on a motorized linear stage (M1 in Fig. IV. 3a), allowing displacement of laser spots in horizontal lateral direction on the surface of the opto-acoustic generator with precision of 0.1 μm . The filter (F in Fig. IV. 3a) was introduced before the photo-detector to avoid its illumination by pump radiation scattered from the sample.

IV.2.2 Diamond anvil cell and the samples

High pressures up to 84 GPa were generated via squeezing of samples between bevelled diamond anvils of Boehler-Almax design having the culet size of 300 μm mounted in a Boehler-Almax Plate DAC [58]. A hole in the centre of a pre-indented stainless steel gasket represented the sample volume filled with ice and a thin iron foil in contact with one of the anvils and the sample. The iron foil served as the opto-acoustic generator for launching coherent acoustic pulses in the ice. A zoomed schematics of the sample arrangement in the DAC is presented in the insert in (Fig. IV. 3b). The sample dimensions in the experiments conducted at 57 GPa and 84 GPa were, respectively, 103 μm and 90 μm in diameter D and 14.4 μm and 13.5 μm in thickness H . The diameter d of the iron opto-acoustic generators were 66 and 40 μm , respectively and their thicknesses about 2 μm at ambient pressure, in both experiments. Pressure was determined from the wavelength of the R1 fluorescence line of ruby grains distributed through the ice sample which red shift with pressure was calibrated earlier [59].

§IV.3. Experimental signals and their processing

Typical transient reflectivity signals recorded in the experiments at 57 and 84 GPa where water ice appears, most probably, in the phase X with ordered positions of protons [44,45] are presented in Fig. IV. 3c. Here, the temporal window spans the delay times necessary for a one way propagation of the photo-generated coherent acoustic pulse from the iron opto-acoustic generator to the ice/diamond interface (see Fig. IV. 3b). The arrival times of the acoustic echoes at the ice/diamond interface, marked by arrows in (Fig. IV. 3c), manifest themselves by an abrupt diminishing in the amplitude of the Brillouin oscillation at 880 ps and 1134 ps for 84 GPa and 57 GPa, respectively.

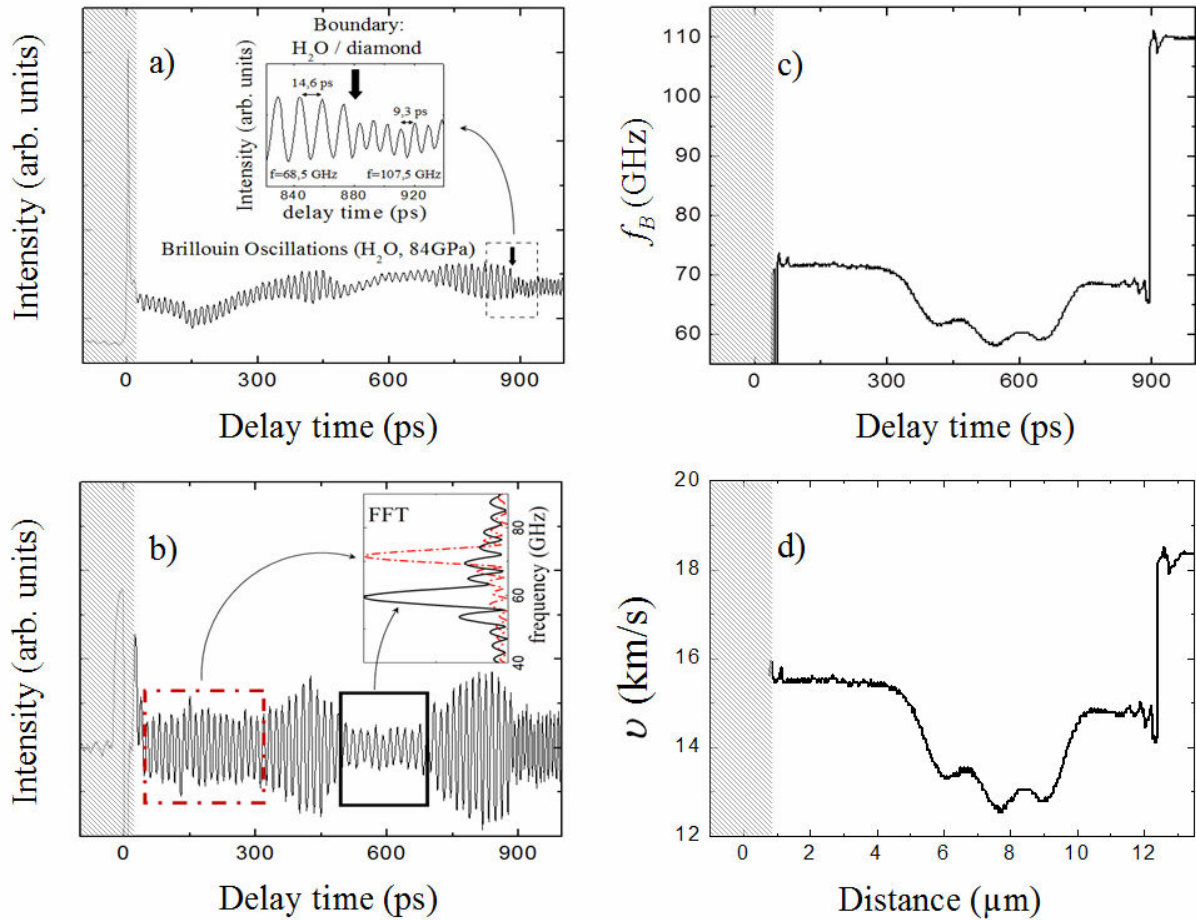


Figure IV. 4. Revealing in-depth spatial inhomogeneity of H₂O ice X at Megabar pressures. (a): Typical time resolved reflectivity signal in ice compressed in a DAC to 84 GPa. The vertical arrow marks the time of transmission of the laser-generated acoustic pulse across the interface of ice with diamond. Insert: zoom of the signal in the vicinity of the ice/diamond interface. (b) TDBS signal obtained by filtering from the signal in (a) of the time-varying thermo-reflectance contribution caused by transient heating of the sample. Insert: Fourier spectra of the signal inside two temporal windows, marked by rectangles, demonstrate shift of the Brillouin frequency from 60 GHz up to about 73 GHz, indicating spatial inhomogeneity of the ice sample. For each time - window the obtained frequency value is an average over multiple crystallites in the volume from which the signal is collected. The lateral size of the probed volume is determined by the elliptical intensity correlation function with the axes of 3 μm and of 4.5 μm FWHM for the pump and probe beams. The cross sectional area of the tested volume can be estimated as 10 μm^2 . The axial, i.e., in-depth, dimensions of the probed sample volumes are determined by the duration of the used time-windows and exceed, in this particular case, 3 μm . (c): Temporal profile of the Brillouin frequency of the TDBS signal shown in (b). Fourier transform was performed in the rectangular moving temporal window of 100 ps duration corresponding to the in-depth distance of about 1.5 μm . (d): Spatial variation of the longitudinal sound velocity obtained from the temporal dependence of the Brillouin frequency shown in (c) using the extrapolated refractive index values of ice[39]. The coordinate in (d) is evaluated by integrating the sound velocity over acoustic propagation time only in a part of the experimental window, which does not include short delay times (shaded in Fig. IV. 4) where the determination of Brillouin frequency is not enough certain because of imperfect filtering of the thermo reflectance contribution at GHz frequencies. Thus, the distance in (d) should be measured relative to the ice/diamond interface.

In (Fig. IV. 3c) and especially in the insert in (Fig. IV. 4a) it is clearly seen, without any signal processing, that the transmission of the acoustic pulse across ice/diamond interface is also accompanied by an abrupt increase in the frequency of the oscillating part of transient reflectivity. These observations are in accordance with the estimated weak reflection, of less than 15 % in

amplitude, of acoustic waves from ice/diamond interface, much lower photo-elastic (acousto-optic) constants of diamond in comparison with those of ice at the optical probe wavelength and larger Brillouin frequency shifts in diamond than in ice measured by the classic BS at similar pressures [36]. Value of this arrival time is known to provide information on the acoustic velocity averaged over the path of the coherent acoustic pulse and on the sample thickness [32,33,43,46,47].

The non-monotonous variations in time of the Brillouin oscillation amplitude before the arrival of the coherent acoustic pulse at the ice/diamond interface which are observable in Figs. IV. 3c, 4a, 4b without any signal processing are a strong indication of the spatial inhomogeneity, i.e., polycrystallinity and texturing, of the samples. They cannot be attributed to the beatings of TDBS signals of different frequencies and are manifestations of texturing in the distribution of both photo-elastically (acousto-optically) and elastically anisotropic sub μm grains composing the ice aggregate.

Further indication of the spatial inhomogeneities could be variations with the delay time of the frequency of Brillouin oscillation [31-33.] For the bulk of the ice X sample this can be revealed by Fourier transform performed inside of an appropriately chosen time window after filtering from the total time-resolved reflectivity signal of the time-varying contribution of thermo-reflectance caused by sample heating [32,33]. This signal processing leads to the TDBS signal which is due to the interaction of the probe light with photo-generated acoustic pulse only (Fig. IV. 4b). The plots in the insert of Fig. IV. 4b as well as all other FFT plots calculated in this work were clearly dominated by a single strong peak related to the Brillouin frequency of the longitudinal sound wave. The $\pm 10\%$ deviations of the Brillouin frequencies from their average, revealed here (insert in Fig. IV. 4b), clearly indicate the presence of spatial elastic inhomogeneities in the ice sample due to polycrystallinity/texturing.

Performing Fourier transform in a continuously moving smoothed time-window of appropriately chosen duration and taking the frequency of the maximum in the spectra, it is possible to extract the temporal-profile of the dominant Brillouin frequency along the particular path of the coherent acoustic pulse propagation. Changing of the time-window size allows different degrees of averaging along the sound propagation direction. The resolution of such in-depth profiling of the spatially inhomogeneous media using TDBS is known to be limited either by the spatial length of the coherent acoustic pulse or by restrictions introduced by specific signal processing techniques [32,33]. In present experiments the duration of the emitted longitudinal acoustic pulse is controlled by the pump laser pulse duration of 1.9 ps and its width in ice near the opto-acoustic generator is about 30 nm at 84 GPa (see Appendix C). The observed abrupt changes in the amplitude and frequency of the Brillouin oscillations upon the arrival of the acoustic pulse on the ice/diamond interface (Fig. IV. 4a) indicate that, although this pulse could be broadened by bulk high-frequency absorption and scattering, the duration of the acoustic pulse does not exceed the Brillouin period of about 15 ps corresponding to

about 0.23 μm spatial scale at 84 GPa. In this Chapter signal analysis the windows which FWHM exceeds the Brillouin periods are used for the Fourier transforms. Thus, depth-profiling with the same in-depth spatial resolution (controlled by the duration of the moving Fourier transform window) throughout the whole sample thickness is achieved by the simplest signal processing technique. In-depth spatial resolution controlled by the acoustic pulse duration, achievable by advanced methods of signal processing [32,33], is beyond the scope of the present analysis. In Fig. IV. 4 (c) the temporal profile of the Brillouin frequency for the TDBS signal shown in Fig. IV. 4 (b) obtained with the moving rectangular time-window of 100 ps corresponding to the in-depth spatial resolution of about 1.5 μm are presented.

In the polycrystalline ice sample the photo-generated coherent acoustic pulse, which is initially launched normally to the Fe/ice interface and propagates parallel to the direction of the probe laser beam, could be refracted when crossing such plane interfaces between the grains, which are not parallel to the Fe/ice interface. Thus, in general, the coherent acoustic pulse propagates non-collinearly to the probe light. In this case the evaluation of the momentum-conservation triangle composed of the wave vectors of an acoustic phonon and of the incident and of the scattered probe light photons leads to the following solution for the Brillouin frequency f_B [32,43].

$$f_B \cong 2n\nu\cos\theta/\lambda_0. \quad (\text{IV.1})$$

Here ν denotes the speed of the acoustic wave along particular direction of its propagation in elastically anisotropic media, λ_0 is the wavelength of the probe light in vacuum, n is the optical refractive index of the media for the probe light and θ is the angle between the propagation directions of the probe light and the sound. In general, three factors in equation (IV. 1), i.e., θ , n and ν , could be responsible for different values of the Brillouin frequency, when the coherent acoustic pulse travels along its propagation path. It was estimated theoretically and confirmed by additional experiments that variations of the refractive index are playing negligible role in comparison with those of sound velocity (see Section IV.4) In Section IV.5 it will be demonstrated theoretically that variations caused by the acoustic beam refractions could be also neglected in the first approximation. Thus, in the following it can be assumed that the experimentally revealed variations in the Brillouin frequency are due to the variations of the sound velocity only, i.e., that they are dominantly caused by the different orientations of elastically anisotropic grains or groups of grains in the polycrystalline ice aggregate. As an example, assuming in equation (IV.1) $\theta = 0$ and taking the refractive index of the ice from the

literature [39] it is straightforward to obtain from the dependence in Fig. 2(c) the dependence of the acoustic velocity in ice first on time and then on the in-depth coordinate (Fig. IV. 4 (d)).

Experimentally observed spatial inhomogeneity of the polycrystalline aggregates of ice X (Fig. IV. 4 (d)) can be deeper characterized in two-dimensional imaging experiments, performing such TDBS measurements in several consecutive spatial positions along a lateral sample coordinate. In Fig. IV. 5, in order to reveal large scale inhomogeneities in the ice X aggregate, the Brillouin frequency distribution obtained with the in-depth spatial resolution of about 0.9 μm is presented. The resolution is determined by the half-width at half-maximum of the Hanning temporal window chosen for the Fourier transform.

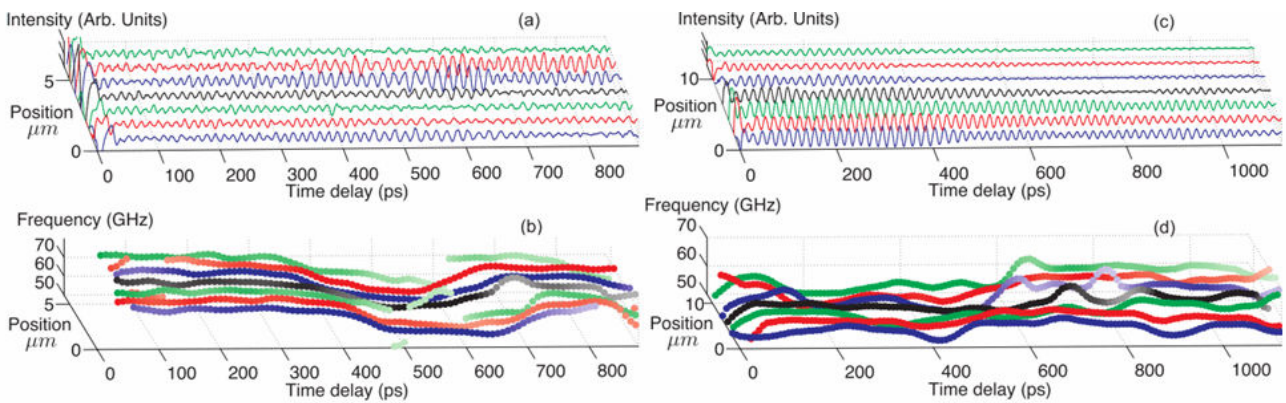


Figure IV. 5. Revealing μm -scale texture in polycrystalline H₂O ice aggregate at Megabar pressures via two dimensional imaging by time-domain Brillouin scattering technique with in-depth spatial resolution of $\sim 0.9 \mu\text{m}$. (a): TDBS signals in H₂O ice at 84 GPa, obtained by displacing the sample relative to the co-focused pump and probe laser beams in a lateral direction, i.e., parallel to the ice/diamond interface, by 1 μm steps. The spatial in-depth distance of 1 μm corresponds here to ~ 65 ps delay time. (b): Two-dimensional images of the Brillouin frequency magnitude obtained by processing the signals in (a). (c) TDBS signals in H₂O ice at 57 GPa, obtained by displacing the sample a in lateral direction by 2 μm steps. The spatial in-depth distance of 1 μm corresponds here to ~ 75 ps delay time. (d): Two-dimensional images of the Brillouin frequency magnitude obtained by processing the signals in (c). The isometric representation of the TDBS signals and of the temporal dependences allows better recognize their changes with position on the sample. In (b) and (c) the signal amplitude is correlated with the symbols color: the darker is the symbol - the higher is the maximum amplitude of the Brillouin signal, and vice-versa. Image (b) reveals a clear large-scale layering of the ice aggregate at 84 GPa in the direction normal to the diamonds surfaces. The thickness of the layers in this large-scale texture is around 3 – 5 μm . The image (d) of ice at 57 GPa reveals two regions, with much less pronounced than at 84 GPa in-depth layering, separated laterally. Visually the lateral separation in (d) takes place in the middle of the laterally scanned region. In addition, smaller scale inhomogeneities, with the thickness about 1 μm , controlled by the intentionally reduced spatial resolution, are observed at some depth positions at both pressures.

The panels (b) and (d) in Fig. IV. 5 represent the dominant frequency of the reflectivity signals as a function of time. The dominant frequency values at each time are obtained from a spectrogram analysis of the temporal signals with a Hanning weighted window of 133 ps (128 points at 0.9595 THz sampling frequency). For each central time of this sliding analysis window, every ~ 8 ps, the spectral component with the maximum amplitude is extracted. The frequency determination precision is improved by interpolating the spectrum with a spline function, which provides frequency steps of 0.2

GHz. The maximum amplitude is used for the color scale of the plotted symbols. Thus, the darker the symbol is, the larger is the maximum amplitude of the Brillouin signal, and vice-versa.

Fig. IV. 5b and 5d show the time-resolved profiles of the Brillouin frequency, which will be called hereafter “images”, obtained for the ice sample at 84 GPa and 57 GPa, respectively, by its displacing in a lateral direction.

The results presented in Fig. IV. 5 clearly demonstrate the ability of the TDBS technique to reveal texturing of transparent polycrystalline aggregates such as the ice sample under consideration here with the spatial scale better than 1 μm .

The estimated from independent XRD measurements characteristic dimension of the individual crystallites in the ice X aggregate at the considered pressures of 57 – 84 GPa is 0.45 μm . For this two-dimensional XRD patterns of the H₂O ice VII and ice X samples compressed in a DAC were collected using a monochromatic synchrotron radiation of the beam-line P2.02 (Petra III, HASYLAB, DESY) [60]. The patterns were collected from sample areas of about 15x15 μm^2 ; the sample thickness was also about 15 μm . The samples were rotated by about 4 degrees around the vertical axis in order to increase the number of grains in the Bragg diffraction condition. These measurement conditions led to a smooth, without any gaps, distribution of intensity along diffraction rings for all observed *hkl* reflexes, which suggests a relatively large number of randomly oriented crystallites covering the full solid angle 4π . In order to estimate the smallest number of grains leading to smooth diffraction rings, it was necessary to know the solid angle covered by a single grain under the present experimental conditions. To find it the divergence angle of the X-ray beam, focussed on the sample in a DAC by a compound reflective lenses (CRL) [61] was required. The angle was estimated to be about 0.32 mrad using the information available on the web-site of the synchrotron beam-line [62]: The CRL had an acceptance of 400 μm , and was located at the distance of 1.2 m from the sample. The effective divergence is, however, larger and approaches about 0.8 mrad due to the fact that the diffracted spot on the 2D detector, located at the distance of 500 mm from the sample, is similar to the detector pixel size of 0.2 mm. Combining the effective divergence with the angle of rotation around the vertical axis the solid angle covered by diffraction from a single grain was estimated to be $5.6 \cdot 10^{-5}$. Taking into account cubic symmetry of the crystal structure of ice VII and ice X the number of crystallites needed to cover the 4π solid angle by uniform XRD rings was estimated at about 37000. Accounting for the sample volume illuminated with the X-ray beam (s. above) the average size of crystallites in the samples at 57-84 GPa was estimated to be $\leq 0.45 \mu\text{m}$.

In order to check the sensitivity of the TDBS technique to in-depth inhomogeneities at sub-micrometer scale, the signals were processed in a moving temporal window of 17 ps duration, approximately corresponding to a single period of the Brillouin oscillation at 84 GPa. The expected

spatial resolution of about 0.26 μm is still controlled by the duration of the moving window. Results of the processing of the above shown TDBS signals (Fig. IV 5a) in the delay time interval from 100 ps to 400 ps are presented in Fig. IV. 6 where strong variations of the BS frequency (up to $\pm 10\%$) and, accordingly, of the longitudinal sound velocity by moving in-depth (corresponds to the delay-time axis) can be recognized. The characteristic spatial scale of these variations is 0.26-0.6 μm . Here a relatively large cross section of $\sim 10\ \mu\text{m}^2$ of the opto-acoustically tested volume and a small size of grains of $\sim 0.45\ \mu\text{m}$ should be borne in mind, implying that the recorded BS signal (at any delay time) is averaged in both lateral directions over about 50 individual grains. A large change of the BS frequency by moving in-depth to the next layer of grains (increase or decrease of the delay time by 20-30 ps) suggests a significant degree of crystallographic ordering in each of the layers but also a significant difference in the average crystallographic orientation of the adjacent ordered layers. This could be considered as a strong indication of the sample texturing parallel to the anvil culets and perpendicular to the direction of the sound pulse propagation. On the other hand, it is impossible to recognise any pattern by shifting of the sample in a lateral direction (Fig. IV. 4a) and 4b)) even though the used step of 1 μm implies a partial overlapping of the examined volumes of the adjacent depth profiles of the BS frequency. This observation excludes the above discussed possibility of the sample texturing parallel to the diamond anvils, at least on the scale of 1 μm , in the lateral directions. The only possible model which could be suggested at the moment is that the sample body contains small mesoscopic groups of oriented crystallites having the shape of discs or lenses. The depth/height of the oriented groups should be comparable with the size of one grain (0.3-0.6 μm) and their lateral dimension/diameter should not significantly exceed 1 μm . That means that such a group contains between 4 and 10 ice crystallites with a preferential mutual ordering. Thus, the measurement with a small time-window of 17 ps could have revealed a some degree of texturing of the present ice sample compressed to 84 GPa at sub- μm scale. However, the size of the ordered/coherent regions is small and does not significantly extend in lateral directions over 1 μm . Note, that characteristic direction of texturing, parallel to the diamond culets, recognised at the large scale in Fig. IV. 5b) and 6c) and at the short scale in Fig. IV. 6, appears to be plausible considering the geometry of the sample and the uniaxial compression of the sample confined in the gasket.

It is worth noting here that the confirmation by the TDBS scattering technique of the sub- μm size of individual crystallites provides us the opportunity to make a general statement that the averaging in the present experiments is not caused just by the large number of crystallites scattering probe light in the tested volume but is also due to the strong diffraction of the light inside the scattered probe beam on its way to the detector. Actually, for the wavelength of the probe light of about 0.44 μm

in ice X at 84 GPa, a part of the probe laser beam scattered in a grain with the diameter not exceeding 0.45 μm will diffract at distances shorter than 0.6 μm .

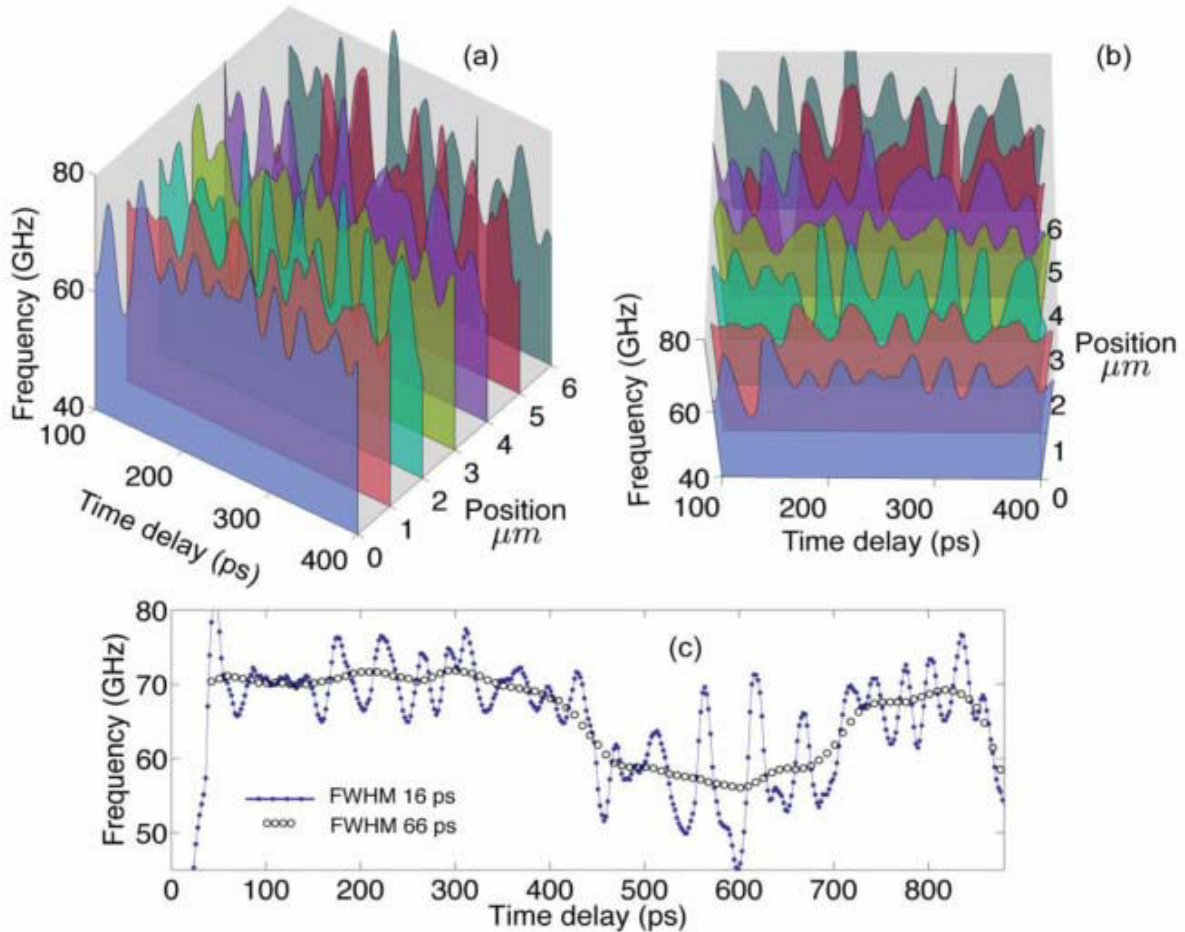


Fig. IV. 6. Revealing sub- μm -scale texture in polycrystalline H₂O ice aggregate at Megabar pressures via two-dimensional imaging by time-domain Brillouin scattering technique with in-depth spatial resolution of $\sim 0.26 \mu\text{m}$. (a) and (b): Two-dimensional depth profiles of the Brillouin frequency in H₂O ice at 84 GPa, obtained by displacing the sample relative to the pump and probe co-focused laser beams in a lateral direction, i.e., parallel to the ice/diamond interface. The profiles in the figure are measured in six particular positions of laser beams shifted with respect to each other in the same direction by 1 μm . The size of the moving time window for the Fourier transform is 17 ps, providing the in-depth spatial resolution of 0.26 μm . While the 3D representation in (a) makes clear the spatial order of the measurements, the view in (b) of the same profiles provides a better understanding of both in-depth and lateral structuring. The color code for the measured velocity profiles is the same in both images. The temporal images are presented starting at the 100 ps delay time in order to avoid the region of pulse propagation in the vicinity of the Fe photo-generator where the results are commonly less precise because of non-perfect elimination of the high-amplitude thermo-reflectance contribution from the time-resolved reflectivity data. (c): Superposition of the short-scale texturing revealed in Fig. IV. 6a),b) with the coarse scale texturing revealed in Fig. IV. 5b). The variations of the Brillouin frequency are extracted from the TDBS signal accumulated at 1 μm lateral coordinate in Fig. IV. 5b) and 4a),b). The maximum changes of the Brillouin frequency relative to the average level are about 20%.

The diffraction length was estimated by the ratio of the surface area of the scatterer to the probe laser wavelength in the compressed sample. Consequently, the corrugations of the probe wave front caused by its scattering at the corrugated front of the coherent acoustic pulse propagating simultaneously in multiple crystallites is effectively smoothed by the diffraction at sub- μm scale. Thus,

the detected signal provides information of the phase variation of the smoothed front of the scattered probe light and, consequently, on diffraction-averaged Brillouin frequency.

§IV.4. On the role of the induced optical anisotropy

In optically anisotropic grains the light experiences double or triple refraction and the optical rays, characterized by different refractive indexes, propagate after refraction with different velocities, which in addition depend on the direction of rays propagation relative to crystallographic axes [48,49]. However the ice phases VII and X examined here are cubic and, thus, optically isotropic.

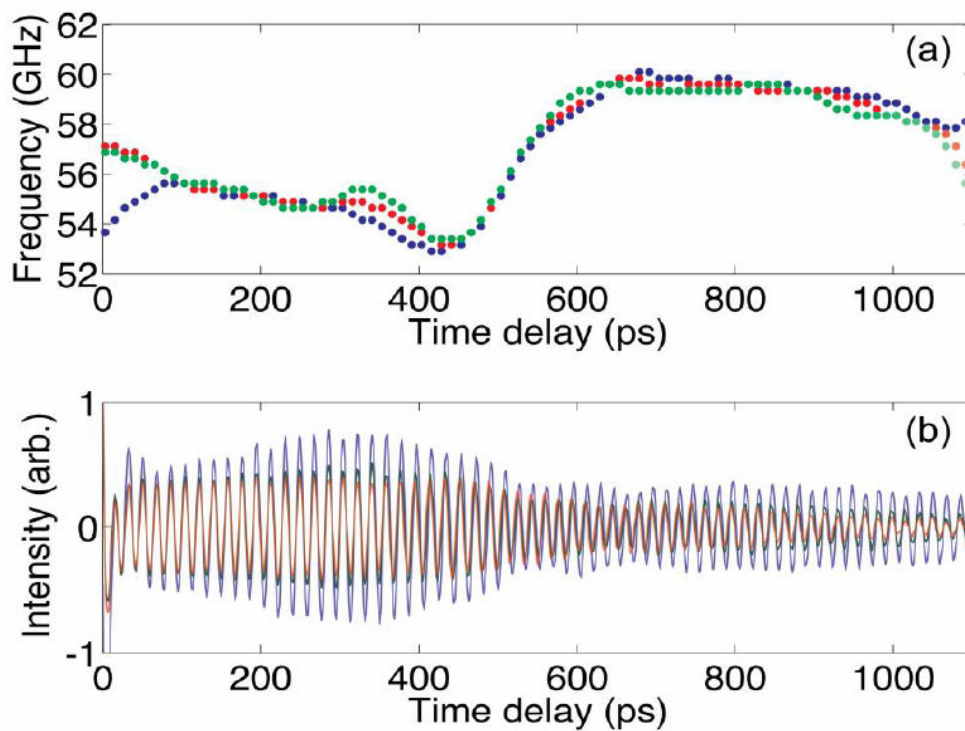


Fig. IV. 7. Revealing optical anisotropy of the cubic polycrystalline ice aggregate in diamond anvil cell induced by non-hydrostatic loading. (a): Variations of the Brillouin frequency with time delay extracted from TDBS signals presented in (b) which were detected at 50 GPa for the probe light pulses of three different linear polarizations rotated in steps of 60°. Differences in the curves in (a) indicate that polarization-dependent effects are present in the experimental system. However, there could be several physical phenomena contributing to the variation of the Brillouin frequency with the polarization of probe light in (a) (see Appendix D). In particular, stress-induced optical anisotropy of both ice aggregate and of the diamond anvil could be potentially involved. Although currently it is impossible to identify unambiguously the physical reasons of the polarization-dependent effect visible in (a), this experimental test clearly indicates the weakness of the effect since the relative changes of Brillouin frequency do not exceed 2%. Thus possible variations of the refractive index of ice due to induced optical anisotropy cannot be responsible for the 20% variations in the Brillouin frequency revealed in Figs IV. 4 and 6 and could be neglected when using equation (IV.1) for the estimates of the acoustic velocity.

Consequently, variations of the refractive index n could be caused in the samples under the examination only by anisotropy induced by nonhydrostatic stress component, i.e., due to uniaxial loading [50]. The order of magnitude estimates (see Appendix D) demonstrate that induced optical

anisotropy could cause variations of the refractive index of $\Delta n / \langle n \rangle \propto 5 \cdot 10^{-4}$, which are largely negligible in the present experiments. Here chevrons $\langle \dots \rangle$ denote average values. However, in view of the complexity of the phenomena of stress-induced anisotropy and lack of data on the photo-elastic tensors of the H₂O ices VII and X, additional test experiments with variable linear polarisation of the probe beam were conducted.

The results presented in (Fig. IV. 7) confirm that optical anisotropy is indeed induced in the system but it is weak and, thus, the variations of the refractive index in equation (IV.1) could be neglected.

§IV.5. On the role of the acoustic refraction and diffraction

The maximal expected deviations in the direction of the coherent acoustic pulse propagation are estimated in the frame of the acoustic rays theory in Appendix E. These estimates predict that the dominant cause of the relative variations of the Brillouin frequency $|\Delta f_B| / \langle f_B \rangle$ in the reported experiments are the sound velocity variations $|\Delta v| / \langle v \rangle \propto |\Delta f_B| / \langle f_B \rangle \leq 0,2$, while the dependence on $\cos \theta$ in equation (IV. 1) can be neglected in the first approximation $\Delta(\cos \theta) / \langle \cos \theta \rangle \leq 0.04$.

Importantly, there is also an additional and more important factor, specific to microcrystalline samples, which could significantly diminish the maximum effective angles that should be used in the estimates based on equation (IV. 1). In fact, when the acoustic pulse crosses a layer of differently oriented crystallites, distributed laterally, the phase front of the acoustic pulse has a tendency to corrugation, because of the difference in the magnitudes and the directions of the sound velocity in different crystallites. However, this tendency is strongly suppressed by the diffraction phenomena smoothing the amplitude and phase differences between the different parts of the acoustic beam. The shortest 30 nm length of the acoustic pulse, realized in the experiments in the vicinity of the Fe opto-acoustic generator (see Appendix C), corresponds to the characteristic acoustic wavelength of 0.2 μm (in ice X at 84 GPa). Consequently the lateral corrugations of the acoustic pulse, which could accumulate in its refraction inside the crystallites with the dimensions below 0.45 μm , are continuously washed out by the diffraction at distances below 1.2 μm . Thus, while the diffraction of the total acoustic beam plays negligible role in the reported experiments, the diffraction inside the acoustic beam supports the propagation of all parts of the beam quasi-collinear to the DAC axis.

§IV.6. On the amplitude of the TDBS signal

The discussion presented in Appendix F indicates that non-monotonous variations of the TDBS signal amplitude in time in the conducted experiments (see Figs. IV 3 (c) and 5 (a) and (c), for example) is not the manifestation of beatings/interference among different frequency components of the signal but is rather the second, in addition to Brillouin frequency variation in time, direct manifestation of disorientation of grains or groups of grains in the examined polycrystalline H₂O ice aggregates.

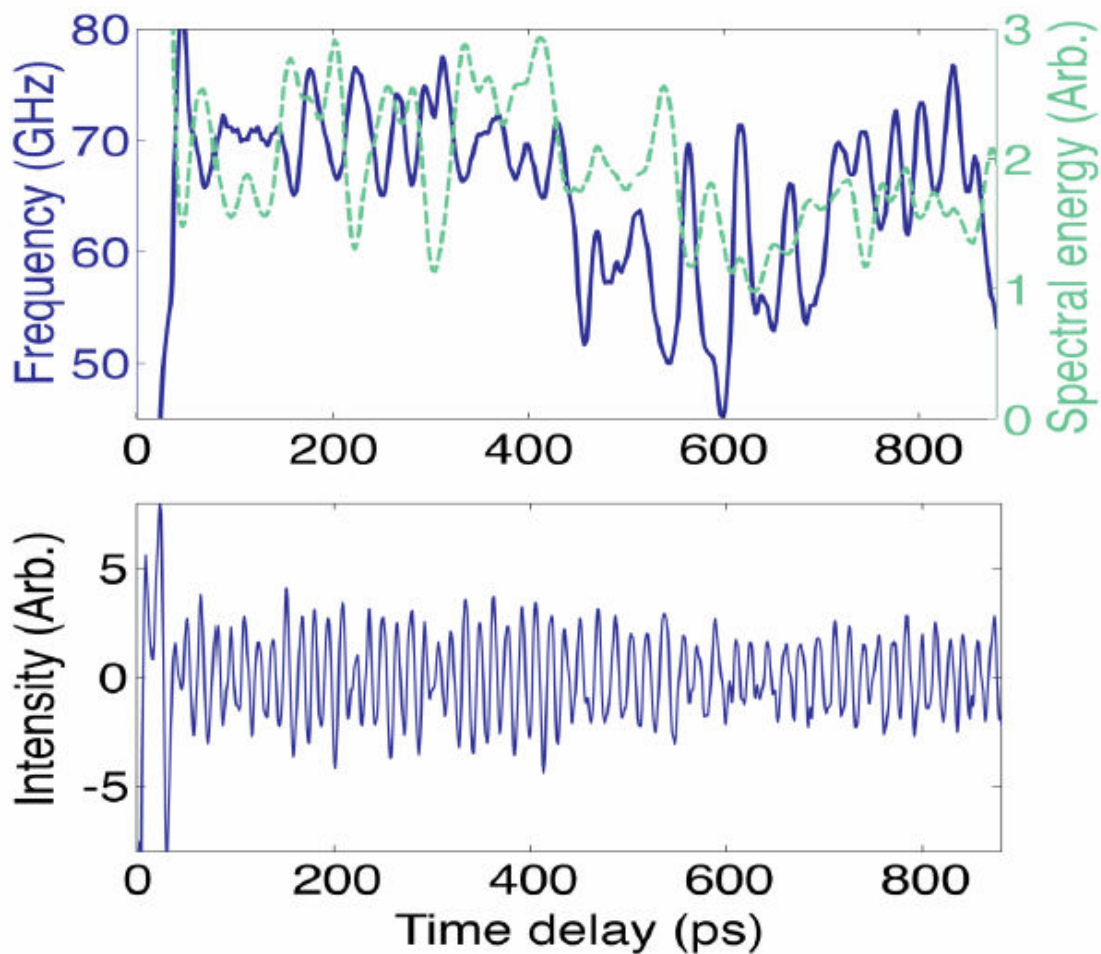


Figure IV. 8. Correlation in temporal dynamics of the amplitude and frequency of the TDBS signal in ice X at 84 GPa accompanying the in-depth variations in orientations of crystallites or their groups. (a): Simultaneous presentation, for comparison, of the temporal dynamics of the amplitude (green dashed line) and of the frequency (blue solid line), determined for a Brillouin oscillation signal measured in a particular point of the sample at 84 GPa and shown in (b). The results presented in (a) definitely demonstrate the expected correlation between the variations of the frequency and the amplitude at short sub- μm spatial scale, confirming that the physical origin of both is in the orientational texture of the ice sample. Note that variations of frequency and amplitude are mostly in anti-phase. The correlations between the frequency and the amplitude at larger, i.e., μm , spatial scale are obscured by the influence on the TDBS signal amplitude of absorption/scattering of both the coherent acoustic pulse and the probe light.

Actually, cubic crystallites of ice being optically isotropic are anisotropic photo-elastically (acousto-optically) [49,51]. The magnitude of the effective photo-elastic constant, which couples collinearly propagating sound and light, depends on the direction of their propagation inside individual crystallites. Then the amplitude of the TDBS oscillation is expected to be different in the crystallites differently oriented relative to the sample normal. Fig. IV. 8 compares the measured variations of the amplitude and frequency, revealing their in-coherence dynamics at sub- μm spatial scale: the variations of the amplitude and the frequency are mostly taking place in anti-phase. These experimental observations strongly indicate that the physical origin of both is in the orientational texture of the crystallites in the sample.

Since the amplitude A of the Brillouin oscillation is directly proportional to the effective photoelastic constant and inverse proportional to the square root of the acoustic velocity, ($A \propto pn^{-1}(\nu\rho)^{-1/2}$, where p and ρ denote the photo-elastic constant and density, respectively) [32,52], it could be expected that the photo-elastic anisotropy provides the dominant contribution in comparison with elastic anisotropy to the non-monotonous variations of the amplitude of the Brillouin oscillations in polycrystalline aggregates. The conducted estimates, using the data in Fig. IV. 8 demonstrate that the magnitude of the amplitude variations significantly exceeds what could have been expected due to the variations of the acoustic velocity only, i.e., $\Delta A/\langle A \rangle \propto -1/2(\Delta\nu/\langle \nu \rangle) \propto -1/2(\Delta f_B/\langle f_B \rangle)$. This indicates an important role of acousto-optic (photo-elastic) anisotropy.

§IV.7. Measurements of sound velocities

The TDBS technique was also used to measure the longitudinal acoustic velocities in H₂O ice up to 84 GPa. In (Fig. IV. 9) typical time resolved reflectivity signals in ice compressed in a DAC to 84 GPa (a) and to 57 GPa (c) are presented together with the corresponding temporal profiles of the Brillouin frequency in (b) and (d). It can be seen from this figure that TDBS technique allows to determine the time of the acoustic pulse propagation between Fe/ice and ice/diamond interfaces (see Fig. IV. 3b)) at each pressure (marked by END in Fig. IV. 9) and minimal (maximal) longitudinal wave velocity in H₂O ice at each pressure for a particular propagation path (which can be extracted from the values of Brillouin frequencies marked by MIN and MAX in Fig. IV. 9). Knowing this, the average, minimum and maximum longitudinal wave velocity of H₂O up to 84 GPa were determined.

To find the average longitudinal wave velocity, optical interferometry was applied (see Chapter III) to determine the product Hn of the ice layer thickness between Fe/ice and ice/diamond interfaces

H (see Fig. IV. 3b)) and the optical refractive index n of H₂O ice at the probe beam wavelength. Then using the values of n extrapolated from the published data [39] H was estimated. The propagation times of the acoustic pulse between Fe/ice and ice/diamond interface were measured at each pressure in three different positions of the sample via determination of the time moment when the abrupt change in the Brillouin oscillation amplitude takes place (see Fig. IV. 9 and also Fig. I. 6 for comparison), three averaged velocities were estimated and their average value was found (see Fig. IV. 10).

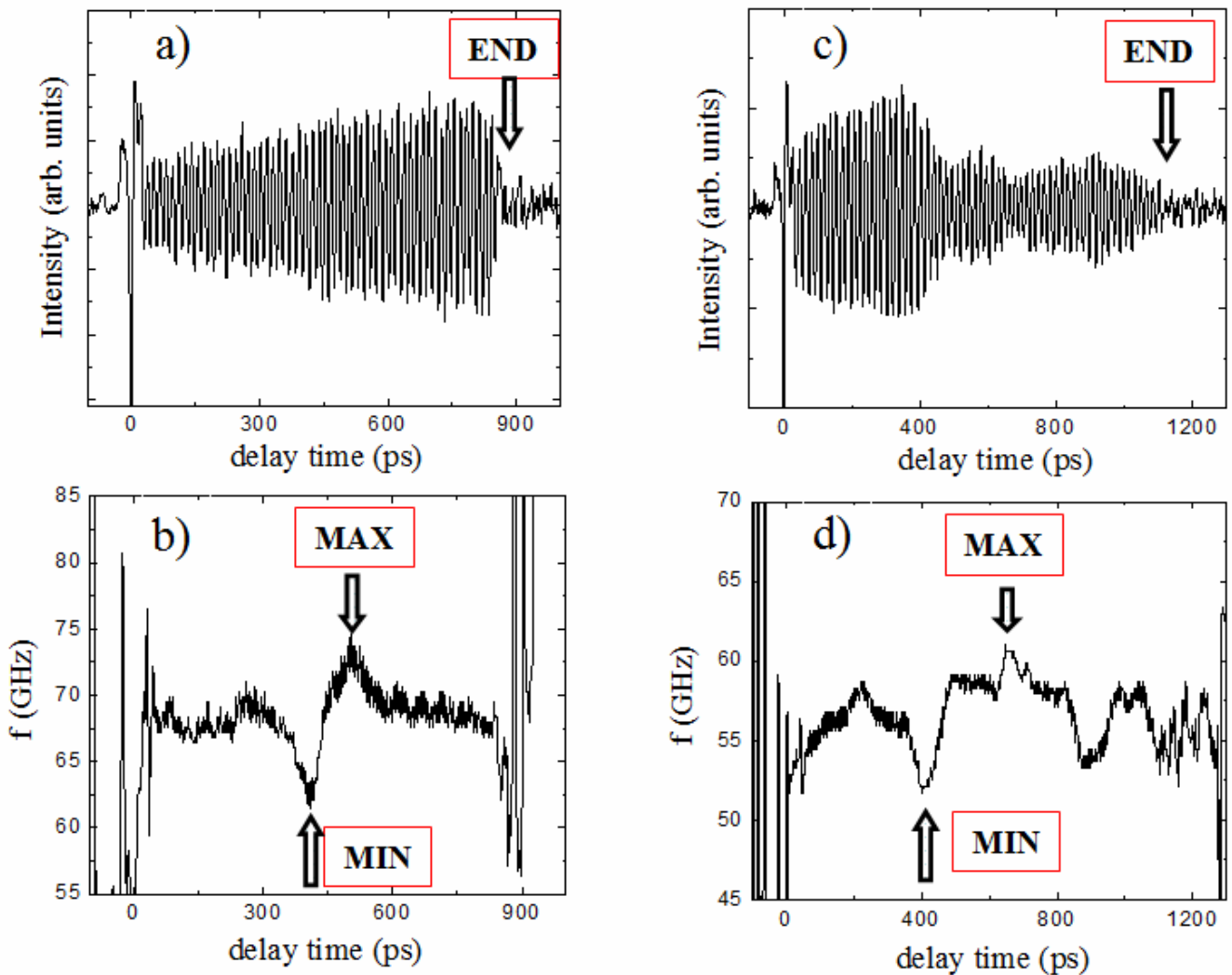


Fig. IV. 9. Typical time resolved reflectivity signal in ice compressed in a DAC to 84 GPa (a) and to 57 GPa (c). (b) and (d): Temporal profiles of the Brillouin frequency of the TDBS signals shown in (a) and (c). Fourier transform was performed in the rectangular moving temporal window of 40 ps duration.

For example, estimated averaged sound velocities at 84 GPa and 57 GPa are 15500 m/s and 13500 m/s, respectively, are in a very good agreement with the values of the aggregate sound velocities of ice measured by classic BS [35,36].

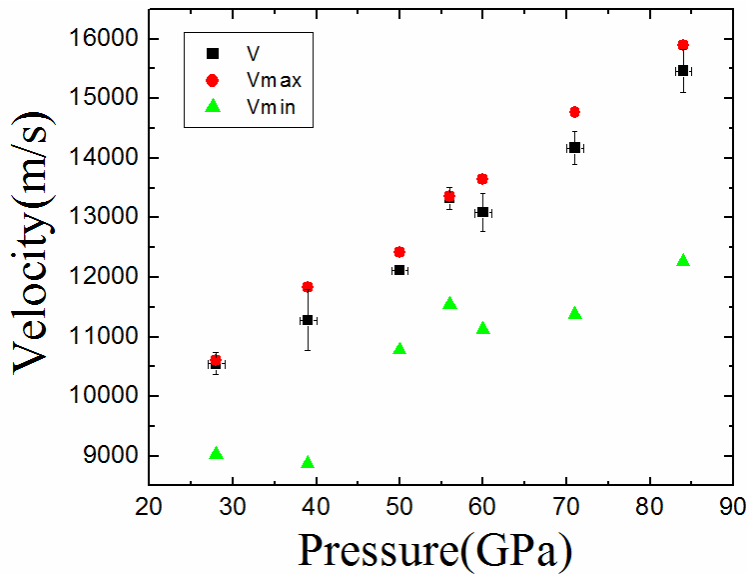


Figure IV. 10. The average, minimum and maximum longitudinal wave velocity of H₂O up to 84 GPa. The average longitudinal wave velocity V was found due to the measurements of the thickness of the sample H and the propagation times of the acoustic pulse through H₂O at all pressures (see Chapter III and Fig. IV. 9.). The minimum (maximum) value of the Brillouin frequency from the data detected in three different points of the samples was used to determine the minimal (maximal) longitudinal wave velocity, using n extrapolated from [39].

The so-called envelop method [38] was also applied to find C_{11} modulus in the experimental samples. For this the minimum value of the Brillouin frequency from the data detected in three different points of the samples was found, and the minimal longitudinal wave velocity was determined, using n extrapolated from [39]. The minimal velocity in cubic crystallites is along the [100] direction and depends only on C_{11} and the density of ice. Taking the values of densities reported in [45] it found found that $C_{11} = 480$ GPa at 84 GPa and $C_{11} = 350$ GPa at 57 GPa in a reasonable agreement with the values of 540 GPa and 350 GPa, respectively, extracted by classical BS [36].

§IV.8. Discussion and conclusions

In this work a high in-depth resolution of about $0.26 \mu\text{m}$ in H₂O ice samples compressed in a DAC to 57 and 84 GPa was obtained. This value is significantly below the estimated average crystallite size in these samples. Apparently, this result can be achieved for any other transparent material compressed in a DAC to similar or higher pressures. No other technique can provide today such a detailed visualisation of a polycrystalline aggregate microstructure of a chemically homogeneous material compressed in a DAC, especially along the axial direction. Even the simplest signal processing, applied in the present work for processing of the TDBS signals, provides access to characterization both of the in-depth dimensions of the micro-crystallites and of the texturing of the polycrystalline ice aggregates at different spatial scales from $0.26 \mu\text{m}$, controlled by signal processing, up to about $10 \mu\text{m}$, controlled by the total thickness of the ice layer.

From the experimental geometry used in the present work follows that even when the shortest moving time-window for the Fourier transform of 17 ps is used, the collected TDBS signal and the derived frequency/sound velocity is an average over about 50 grains. This is because the grain size was estimated to be about 0.45 μm , the lateral surface area tested by overlapping probe laser beam and coherent acoustic beam is about 10 μm^2 and the wavelength of the probe laser light when propagating in ice at Mbar pressures is approximately 0.44 μm . Thus, it is difficult to access in the present sample and experiment geometry, at any position in the sample, the extreme sound velocity values, corresponding to the specific directions in a single crystal of ice X. The highest sound velocity observed in the present work by scanning through the sample will be lower than the maximal possible sound velocity in a single crystal ice X (along the $\langle 111 \rangle$ direction of a cubic crystal). Similarly, the lowest sound velocity detected here represents the upper bound for the lowest possible sound velocity in a single crystal ice X (along the $\langle 100 \rangle$ direction of a cubic crystal). One of the ways to approach the limiting sound velocity values would be to use coarse powder or single crystals as starting samples. The grains could break on pressure increase due to non-hydrostatic loading or after phase transitions but the fragments could still remain big enough to deliver to the detector the TDBS signals corresponding to individual grains. In the particular case of water, single crystals of ice VI and VII can be easily obtained by a slow compression at about 1 GPa when crossing the melting curve [35,53]. Another way involves a significant improvement of the lateral resolution of the experimental set-up below 0.45 μm by application of advanced focusing methods. Combined with the already available high in-depth resolution, the improved lateral resolution would make possible determination of the limit values of sound velocities as well as a 3D-visualization of transparent polycrystalline aggregate microstructure (from grain to grain) at Megabar pressures.

The time-domain BS technique could have other, in addition to improved spatial resolution, advantages in comparison with the classic frequency-domain BS technique. The applicability of classic BS is importantly reduced and even could be impossible in the case when the Brillouin spectral lines of the sample overlap with the Brillouin lines from the diamond anvils or from the pressure transmitting medium [24,54], which are inevitably simultaneously detected for samples compressed in a DAC. This problem does not exist for the time-domain BS technique because the scattering of light by coherent acoustic phonons takes place in the sample only, well before the photo-generated acoustic pulse reaches the sample/diamond or sample/pressure-medium interface. Moreover, the TDBS allows a direct comparison of sound velocities and/or elastic moduli of two and more different sample materials placed simultaneously in the high-pressure volume of a DAC.

Conclusions

In conclusion, in this Chapter the laser ultrasonic measurements in a diamond anvil cell were presented. The developed here TDBS – based imaging technique provides for each crystallite (or a group of crystallites) in chemically homogeneous transparent aggregate usable information on its orientation (if the material is elastically anisotropic) as well as on the value of the elastic modulus along the direction of the sound propagation. This extends the basis for a successful application of highly developed micromechanical models of solids deformation at Mbar pressure. On long term, such experiments extended to Earth's minerals and high or low temperatures would insure a significant progress in understanding of convection of the Earth's mantle and thus evolution of this and other planets.

The achieved two-dimensional imaging of the polycrystalline aggregate in-depth and in one of the lateral directions indicates the feasibility of three-dimensional imaging of transparent samples compressed in a DAC with previously not accessible resolution of tens of nanometers in-depth. The lateral spatial resolution is controlled by the pump and the probe laser pulses focusing. In perspective, an improved signal processing of such TDBS data should provide opportunity to follow evolution of several Brillouin frequencies in time domain, revealing simultaneous propagation of the coherent acoustic pulse across several mutually disoriented crystallites. In the future, TDBS experiments, conducted both with longitudinal and shear [55-57] coherent acoustic pulses at several different angles of probe light incidence [32,46,47] could give access to the determination of the spatial positions, dimensions and orientation, i.e., morphological and orientational texture, of the optical refractive index and of all elastic moduli of the individual grains inside polycrystalline transparent aggregates compressed to Megabar pressures.

References (IV)

1. Ahrens, T. J. (ed.) *A Handbook of Physical Constants – AGU Reference, Shelves 1-3* (American Geophysical Union, Washington DC, 1995).
2. Stacey, F. D. *Physics of the Earth* (Brookfield Press, Brisbane, 1992).
3. Dutel, G. D., Langlois, P., Tingaud, D. & Dirras, G. *Room-temperature deformation micro-mechanisms of polycrystalline nickel processed by spark plasma sintering.* **Materials Characterization** **79**, 76-83 (2013).
4. Hirsekor, S. *The scattering of ultrasonic waves by polycrystals.* **J. Acoust. Soc. Am.** **72**, 1921 (1982).
5. Sayers, C. M. *Ultrasonic velocities in anisotropic polycrystalline aggregates.* **J. Phys. D: Appl. Phys.** **18**, 2157 (1982).
6. Andrews, J. C., Meirer, F., Liu, Y., Mester, Z. & Pianetta, A. *Transmission X-ray microscopy for full-field nano imaging of biomaterials.* **Microsc. Res. Tech.** **74**, 671–681 (2011).
7. Ice, G. E. et al. *At the limit of polychromatic microdiffraction.* **Mater. Sci. Eng. A** **524**, 3–9 (2009).
8. Larson, B. C., Yang, W., Ice, G. E., Budai, J. D. & Tischler, J. Z. *Three-dimensional X-ray structural microscopy with submicrometre resolution.* **Nature** **415**, 887-890 (2002).
9. Jiang, H. et al. *Three-dimensional coherent X-ray diffraction imaging of molten iron in mantle olivine at nanoscale resolution.* **Phys. Rev. Lett.** **110**, 205501 (2013).
10. Shi, C. Y. et al. *Formation of an interconnected network of iron melt at Earth's lower mantle conditions.* **Nat. Geosci.** **6**, 971-975 (2013).
11. Nisr, C. et al. *High resolution three-dimensional X-ray diffraction study of dislocations in grains of MgGeO₃ post-perovskite at 90 GPa. .* **J. Geophys. Res.** **117**, B03201 (2012).
12. Nisr, C., Ribárik, G., Ungár, T., Vaughan, G. B. M. & Merkel, S. *Three-dimensional X-ray diffraction in the diamond anvil cell: application to stishovite.* **High Pressure Res.** **34**, 158–166 (2014).
13. Ice, G. E., Dera, P., Liu, W. & Mao, H.-K. *Adapting polychromatic X-ray microdiffraction techniques to high-pressure research: energy scan approach.* **J. Synchrot. Radiat.** **12**, 608–617 (2005).
14. Ding, Y. et al. *Nanoscale diffraction imaging of the high-pressure transition in Fe_{1-x}O.* **Appl. Phys. Lett.** **100**, 041903 (2012).
15. Lin, Y., Zeng, Q., Yang, W. & Mao, W. L. *Pressure-induced densification in GeO₂ glass: A transmission x-ray microscopy study.* **Appl. Phys. Lett.** **103**, 261909 (2013).
16. Yang, W. et al. *Coherent diffraction imaging of nanoscale strain evolution in a single crystal under high pressure.* **Nat. Commun.** **4**, 1680 (2013).
17. Polian, A. in *Frontiers of High-Pressure Research* (eds. Hochheimer, H. D. & Etters, R. D.) (Plenum Press, New York, 1991).
18. Polian, A. *Brillouin scattering at high pressure: an overview.* **J. Raman Spectrosc.** **34**, 633 (2003).
19. Sinogelkin, S. et al. *A Brillouin spectrometer interfaced with synchrotron X-radiation for simultaneous x-ray density and acoustic velocity measurements.* **Rev. Sci. Instrum.** **77**, 103905 (2006).
20. Gusev, V. & Karabutov, A. *Laser Optoacoustics* (AIP, New York, 1993).
21. Scruby, C. B. & Drain, L. E. *Laser Ultrasonics Technique & Applications* (Taylor and Francis Group, New York, 1990).
22. Nelson, K. A., Miller, R. J. D., Lutz, D. R. & Fayer, M. D. *Optical generation of tunable ultrasonic waves.* **J. Appl. Phys.** **53**, 1144 (1982).
23. Abrahamson, E. H., Slutsky, L. J. & Brown, J. M. *Elastic constants, interaction forces, and equation of state of β -oxygen at high pressure.* **J. Chem. Phys.** **100**, 4518 (1994).
24. Baer, B. J., Brown, J. M., Zaug, J. M., Schiferl, D. & Chronister, E. L. *Impulsive stimulated scattering in ice VI and ice VII.* **J. Chem. Phys.** **108**, 4540 (1998).
25. Crowhurst, J. C. et al. *Surface acoustic waves in the diamond anvil cell: an application of impulsive stimulated light scattering.* **Phys. Rev. B** **64**, 100103 (2001).
26. Crowhurst, J. C., Goncharov, A. F. & Zaug, J. M. *Impulsive stimulated light scattering from opaque materials at high pressure.* **J. Phys.: Condens. Matter** **16**, S1137 (2004).
27. Thomsen, C., Grahn, H. T., Maris, H. J. & Tauc, J. *Surface generation and detection of phonons by picosecond light pulses.* **Phys. Rev. B** **34**, 4129 (1986).

28. Decremps, F., Belliard, L., Perrin, B. & Gauthier, M. *Sound velocity and absorption measurements under high pressure using picosecond ultrasonics in a diamond anvil cell : application to the stability study of AlPdMn.* **Phys. Rev. Lett.** **100**, 035502 (2008).
29. Chigarev, N. et al. *Laser generation and detection of longitudinal and shear acoustic waves in a diamond anvil cell.* **Appl. Phys. Lett.** **93**, 181905 (2008).
30. Armstrong, M. R., Crowhurst, J. C., Reed, E. J. & Zaug, J. M. *Ultrafast high strain rate acoustic wave measurements at high static pressure in a diamond anvil cell.* **Appl. Phys. Lett.** **92**, 101930 (2008).
31. Grahn, H. T., Maris, H. J. & Tauc, J. *Picosecond ultrasonics.* **IEEE J. Quantum Electron.** **25**, 2562 (1989).
32. Lomonosov, A. M. et al. *Noncontact subsurface investigations of mechanical and optical properties of nanoporous low-k material thin film.* **ACS Nano** **6**, 1410 (2012).
33. Mechri, C. et al. *Depth-profiling of elastic inhomogeneities in transparent nanoporous low-k materials by picosecond ultrasonic interferometry.* **Appl. Phys. Lett.** **95**, 091907 (2009).
34. Polian, A. & Grimsditch, M. *Brillouin scattering from H₂O: Liquid, ice VI, and ice VII.* **Phys. Rev. B** **27**, 6409 (1983).
35. Shimizu, H., Ohnishi, M., Sasaki, S. & Ishibashi, Y. *Relation in dense H₂O ice VII.* **Phys. Rev. Lett.** **74**, 2820 (1995).
36. Ahart, M. et al. *Brillouin scattering of H₂O ice to megabar pressures.* **J. Chem. Phys.** **134**, 124517 (2011).
37. Polian, A. & Grimsditch, M. *New high-pressure phase of H₂O: ice X.* **Phys. Rev. Lett.** **52**, 1312 (1984).
38. Zha, C.-S., Mao, H.-K., Hemley, R. J. & Duffy, T. S. *Recent progress in high-pressure Brillouin scattering: olivine and ice.* **Rev. High Pressure Sci. Technol.** **7**, 739 (1998).
39. Zha, C.-S., Hemley, R. J., Gramsch, S. A., Mao, H.-K. & Bassett, W. A. *Optical study of H₂O ice to 120 GPa: dielectric function, molecular polarizability, and equation of state.* **J. Chem. Phys.** **126**, 074506 (2007).
40. Ko, J.-H., Kim, T. H., Roleder, K., Rytz, D. & Kojima, S. *Precursor dynamics in the ferroelectric phase transition of barium titanate single crystals studied by Brillouin light scattering.* **Phys. Rev. B** **84**, 094123 (2011).
41. Koski, K. J. & Yarger, J. L. *Brillouin imaging.* **Appl. Phys. Lett.** **87**, 061903 (2005).
42. Scarcelli, G. & Yun, S. H. *Confocal Brillouin microscopy for three-dimensional mechanical imaging.* **Nat. Photonics** **2**, 39-43 (2008).
43. Cote, R. & Devos, A. *Refractive index, sound velocity and thickness of thin transparent films from multiple angles picosecond ultrasonics.* **Rev. Sci. Instrum.** **76**, 053906 (2005).
44. Loubeyre, P., LeToullec, R., Wolanin, E., Hanfand, M. & Hausermann, D. *Modulated phases and proton centering in ice observed by X-ray diffraction up to 170 GPa.* **Nature** **397**, 503-506 (1999).
45. Sugimura, E. et al. *Compression of H₂O ice to 126 GPa and implications for hydrogen-bond symmetrization: Synchrotron x-ray diffraction measurements and density-functional calculations.* **Phys. Rev. B** **77**, 214103 (2008).
46. Devos, A., Cote, R., Caruyer, G. & Lefèvre, A. *A different way of performing picosecond ultrasonic measurements in thin transparent films based on laser wavelength effects.* **Appl. Phys. Rev.** **86**, 211903 (2003).
47. Mechri, C., Ruello, P. & Gusev, V. *Confined coherent acoustic modes in a tubular nanoporous alumina film probed by picosecond acoustics methods.* **New J. Phys.** **14**, 023048 (2012).
48. Born, M. & Wolf, E. *Principles of Optics* (Pergamon Press, London, 1970).
49. Ramachandran, G. N. & Ramaseshan, S. in *Encyclopedia of Physics* (ed. Flugge, S.) 1-217 (Springer, Berlin, 1961).
50. Singh, A. K. *The lattice strains in a specimen (cubic system) compressed nonhydrostatically in an opposed anvil device.* **J. Appl. Phys.** **73**, 4278 (1993).
51. Xu, J. & Stroud, R. *Acousto-Optic Devices: Principles, Design, and Applications* (Wiley, New York, 1992).
52. Gusev, V., Lomonosov, A. M., Ruello, P., Ayouch, A. & Vaudel, G. *Depth-profiling of elastic and optical inhomogeneities in transparent materials by picosecond ultrasonic interferometry: Theory.* **J. Appl. Phys.** **110**, 124908 (2011).
53. Haselton, H. T. j., Chou, I.-M., Shen, A. H. & Bassett, W. A. *Techniques for determining pressure in the hydrothermal diamond-anvil cell: Behavior and identification of ice polymorphs (I, III, V, VI).* **Am. Miner.** **80**, 1302-1306 (1995).
54. Jiang, F., Speziale, S. & Duffy, T. S. *Single-crystal elasticity of brucite, Mg(OH)₂, to 15 GPa by Brillouin scattering.* **Am. Miner.** **91**, 1893-1900 (2006).

55. Hurley, D., Wright, O. B., Matsuda, O., Gusev, V. E. & Kolosov, O. V. *Laser picosecond acoustics in isotropic and anisotropic materials.* **Ultrasonics** **38**, 470-474 (2000).
56. Pezeril, T. et al. *Laser acoustics with picosecond collimated shear strain beams in single crystals and polycrystalline materials.* **Phys. Rev. B** **73**, 132301 (2006).
57. Pezeril, T., Klieber, C., Andrieu, S. & Nelson, K. A. *Optical generation of gigahertz frequency shear acoustic waves in liquid glycerol.* **Phys. Rev. Lett.** **102**, 107402 (2009).
58. Boehler, R. *New diamond cell for single-crystal x-ray diffraction.* **Rev. Sci. Instrum.** **77**, 115103 (2006).
59. Mao, H.-K., Xu, J. & Bell, P. M. *Calibration of the ruby pressure gauge to 800 kbar under quasi-hydrostatic conditions.* **J. Geophys. Res.** **91**, 4673-4676 (1986).
60. Liermann, H.-P. et al. *The extreme conditions beamline at PETRA III, DESY: Possibilities to conduct time resolved monochromatic diffraction experiments in dynamic and laser heated DAC.* **J. Phys.: Conference Series** **215**, 012029 (2010).
61. Lengeler, B. et al. *Imaging by parabolic refractive lenses in the hard X-ray range.* **J. Synchrot. Radiat.** **6**, 1153-1167 (1999).
62. Extreme Conditions Beamline (ECB) P02.2. URL: photon-science.desy.de/facilities/petra_iii/beamlines/p02_hard_x_ray_diffraction_beamline/ecb/index_eng.html (2014)

Conclusions and perspectives

The present PhD research work was devoted to the use of laser ultrasound in high-pressure physics for investigation of elastic behaviour of matter at ultrahigh pressures. The research was conducted using the recently established technique of laser ultrasonic measurements in a diamond anvil cell which allows investigation of the sound propagation and determination of the acoustic wave velocities at ultrahigh pressures.

Conclusions

In the theoretical part of this PhD thesis the analytical descriptions for the directivity patterns of ultrasound, emitted from the laser-irradiated interface between two isotropic solids, are presented. The derived solutions are valid for arbitrary combinations of transparent and opaque materials. The directivity patterns are derived by accounting for the specific features of the sound generation, appearing thanks to the thermo-elastic stresses distributed in the volume which are essential for laser ultrasonics. The analytical solutions for the profiles of longitudinal and shear acoustic pulses emitted in different directions are also evaluated. This analytical description has been already successfully applied in interpretation of some earlier existing experimental observations of laser ultrasound in diamond anvil cell.

In the experimental part of this PhD thesis, the picosecond laser ultrasonics measurements in a diamond anvil cell conducted for investigation of the sound propagation and determination of the acoustic wave velocities at ultrahigh pressures are presented. The technique of picosecond ultrasonic interferometry, also called time-domain Brillouin scattering, is applied to depth-profiling of polycrystalline aggregate of H₂O ice compressed in a diamond anvil cell to Megabar pressures. The characteristic dimensions of elastic inhomogeneities and texturing of polycrystalline ice in the direction, normal to the diamond anvil surfaces, are revealed with sub-micrometer spatial resolution via time-resolved measurements of variations in the propagation velocity of the acoustic pulse travelling in the compressed sample. The developed imaging technique provides for each crystallite (or a group of crystallites) in chemically homogeneous transparent aggregate, usable information on its orientation as well as on the value of the elastic modulus along the direction of the sound propagation. Also this technique was used to measure the acoustic velocities in H₂O ice up to 84 GPa.

A special part in the PhD thesis is devoted to the description of the experiments undertaken for determining the thickness and the refractive index of the ice in the diamond anvil cell under pressure. Both of these parameters can be necessary to determine the acoustic velocities via laser ultrasonic experiments in a diamond anvil cell. The measurements of the thickness and of the refractive index are based on broadband interference of light in diamond anvil cell. Two different ways of measuring the refractive index of ice are considered. Refractive index of ice is measured by both methods up to 31 GPa. The thickness, transverse size and the volume of ice as a function of pressure are obtained

Perspectives

The analytical descriptions for the directivity patterns of ultrasound inside a diamond anvil cell provide straight opportunity to predict the acoustic field which is formed in the diamond anvil cell at high pressures. The developed theory can be applied in the future for the dimensional scaling the LU-DAC experiments, optimization of these experiments (in terms of a choice of the optimal directions/positions for acoustic waves detection) and the interpretation of the experimental results. It is also possible that this theory can be used for determining phase transitions or creation of new substances under pressure inside the diamond anvil cell. In both these cases, the elastic properties of the material may change dramatically with increasing pressure. Then, the characteristic structures of the directivity patterns of laser ultrasound, related to the elastic properties of material, can also exhibit sudden changes with increasing pressure providing indication of phase transition or creation of new substance.

Laser ultrasonic technique, applied in the experimental part of this PhD research, can be extended to obtain three-dimensional images of acoustic inhomogeneities in transparent material inside a diamond anvil cell. So, this technique opens opportunities for the study of formation and evolution of texture in transparent microcrystalline aggregates on pressure change. This extends the basis for a successful application of highly developed micromechanical models of solids deformation at Mbar pressure. On long term, such experiments extended to Earth's minerals and high or low temperatures would insure a significant progress in understanding of convection of the Earth's mantle and thus evolution of this and other planets.

Appendices

Appendix A.

Directivity patterns of laser ultrasound emitted from the interface of two solids in the 3D case

The solution for the directivity pattern in the point-source configuration can be derived by an approach which is similar to the one shown in the main text for the 2D case. The spatial Fourier transform along the x -axis in 2D is replaced in the case of 3D and cylindrical symmetry by the Hankel (Fourier-Bessel) transform along the transverse radial coordinate r_{\perp} in the (x,y) plane. The only modification in the solutions for the acoustic potentials and the temperature field in the reciprocal spaces is the replacement of k_x by k_{\perp} , which is the projection of the wave-vectors on the (x,y) plane. Equation (II.13) is replaced by the inverse Hankel transform over k_{\perp} , which can be calculated by the method of steepest descent.^{1,2} This results in the following form of Eq. (II.14) in the 3D case

$$\begin{pmatrix} \tilde{\phi}_1(\omega, r, \theta) \\ \tilde{\psi}_1(\omega, r, \theta) \end{pmatrix} = \cos \theta \begin{pmatrix} k_{\parallel} \tilde{\phi}_1(\omega, k_{\parallel} \sin \theta) \\ k_{\parallel} \tilde{\psi}_1(\omega, k_{\parallel} \sin \theta) \end{pmatrix} \frac{i}{r} \begin{pmatrix} e^{-ik_{\parallel}r} \\ e^{-ik_{\parallel}r} \end{pmatrix}. \quad (\text{A1})$$

So just the multiplier, $\sqrt{ik_{\parallel}r}/(2\pi r)$, characteristic to 2D geometry, is replaced in 3D cylindrical geometry by $ik_{\parallel}r/r$. This provides correct diminishing of the acoustic wave amplitude with distance from the source, $\propto 1/r$, and modifies the profiles of the emitted acoustic pulses. The description of the normal strain in Eq. (II.28) is modified into

$$\tilde{\eta}(\omega, r, \theta) = -\frac{P_1 I}{2\nu_1^2} \frac{1}{r} |\Xi_{\phi}(\theta)| \omega \tilde{\Phi}(\omega \sin \theta / \nu_{\parallel}) \tilde{f}(\omega) e^{-ik_{\parallel}r + i\pi/2 + i\varphi_{\Xi}} \quad (\text{A2})$$

and the description of the shear strain in Eq. (II.29) is modified into

$$\tilde{\eta}_{r_{\perp}z}(\omega, r, \theta) = \frac{1}{2} \left(\frac{\partial \tilde{u}_{r_{\perp}}}{\partial z} + \frac{\partial \tilde{u}_z}{\partial r_{\perp}} \right) = -\frac{P_1 I}{2\nu_1^2} \frac{1}{r} |\Xi_{\psi}(\theta)| \cos(2\theta) \omega \tilde{\Phi}(\omega \sin \theta / \nu_{\parallel}) \tilde{f}(\omega) e^{-ik_{\parallel}r + i\pi/2 + i\varphi_{\Xi}}. \quad (\text{A3})$$

The dependence of both strain profiles on time can be factorized by the same integral:

$$\eta(\tau = t - r/\nu) = \frac{1}{2\pi} \int_{-\infty}^{+\infty} \omega \tilde{\Phi}(\omega \sin \theta / \nu) \tilde{f}(\omega) e^{i\omega\tau + i\pi/2 + i\varphi_{\Xi}} d\omega. \quad (\text{A4})$$

The integral in Eq. (A4), in case, where the description of laser radiation is given in Eq. (II.18), can be calculated analytically. It should not be forgotten, however, that, when integrating over negative frequencies, the integrand should be modified to provide finally real valued profile. The result of the integration is

$$\begin{aligned} \eta(\tau) &= \frac{\sqrt{\pi} d\tau_L}{\tau_a^2} \frac{\partial}{\partial \bar{\tau}} \left\{ e^{-\bar{\tau}^2} [\cos \varphi_{\Xi} + i \operatorname{erf}(i\bar{\tau}) \sin \varphi_{\Xi}] \right\} \equiv \frac{\sqrt{\pi} d\tau_L}{\tau_a^2} \frac{\partial}{\partial \bar{\tau}} \Psi(\bar{\tau}) \\ &= \frac{\sqrt{\pi} d\tau_L}{\tau_a^2} \left\{ -\frac{2}{\sqrt{\pi}} \sin \varphi_{\Xi} - 2\bar{\tau} e^{-\bar{\tau}^2} [\cos \varphi_{\Xi} - \operatorname{erfi}(\bar{\tau}) \sin \varphi_{\Xi}] \right\} \equiv \frac{\sqrt{\pi} d\tau_L}{\tau_a^2} \Theta(\bar{\tau}) \end{aligned} \quad (\text{A5})$$

where all the notations are the same as in the 2D case analyzed in Section 6 and erf is the error function (probability integral). The evaluated (with the use of Eq. (A5)) profiles of the compression/dilatation strain pulses in 3D geometry, relevant to the earlier reported experiments in point-source-point-receiver configuration^{3,4}, are presented in Fig. A. 1. The angle-dependent functions,

providing modulation of the directivity patterns of laser ultrasound, emitted by delta-localized sources and described by the amplitudes of the solutions in Eqs. (II.23) and (II.24), are presented for the 3D case in Fig. A. 2. They are evaluated for the same parameters of material and laser pulses as in the 2D case in Section II.5.

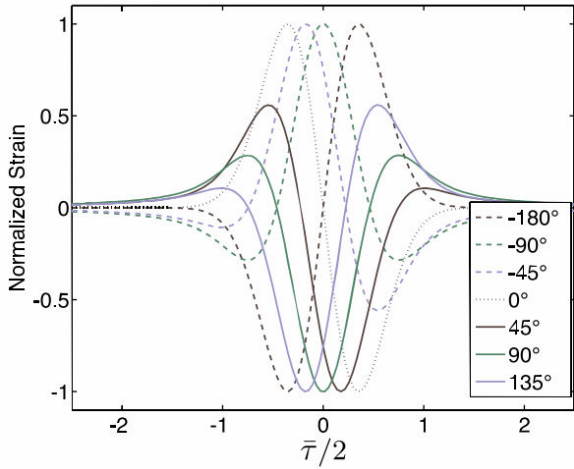


Figure A. 1. Normalized strain profiles for acoustical pulses emitted by focusing 3D Gaussian beam of Gaussian laser pulses on the interface between opaque and transparent media. Profiles are presented for various possible phases of the directivity pattern of delta-localized sources.

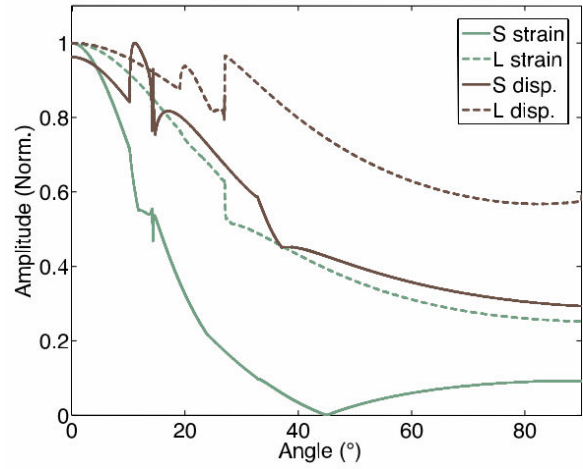


Figure A. 2. Additional modulations of delta-localized sources directivities, which are caused by finite duration of the laser pulse and finite width of the laser focus, for emission of acoustic strain and acoustic displacements in 3D geometry. The modulation functions for compression/dilatation waves are evaluated for non-dimensional parameter $\bar{\tau}_{L,l} \equiv \tau_L v_l / d = 0.59$. The modulation functions for shear waves are evaluated for non-dimensional parameter $\bar{\tau}_{L,l} \equiv \tau_L v_l / d = 0.32$.

Appendix B.

Directivity patterns of laser ultrasound emitted from mechanically free and rigid surfaces

The directivity patterns of laser ultrasound emitted due to laser-irradiation of the mechanically free surface of iron, which are computed as an asymptotic case of the general formulas in Eq. (II.23) and (II.24), are presented in Fig. B. 1.

On the one hand the comparison of Fig. B. 1 with the well-documented results existing in the literature for the mechanically free surface,^{5,6,7} confirms the validity of our analytical theory in this limiting case. On the other hand the results presented in the right column in Fig. B. 1 clearly illustrate in this simplest case the role played in the structuring of the directivity patterns by the critical angles and the zeros in the transmission/reflection coefficients, which is revealed in Section II.4. The maximum in the directivity of the amplitudes of the shear waves is near the critical angle $\theta_{t1/n} = \arcsin(v_{t1} / v_{l1}) \approx 32.8^\circ$, which manifests itself also in the directivity pattern of the phase. Above this critical angle, the shear acoustic waves are emitted in Fe due to the mode conversion in reflection from the interface of the evanescent compression/dilatation waves generated by laser radiation in Fe. Shear waves become the only wave transporting the acoustic energy from the interface. The splitting of the directivity pattern for the amplitudes of the shear waves into two lobes is caused by the absence of mode conversion of the compression/dilatation waves in reflection from a mechanically free surface at the angle of 45° ($R_{ll}^{11} = 0$). This zero reflectivity manifests itself as 180 phase jump in the directivity pattern of phase. The directivity patterns of the shear ultrasound emitted from mechanically free surface confirm the following general statement formulated in Section II.4. If

the zero in reflection/transmission coefficient for compression/dilatation wave is achieved at angles larger than the largest critical angle, then the local maximum in the amplitude directivity pattern could be achieved between this zero reflection/transmission angle and 90°, and not between the largest critical angle and 90°.

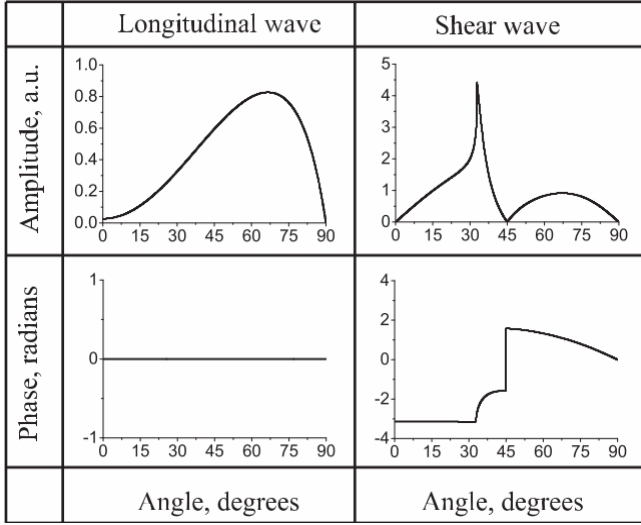


Figure B. 1. Amplitude and phase directivity patterns for longitudinal and shear ultrasound emitted by delta-localized sources, created by laser-irradiation of mechanically free surface of iron.

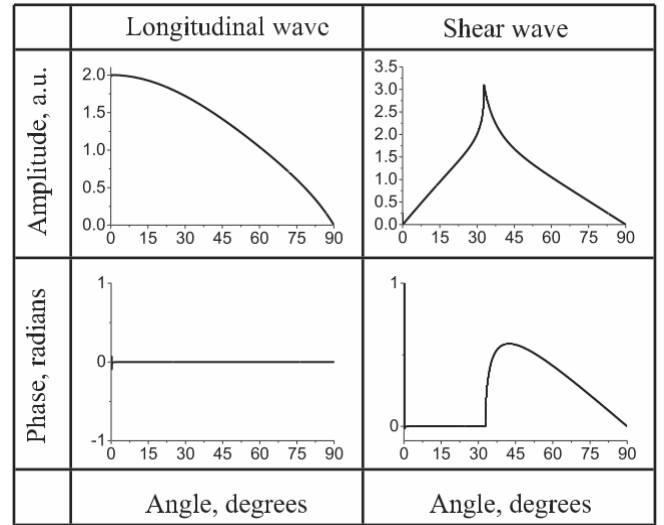


Figure B. 2. Amplitude and phase directivity patterns for longitudinal and shear ultrasound emitted by delta-localized sources, created by laser-irradiation of interface between and an infinitely rigid transparent solid media.

The directivity patterns of the laser ultrasound emitted due to laser-irradiation of the surface of iron in contact with absolutely rigid medium (2) are presented in Fig. B. 2. They are computed by importantly increasing the sound velocities and the shear rigidity in medium (2) relative to the corresponding values in diamond in Eqs. (II.23) and (II.24). We have also derived the analytical formulas for the directivity patterns of laser ultrasound in Fe, assuming the surface of Fe is immobile (surface boundary conditions of zero mechanical displacements),

$$\Xi_{\phi}(\theta) \equiv 1 + R_{ll}^{11}(\theta) = \frac{2 \cos \theta \sqrt{(\nu_{l1} / \nu_{l1})^2 - \sin^2 \theta}}{\sin^2 \theta + \cos \theta \sqrt{(\nu_{l1} / \nu_{l1})^2 - \sin^2 \theta}}, \quad (\text{B1})$$

$$\Xi_{\psi}(\theta) \equiv \frac{\cos \theta}{\sqrt{(\nu_{l1} / \nu_{l1})^2 - \sin^2 \theta}} R_{ll}^{11}(\theta) = \frac{2 \cos \theta \sin \theta}{\sin^2 \theta + \cos \theta \sqrt{(\nu_{l1} / \nu_{l1})^2 - \sin^2 \theta}}. \quad (\text{B2})$$

On the one hand the comparison of results in Fig. B. 2 with those which can be obtained directly from Eqs. (B1) and (B2), confirms the validity of our analytical theory in this limiting case. On the other hand the results presented in the right column in Fig. B. 2 clearly illustrate in this simplest case the role played in the structuring of the directivity patterns by the critical angles and the zeros in the transmission/reflection coefficients, revealed in Section II.4. The maximum in the directivity of the amplitudes of the shear waves is near the critical angle $\theta_{l1/l1} = \arcsin(\nu_{l1} / \nu_{l1}) \approx 32.8^\circ$, which manifests itself also in the directivity pattern of the phase. Above this critical angle shear acoustic waves become the only wave transporting the acoustic energy from the interface. The situation is very similar to the case of mechanically free surface, because the same single critical angle exists in both limiting cases. However in the case of absolutely rigid interface there is no splitting of the directivity pattern for the amplitudes of the shear waves into two

lobes, because there is always nonzero mode conversion into shear waves of the compression/dilatation waves in reflection ($R_{tt}^{11} \neq 0$ when $0^\circ < \theta_{t1} < 90^\circ$).

Appendix C.

On the duration of the photo-generated acoustic pulse and ultimate in-depth spatial resolution of time-domain Brillouin scattering

In depth-profiling of the spatially inhomogeneous media the in-depth spatial resolution of TDBS is known to be limited either by the spatial length of the coherent acoustic pulse or by restrictions introduced by specific signal processing techniques^{8,9}. In our experiments the coherent picosecond acoustic pulse is predominantly generated by the thermo-elastic mechanism in the iron foil, because of the negligible energy transport from iron into ice caused by weak thermal diffusivity of ice in comparison with that of iron¹⁰. As the duration of the picosecond blue pump laser pulse (1.9 ps at FWHM) exceeds the characteristic time of the longitudinal acoustic wave propagation across the region of the absorbed optical energy release in iron, the duration of the photo-generated acoustic pulse is controlled by the duration of the laser pulse¹¹. Note that the depth of lattice heating in Fe does not importantly broaden relative to the depth of the blue light penetration, because of the relatively strong coupling of the electrons and the phonons in Fe. Even for the overestimated depth of the energy release zone, 15 nm at FWHM, the time of sound propagation across it with the velocity of $8.4 \cdot 10^3$ m/s Ref.¹² is shorter than the duration of the laser pulse. So the length of the coherent acoustic pulse launched into the ice sample near its interface with the Fe foil is estimated to be of about 30 nm at pressures of the experiment. This provides the best possible in-depth spatial resolution unless the amplitude of the launched pulse is so strong that the nonlinear acoustic effects could lead to weak shock front formation. In the latter case, which is actually not realized in our experiments, the spatial resolution could be controlled by the width of the shock front, which could be shorter than the width of the initially launched acoustic pulse^{13,14}. In our linear case the situation is, in a certain sense, opposite to the case of the nonlinear acoustics. Due to the preferential absorption and scattering of high frequency components, the initially launched coherent acoustic pulse is continuously broadening along its propagation path. However, the abrupt variations in the Brillouin oscillations amplitude and frequency observed experimentally by passing the ice/diamond interface (Figs. IV. 3 (c) and 2 (a)) indicate that the acoustic pulse is shorter than the Brillouin period even when arriving at the end of the ice sample. Thus, the duration of the acoustic pulses does not influence the spatial resolution of the images obtained in the present Communication provided the moving time windows are equal to or larger than the Brillouin period.

Appendix D.

On the role of the induced optical anisotropy

In optically anisotropic grains the light experiences double or triple refraction and the optical rays, characterized by different refractive indexes, propagate after refraction with different velocities, which in addition depend on the direction of rays propagation relative to crystallographic axes^{15,16}. However the ices VII and X of our interest here are cubic and, thus, optically isotropic. Consequently, the variations of the refractive index n could be caused in our samples only by anisotropy induced by nonhydrostatic stress component, i.e., due to uniaxial loading¹⁷. Strong induced anisotropy could potentially cause splitting of the Brillouin frequency peak in TDBS experiments conducted with linearly polarized light¹⁸. The splitting effect in polarized probe light is replaced by broadening and shift of the Brillouin frequency line in our experiments conducted with circular polarized light. Note that even under uniaxial loading cubic crystals in general become biaxial¹⁵ and exhibit triple refraction. An order-of-magnitude estimates demonstrate that induced optical anisotropy is negligible in our

experiments. For example, in the experiments we consider as conducted at 84 GPa, this pressure was measured in the centre of the DAC where the data were accumulated, while at the edge of the ice sample at the distance $R=D/2=45 \mu\text{m}$ from the centre the measured pressure was by $\Delta P = 4 \text{ GPa}$ lower. This suggests presence of a uniaxial stress component parallel to the load axis of the DAC which value t can be estimated from $t \approx H(\Delta P/R)$, e.g. Ref.¹⁹ where the thickness H of the sample is $13.5 \mu\text{m}$. In the considered case we obtained $t \approx 1 \text{ GPa}$. The characteristic value of the photo-elastic (acousto-optic) parameter $\partial n/\partial P$ can be estimated from the experimental curve $n = n(P)$ in Fig. 3 of Ref. 25 by $\partial n/\partial P \approx 10^{-3} \text{ 1/GPa}$ at 84 GPa. Thus, an order-of-magnitude estimate for the possible difference in the refractive indexes of different optical rays in nonhydrostatically compressed H_2O ice is $\Delta n \propto (\partial n/\partial P)t \approx 10^{-3}$. For the refractive index of $n \approx 1.8$, estimated from the data in Ref.²⁰ at $P=84 \text{ GPa}$ for the probe wavelength of 808 nm, this results in $\Delta n/n \propto 5 \cdot 10^{-4}$, indicating that the variations of the refraction index in equation (IV.1) is largely negligible. However, in view of the complexity of the phenomena of stress-induced anisotropy and of the lack of data on the photoelastic tensor of H_2O ice VII and X, we conducted additional test experiments with variable linear polarisation of the probe beam. In Fig. IV. 7 (a) we present three dependences on time of the Brillouin frequency, which are extracted from TDBS signals detected at 50 GPa in the same position of the sample but using instead of circularly polarized probe light linearly polarized light of three different polarizations rotated in steps of 60 degrees. The results in Fig. IV. 7 (a) indicate that in our experimental system there are polarization-dependent effects. However, there could be different physical phenomena contributing to the variation of the Brillouin frequency with the polarization of probe light in Fig. IV. 7 (a). The experimentally observed shifts in Brillouin frequency could be attributed to the stress-induced optical anisotropy of cubic ice only under the conditions that only the polarization of the probe light incident on the surface of the ice is changing, when we rotate its polarization outside the DAC. Only in this case the experiments provide direct access to the refractive indexes of the different probe rays in cubic ice with stress-induced anisotropy, because the only variable parameter influencing the detected Brillouin frequency will be the distribution/repartition of probe light among different rays interacting with the acoustic pulse. However, in general, this ideal condition is difficult to achieve because, firstly, the position of light beam incident on the diamond, and consequently on the ice, could be slightly shifted when optical elements are used to rotate its polarization and, secondly, the position of the probe, the shape of the light focus and the polarization of the probe on the ice surface all could be influenced by polarization-dependent optical phenomena in diamond, caused by its natural optical anisotropy and important induced optical anisotropy due to strongly nonuniform stress generated in the uniaxially loaded anvils²¹⁻²³. For example, the shift of the probe focus and modification of its shape on the surface of the ice could cause the shift of the detected Brillouin frequency even in case of negligible induced optical anisotropy of cubic ice if the photo-generated acoustic pulse propagates simultaneously across just two or more crystallites with different sound velocities along acoustic pulse propagation direction. In this case rotation of probe light polarization incident on the DAC could cause the redistribution of the probe light incident on the different parts of the acoustic beam cross section and to possible modification of the Brillouin frequency, because different cross sections of the acoustic beam are propagating with different velocities. It is worth mentioning, that stresses in the diamond anvils cause optical anisotropy of the anvils even close to their symmetry axis. They were reported to result, for example, in distortion/transformation of the initially linearly polarised laser light into elliptical²⁴. Although currently we are not able to identify precisely the physical reasons of the polarization-dependent effect reported in Fig. IV. 7 (a), we believe this experimental test clearly indicates the weakness of the effect. Relative changes of Brillouin frequency in Fig. IV. 7 (a) do not exceed 2 %. Thus, variations of the refractive index in equation (IV.1) cannot be responsible for the 20% variations in the Brillouin frequency revealed in Figs. IV. 4 and 6 and could be neglected when using equation (IV.1) for the estimates of the acoustic velocity.

Appendix E.

On the role of the acoustic rays refraction

The following considerations indicate that the dependence of the BS frequency on $\cos\theta$ can be neglected in equation (IV.1) in comparison with the dependence on the sound velocity. When the acoustic wave is incident obliquely from an elastically isotropic medium (1) on its interface with an elastically isotropic medium (2) the direction of the transmitted wave shifts from the direction of the incident wave by a certain angle θ' . If we denote by $v_{1,2}$ the sound velocities in the first and the second medium, respectively, then in the case $v_1 > v_2$ the maximum refraction takes place at grazing incidence ($|\theta'|_{\max} = \pi/2 - \arcsin(v_2/v_1)$), while in the case $v_1 < v_2$ it takes place at critical angle of incidence $\theta_{cr} = \arcsin(v_1/v_2)$ ($|\theta'|_{\max} = \pi/2 - \theta_{cr} = \pi/2 - \arcsin(v_1/v_2)$). It is worth noting that refraction angle relative to the initial propagation direction, accumulated through successive incidence at different angles on multiples interfaces, can't exceed the maximum refraction angle of single scattering. The maximum refraction angle obviously diminishes with diminishing difference between the acoustic velocities in the contacting materials. In the limiting case of small difference of sound velocities, denoting $v_1 = (v_1 + v_2)/2 + (v_1 - v_2)/2 \equiv \langle v \rangle + \Delta v$ and $v_2 = \langle v \rangle - \Delta v$, with $|\Delta v|/\langle v \rangle \ll 1$, we estimate $|\theta'|_{\max} \approx |\Delta v|/\langle v \rangle$. This clear asymptotic result indicates that in polycrystalline samples with a weak elastic anisotropy of grains, i.e., with $|\Delta v|/\langle v \rangle \ll 1$, the contribution to relative variations of the Brillouin frequency $\Delta f_B / \langle f_B \rangle$ in Eq. (IV.1), which is coming from the directional variations in the sound velocity and is proportional to $\Delta v / \langle v \rangle$, dominates over the contribution due to possible refraction of sound, which is proportional to $\Delta(\cos\theta) / \langle \cos\theta \rangle \leq 1 - \cos(|\theta'|_{\max}) \approx (\Delta v / \langle v \rangle)^2 \ll |\Delta v| / \langle v \rangle$. In these estimates, for the values of $v_{1,2}$ we should use the values of the maximum and the minimum values of the direction-dependent sound velocity in the microcrystals. From the experimental data on the elastic moduli of H₂O ice at 40 GPa presented in Ref.²⁵ we estimate that the maximum longitudinal velocity (in [111] direction) is about 20% higher than the minimum longitudinal velocity (in [100] direction). This provides $|\Delta v|/\langle v \rangle \leq 0.1$ and indicates that the contribution of variations in θ to the variations in the Brillouin frequency in equation (IV.1) is at the level below 1%. Although in accordance with Ref.²⁵ the anisotropy increases with increasing pressure, we believe that even in our experiments, which are conducted at higher pressures, the variations in the Brillouin frequency from grain to grain are largely dominated by possible changes in the sound propagation velocity and not in the sound propagation direction. In fact in our experimental results in Fig. IV. 5, revealing large-scale texturing both at 57 GPa and 84 GPa, the maximum changes of the Brillouin frequency relative to the average level are about 10% ($|\Delta f_B|/\langle f_B \rangle \leq 0.1$) and then $\Delta(\cos\theta) / \langle \cos\theta \rangle \leq 0.01$. Even when superposing the short-scale texturing revealed in Fig. IV. 6 (a) and (b) with the large scale texturing in Fig. IV. 5 (b) the maximum changes of the Brillouin frequency relative to the average level in Fig. IV. 6 (c) are about 20% ($|\Delta f_B|/\langle f_B \rangle \leq 0.2$, $\Delta(\cos\theta) / \langle \cos\theta \rangle \leq 0.04$). Consequently, in accordance with above presented estimates, the dependence on $\cos\theta$ in Eq. (IV. 1) is largely dominated by the dependence on the acoustic velocity.

Appendix F.

On the amplitude of the time-domain Brillouin scattering signal

The following considerations indicate the dominant role of the photo-elastic and elastic anisotropy of cubic ice in the experimentally observed variations of the TDBS signal amplitude by propagation

through the sample. In principle, the non-monotonous changes in the amplitude of the oscillations revealed in TDBS (Fig. IV. 3 (c)) could be caused by beatings/interference between two or more oscillations at different frequencies. Simultaneous detection of several frequencies by TDBS would be expected if, for example, the elastically isotropic opto-acoustic generator, Fe-foil in our case, launches in elastically anisotropic H₂O ice not only the quasi-longitudinal acoustic pulse, which currently dominates in all our signals, but also one or two quasi-transverse acoustic pulses, propagating at velocities importantly slower than the quasi-longitudinal one and resulting in TDBS signals at very different frequencies. Generation of quasi-shear acoustic pulses by mode conversion of the longitudinal acoustic pulses at the interface between isotropic light absorbing photo-acoustic generator and anisotropic transparent elastic media was earlier reported²⁶, and beatings in the TDBS signals, caused by the interference of the Brillouin oscillations induced by quasi-longitudinal and quasi-shear waves, were observed²⁶⁻³⁰. Our experiments currently indicate that either the mode conversion of the longitudinal pulse into quasi-shear pulses at the Fe/ice interface and the mode conversion of quasi-longitudinal pulse into quasi-shear pulses at the interfaces between differently oriented crystallites are inefficient or the photo-elastic detection of quasi-shear waves is inefficient, or both. Several frequencies can be potentially found in TDBS signals in optically anisotropic media because of splitting of the probe laser beam in such media into two or three independent beams, which are characterized by different values of the refractive indexes¹¹. However, cubic H₂O ice is optically isotropic and our additional testing measurements have demonstrated that optical anisotropy, induced by possible deviation of mechanical loading of crystallites in DAC from the hydrostatic conditions, is negligibly small (see Fig. IV. 7). It is also worth mentioning here that the period of possible beatings in TDBS signal amplitude, when two oscillations at different frequencies, f_1 and f_2 , are contributing to it, is equal to $1/|f_1-f_2|$. Thus, even if we estimate the difference between frequencies corresponding to ordinary and extraordinary light, $|f_e-f_o|$, by double frequency shift detected in Fig. IV. 7, i.e., about 2 GHz, the expected beating period will be 500 ps, i.e., much longer than the time interval where birefringence is observed in this Figure. This is an additional argument in favor of the conclusion that the observed non-monotonous variations of TDBS signal amplitude are not caused by optical anisotropy.

Finally, the detection of several frequencies could be expected in polycrystalline samples if the photo-generated acoustic pulse and the probe light propagate simultaneously across several differently oriented crystallites. This could be possible not only if the diameters of the acoustic and probe laser beams are importantly larger than the characteristic dimension of the grains in lateral direction, i.e., in the plane parallel to the surface of the photo-generator, but also in the case when they are narrower than the individual grains but propagate along an interface of two grains, which is inclined relative to sound propagation direction, or they propagate along the interface separating larger groups of similarly oriented crystallites. In our experiments reported here the diameters of the acoustic and the probe beams are exceeding the estimated dimensions of the individual crystallites, so the first and the third of the mentioned situations seem to be more relevant. However, in both these cases the situations when the cross section areas of the acoustic pulse in two differently oriented domains of ice are close in magnitude, leading to two oscillations of comparable amplitudes and to possibility of important beatings, are rare. In fact, in the experimental data presented in Fig. IV. 5 the signal processing has not revealed two frequency peaks of comparable amplitudes along the complete paths of the photo-generated acoustic pulses.

The above discussion leads to the conclusion that non-monotonous variations of the TDBS signal amplitude in time are not manifestation of beatings/interference among different frequency components of the signal. They are rather the second, in addition to Brillouin frequency variation, direct manifestation of disorientation of grains or group of grains in our polycrystalline H₂O sample.

References(A)

1. W. M. Ewing, W. S. Jardetzky, F. Press, *Elastic Waves in Layered Media* McGRAW-HILL, New York, (1957).
2. G. F. Miller, H. Purcey, *The Field and Radiation Impedance of Mechanical Radiators on the Free Surface of a Semi-Infinite Isotropic Solid* **Proc. R. Soc. London Ser. A** **223**, 521 (1954).
3. N. Chigarev, P. Zinin, L-C. Ming, G. Amulele, A. Bulou, V. Gusev, *Laser generation and detection of longitudinal and shear acoustic waves in a diamond anvil cell* **Appl. Phys. Lett.** **93**, 181905 (2008).
4. P. V. Zinin, N. Chigarev, D. Mounier, A. Bulou, L. C. Ming, T. Acosta, V. Gusev, *Evaluation of elastic properties of iron in diamond anvil cell by laser ultrasonics technique* **J. Phys.: Conf. Series** **215**, 012053 (2010).
5. P. Zhang, C. F. Ying, J. Shen, *Directivity patterns of laser thermoelastically generated ultrasound in metal with consideration of thermal conductivity* **Ultrasonics** **35**, 238 (1997).
6. B. Yuhai, P. Liwei, F. Qiping, Y. Yuping, Y. Chongfu, *Experimental studies of directivity patterns of laser generated ultrasound in neutral glasses* **Ultrasonics** **33**, 429 (1995).
7. W. Japing, S. Dufang, H. Yulong, *Study of the directivity of laser generated ultrasound in solids* **J. Appl. Phys.** **83**, 1207 (1998).
8. Lomonosov, A. M. et al. *Noncontact subsurface investigations of mechanical and optical properties of nanoporous low-k material thin film.* **ACS Nano** **6**, 1410 (2012).
9. Mechri, C. et al. *Depth-profiling of elastic inhomogeneities in transparent nanoporous low-k materials by picosecond ultrasonic interferometry.* **Appl. Phys. Lett.** **95**, 091907 (2009).
10. Nikitin, S. M. et al. *Directivity patterns and pulse profiles of ultrasound emitted by laser action on interface between transparent and opaque solids: Analytical theory.* **J. Appl. Phys.** **115**, 044902 (2014).
11. Gusev, V. & Karabutov, A. *Laser Optoacoustics* (AIP, New York, 1993).
12. Fiquet, G., Badro, J., Guyot, F., Requardt, H. & Krisch, M. *Sound velocities in iron to 110 gigapascals.* **Science** **291**, 468 (2001).
13. Gusev, V. *Detection of nonlinear picosecond acoustic pulses by time-resolved Brillouin scattering.* **J. Appl. Phys.** **116**, 064907 (2014).
14. Klieber, C., Gusev, V. E., Pezeril, T. & Nelson, K. A. *Nonlinear acoustics at GHz frequencies in a viscoelastic fragile glass former.* <http://arxiv.org/abs/1403.3222> (2014).
15. Born, M. & Wolf, E. *Principles of Optics* (Pergamon Press, London, 1970).
16. Ramachandran, G. N. & Ramaseshan, S. in *Encyclopedia of Physics* (ed. Flugge, S.) 1-217 (Springer, Berlin, 1961).
17. Singh, A. K. *The lattice strains in a specimen (cubic system) compressed nonhydrostatically in an opposed anvil device.* **J. Appl. Phys.** **73**, 4278 (1993).
18. Lejman, M. et al. *Giant ultrafast photo-induced shear strain in ferroelectric BiFeO₃.* **Nat. Commun.** **5**, 4301 (2014).
19. Eremets, M. *High pressure experimental methods* (Oxford University Press, Oxford, 1996).
20. Zha, C.-S., Hemley, R. J., Gramsch, S. A., Mao, H.-K. & Bassett, W. A. *Optical study of H₂O ice to 120 GPa: dielectric function, molecular polarizability, and equation of state.* **J. Chem. Phys.** **126**, 074506 (2007).
21. Bruno, M. S. & Dunn, K. J. *Stress analysis of a beveled diamond anvil.* **Rev. Sci. Instrum.** **55**, 940-943 (1984).
22. Hanfland, M. & Syassen, K. *A Raman study of diamond anvils under stress.* **J. Appl. Phys.** **57**, 2752-2756 (1985).
23. Merkel, S., Hemley, R. J., Mao, H.-K. & Teter, D. M. in *Science and Technology of High Pressure, Proceedings of the AIRAPT-17* (eds. Manghnani, M. H., Nellis, W. J. & Nicol, M. F.) 68-73 (University Press, Hyderabad, 2000).
24. Ninet, S., Datchi, F., Saitta, A. M., Lazzeri, M. & Canny, B. *Raman spectrum of ammonia IV.* **Phys. Rev. B** **74**, 104101 (2006).
25. Zha, C.-S., Mao, H.-K., Hemley, R. J. & Duffy, T. S. *Recent progress in high-pressure Brillouin scattering: olivine and ice.* **Rev. High Pressure Sci. Technol.** **7**, 739 (1998).
26. Bienville, T. & Perrin, B. in *Proceedings of the World Congress on Ultrasonics 2003*, 813-816 (Paris, 2003).
27. Matsuda, O., Wright, O., Hurley, D., Gusev, V. & Shimizu, K. *Coherent shear phonon generation and detection with ultrashort optical pulses.* **Phys. Rev. Lett.** **94**, 095501 (2004).

28. Matsuda, O., Wright, O. B., Hurley, D. H., Gusev, V. E. & Shimizu, K. *Coherent shear phonon generation and detection with picosecond laser acoustics.* **Phys. Rev. B** **77**, 224110 (2008).
29. Ruello, P. et al. *Photoexcitation of gigahertz longitudinal and shear acoustic waves in BiFeO₃ multiferroic single crystal.* **Appl. Phys. Lett.** **100**, 212906 (2012).
30. Wen, Y.-C., Ko, T.-S., Lu, T.-C., Kuo, H.-C. & Chyi, J.-I. S., C.-K. *Photogeneration of coherent shear phonons in oriented wurtzite semiconductors by piezoelectric coupling.* **Phys. Rev. B** **80**, 195201 (2009).

Abstract

Knowledge of pressure-dependences of sound velocities and elastic moduli of liquids and solids at Megabar pressures and evolution of texture of polycrystalline solids on compression is of extreme importance for a few branches of natural sciences such as condensed matter physics, physics of the Earth and planetology, as well as for monitoring and predicting of earthquakes and tsunamis or nuclear weapons test control.

This PhD research work is devoted to the use of laser ultrasound in high-pressure physics. The research is done using the recently established technique of laser ultrasonic measurements in a diamond anvil cell which allows investigation of the sound propagation and determination of the acoustic wave velocities at ultrahigh pressures. Time domain Brillouin scattering was applied here to depth-profiling of polycrystalline aggregate of ice compressed in a diamond anvil cell to Megabar pressures. The technique allowed examination of characteristic dimensions of elastic inhomogeneities and texturing of polycrystalline ice in the direction, normal to the diamond anvil surfaces with sub-micrometer spatial resolution via time-resolved measurements of variations in the propagation velocity of the acoustic pulse travelling in the compressed sample. It was applied to measure the acoustic velocities in H₂O ice up to 84 GPa. The developed imaging technique provides, for each crystallite (or a group of crystallites) in chemically homogeneous transparent aggregate, usable information on its orientation as well as on the value of the elastic modulus along the direction of the sound propagation. This extends the basis for a successful application of highly developed micromechanical models of solids deformation at Mbar pressure. On long term, such experiments extended to Earth's minerals and high or low temperatures would insure a significant progress in understanding of convection of the Earth's mantle and thus evolution of this and other planets.

Auxiliary experiments to determine the thickness of the ice in the diamond anvil cell and the refractive index of ice under pressure are described. These measurements are based on broadband interference of light in diamond anvil cell. Two different ways of measuring the refractive index of ice are considered. Refractive index of ice was measured by both methods up to 31 GPa. The thickness, transverse size and the volume of ice as function of pressure are obtained.

Analytical description for the directivity patterns of ultrasound, emitted from the laser-irradiated interface between two isotropic solids, is developed. The directivity patterns are derived both in two-dimensional and in three-dimensional geometries by accounting for the specific features of the sound generation by the photo-induced mechanical stresses distributed in the volume, essential in the laser ultrasonics. The derived mathematical formulas provide straight opportunity to predict the acoustic field, which is formed in the diamond anvil cell after photo-generation and several reflections of bulk acoustic waves at the interfaces. The developed theory can be applied in the future for the dimensional scaling of the laser ultrasonic measurements in a diamond anvil cell, the optimization of these experiments and the interpretation of the experimental results.

Key words: *picosecond laser ultrasonics, high pressure, diamond anvil cell, condensed matter (H₂O), analytical theory of laser ultrasound in diamond anvil cell, refractive index of transparent media at high pressures, Brillouin oscillations, acoustic properties of H₂O up to 84 GPa.*